

# Silicon Vacancy Colour Centres in Diamond: Coherence Properties & Quantum Control

Dissertation

zur Erlangung des Grades  
des Doktors der Naturwissenschaften  
der Naturwissenschaftlich-Technischen Fakultät  
der Universität des Saarlandes

von

Jonas Nils Becker

Saarbrücken

2017

Tag des Kolloquiums: 18.12.2017

Dekan: Univ.-Prof. Dr. Guido Kickelbick

Mitglieder des Prüfungsausschusses: Univ.-Prof. Dr. phil. Christopher Kay  
Univ.-Prof. Dr. Christoph Becher  
Univ.-Prof. Dr. Gregor Jung  
Prof. Dr. Jean-François Roch  
Dr. Herbert Wolf

# Eidesstattliche Versicherung

Hiermit versichere ich an Eides statt, dass ich die vorliegende Arbeit selbstständig und ohne Benutzung anderer als der angegebenen Hilfsmittel angefertigt habe. Die aus anderen Quellen oder indirekt übernommenen Daten und Konzepte sind unter Angabe der Quelle gekennzeichnet. Die Arbeit wurde bisher weder im In- noch im Ausland in gleicher oder ähnlicher Form in einem Verfahren zur Erlangung eines akademischen Grades vorgelegt.

**Ort, Datum**

---

**Unterschrift**

---



# Abstract

The scope of this thesis is to investigate the coherence properties of negatively charged silicon vacancy centres ( $\text{SiV}^-$ ) in diamond and to establish techniques to coherently control their quantum state, aiming at applications in quantum information processing. For the first time, using coherent population trapping (CPT) in magnetic fields, we determine the centres ground state electron spin coherence time to amount to 45 ns at 4.2 K. To investigate the limiting processes, we realize a confocal microscope operating in a dilution refrigerator at temperatures as low as 12 mK. Using further CPT and optical pumping experiments, we identify a resonant coupling to a spin bath as a source of decoherence persisting at millikelvin temperatures, in addition to phonon-mediated processes at higher temperatures. Using Raman transitions we realize optical Rabi oscillations, Ramsey interference and spin echo measurements to validate these findings and simultaneously demonstrate coherent control at 12 mK. We further extend these techniques to achieve full resonant and Raman-based all-optical coherent control using laser pulses as short as 1 ps, reaching exceptional control speeds. Finally, we demonstrate for the first time coherent manipulation of  $\text{SiV}^-$  ensembles using stimulated Raman adiabatic passage and Raman absorption of a weak signal aided by a strong control pulse as a proof-of-principle experiment towards a  $\text{SiV}^-$ -based Raman quantum memory.



# Kurzzusammenfassung

In dieser Arbeit werden die Kohärenzeigenschaften negativ geladener Silizium-Fehlstelle-Farbzentren ( $\text{SiV}^-$ ) in Diamant untersucht und Techniken zu deren kohärenter Kontrolle entwickelt, mit dem Ziel sie für die Quanteninformationsverarbeitung nutzbar zu machen. Mittels "coherent population trapping" (CPT) in Magnetfeldern wird erstmals die Elektronenspin-Kohärenz einzelner  $\text{SiV}^-$  bestimmt und eine Kohärenzzeit von 45 ns bei 4.2 K ermittelt. Weitere Untersuchungen in einem Verdünnungskryostat bei Temperaturen von bis zu 12 mK identifizieren eine resonante Kopplung an ein Spinbad als wichtigste Quelle von Dekohärenz im Millikelvin-Regime, während bei höheren Temperaturen zusätzlich Phononen-assistierte Prozesse relevant werden. Dies wird durch Raman-basierte optische Rabi-, Ramsey- und Spin Echo-Experimente bestätigt, welche gleichzeitig kohärente Kontrolle bei 12 mK demonstrieren. Unter Verwendung ultrakurzer Laserpulse werden diese Techniken schließlich erweitert und erstmalig resonante sowie Raman-basierte optische kohärente Kontrolle auf der Pikosekunden-Skala realisiert. Abschließend wird auch die kohärente Manipulation von  $\text{SiV}^-$ -Ensembles untersucht und kohärenter Populationstransfer mittels stimuliertem adiabatischem Raman-Transfer sowie Raman-Absorption eines schwachen Signals mittels eines starken Kontrollfelds demonstriert. Diese Experimente bilden die Grundlage für die Entwicklung eines  $\text{SiV}^-$ -basierten optischen Quantenspeichers.



# Contents

<b>Introduction</b>	<b>i</b>
<b>1 The silicon vacancy colour centre in diamond</b>	<b>1</b>
1.1 The diamond host lattice . . . . .	1
1.1.1 Crystallographic properties . . . . .	1
1.1.2 Physical properties . . . . .	3
1.1.3 Natural diamonds & diamond synthesis . . . . .	4
1.2 The silicon vacancy . . . . .	6
1.2.1 Charge state & constituents . . . . .	6
1.2.2 Spectral properties . . . . .	7
1.2.3 Structural properties . . . . .	11
1.2.4 Electronic structure . . . . .	12
<b>2 Light-matter interactions</b>	<b>23</b>
2.1 A two-level atom interacting with light . . . . .	24
2.1.1 The two-level Hamiltonian . . . . .	24
2.1.2 Optical Bloch equations and the density matrix . . . . .	26
2.1.3 Rabi oscillations, Ramsey interference and Hahn echo . . . . .	29
2.2 Coherence in three-level systems . . . . .	33
2.2.1 Autler-Townes splitting, coherent population trapping and electro- magnetically induced transparency . . . . .	34
2.2.2 Stimulated Raman adiabatic passage . . . . .	36
2.3 The double- $\Lambda$ system . . . . .	39
<b>3 Sample preparation &amp; optical setups</b>	<b>43</b>
3.1 Fabrication of single-emitter samples . . . . .	44
3.1.1 Diamond substrate pre-selection . . . . .	44
3.1.2 Silicon ion implantations . . . . .	46
3.1.3 Fabrication of solid immersion lenses . . . . .	49
3.2 Fabrication of ensemble samples . . . . .	53
3.3 Optical setups . . . . .	54
3.3.1 The confocal microscope . . . . .	55
3.3.2 The coherent population trapping experiment . . . . .	58
3.3.3 The dilution refrigerator experiment . . . . .	61

3.3.4	The coherent control experiment . . . . .	69
<b>4</b>	<b>Experimental results I: Single SiV<sup>-</sup> centres</b>	<b>73</b>
4.1	Sample & emitter properties . . . . .	74
4.2	Coherent population trapping . . . . .	78
4.3	Millikelvin experiments . . . . .	88
4.3.1	Measurement of orbital and spin relaxation rates . . . . .	88
4.3.2	Measurement of ground state spin coherence . . . . .	96
4.4	Ultrafast all-optical coherent control . . . . .	103
4.4.1	Resonant coherent control . . . . .	106
4.4.2	Transition dipole moments & quantum efficiency . . . . .	108
4.4.3	Raman-based ground state control . . . . .	112
<b>5</b>	<b>Experimental results II: ensembles of SiV<sup>-</sup> centres</b>	<b>119</b>
5.1	Concept of a Raman quantum memory . . . . .	120
5.2	Ultrafast Ramsey interference and Hahn echo . . . . .	125
5.3	Stimulated Raman Adiabatic Passage . . . . .	127
5.4	Raman absorption . . . . .	130
<b>6</b>	<b>Outlook &amp; Summary</b>	<b>139</b>
6.1	Outlook . . . . .	139
6.2	Summary . . . . .	144
6.2.1	Single SiV <sup>-</sup> centres . . . . .	144
6.2.2	SiV <sup>-</sup> ensembles . . . . .	146
	<b>Appendices</b>	<b>149</b>
<b>A</b>	<b>MATLAB scripts &amp; functions</b>	<b>151</b>
A.1	Simulations of coherent population trapping . . . . .	151
A.2	Coherent control and ensemble simulations . . . . .	154
<b>B</b>	<b>Transmission &amp; reflection curves</b>	<b>159</b>
B.1	Fabry-Pérot etalon properties . . . . .	159
B.2	Dilution refrigerator windows . . . . .	160
	<b>Bibliography</b>	<b>161</b>
	<b>Publications</b>	<b>181</b>





# Introduction

Information processing using classical silicon-based computers experienced an exceptionally rapid growth over the past decades and fundamentally influenced our everyday life as well as research and technological development in many different ways. In such a classical computer information is encoded in binary digits (bits), which can take on two different basis states, 0 or 1. This information is then processed using Boolean logic, i.e. a set of basic logic gates such as AND, OR or NOT, each of which can in turn be represented by a combination of so-called universal gates like NAND (not-AND) or NOR (not-OR) [1]. In modern computers, these gates are implemented in silicon-based integrated circuits using transistors and the bit values are represented by voltage amplitudes [2]. Lithographic processes enable the fabrication of billions of transistors on a single chip with structure sizes currently reaching down to 14 nm. The computational power of such a chip is fundamentally limited by the number of gates i.e. the amount of transistors per device. Already in 1965, Gordon Moore, co-founder of Intel, predicted a doubling of the number of transistors in a computer chip each year [3]. While in reality a slightly slower evolution with a doubling every 18 months has been observed, even today's most modern computer chips still obey this rule, widely known as "Moore's law". However, classical computing has two major limitations: First, the binary nature of this type of computing imposes some fundamental limits to the way such a device performs calculations and certain computational tasks cannot be computed efficiently at all using a classical machine, even on the most modern supercomputers [4]. Examples for such tasks are e.g. the factorization of large prime numbers [5], certain optimization problems such as the famous travelling salesman problem [6] or the precise calculation of physical, chemical or biological properties of complex compounds [7]. Secondly, while transistors are expected to shrink even further, allowing even more of them to be fabricated on a chip, this trend cannot go on indefinitely with structure sizes approaching atomic limits [8]. At this point classical physics will break down and the properties of such a computer chip will be governed by the rules of quantum mechanics, rendering conventional information processing impossible [9].

In contrast to classical computing, quantum information processing (QIP) systems attempt to turn the emergence of quantum mechanical phenomena at atomic scales into a powerful tool. A device deliberately harnessing such effects could overcome many of the above-mentioned limitations and developing it has triggered significant efforts in fundamental research and engineering in the past decades [10]. The basic computational unit of such a QIP device is the quantum bit (qubit) [11]. Just like its classical equivalent the qubit is constructed from two orthonormal basis states which in quantum mechanics are represented by two state vectors  $|0\rangle$  and  $|1\rangle$ . However, in contrast to the bit, a qubit

cannot only take on two discrete values but also arbitrary superpositions of the form  $|\Psi\rangle = \alpha|0\rangle + \beta|1\rangle$  with  $\alpha^2 + \beta^2 = 1$ . Thus, figuratively speaking, a qubit represents 0 and 1 at the same time, giving rise to a unique way of processing information oftentimes termed "quantum parallelism" [12]. This feature allows a quantum computer utilizing quantum algorithms to tackle problems that cannot be computed on classical machines such as prime number factorization [13] or searching large, unsorted databases [14]. Moreover, QIP devices have additional applications such as quantum cryptography [15] for provably secure communication, metrology [16] or quantum simulation [7] with fascinating applications in materials science and pharmacological research.

To construct a qubit, in principle, any quantum mechanical system with at least two distinct energy levels will do. In reality however, a system has to fulfil the following list of criteria, defined by D. DiVincenzo, to be suitable to form a basic building block of a QIP technology [17]:

1. **A scalable and well-defined physical system** To realize a QIP device with meaningful computational capabilities a single qubit does not suffice but a larger number of qubits forming a collective quantum state is necessary. The qubits are then said to be entangled, meaning that their state cannot be written as a simple product of single-qubit states and for N qubits its dimensionality scales as  $2^N$ . This exponential scaling is a major advantage compared to classical machines, the computational power of which only scales linearly with the number of bits. Therefore, a few tens of qubits is already enough to realize a powerful quantum computer with real-world applications. An important prerequisite for the qubits to become entangled also is their indistinguishability, a challenging property especially in solid state matrices where environmental effects tend to locally alter qubit properties. Moreover, the term "well-defined" refers to the fact that the internal level structure and dynamics of the qubit is well-known.
2. **A method to initialize the qubits** Before starting a computation the system consisting of N qubits needs to be initialized into a defined common state such as  $|00\dots0\rangle$ . This can either be achieved by simply letting the system relax into its ground state or, a suitable system provided, by pumping the system into a defined state by e.g. applying optical fields.
3. **Long relevant coherence times** The coherence time of a qubit can be understood as the time it takes for the superposition state  $|\psi\rangle = \alpha|0\rangle + \beta|1\rangle$  to decay into a statistical mixture  $\rho = |\alpha|^2|0\rangle\langle 0| + |\beta|^2|1\rangle\langle 1|$ , that is a state of independent quantum systems without fixed phase relations. This time scale should be much longer than the time needed for a single quantum gate operation. Thus, even if the coherence time of a qubit is short, it can be a viable system for local QIP as long as it can be manipulated rapidly. As a benchmark, DiVincenzo suggested coherence times  $10^4$ - $10^5$  times longer than the gate operation time of the qubit mainly because this allows the implementation of quantum error correction protocols [18].
4. **A universal set of quantum gates** To implement an arbitrary quantum algorithm on a quantum computer a set of quantum logic gates needs to be implemented. Luckily,

it can be shown that, much like in classical computation, arbitrary operations can be realized by a full set of single qubit gates (that is arbitrary control over phase and amplitude of the components of a single-qubit superposition state) as well as a single universal two-qubit gate like the controlled-NOT (CNOT) gate, which flips the state of a target qubit if and only if the control qubit is in  $|1\rangle$  [19].

5. **A qubit-specific measurement capability** To complete a computational task on a QIP system the final state of a target qubit needs to be measured. This measurement should be qubit-specific, i.e. it should leave the rest of the system unperturbed and ideally should be non-destructive, that is it should even leave the state of the target qubit unaltered to allow for subsequent use.

In the past years many different quantum systems [20] have been studied as individual qubits as well as basic multi-qubit systems, amongst them trapped ions [21,22], neutral atoms [23], semiconductor quantum dots [24,25], nitrogen-vacancy centres in diamond [26–28], nuclear spins in molecules [29,30] and superconducting circuits [31,32]. While all of these qubit candidates fulfil some of the criteria above, none of them is convincingly complying with all of them [33]. While the level structures of all these systems are very well understood and specific initialization, manipulation and readout schemes have been developed for most of them, especially scalability remains a recurring issue with many of these systems for fundamentally different reasons: In the case of trapped ions or atoms for example, the indistinguishability of several individual qubits is nearly perfect [34] but photonic interfacing of these systems remains challenging due to limited light collection efficiencies. In contrast to this, solid state-based qubits such as quantum dots are oftentimes favoured as these platforms allow the integration of hundreds of qubits on a compact chip with easy optical access and interfacing via established microscopic techniques or via photonic structures enabling highly efficient interfacing. However, due to local fluctuations of matrix properties like crystal strain the fabrication of a larger number of truly indistinguishable qubits is very challenging in these material systems.

In this thesis we will explore a potentially highly-scalable QIP platform, the negatively charged silicon vacancy colour centre ( $\text{SiV}^-$ ) in diamond [35], and we theoretically as well as experimentally examine its suitability as a basic building block for future quantum technologies. Colour centres are localized atom-sized crystallographic defects consisting of lattice vacancies, impurity atoms or combinations of both in a crystalline solid-state matrix with electronic transitions lying within the band gap of the host material. These transitions lead to a characteristic absorption and emission of light and, in high concentrations, give the host material a characteristic colour, hence the name "colour centre". Due to their well-defined local symmetry and their isolated electronic levels colour centres are frequently considered as "artificial atoms" (or a bit more accurate, molecules). These defects possess orbital as well as electron and nuclear spin degrees of freedom in which quantum information can be encoded into. Because of its exceptionally large band gap ( $\Delta E_{gap}=5.5\text{eV}$ ) diamond is capable of hosting hundreds of different types of centres [36] and itself is an ideal host material for QIP applications for several reasons: First, recent technical advances enable fabrication of synthetic diamond with very high purity and well-definable properties [37,38]. Moreover, by using isotopically purified  $^{12}\text{C}$  precursors diamond, in contrast

to e.g. gallium arsenide, can be made completely spin-free [39], providing an exceptionally low-noise environment for spin qubits [40]. Secondly, its high thermal conductivity and high transparency render it ideal for applications at low temperatures and for the use of optical techniques. In addition, recent developments in diamond nanofabrication allow for the manufacturing of a variety of nanophotonic structures in diamond such as waveguides or photonic crystal and nanobeam cavities which can be used to interface qubits in a scalable on-chip QIP platform [41, 42]. For a recent review on diamond nanophotonics see e.g. [43]. So far, only a handful of the above mentioned myriad of colour centres has been investigated on a single-emitter level with the renowned nitrogen vacancy centre (NV) vastly dominating this field of research in the last decade [44]. The tremendous popularity of the NV is based on its electronic structure: The centre features an electron spin triplet ground state ( $S=1$ ) with a zero-field splitting of about 2.9 GHz between its  $m_s = \pm 1$  and the  $m_s = 0$  spin sublevels [45, 46]. This enables spin manipulation using convenient microwave frequencies. For this spin, coherence times in the microsecond regime have been observed, mainly limited by magnetic-field noise created by substitutional nitrogen impurities and  $^{13}\text{C}$ . In ultra-pure and isotopically enriched diamonds even higher values of up to 2ms have been reported [40]. Moreover, a spin-state dependent fluorescence as well as optical spin initialization into the  $m_s = 0$  can be observed under illumination with non-resonant green light, tremendously simplifying quantum optical experiments with this centre. The application of small magnetic fields leads to a Zeeman splitting between the  $m_s = +1$  and  $m_s = -1$  sublevels in the NV. This can be measured in an optically-detected magnetic resonance (ODMR) experiment by sweeping the microwave frequency across the  $|m_s = +1\rangle \rightarrow |m_s = 0\rangle$  and  $|m_s = -1\rangle \rightarrow |m_s = 0\rangle$  resonances and detecting the changes in spin level by observing the fluorescence intensity under non-resonant illumination. By measuring the Zeeman splitting, the NV can therefore be used as a sensitive and well-localized magnetic field sensor. This rather simple scheme already yields a magnetic field sensitivity of up to  $2\mu\text{T}/\sqrt{Hz}$  using a single NV centre [47]. In addition, several more complex schemes utilizing changes in the spin precession times of the NV have been developed, further improving sensitivities down to a few  $fT/\sqrt{Hz}$  for ensembles of NVs [48], making it comparable to the most advanced SQUID (superconducting quantum interference device) magnetometers [49] without the stringent need for low-temperature operation.

In the context of QIP applications the NV also offers the possibility to transfer quantum information to the built-in and long-lived nuclear spin of  $^{14}\text{N}$  or  $^{15}\text{N}$ . This is made possible by the long spin coherence times of the NV ground state enabling narrow magnetic dipole transitions and hence allowing for addressing individual hyperfine levels via narrowband microwave pulses [50]. This nuclear spin access even allows for the implementation of a CNOT gate between electron and nuclear qubits. An applied nuclear spin state-selective microwave pulse applied between e.g. one of the hyperfine levels of the  $|m_s = 0\rangle$  and  $|m_s = +1\rangle$  electron spin branch hereby only flips the electron spin if the system is in the respective nuclear spin state.

Besides the favourable properties discussed above, the NV centre also has a number of disadvantages, mainly its optical properties: Due to strong interactions with local vibrational modes, the emission spectrum of the NV is dominated by a broad phonon sideband (PSB) ranging from 640 nm up to above 800 nm and only 3-5% of the total fluorescence is emitted into the narrow zero phonon line (ZPL) at 637 nm [51]. While this does not impede a

simple spin read-out as we have discussed it above, it is detrimental for the creation of NV-NV entanglement since these protocols rely on ZPL photons which are only emitted with a probability of less than  $10^{-6}$ . Moreover, the indistinguishability of these photons is further reduced by spectral diffusion processes due to fluctuating electric fields in the environment of the NV which have to be compensated via active electrostatic feedback [52]. Therefore, for the NV only very low bipartite entanglement rates of approximately one event per hour have been demonstrated so far [53], limiting chances for entanglement of multiple NVs without the use of sophisticated techniques to enhance the centre's ZPL emission, such as coupling to microcavities [54]. Hence, while the NV most probably has a bright future in quantum sensing, its use for QIP applications strongly depends on the development of efficient photonic interfaces.

The  $\text{SiV}^-$  centre is destined to improve on these insufficiencies of the NV centre in several ways which we will briefly review here before introducing the centre in greater detail in the following chapter: One of the main advantages of the  $\text{SiV}^-$  is a significantly reduced vibronic coupling compared to the NV, resulting in a channeling of about 80% of the total fluorescence into the ZPL [36, 55] and narrow ZPL linewidths below 1 nm already at room temperature [55, 56]. When cooling the  $\text{SiV}^-$  down to liquid helium temperatures, this ZPL splits up into four fine structure components with linewidths down to 120 MHz, indicating a system with a twofold-split ground and excited state, the components of which are separated by 48 GHz and 258 GHz, respectively, caused mainly by spin-orbit interactions [57]. Structurally, the  $\text{SiV}^-$  is composed of a single silicon atom occupying an interstitial site in between two empty adjacent carbon lattice sites in the diamond unit cell. Including six nearest-neighbour carbon atoms, this gives the defect an inversion-symmetric trigonal antiprismatic symmetry. This high symmetry is what makes the  $\text{SiV}^-$  exceptionally interesting for QIP applications as it renders the system relatively insensitive against perturbations e.g. caused by electric field fluctuations or local variations in crystal strain [57, 58]. On the one hand, this outstanding feature means that quantum information (which is analogue information and thus is susceptible to alterations) encoded in  $\text{SiV}^-$  centres is very well protected against these noise sources. On the other hand, the high symmetry is responsible for very narrow inhomogeneous distributions down to 360 MHz for emitters in high-quality diamond samples and e.g. enabled the demonstration of photon indistinguishability from two separate  $\text{SiV}^-$  centres without any additional frequency tuning technique [59]. Moreover, the  $\text{SiV}^-$  offers a variety of optically allowed transitions even between spin sublevels of opposite spin projection because a difference in spin-orbit interaction strengths causes different effective quantization axes in the ground and excited state. This leads to a partial relaxation of spin selection rules and makes it possible to optically address spin-flipping transitions. Thus, the  $\text{SiV}^-$  offers the unique possibility for an all-optical coherent control of both the orbital and spin degree of freedom without the need to apply additional strain or electric fields to create optical access to the spin levels as it is common in other systems such as quantum dots [25] or NV centres [60]. This optical control, in contrast to the widely used microwave- or radio frequency-based schemes offers a high spatial resolution, as a laser can be very precisely guided onto a specific qubit, a significant advantage for precise coherent control of multi-qubit systems. Moreover, the  $\text{SiV}^-$  offers the possibility of ultrafast coherent control using short and thus broadband

laser pulses and even sub-cycle control [61], that is, control over time scales shorter than the qubit frequency splitting, with pulse lengths in the picosecond regime. This again is a significant advantage, especially for a qubit in the solid state, where interactions with the environment often lead to comparably short coherence times. This is enabled by the large level splittings of the  $\text{SiV}^-$ , minimizing the risk of unwanted cross-excitations when using broadband pulses. For these reasons, the  $\text{SiV}^-$  is a highly promising candidate to realize interfacing of multiple qubits in a solid state system. However, as we will explore in this thesis, the spin coherence of the  $\text{SiV}^-$  is limited to tens of nanosecond due to its inherent electronic structure as well as due to magnetic interactions with its environment. Nevertheless, we will show that this limitation can be overcome for local QIP applications by extremely high control speeds and we will explore techniques to further prolong its spin coherence.

In addition to its use as an individual qubit the  $\text{SiV}^-$  is also a promising candidate for the realization of an ensemble-based optical quantum memory, since even for extremely dense ensembles of  $\text{SiV}^-$  centres inhomogeneous broadenings in the low GHz-regime, lower than the fine structure splitting of the centre, have been reported [62]. Before we take a closer look at the principle and possible implementations of optical quantum memories, we will further motivate their technological value by making a small excursus and discussing some basic properties of quantum information in general and photons as a carrier of quantum information: A unique feature of a quantum superposition is that it cannot be digitized or copied without destroying it. This property, known as the "no cloning theorem" [63] makes storage of quantum information extremely challenging as it implies that a quantum memory itself needs to be a quantum mechanical device. Therefore, the use of photons as qubits to process and distribute quantum information is at the same time ideal and extremely challenging. On the one hand, photons can easily be manipulated using standard optical components and offer a multitude of degrees of freedom to encode quantum information (e.g. polarization, photon number). Furthermore, photons do only weakly interact with each other and their environment, i.e. quantum information encoded in photons is again very well protected from environmental noise. This advantage, on the other hand, simultaneously is the greatest disadvantage of photons as the weak interactions render local storage of quantum information encoded in photons challenging. However, for optical QIP this is a very fundamental technical requirement as the generation of single photons most of the time is a probabilistic process and therefore individual single photon sources need to be synchronized, e.g. by using so-called buffer memories, to allow for a controlled interaction of single photons at specific points in time and space. One method to approach this hurdle is to convert a single photon into a coherent collective excitation, often called a spin wave, in a dense ensemble of quantum systems. The large number of quantum systems hereby compensates for the vanishing interaction probability of the photon with each individual site. In the past years several schemes for such a photon storage such as electromagnetically induced transparency (EIT) [64], controlled reversible inhomogeneous broadening (CRIB) [65], atomic frequency comb memories (AFC) [66] or Raman-based storage [67] have been proposed and experimentally demonstrated in a variety of physical systems. However, many of these memories lack the capability to store short and thus broadband photons, which, however, is desirable to achieve high data rates in optical QIP and quantum communications systems. As we will

explore later in this thesis, the  $\text{SiV}^-$  is a particularly promising system to realize a very broadband memory with potentially very favourable ratios of pulse length and storage time.

This thesis directly builds on previous work performed by C. Hepp et al. [57, 58] in which an extensive investigation of the  $\text{SiV}^-$  centre's electronic structure has been performed, revealing orbital as well as electron spin doublet ground and excited states. However, the coherence properties of both orbital and spin levels remained elusive so far and no experimental scheme to coherently control a quantum state encoded in either of those degrees of freedom has been developed yet. These are the main objectives of this thesis which is structured as follows:

- In chapter 1 we will focus on the physical properties of both diamond as well as the  $\text{SiV}^-$  centre: We will start out with a description of the structural, electronic, optical and phononic properties of diamond and discuss its suitability as a host material for QIP applications. We will then discuss the techniques used to fabricate synthetic diamond as it has been used throughout this work. The second part of this chapter then focuses on the optical and electronic properties of the  $\text{SiV}^-$  centre and we conclude the chapter by briefly reviewing a theoretical model for the electronic structure of this defect developed by Hepp *et al.* in a previous work [57, 58] as it provides a deep level of understanding of the  $\text{SiV}^-$  centre's level structure and electronic interactions which will be a fundamental ingredient for interpreting the results obtained in this work.
- Chapter 2 will then focus on the theoretical concepts of the interaction of light and matter: We will begin by introducing the counter-play of a single coherent light field with a two-level atom and slowly expand this towards a model for multi-level systems interacting with multiple fields, which we will use to analyse the experimental data presented later in this thesis. In this context we will also discuss a number of physical effects related to quantum coherence and introduce the techniques used to measure coherence times and for coherent control.
- In chapter 3 we will then take a closer look at the experimental concepts employed to obtain the results of this thesis: The first part of the chapter will deal with the fabrication process of a diamond sample containing single  $\text{SiV}^-$  centres which we exclusively used to obtain all single-emitter results in chapter 4. Moreover, a brief review of the fabrication of  $\text{SiV}^-$  ensemble samples will be given as these samples have been used for the experiments presented in chapter 5. The second half of the chapter then covers the optical setups used and discusses a number of technical particularities.
- The 4th chapter will then cover the experimental results obtained using single  $\text{SiV}^-$  centres: We will start by presenting the first measurement of the spin coherence time of the  $\text{SiV}^-$  at liquid helium temperatures, the results of which will point us towards the need to perform experiments at even lower temperatures. Therefore, in the second part of this chapter we will present first-time results obtained from single  $\text{SiV}^-$  centres investigated using a home-build confocal microscope in a  $^3\text{He}/^4\text{He}$

dilution refrigerator down to temperatures of 12 mK. This will yield a more complete picture of the  $\text{SiV}^-$  spin coherence and its limitations. Some of the experiments presented there also form the basis for optical coherent control of the  $\text{SiV}^-$  spin degree of freedom. In the third part of the chapter we will then discuss a number of experiments which, for the first time, demonstrate coherent control of the  $\text{SiV}^-$  orbital degree of freedom, solely relying on ultrashort laser pulses. We will first discuss a control scheme using pulses resonant with the ZPL transitions of the  $\text{SiV}^-$  and we will use some of the results to calculate the transition dipole moment and quantum efficiency of the  $\text{SiV}^-$ . We will conclude the chapter by demonstrating full all-optical and coherent sub-cycle control of the  $\text{SiV}^-$  ground state using a single 1 ps long laser pulse.

- Chapter 5 will then focus on the coherence properties and coherent manipulation of dense ensembles of  $\text{SiV}^-$  centres: This chapter mostly focuses on the application of such ensembles in Raman-based quantum memories and therefore we will start out with a discussion of the Raman memory protocol as well as a theoretical estimation of storage efficiencies and times achievable with the currently available ensemble samples. In the second part of the chapter we will then present results obtained from resonant coherent control experiments performed to validate the feasibility of first proof-of-principle memory experiments. The remaining part of the chapter will then deal with experiments paving the way towards the implementation of the Raman memory. For the first time, we will demonstrate coherent transfer within the orbital ground state manifold of the ensemble using two classical, off-resonant pulsed laser fields of picosecond duration in a stimulated Raman adiabatic transfer scheme. Secondly, we will demonstrate Raman-based absorption of a 30 ps long weak coherent state in the ensemble aided by a strong classical pulsed control field, corresponding to the read-in process of a Raman quantum memory.
- In chapter 6 we will then conclude this work and provide an outlook on possible future experiments based on the findings and techniques established in this thesis.

# Chapter 1

## The silicon vacancy colour centre in diamond

We will kick off this chapter with an overview over the fundamental properties of diamond as a host material for colour centres as well as the fabrication of synthetic diamond. The second part of the chapter then focuses on the silicon vacancy defect itself. We will begin this section with a brief historical recapitulation which will include a discussion of the defects spectral properties, charge states and geometric structure. We then use this as a basis to review the electronic structure of the  $\text{SiV}^-$  and to review a group theoretical model of the electronic properties of the defect which has been developed by C. Hepp *et al.* in a former thesis [57, 58].

### 1.1 The diamond host lattice

Carbon is one of the most versatile elements and, in its pure form, appears in several amorphous as well as crystalline modifications. A member of the latter group, diamond, is one of the most extraordinary materials known today, exceeding most other substances in properties like hardness, transparency or thermal conductivity.

#### 1.1.1 Crystallographic properties

Diamond is the cubic allotrope of crystalline carbon. A single unit cell of the diamond crystal structure is displayed in Fig. 1.1(a) (note that the origin in this representation is shifted by  $(0,0,1/2)$  compared to the common origin choice for better visibility of the  $\text{SiV}^-$  structure later on). Diamond crystallizes in the cubic crystal system in space group  $\text{Fd}\bar{3}\text{m}$  (Nr. 227) with a lattice constant of  $a=3.567\text{\AA}$  [68]. The structure is a face-centred cubic (fcc) Bravais lattice with a diatomic basis consisting of atoms at  $(0,0,0)$  and  $(1/4,1/4,1/4)$ . Alternatively, the structure can be visualized as a simple fcc lattice with additional C atoms filling half of the tetrahedral gaps in an alternating fashion or as two individual fcc lattices displaced by  $(1/4,1/4,1/4)$ . All C atoms in this structure are tetrahedrally coordinated and bound to four nearest-neighbour atoms.

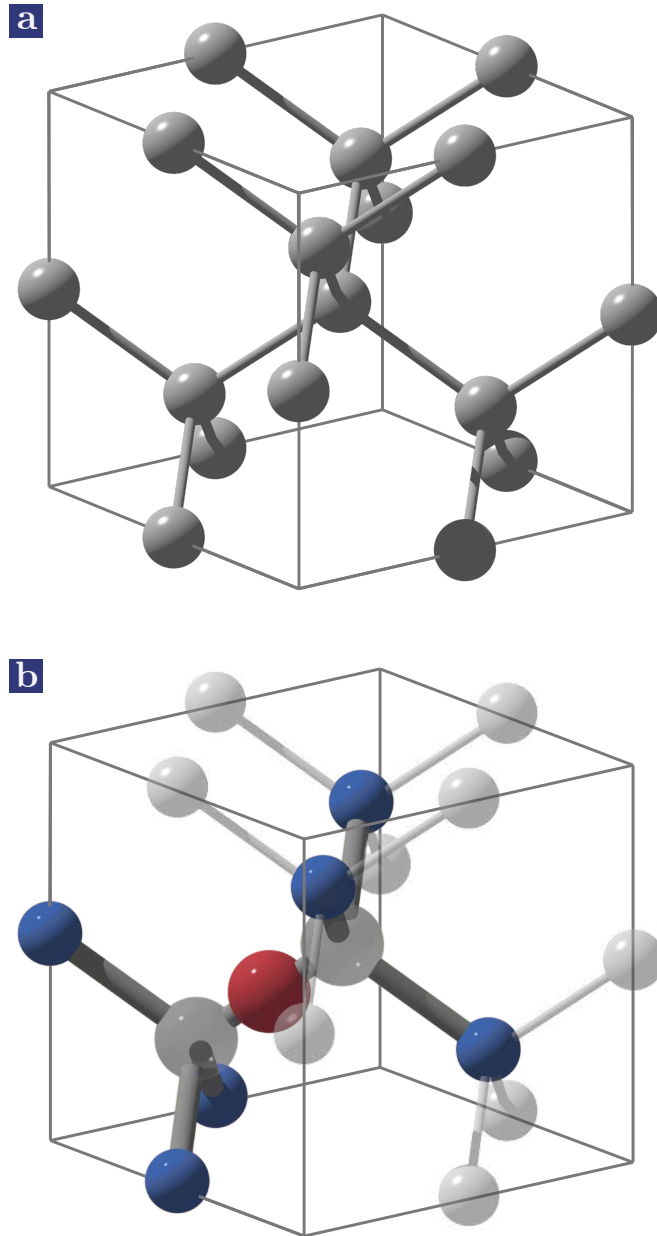


**Figure 1.1: Crystal structures.** (a) Cubic diamond unit cell (space group  $Fd\bar{3}m$ ) with solely tetrahedrally coordinated C atoms (grey). (b) By removing two adjacent C atoms along (111) and adding an interstitial Si atom (red) a SiV<sup>-</sup> centre with its characteristic trigonal-antiprismatic split-vacancy configuration is formed. The six nearest-neighbour C atoms are marked in blue.

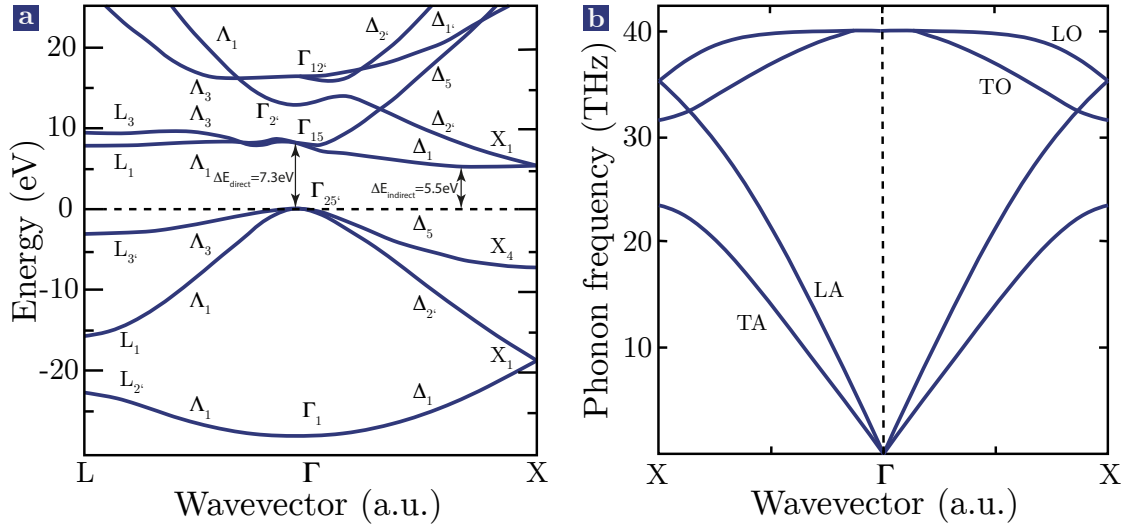


**Figure 1.2: Band structure & phonon dispersion.** (a) Electronic band structure of diamond along the  $\Lambda$ -(L $\rightarrow$  $\Gamma$ ) and  $\Delta$ -line ( $\Gamma \rightarrow$ X) indicating the direct band gap of  $\Delta E_{direct} = 7.3 \text{ eV}$  in the zone centre as well as an indirect band gap of  $\Delta E_{indirect} = 5.5 \text{ eV}$  between  $\Gamma$  and X. Figure adapted from [69]. (b) Phonon-dispersion relation of diamond along (100) displaying transverse acoustic (TA), longitudinal acoustic (LA), transverse optical (TO) and longitudinal optical (LO) phonon branches. Figure adapted from [70].

### 1.1.2 Physical properties

**Electronic band structure** Diamond is the hardest natural material known today and defines the upper end of the Mohs scale of mineral hardness with a value of 10. Under ambient conditions it is completely chemically inert, i.e. it is not affected by any organic solvents, strong acids or bases. Thus, diamond offers a maximally robust environment for qubits. The characteristic feature of the electronic structure of diamond is a very wide indirect band gap with  $\Delta E_{indirect} = 5.5 \text{ eV}$  and an even wider direct gap with  $\Delta E_{direct} = 7.3 \text{ eV}$  [69]. As mentioned in the introduction, this wide gap is what allows diamond to host hundreds of different colour centres, forming localized energy levels within the band gap [36]. The electronic band structure of diamond is displayed in Fig. 1.2(a), the band gaps are indicated in red. The valence band of diamond consists of four different bands (the upper two are degenerate in the range of wavevectors shown here) and an analysis of their wave functions reveals a s-character for the two lower bands while the upper bands are more p-like. Moreover, the small energy difference between s- and p-like bands in the zone centre reflects the  $sp^3$ -hybridization of all C atoms in this covalently bound crystal [71]. These strong covalent bonds are responsible for the unprecedented hardness of diamond. The very wide bandgap makes diamond a semiconductor and leads to an extremely wide light transparency window ranging from 230 nm up to the far infrared region of the electromagnetic spectrum, interrupted only by a two-phonon-absorption region between 2.5 and 6  $\mu\text{m}$  [36]. This high transparency makes diamond an ideal host material for optical experiments. Another important optical property of diamond is its high

refractive index of  $n=2.4$  at 740 nm [36]. On the one hand, this facilitates the fabrication of photonic structures such as waveguides [72] or photonic crystals [41]. On the other hand it severely limits the light extraction efficiency from unstructured bulk diamond as it leads to a very low critical angle for total internal reflection of only  $24.4^\circ$  at the diamond-air interface. This makes the use of structures like nanowires [73] or solid immersion lenses (SILs) a necessity for efficient light collection. In this thesis we will use SILs for collection enhancement and we will discuss their fabrication and properties in Chap. 3.1.3. In any case, about 17% of the light is reflected back into the diamond due to Fresnel reflection, even under perpendicular incidence relative to the surface [74].

**Phononic properties** Besides its electronic properties, the phonon structure is an equally important feature of diamond as a host material for colour centres. In Fig. 1.2(b) the phonon dispersion relation of diamond along the (100) crystal direction is shown exemplarily. Four distinct bands corresponding to the possible phonon modes are visible. With its diatomic basis ( $N=2$ ) diamond can exhibit  $3N=6$  phonon modes, namely two transverse acoustic (TA), a single longitudinal acoustic (LA), two transverse optical (TO) as well as a single longitudinal optical (LO) mode. In acoustic phonons neighbouring atoms move in-phase whereas in optical phonons they move out-of phase. Moreover, transverse modes are characterized by atomic movements perpendicular to the propagation direction of the phonon and longitudinal modes are caused by atomic motions along the propagation direction [75]. In diamond (and in many other cubic materials) the transverse modes, which can be interpreted as two orthogonal vibrational components, are degenerate along most crystal directions (in the words of group theory: they are E-symmetric) whereas the longitudinal modes are non-degenerate (they are of A-symmetry) [76]. Moreover, diamond e.g. compared to the isostructural silicon or germanium features about 3-4 times higher phonon energies. This is a direct consequence of its strong covalent bonds and is of great importance for the properties of colour centres incorporated in the lattice. Since the average phonon energies are high, the contributions of low-energy phonons are reduced compared to other materials. These low-energy contributions, however, can cause a broadening of ZPL transitions and thus the phononic structure of diamond enables low ZPL linewidths already at room temperature [74, 77].

### 1.1.3 Natural diamonds & diamond synthesis

**Natural diamond formation** The formation of natural diamonds requires extreme temperatures of 900-1300°C and pressures of 4.5-6 GPa [78]. Even in the inner earth, these conditions are only met in the stable central regions of the upper mantle below continental plates. It turns out that diamond, under ambient conditions, is not the thermodynamically stable carbon phase but is only kinetically stabilized. Thus, at temperatures above 1500°C, it is rapidly converted into the thermodynamically stable graphite [79]. This means that diamonds formed in the earth's upper mantle have to be transported to the cool surface very rapidly to avoid decomposition. Today it is believed that this is accomplished during so-called deep-source volcanic eruptions which quickly transport material to the surface [80]. A second natural source are meteorites in which diamond is either formed in space during high-energy collisions or during impact. While natural diamonds with

high enough purities for quantum optical applications can be found and terrestrial as well as cosmic diamonds [81] have already been used for such experiments, their exact composition is strongly correlated with their exact origin and varies even within a single diamond mine. This makes the reproducible fabrication of samples based on this material extremely challenging. Therefore, a large-scale quantum technology based on defects in diamond relies on the fabrication of synthetic diamond with well-defined properties.

**Synthetic diamonds & classification** Today, synthetic diamond is used in a variety of applications such as gemstones, electronic devices or cutting tools and its production exceeds the one of natural diamond by more than a factor of 200 [82]. The synthesis of diamond can be carried out via two main processes, high-pressure high-temperature (HPHT) synthesis or chemical vapour deposition (CVD), both of which have their individual advantages and yield diamond with significantly different properties. Therefore, to simplify the following discussion we first introduce the classification of diamond with regard to its composition: The nomenclature which today is still widely used to classify diamonds has been proposed by Robertson *et al.* in 1934 and separates diamonds into two main classes, type I and type II, depending on the presence of a number of infrared absorption bands [83]. These have later been attributed to the presence of nitrogen impurities and a more detailed separation into type Ia, containing aggregates of nitrogen, and type Ib, containing isolated substitutional nitrogen [ $N_s^0$ ] has been made [84]. In contrast to this, type II diamond lacks the above mentioned absorption bands and is thus said to be nitrogen free (though in reality several 100 ppb of [ $N_s^0$ ] can remain in the material without detectable infrared absorption). Type II diamond is further categorized into the purest type IIa with vanishing electrical conductivity and type IIb with p-type conductivity due to the presence of boron impurities.

The HPHT synthesis aims at replicating the natural growth conditions of diamond using carbon precursors and small diamond seed crystals in powerful hydraulic presses, generating pressures of about 5 GPa and temperatures above 1400°C [85]. To enhance the very slow growth rates, molten metals such as Fe, Co or Ni are used as catalysts. These additives greatly limit the purity of the produced diamonds as they can be included into the material in the form of carbides and introduce, in addition to impurities of the carbon precursor, large amounts of substitutional nitrogen. Thus most HPHT diamonds are of type Ib. In recent years also the fabrication of very pure type IIa diamond via HPHT methods has been achieved by using so-called nitrogen getters. These are usually elements such as Ti or Zr with a high affinity towards nitrogen [86]. However it should be noted that, while these diamonds are colourless, they still contain several tens to hundreds of ppb of [ $N_s^0$ ] in addition to possible further impurities from the carbon source, catalyst or getter material. Synthetic diamond with much higher purity can be fabricated via the CVD method. This process aims at the fabrication of diamond in a metastable region of the carbon phase diagram using gaseous precursors [87]. In a first step a carbon precursor such as methane is decomposed in a hydrogen plasma which can e.g. be generated using a microwave source (MWCVD) or a hot tungsten filament (HFCVD). The carbon-containing fragments then adsorb onto a substrate such as diamond (homoepitaxial growth [88]), silicon or iridium (heteroepitaxial growth [89]) and randomly form layers of  $sp^2$ - and  $sp^3$ -hybridized carbon

compounds. The actual diamond synthesis is then achieved due to reaction kinetics as the  $sp^2$  compounds are etched away faster by the hydrogen plasma than the  $sp^3$ -carbon. Therefore, by carefully choosing the carbon content and plasma parameters an effective deposition of pure  $sp^3$ -carbon can be achieved [88]. Since the composition of the gaseous educt gases can be very well controlled, diamonds fabricated via CVD can reach very high purities and samples with  $[N_s^0]$  concentrations below 5 ppb (electron paramagnetic resonance detection limit) and boron impurity concentrations below 0.5 ppb (limit of secondary ion mass spectrometry) are commercially available (Element Six Ltd, electronic grade diamond plates). By using isotopically purified precursors, this method even allows for the fabrication of isotopically engineered samples providing truly spin-free environments for electron and nuclear spin qubits [40]. However, while the chemical purity of CVD diamond can be very high, the material often exhibits a significant amount of crystal strain caused by growth imperfections. In contrast, HPHT diamonds are largely free of strain as crystal imperfections are annealed out at elevated temperatures and pressures during growth. Since crystal strain can be detrimental to the properties of colour centres incorporated into the diamond, a careful choice of the appropriate substrate is inevitable. All single centres investigated throughout this work will be hosted in type IIa HPHT diamond because the  $\text{SiV}^-$  centres in this material have been found to have very good spectral properties and brightnesses, essential for the experiments presented here. In the following section we will now first discuss the general spectral and electronic properties of the  $\text{SiV}^-$  before we take a look at the sample specific properties in Chap. 4.1.

## 1.2 The silicon vacancy

After having reviewed the properties of the host lattice, in this part of the chapter we will now take a closer look at the properties of the  $\text{SiV}$  defect and we will largely follow the historical time line by first discussing the experiments which have been used to identify the constituents and different charge states of the centre before reviewing its spectral and electronic properties in more detail.

### 1.2.1 Charge state & constituents

**Charge state** The  $\text{SiV}$  is known to exist in two different optically active charge states with ZPL transitions at 737 nm (1.68 eV) [90,91] and 946 nm [92]. While there has been some debate about the assignment of these lines to specific charge states [91,93] experiments involving annealing as well as irradiation with ultraviolet light suggest that the 1.68 eV line is related to a singly negatively charged centre while the emission at 946 nm is attributed to a neutral defect [92,94]. This is further backed up by density functional theoretical (DFT) calculations [91]. However, due to a very low quantum efficiency, individual  $\text{SiV}^0$  sites have not been observed until recently [95] and the extremely low count rates currently render this charge state vain for quantum optical experiments reaching beyond basic spectroscopic investigations. Therefore, this thesis focuses exclusively on the much brighter  $\text{SiV}^-$ .

**Atomic constitution** The first study mentioning fluorescence at 738 nm (1.68 eV) has been performed by Vavilov *et al.* in 1980 [96] by observing cathodoluminescence from

natural diamonds. Shortly after, Zaitsev *et al.* related this fluorescence to a defect containing Si [97]. This has later been confirmed by Collins *et al.* [98] and Ruan *et al.* [99] in ion implantation studies, both however concluded wrong compositions of the defect. From implantations in N-containing diamond Collins *et al.* concluded the involvement of Si and N while Ruan *et al.* concluded a Si<sub>2</sub>-containing defect from the implantation yield dependence from the ion dose. The fact that Collins *et al.* found a correlation between N content and 1.68 eV fluorescence has later been explained by Edmonds *et al.* as a charge transfer from the [N<sub>s</sub><sup>0</sup>] donor to the SiV<sup>0</sup> creating additional SiV<sup>-</sup> [100]. This is another strong indication that the 1.68 eV centre is in fact a negatively charged defect. Shortly after, Clark & Dickerson clarified the composition by implanting Si followed by electron irradiation and high-temperature annealing in diamonds containing only small amounts of nitrogen [101]. Directly after implantation they found only small 1.68 eV fluorescence but strong fluorescence of the neutral vacancy defect (GR1) at 1.67 eV. The latter one vanished upon annealing as vacancies in diamond become mobile above 800°C and recombine with the implanted Si or are annealed out. With this experiment they conclusively demonstrated the involvement of a vacancy in the defect and correctly concluded its now widely accepted composition of a single Si and a carbon vacancy.

### 1.2.2 Spectral properties

**Solid-state fluorescence spectra** In this section we will review the spectral properties of the SiV but before we do so we will briefly introduce the general structure of the emission spectrum of a localized defect in a solid state matrix which comprises some additional features compared to the emission of e.g. an isolated atom. These differences arise from the fact that the defect couples to its crystalline environment via phonons, i.e. quantized vibrations of the host lattice (lattice modes) or of the defect itself (local modes). This gives rise to two main features in the fluorescence spectrum of such a defect, a zero phonon line (ZPL) involving only purely electronic transitions without the involvement of phonons and red- as well as blue-shifted phonon side bands (PSBs) involving the creation or annihilation of vibrations. This electron-phonon coupling arises from the fact that optical excitation of the defect essentially instantaneously alters the spatial distribution of the electronic wave function, leaving the surrounding nuclei in an energetically unfavourable configuration from which they then relax back into their new equilibrium position. Vice versa, a lattice vibration altering the local atomic arrangement of the defect will thus cause perturbations to the electronic charge distribution. This causes the coupling between the defects electronic and vibrational degrees of freedom. Assuming a ground state of zero electronic energy and taking into account interaction with lattice vibrations the total ground state energy can be expressed by the harmonic potential

$$V_g = \frac{1}{2} \sum_i m_i \omega_i^2 Q_i^2 \quad (1.1)$$

with effective masses  $m_i$ , vibrational frequencies  $\omega_i$  and generalized nuclear displacements  $Q_i$ . The summation hereby indicates that the system can not only interact with a single

but with a multitude of vibrational modes [77]. Analogously, we can write

$$V_e = E_e + \frac{1}{2} \sum_i m_i \omega_i^2 Q_i^2 + \sum_i a_i Q_i + \sum_{i,j} b_{i,j} Q_i Q_j \quad (1.2)$$

for the excited state with a purely electronic contribution  $E_e$ . The term  $\sum_i a_i Q_i$  hereby introduces a displacement of the excited state harmonic parabola with respect to the ground state due to the nuclear reorientation and is called linear electron phonon (or vibronic) coupling. According to the so-called *Franck-Condon principle* the excitation of the electrons is said to be "vertical", i.e. much faster than the time it takes for the nuclei to adapt to the altered charge distribution [102, 103]. The system is therefore excited into a vibrational excited state of the electronic excited state, determined by the square of the overlap integral between the vibrational wave functions of ground and excited state. Due to the finite lifetime of the electronic excited state the system then has time to relax to the vibrational ground state of the excited state and from there decays back into the ground state under optical emission. This process again can be considered "vertical" and therefore the system will end up in a vibrationally excited level of the ground state, giving rise to an emission frequency shifted relative to the purely electronic transition causing PSBs. Thus, the smaller the linear vibronic coupling, the more likely is the emission of a photon into the ZPL. In addition to the frequency shift due to the linear interaction, the quadratic coupling term  $\sum_{i,j} b_{i,j} Q_i Q_j$  can cause temperature-dependent changes to the PSBs and differences in the shapes of PSBs in absorption and emission [77, 104]. The ratio of light that is emitted into the ZPL and the PSBs is characterized by the so-called Huang-Rhys factor  $S$  according to

$$\exp^{-S} = \frac{I_{ZPL}}{I_{ZPL} + I_{PSB}} \quad (1.3)$$

with the intensities  $I_{ZPL,PSB}$  of ZPL and PSB, respectively. The Huang-Rhys factor indicates the number of phonons involved in the most likely transition in a system between its ground and excited state [84]. For applications in QIP, systems with a strong zero phonon line are desirable for several reasons: First, to achieve a robust operation of an optical qubit in the presence of potential sources of stray light, narrowband filtering is desirable, which, however, is not compatible with broad PSBs. Secondly and even more importantly, to interface individual qubits, atom-photon entanglement needs to be created which relies on driving specific transitions between electronic states to create e.g. entanglement between a spin state and the polarization of an emitted photon [105]. Moreover, the entanglement of two qubits e.g. relies on coincidence measurements of indistinguishable photons from each individual system and therefore an intense emission into a narrow spectral window is desirable to achieve meaningful entanglement rates [106].

**Absorption properties** Before we investigate the emission spectrum of the SiV<sup>-</sup> we will briefly review its absorption properties. Besides resonant excitation of the ZPL at 737 nm Iakoubovskii *et al.* found the centre to be excitable off-resonantly in a very broad spectral range between approximately 500 nm and 730 nm [107]. Moreover, they found that the shape of the absorption spectrum below 605 nm coarsely agrees with the shape of

the above-band-gap absorption in diamond and concluded that the  $\text{SiV}^-$  ground state is located 2.05 eV below the conduction band edge [108]. This contradicts earlier theoretical work [91] placing the  $\text{SiV}^-$  deep inside the band gap. Using absorption and polarization measurements, Rogers *et al.* recently attempted to clarify this issue by identifying a second excited state about 600 nm above the ground state, originating from the  $a_{1g}$  orbital [109]. They conclude that both the ground and this second excited state are of even parity and thus a direct electronic transition is parity-forbidden, explaining the absence of an additional ZPL. However, the authors conclude that transitions involving phonons are allowed and thus this excited state features a broad PSB into which off-resonant excitation up to about 640 nm takes place. This concept is however contradicted by recent density functional theoretical calculations performed by Gali and Maze who conclude that this absorption is rather due to an  $A_{2u}$ -symmetric excited state originating from an  $a_{2u}$  orbital located inside the diamond valence band. Due to the presence of the band the state is broadened accounting for the wide-spread absorption [110,111]. Below, we will revisit the results of Gali and Maze in greater detail when discussing the electronic structure of the  $\text{SiV}^-$ . For longer wavelengths the excitation then occurs into higher vibronic levels of the regular excited state corresponding to the ZPL at 737 nm [58,109].

**Room temperature fluorescence** A typical room-temperature fluorescence spectrum (blue line and dots) of a single  $\text{SiV}^-$  in bulk diamond is shown in Fig. 1.3(a) displaying the strong ZPL at 738 nm, characteristic for  $\text{SiV}^-$  defects in close-to-ideal crystal environments [113,114] with linewidths ranging from  $\sim 5$  nm [115] down to below 1 nm [55,56]. In strongly strained environments the ZPL is found to be drastically shifted and ZPLs between 730 nm and 750 nm have e.g. been observed in nanodiamonds [55,56]. A major advantage of the  $\text{SiV}^-$  compared to other solid state quantum systems is its exceptionally low Huang-Rhys factor, i.e. a large proportion of the fluorescence is emitted into the narrow ZPL. For the  $\text{SiV}^-$  Huang-Rhys factors in the range of  $S=0.08-0.35$  [55,115–117] have been measured in nanodiamonds and bulk diamond, vastly outperforming its biggest competitor, the NV centre, with a Huang-Rhys factor of  $S=3.65$  [36]. Due to this very low Huang-Rhys factor only a very weak PSB sideband is visible in the fluorescence spectrum a zoom into which is shown in the insert of Fig. 1.3(a). In this PSB, a number of distinct spectral features have been identified e.g. in [118] with peaks at  $\sim 42$  meV,  $\sim 64$  meV,  $\sim 129$  meV and  $\sim 178$  meV relative to the ZPL being the most prominent ones (a complete list of sideband features and a literature review can be found in [119]). While the exact origin of many of these features is still subject to debate, in a recent work, using polarization and isotopic shift measurements, Dietrich *et al.* identified the 64 meV peak (which is also the most intense feature in the PSB) as a local vibrational mode of the Si atom in the  $\text{SiV}^-$  while they conclude that the features at 42 meV and 129 meV are likely to arise from de-localized lattice modes [115].

**Low temperature spectra** If the  $\text{SiV}^-$  is cooled down from room temperature to liquid helium temperatures (4.2 K) the ZPL shifts to higher energies by about 1 nm and a four-line fine structure emerges starting with a split into a doublet at about 100 K of which each line again splits below approximately 50 K. The shift in line positions

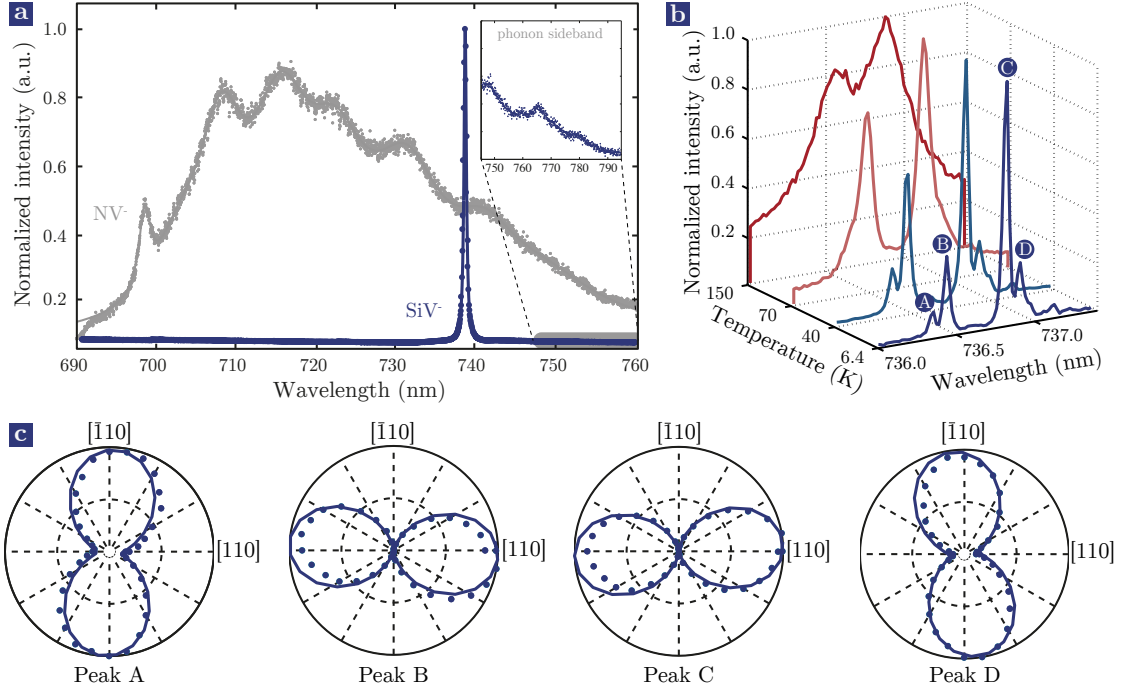


**Figure 1.3: SiV<sup>-</sup> fluorescence spectra.** (a) Room-temperature fluorescence spectrum of the SiV<sup>-</sup> (blue) showing a narrow and intense ZPL at 738 nm. For comparison a typical NV<sup>-</sup> fluorescence spectrum (grey) is shown in the background. The inset displays the weak PSB of the SiV<sup>-</sup>. (b) Series of ZPL photoluminescence spectra for variable temperatures showing the evolution of the characteristic four-line fine structure for temperatures below approximately 100 K. (c) Polarization of the fluorescence emitted from the individual fine structure lines under off-resonant excitation at 690 nm and 4 K along [110] (reproduced from [112]).

hereby follows a  $T^3$  dependence [120, 121] which Jahnke *et al.* identified to be caused by a second-order linear interaction with E-symmetric phonons [121, 122] while additional contributions due to the thermal expansion of the lattice appear to be negligible. The fine structure has been first observed by Clark *et al.* [90] as well as Sternschulte *et al.* [114], while limited spectral resolutions and sample quality prevented its observation in early low-temperature experiments [101]. A temperature-dependent spectrum of the SiV<sup>-</sup> fine-structure is depicted in Fig. 1.3(b) clearly showing the evolution of the four transitions as temperature is decreased. From here on out we will refer to these four optical transitions as A, B, C and D in ascending order of wavelengths. From the relative intensities of the four lines and their changes with temperature the authors of [90, 114] already inferred a split doublet ground and excited state with a ground state splitting of  $\Delta E_g = 48$  GHz and an excited state splitting of  $\Delta E_e = 259$  GHz. Sternschulte *et al.* further validated this in additional measurements by applying uniaxial stress and magnetic fields [62], although with very limited spectral resolution. In [121, 122] Jahnke *et al.* recently also measured the temperature dependence of the level splittings. The authors showed a  $T^2$  dependence of both ground and excited state splitting and, like the ZPL line shift, attribute it to second-

order linear interactions with E-symmetric phonons. A much more detailed investigation of the spectral properties of the  $\text{SiV}^-$  in magnetic fields of up to 7 T has recently been performed by Hepp *et al.* There, they demonstrated that each of the four lines splits into four components when a magnetic field is applied [57, 58]. We will discuss these results in further detail later on while discussing the electronic structure of the  $\text{SiV}^-$ . Using dense ensembles, the authors of [90] also identified two additional structurally identical but weaker fine structures red-shifted to the main pattern and related these to the less abundant natural Si isotopes  $^{29}\text{Si}$  and  $^{30}\text{Si}$  while the main lines correspond to  $^{28}\text{Si}$  as the intensities of the individual quartets scaled with the abundances of the individual isotopes. A similar high-resolution photoluminescence excitation spectrum of a non-isotopically pure  $\text{SiV}^-$  ensemble used in this thesis can be found in Chap. 5.

### 1.2.3 Structural properties

Besides its spectral properties a model for the geometric structure of the  $\text{SiV}^-$  in the diamond lattice is an important prerequisite for a detailed model of its electronic structure. Using different calculation methods, two competing theoretical predictions for the structure of the  $\text{SiV}^-$  evolved: By employing restricted open-shell Hartree-Fock calculations Moliver *et al.* [93] predicted a  $C_{3v}$  symmetry for the defect, similar to the NV centre, with the Si being in a non-central position between two empty C lattice sites. Since this symmetry does not account for the observed fine structure, as it does not allow for degenerate ground states, the authors propose a tunnel-coupling model in which the Si atom dynamically moves between positions centred around the interstitial lattice site creating symmetric and anti-symmetric wave functions with different energies to account for the four lines. In contrast to this, using density functional theory, Goss *et al.* predicted an inversion symmetric defect belonging to the point group  $D_{3d}$  with the Si atom occupying the interstitial lattice site in between two empty C lattice positions [91]. This symmetry directly predicts orbitally degenerate ground and excited states, the degeneracy of which might be lifted to account for the fine structure spectrum of the defect. A direct experimental investigation of the exact structure of the defect is not feasible. Instead, using measurements of the polarization of light absorbed or emitted by the  $\text{SiV}^-$  can be used to determine dipole orientations which allow conclusions about the orientation of the defect inside the diamond lattice. Both theoretical models above require the defect to be oriented along the  $\langle 111 \rangle$  directions of the diamond unit cell as only this direction can account for the three-fold rotational symmetry of both predictions. The earliest polarization measurements have been performed by Brown and Rand in which they deduced a  $\langle 110 \rangle$  orientation of the defect from an ensemble of  $\text{SiV}^-$  centres in which the measurement is severely aggravated by the presence of defects along all equivalent  $[111]$  directions. Note that a polarization along  $\langle 110 \rangle$  can also be measured for a defect aligned along  $\langle 111 \rangle$  as it corresponds to the projection of the  $[111]$  direction onto the  $(100)$  observation plane. Using several individual defects in nanoislands of well-defined crystal orientation, heteroepitaxially grown on Ir substrates, Neu *et al.* revisited the polarization properties of the  $\text{SiV}^-$ , identifying a  $\langle 110 \rangle$  orientation, consistent with the theoretically predicted alignment, but also several centres with polarizations along  $\sim[100]$  or  $\sim[010]$  [56]. This controversy has recently been resolved by Hepp *et al.* showing that these tilted polarizations are caused by crystal strain [58], which is considerable in the

samples used by Neu *et al.* due to the heteroepitaxial growth. In [112] as well as [57, 58] we recently presented emission polarization measurements for all fine structure transitions of  $\text{SiV}^-$  centres in low-strain bulk diamond. Such a measurement is shown in Fig. 1.3(c) and confirms the  $\langle 110 \rangle$  orientation of the fine structure polarizations. The small tilt angles relative to the  $[110]$  of the polarizations in this measurement are again attributed to a small residual strain. From the theoretical model of the centre's electronic structure, which we will discuss in greater detail in the following section we determined that the two inner lines, B and C, are related to a main dipole (z-dipole) along the  $\langle 111 \rangle$  crystal directions while lines A and D correspond to perpendicular XY-dipoles. This dipole emits circularly polarized light along  $[111]$  which projected onto the  $(100)$  observation plane (which is tilted by  $54.7^\circ$  relative to the  $[111]$  direction) appears elliptical (linear but with significantly reduced contrast) [57, 58, 112]. In conclusion, the polarization measurements are a strong indication for a defect aligned along  $\langle 111 \rangle$ . This has been further supported by electron paramagnetic resonance measurements performed by D'Haenens-Johansson *et al.* who found a  $\langle 111 \rangle$  orientation for the neutral charge state of the defect and, as discussed above, related its fluorescence to the  $\text{SiV}^-$  via UV-irradiation and annealing experiments [92]. Moreover, they were able to confirm the  $D_{3d}$  symmetry for the  $\text{SiV}^0$ , hence tentatively validating the theoretical calculations of Goss *et al.* These calculations have recently been backed up by additional density functional theoretical calculations by Gali and Maze using functionals which are further optimized to calculate properties of defects in diamond [110]. A representation of the resulting trigonal-antiprismatic and inversion symmetric defect can be found in Fig. 1.1(b) with the Si atom (red) centred in between two empty C lattice sites (dark grey transparent) and surrounded by six equivalent nearest-neighbour C atoms (blue). In the following section we will now discuss a second experimental evidence for this structure, the splitting of the optical lines in an external magnetic field.

#### 1.2.4 Electronic structure

**The unperturbed  $\text{SiV}^-$**  Building up on the trigonal-antiprismatic geometric structure of the  $\text{SiV}^-$  proposed by Goss *et al.* and validated by EPR and polarization measurements as discussed in the previous section, Hepp *et al.* developed a theoretical model of the defects electronic structure based on group theoretical principles. They validated this model using additional spectroscopic measurements performed in external magnetic fields of up to 7 T strength. In this section we will review their results and the model to establish a profound knowledge of the  $\text{SiV}^-$  centre's electronic structure which will be important to understand the experiments and results of this thesis. Moreover, for the analysis of basic emitter properties in Chap. 4 we will occasionally revert back to this model. While we here merely present the main results and features of the model, a detailed description as well as an introduction to group theory can be found in [57, 58].

Let us first review their most important experimental results: By measuring fluorescence spectra of the ZPL of single  $\text{SiV}^-$  centres in varying magnetic fields under off-resonant excitation and at liquid helium temperatures Hepp *et al.* obtained spectral maps showing several important features: First, they observed a splitting of each of the four lines into four components, pointing towards an electronic spin with  $S=1/2$ . This is consistent with EPR measurements of the  $\text{SiV}^0$  performed by D'Haenens-Johansson *et al.* who identified

this defect as a S=1 system [92]. Secondly, they observe level anticrossings (or avoided crossings) between several spectral lines, a clear sign for a spin orbit interaction. Thirdly, the investigation of an ensemble of SiV<sup>-</sup> centres with a field aligned along [001] yielded the exact same splitting pattern as obtained for the single SiV<sup>-</sup>. The only crystal directions which allow for all possible defect orientations in the ensemble to be equivalent under this field orientation are the  $\langle 111 \rangle$  directions. This is the first direct proof that the SiV<sup>-</sup> is aligned along this direction. Starting out from these experimental results and the D<sub>3d</sub>-symmetry of the defect discussed above Hepp *et al.* then derived a theoretical model to analyse their findings and to reveal the SiV<sup>-</sup> electronic structure. We will now briefly review this model: We first derive the symmetry-adapted form of the electron orbitals of the SiV<sup>-</sup>. These electron orbitals have two possible contributions: First, the six nearest-neighbour carbon atoms adjacent to the unoccupied C lattice sites possess unsatisfied valences, so-called dangling bonds. Using group theory we can project these orbitals onto the irreducible representations of the D<sub>3d</sub> point group yielding symmetry-adapted linear combinations (SALCs) of the form  $a_{1g}, a_{2u}, e_{xg}, e_{yg}, e_{xu}$  and  $e_{yu}$ . The label  $a$  hereby refers to a basis function corresponding to a rotational-symmetric one-dimensional representation  $A_{1g}$  while the  $e$  describe basis functions corresponding to two-dimensional representations  $E$ . The labels  $g$  and  $u$  refer to even and odd parity under inversion while while 1 and 2 refer to even and odd parity under 180° rotation perpendicular to the main symmetry axis (which is [111]). Finally, the labels  $x$  and  $y$  denote the two orthogonal basis functions of the two-dimensional representations  $E_{g,u}$ . Secondly, the Si atom itself also possesses unsatisfied orbitals which we describe by hydrogen-like wave functions of the form  $s, p_x, p_y, p_z$  which under D<sub>3d</sub> symmetry can be re-written as  $a_{1g}^{Si} (s), a_{2u}^{Si} (p_z), e_{xu}^{Si} (p_x)$  and  $e_{yu}^{Si} (p_y)$ . Moreover, while the dangling bond and Si single electron orbitals of equal symmetry might mix, recent *ab initio* calculations [110] indicate this mixing to be very small since the Si states are far away in energy (the lowest Si orbital  $a_{1g,Si}$  is located about 0.7 eV above the upper most C dangling bond orbital  $e_g$  [110]). Hence, in very good approximation, we can describe the SiV<sup>-</sup> electronic structure to consist only of C dangling bond orbitals. From *ab initio* calculations [110] the energetic order of the single electron orbitals is then determined to be  $a_{1g} \rightarrow a_{2u} \rightarrow e_{xu} = e_{yu} \rightarrow e_{xg} = e_{yg}$  in increasing order of energy [110]. These orbitals are then successively filled with the 11 electrons of the SiV<sup>-</sup> of which six originate from the C dangling bonds, four from the Si valence electrons and one additional electron from a nearby donor site accounting for the negative charge state. With this we obtain the electron configurations for ground and excited states displayed in the left part of Fig. 1.4 and corresponding to a  ${}^2E_g$  ground as well as  ${}^2E_u$  and  ${}^2A_{2u}$  excited states (note that in the model of Rogers *et al.* the second excited state is of the form  ${}^2A_{1g}$ ). In this representation electrons are indicated by blue and holes by yellow arrows. From these configurations it is apparent that the SiV<sup>-</sup> possesses a single unpaired electron (or a single hole) and the ZPL at 738 nm corresponds to the excitation of an electron from the  $e_u$  to the  $e_g$  level. Since both the ground and the excited state are orbitally and spin degenerate this model so far is not sufficient to reproduce the four-line fine structure of the SiV<sup>-</sup>. Hence, additional interaction terms to lift the degeneracies are necessary which are included in the following using perturbation theory.

**Spin-orbit & Jahn-Teller interaction** In the following, we describe the system with the basis states  $|e_{gx} \uparrow\rangle, |e_{gx} \downarrow\rangle, |e_{gy} \uparrow\rangle, |e_{gy} \downarrow\rangle$  and  $|e_{ux} \uparrow\rangle, |e_{ux} \downarrow\rangle, |e_{uy} \uparrow\rangle, |e_{uy} \downarrow\rangle$  for the  ${}^2E_g$  ground and the  ${}^2E_u$  excited state, respectively. In absence of external fields such as magnetic fields we consider two different perturbations to lift the degeneracy in the ground and excited state. As a first effect we include a spin orbit coupling (SO) as the E-symmetric states feature non-zero orbital angular momentum and the spectral maps measured in [57, 58] show clear signs of the presence of this effect. The corresponding Hamiltonian  $H_{g,e}^{SO}$  for the ground (g) and excited state (e) is given by  $H_{g,e}^{SO} = \lambda_{g,e} L \cdot S$  with the orbital operator  $L = (L_x, L_y, L_z)$  and the electronic spin operator  $S = (S_x, S_y, S_z)$ . It can be shown that, in the basis introduced above, the components  $L_x$  and  $L_y$  only couple the basis states to non-degenerate levels like  $a_{1g}$  or  $a_{2u}$  which for the SiV<sup>-</sup> (in contrast to the NV) are far away in energy, leading to negligible mixing. Hence  $L_x$  and  $L_y$  vanish for the SiV<sup>-</sup> and the total symmetry-adapted SO Hamiltonian can be written as

$$H_{g,e}^{SO} = \lambda_{g,e} L \cdot S = \lambda_{g,e} L_z \cdot S_z = \lambda_{g,e} \begin{pmatrix} 0 & i \\ -i & 0 \end{pmatrix} \otimes \frac{1}{2} \begin{pmatrix} 1 & 0 \\ 0 & -1 \end{pmatrix} \quad (1.4)$$

Moreover, the group theoretical considerations for the symmetries of the dangling bond and Si-centred orbitals show that due to symmetry an admixture of Si orbitals is not possible for the ground but for the excited state. Even if this admixture is small, as indicated by DFT calculations [110], we therefore expect a stronger SO coupling in the excited than in the ground state as SO coupling scales with the atomic number Z as  $Z^4$ . Thus even a small admixture of the significantly heavier Si can cause drastic changes in the strength of this interaction. Secondly, Hepp *et al.* consider a Jahn-Teller (JT) interaction as an additional effect lifting the degeneracy of the E states. According to the Jahn-Teller theorem each partially filled orbitally degenerate state in a system is unstable and the system strives to lift the degeneracy by undergoing a distortion, i.e. by lowering the symmetry [123]. For the SiV<sup>-</sup> both ground and excited state are therefore unstable and a JT effect has to be considered. The JT effect is a purely orbital interaction coupling states via vibrational modes of the lattice and, in its symmetry-adapted form, denotes a linear vibronic coupling of the form  $E \otimes e$  between degenerate electronic levels E and phonon modes e (we use upper and lower case letters to distinguish between the representations of the electronic states and the vibrational modes). The corresponding Hamiltonian  $H_{g,e}^{JT}$  is then given by

$$H_{g,e}^{JT} = \begin{pmatrix} \Upsilon_{x,g} & \Upsilon_{y,g} \\ \Upsilon_{y,g} & -\Upsilon_{x,g} \end{pmatrix} \otimes \begin{pmatrix} 1 & 0 \\ 0 & 1 \end{pmatrix} \quad (1.5)$$

in which the multiplication with the identity matrix is used to expand this purely orbital Hamiltonian to the above-mentioned basis including the spin sublevels. We would here like to note that potentially present crystal strain as well as according to the Wigner Eckart theorem any other purely orbital perturbation acts on the electronic states the same way the JT effect does [58, 124]. Hence their Hamiltonians look virtually identical and in a real SiV<sup>-</sup> their joint effects cannot easily be distinguished. While we neglect additional contributions from crystal strain in the following a detailed discussion of its effects can be

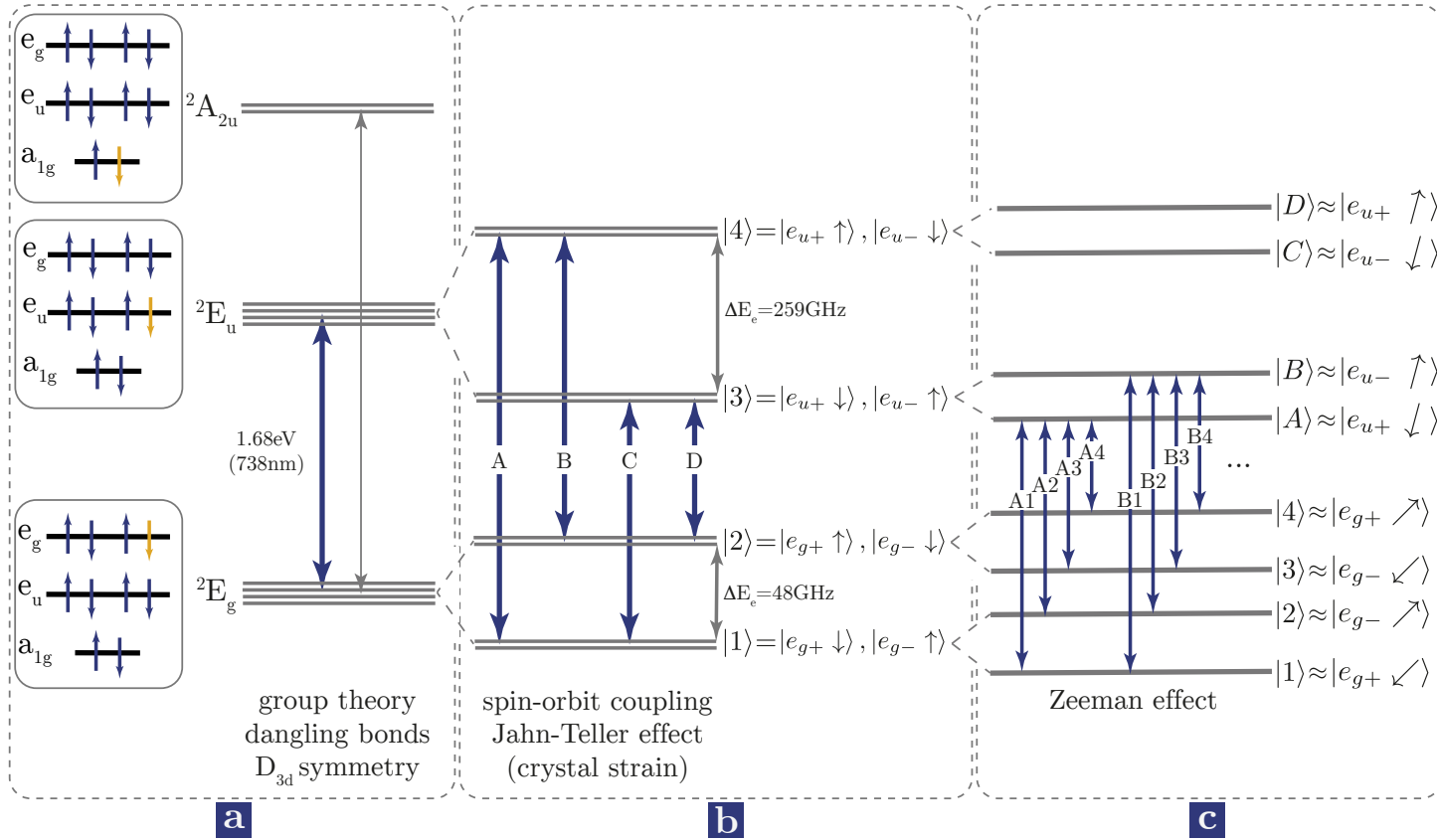


**Figure 1.4: SiV<sup>-</sup> level scheme.** Individual electron configurations of the  ${}^2E_g$  ground and the  ${}^2E_u$  and  ${}^2A_{2u}$  excited states as well as resulting unperturbed level scheme (a). The orbital degeneracies of the unperturbed  ${}^2E_g$  and  ${}^2E_u$  states are lifted by spin orbit coupling, Jahn-Teller interaction and potentially crystal strain, causing a ground state splitting of  $\Delta E_g = 48$  GHz and an excited state splitting of  $\Delta E_e = 259$  GHz in unstrained SiV<sup>-</sup> centres (b). The degeneracies of the electronic spin levels can then be lifted via a Zeeman interaction by applying external magnetic fields (c). Further details can be found in the main text.

found in [58]. The total Hamiltonian  $H_{g,e} = H_{g,e}^0 + H_{g,e}^{SO} + H_{g,e}^{JT}$ , including the SO and JT interactions can now be used to simulate the SiV<sup>-</sup> spectrum. To realize this we diagonalize  $H_{g,e}$  to find the eigenstates of the system and determine the intensity of the respective optical transitions by calculating their transition probability P according to Fermi's golden rule

$$P = 2\pi\rho_f |\langle\psi_f|p|\psi_i\rangle|^2 \quad (1.6)$$

with the final density of states  $\rho_f$ , dipole operator p as well as initial and final states  $\psi_{i,f}$ , respectively. Moreover, in  $D_{3d}$  symmetry we can write the dipole operator  $p = e \cdot r$  (with position operator r) as

$$\begin{array}{ccc} \begin{array}{l} \langle e_{gx} | \\ \langle e_{gy} | \end{array} & \begin{array}{cc} |e_{ux}\rangle & |e_{uy}\rangle \\ \left[ \begin{array}{cc} e & 0 \\ 0 & -e \end{array} \right] \end{array} & \begin{array}{l} \langle e_{gx} | \\ \langle e_{gy} | \end{array} & \begin{array}{cc} |e_{ux}\rangle & |e_{uy}\rangle \\ \left[ \begin{array}{cc} 0 & -e \\ -e & 0 \end{array} \right] \end{array} & \begin{array}{l} \langle e_{gx} | \\ \langle e_{gy} | \end{array} & \begin{array}{cc} |e_{ux}\rangle & |e_{uy}\rangle \\ \left[ \begin{array}{cc} e & 0 \\ 0 & e \end{array} \right] \end{array} & (1.7) \\ & p_x & & p_y & & p_z \end{array}$$

for the orbital states of the above introduced basis as it only acts on the orbital part of the wavefunction. Simulations using this model for the emitters used throughout this thesis can be found in Fig. 4.1. Moreover, the three components  $p_x$ ,  $p_y$  and  $p_z$  can be interpreted as individual dipoles along  $(1\bar{2}1)$ ,  $(\bar{1}01)$  as well as the high-symmetry axis of the SiV<sup>-</sup>  $(111)$ . From comparison with experimental data we can then conclude that the inner lines B and C of the fine structure show only contributions of the Z dipole and hence are linearly polarized (cf. Fig 1.3(c)). The outer line A and D however contain equal contributions of both the X and Y dipole and thus emit circularly polarized light along  $(111)$  which, projected onto the direction of observation in Fig 1.3(c) (in this case  $(001)$ ) appears to be elliptically polarized [57, 58].

Moreover, by fitting experimental spectra with this model Hepp *et al.* showed that the contribution of the JT effect to the total orbital splitting is on the order of only 10% and thus SO coupling is the dominating interaction lifting the degeneracy. Hence, it is convenient to neglect the JT effect and, in very good approximation, to treat the system in the eigenbasis of the SO Hamiltonian with the eigenstates  $|e_{g,u+} \uparrow\rangle$ ,  $|e_{g,u+} \downarrow\rangle$ ,  $|e_{g,u-} \uparrow\rangle$ ,  $|e_{g,u-} \downarrow\rangle$  with  $e_{\pm} = \mp(e_x \pm ie_y)$ . In this basis we can then express the level scheme of the SiV<sup>-</sup> in absence of any external fields as depicted in Fig. 1.4(b) with two orbital ground and excited state branches, each still being spin degenerate and the four optical transitions A, B, C, D linking them.

**Zeeman interaction** To access the SiV<sup>-</sup> centre's spin degree of freedom an external magnetic field can be applied, lifting the spin degeneracy through a Zeeman interaction.

The corresponding symmetry-adapted Hamiltonian  $H_{g,e}^Z$  can then be written as

$$H_{g,e}^Z = q\gamma_L L \cdot B + \gamma_S S \cdot B \quad (1.8)$$

$$= q\gamma_L \begin{pmatrix} 0 & 0 & iB_z & 0 \\ 0 & 0 & 0 & iB_z \\ -iB_z & 0 & 0 & 0 \\ 0 & -iB_z & 0 & 0 \end{pmatrix} \quad (1.9)$$

$$+ \gamma_S \begin{pmatrix} B_z & (B_x - iB_y) & 0 & 0 \\ (B_x + iB_y) & -B_z & 0 & 0 \\ 0 & 0 & B_z & (B_x - iB_y) \\ 0 & 0 & (B_x + iB_y) & -B_z \end{pmatrix} \quad (1.10)$$

with the orbital and electron gyromagnetic ratios  $\gamma_L = \mu_B/\hbar$  and  $\gamma_S = 2\mu_B/\hbar$  (with Bohr magneton  $\mu_B$ ), the vectorial magnetic field  $B = (B_x, B_y, B_z)$  in the internal reference frame of the  $\text{SiV}^-$ , the spin operator  $S = \hbar/2(\sigma_x, \sigma_y, \sigma_z)$  (with Pauli spin matrices  $\sigma_{x,y,z}$ ) and the orbital operator  $L$  introduced above. Moreover, in [57, 58] it has been shown that in the presence of even a weak JT interaction the orbital angular momentum and thus the orbital gyromagnetic ratio is quenched. This is implemented using the quenching factor  $q$  solely acting on the orbital part of  $H_{g,e}^Z$  with  $q$  being on the order of 0.1. Again, by neglecting JT contributions the eigenstates of the resulting total Hamiltonian  $H_{g,e} = H_{g,e}^0 + H_{g,e}^{SO} + H_{g,e}^Z$  in the basis of the SO-coupled system leads to the level scheme depicted in Fig. 1.4(c) with four non-degenerate magnetic sublevels in the ground and the excited state and 16 optical transitions linking them. From here on out we will use the labels  $|1\rangle \dots |4\rangle$  for the ground state magnetic sublevels and the labels  $|A\rangle \dots |D\rangle$  for the spin sublevels of excited state, both in increasing order of energy, whenever an external magnetic field is applied to the  $\text{SiV}^-$ . Moreover, optical transitions will be identified by their initial and final states, e.g. A1. Using the full model in comparison with spectral maps measured at varying magnetic fields, Hepp *et al.* were able to obtain a detailed picture of the  $\text{SiV}^-$  electronic structure. A similar map as well as simulations employing this model for one of the single  $\text{SiV}^-$  centres used throughout this thesis can be found in Fig. 4.2. The data therein has been measured at an angle of  $70.5^\circ$  between the external magnetic field and the (111) high symmetry axis of the  $\text{SiV}^-$ . One important feature of this spectral map is the presence of all 16 optical transitions, even those between sublevels of opposite spin, which, according to spin selection rules, should be forbidden and thus unobservable. To understand this peculiarity it is helpful to calculate the explicit eigenvectors  $|\psi\rangle = \alpha|e_{g,u+}\uparrow\rangle + \beta|e_{g,u+}\downarrow\rangle + \gamma|e_{g,u-}\uparrow\rangle + \delta|e_{g,u-}\downarrow\rangle$  of all sublevels and to express them in terms of the contributions of their basis states in the SO-coupled basis with the respective expansion coefficients  $\alpha \dots \delta$ . The resulting histograms displaying the absolute squares  $|\alpha|^2 \dots |\delta|^2$  of these coefficients are shown in Fig. 1.5(a,b) for the ground and excited state levels, respectively. From these histograms it is apparent that, while the excited state levels depicted in Fig. 1.5(b) almost exclusively contain contributions of the basis states of one spin projection, the ground states shown in Fig. 1.5(a) contain significant contributions of basis states of both spin projections. This spin mixing is a direct consequence of the presence of off-axis magnetic field components  $B_x$  and  $B_y$  for fields not aligned with the (111) direction. To better visualize this we can

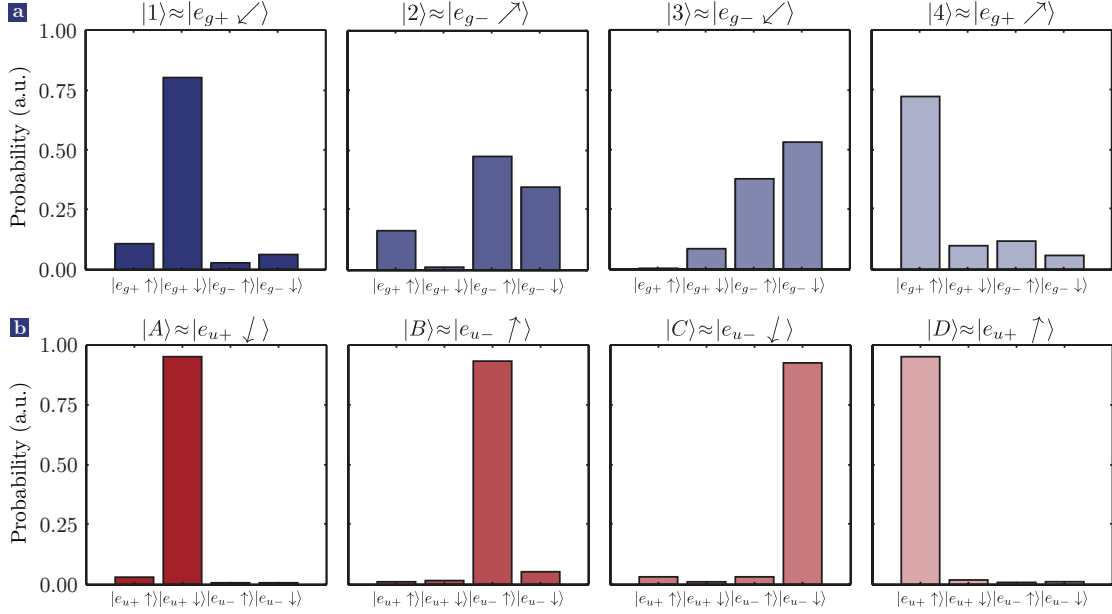


**Figure 1.5: SiV<sup>-</sup> ground & excited state eigenvectors.** Explicit eigenvectors  $|\psi\rangle = \alpha |e_{g,u+} \uparrow\rangle + \beta |e_{g,u+} \downarrow\rangle + \gamma |e_{g,u-} \uparrow\rangle + \delta |e_{g,u-} \downarrow\rangle$  for the ground (a) and excited state sublevels (b) expressed in terms of the basis states of the SO-coupled basis at a magnetic field of B=4 T applied under an angle of 70.5° with respect to the (111) high symmetry axis of the SiV<sup>-</sup>. The histograms show the absolute squares  $|\alpha|^2 \dots |\delta|^2$  of the complex expansion coefficients.

write the joint Hamiltonian of SO and Zeeman interaction in the SO-coupled basis as

$$H_{g,e}^{SO} + H_{g,e}^Z = \begin{pmatrix} \lambda + \gamma_S B_z & \gamma_S B_x & 0 & 0 \\ \gamma_S B_x & -\lambda - \gamma_S B_z & 0 & 0 \\ 0 & 0 & -\lambda + \gamma_S B_z & \gamma_S B_x \\ 0 & 0 & \gamma_S B_x & \lambda - \gamma_S B_z \end{pmatrix} \quad (1.11)$$

where we assume  $B=(B_x, 0, B_z)$  for simplicity. From this it is apparent that the off-axis components  $B_x$  lead to off-diagonal terms in the Hamiltonian coupling basis states of opposite spin projection. Moreover, this Hamiltonian also shows that the off-axis components only couple states from different orbital branches such as  $|e_{g+} \uparrow\rangle$  and  $|e_{g+} \downarrow\rangle$ . Hence, this coupling is small if the energetic distance between these states becomes large. This is the case for the excited state in which SO is about 5 times stronger than in the ground state, resulting in an almost negligible spin mixing. This effect can also be explained in terms of different quantization axes in the ground and excited state. The angle of the quantization axis is determined by the competition between the SO coupling with angular momentum components along (111) and the external magnetic field applied at an angle of 70.5°. While the strong SO coupling causes an excited state quantization axis which is only very slightly tilted with respect to (111), the much weaker ground state SO coupling results in a significantly tilted quantization axis, even for moderate off-axis magnetic field strengths. Due to these significantly different quantization axes in ground and excited

state, all excited state spin sublevels show significant overlap with all ground state spin sublevels and hence none of the dipole matrix elements  $\langle 1, 2, 3, 4 | p | A, B, C, D \rangle$  are zero. Therefore all optical transitions, even those between sublevels of opposite spin projection, are at least weakly allowed for magnetic fields not aligned with the (111) direction and hence all 16 transitions show up in the fluorescence spectrum. At this point we would also like to stress that this process can in principle be fully suppressed by aligning the field along the high-symmetry axis of the  $\text{SiV}^-$  resulting in vanishing off-axis magnetic field terms and thus equal quantization axis in the ground and excited state. However, as we will see in the following chapters, the fact that it is possible to address "spin-flipping" optical transitions utilizing off-axis fields will be a key factor enabling us to perform many of the experiments presented in this thesis and hence we will frequently revert back to this spin mixing phenomenon. Additionally, also transitions within the ground and excited state manifolds of the  $\text{SiV}^-$  take place. For the excited state manifold the underlying dynamics has been investigated by Müller *et al.* by resonantly exciting into one of the excited state levels and measuring the resulting ZPL spectrum [125]. The authors observed that e.g. upon excitation into the lower excited state spin level  $|A\rangle$  solely optical lines originating from this level can be observed while excitation into level  $|C\rangle$  of the upper excited state orbital branch featuring the same spin projection as  $|A\rangle$  resulted in spectral lines originating from both levels. The same systematics has been found for the  $|B\rangle$  and  $|D\rangle$  levels. From this, the authors conclude on the one hand that a spin state-preserving relaxation process between the excited state magnetic sublevels, faster than the excited state lifetime of about 1.8 ns, has to take place. On the other hand, the lack of lines corresponding to the higher lying branches upon excitation of  $|A\rangle$  or  $|B\rangle$  points towards a thermally activated process. In [121] Jahnke *et al.* found a similar but slower process within the ground state manifold and were able to identify and model the underlying process as a first-order phonon transition involving single E-symmetric phonons resonant with the ground or excited state level splittings  $\Delta E_{g,e}$  (note that this again is a purely orbital interaction and, as discussed above, the corresponding Hamiltonian features the same structure and properties as the JT Hamiltonian. Hence, under  $D_{3d}$  symmetry only E-symmetric phonons will couple the E-symmetric ground state levels [58, 121, 122]). Their model indicates a thermalization rate

$$\gamma_+ = 2\pi\chi\rho\Delta E_{g,e}^3 n(\Delta E_{g,e}, T) \quad (1.12)$$

and a relaxation rate

$$\gamma_- = 2\pi\chi\rho\Delta E_{g,e}^3 [n(\Delta E_{g,e}, T) + 1] \quad (1.13)$$

with the phonon number

$$n(\Delta E_{g,e}, T) = \frac{1}{\exp(\frac{\hbar\Delta E_{g,e}}{k_B T}) - 1} \quad (1.14)$$

given by a Boltzmann distribution and proportionality constants  $\chi$  and  $\rho$  [122]. For temperatures  $T \gg \hbar\Delta E_{g,e}/k_B$  we can then perform the Taylor expansion of the Boltzmann factor leading to the approximate rates

$$\gamma_+ \approx \gamma_- \approx 2\pi\chi\rho\Delta E_{g,e}^2 k_B T. \quad (1.15)$$

From this  $\Delta E_{g,e}^2$ -dependence, originating from the frequency-scaling of the phonon density of states, it is apparent why the relaxation process in the excited state as observed by Müller *et al.* is considerably faster than the ground state relaxations observed by Jahnke *et al.* In Chap. 4.2 we will revert back to these thermalization processes and discuss their implications for the spin coherence properties of the SiV<sup>-</sup>.

**Absolute energies & shelving state** Now that we have established a detailed picture of the SiV<sup>-</sup> centre's electronic structure and electron configuration in ground and excited state, let us take a closer look at the absolute energetic positioning of the individual states relative to the diamond band gap. The discussion presented here is based on recent DFT calculations performed by Gali and Maze [110]. While, as mentioned above, early investigations placed the SiV<sup>-</sup> ground state about 2.05 eV below the conduction band edge of diamond [108] these new calculations come to a drastically different result. According to the simulations of Gali and Maze, the states of the SiV<sup>-</sup> are localized around the valence band edge of diamond. In particular, the fully occupied  $e_u$  orbital in the  ${}^2E_{g,SiV^-}$  ground state is localized within the valence band while the  $e_g$  orbital carrying the hole lies about 0.8 eV above the valence band maximum (VBM). The resulting electron configuration is depicted in the lower left diagram of Fig. 1.6. Upon excitation of an electron from the  $e_u$  to the  $e_g$  level this situation changes and the  $e_u$  orbital now containing the hole is placed about 0.12 eV above the valence band edge in the resulting  ${}^2E_{u,SiV^-}$  excited state. This allows narrowband optical transitions and the calculated transition energy of 1.72 eV for the  ${}^2E_{u,SiV^-} \rightarrow {}^2E_{g,SiV^-}$  transition agrees well with the experimentally measured value of 1.68 eV for the SiV<sup>-</sup> ZPL. Moreover, the authors demonstrate that the charge distribution in both states is very similar and mostly only differ in phase. Hence, no significant changes in the potentials experienced by the ions will occur upon optical excitation or relaxation which agrees well with the observed low Huang Rhys factor of the SiV<sup>-</sup>. Additionally, in earlier experiments performed by Neu *et al.* [55, 126] an effective three-level model including a long-lived shelving state had to be used to explain a bunching for small correlation times  $\tau$  observed in  $g^{(2)}(\tau)$  intensity autocorrelation measurements. However, the exact nature of this shelving state remained elusive until now and even the detailed group theoretical model developed by Hepp *et al.* contains no conclusive hint about the nature of this state. The calculations of Gali and Maze however reveal that the valence band edge of the diamond is strongly perturbed by the presence of the SiV<sup>-</sup> resulting in additional localized  $e_{g,VBM}$  and  $a_{1g,VBM}$  orbitals from which electrons can as well be excited into the  $e_g$  orbital of the SiV<sup>-</sup>. This results in two additional excited state configurations with  ${}^2E_{g,VBM}$  (upper right diagram in Fig. 1.6) and  ${}^2A_{1g,VBM}$  (lower right diagram) symmetry. Since the absolute energy of the  ${}^2E_{g,VBM}$  is calculated to be only 0.1 eV lower than the  ${}^2E_{u,SiV^-}$  excited state of the SiV<sup>-</sup>, an efficient non-radiative  ${}^2E_{u,SiV^-} \rightarrow {}^2E_{g,VBM}$  transition is possible. Due to the fact that both VBM states are of even parity their decay into the likewise even ground state of the SiV<sup>-</sup> is optically forbidden and hence these states can act as long-lived shelving levels. Moreover, in [127] Neu *et al.* observed an additional, so far unexplained, optical transition at 823 nm which, by using fluorescence cross-correlation measurements has been related to the SiV<sup>-</sup>. The simulations of Gali and Maze indicate that this line might be a result of the decay of the  ${}^2A_{1g,VBM}$  shelving state into the ground state in the presence of

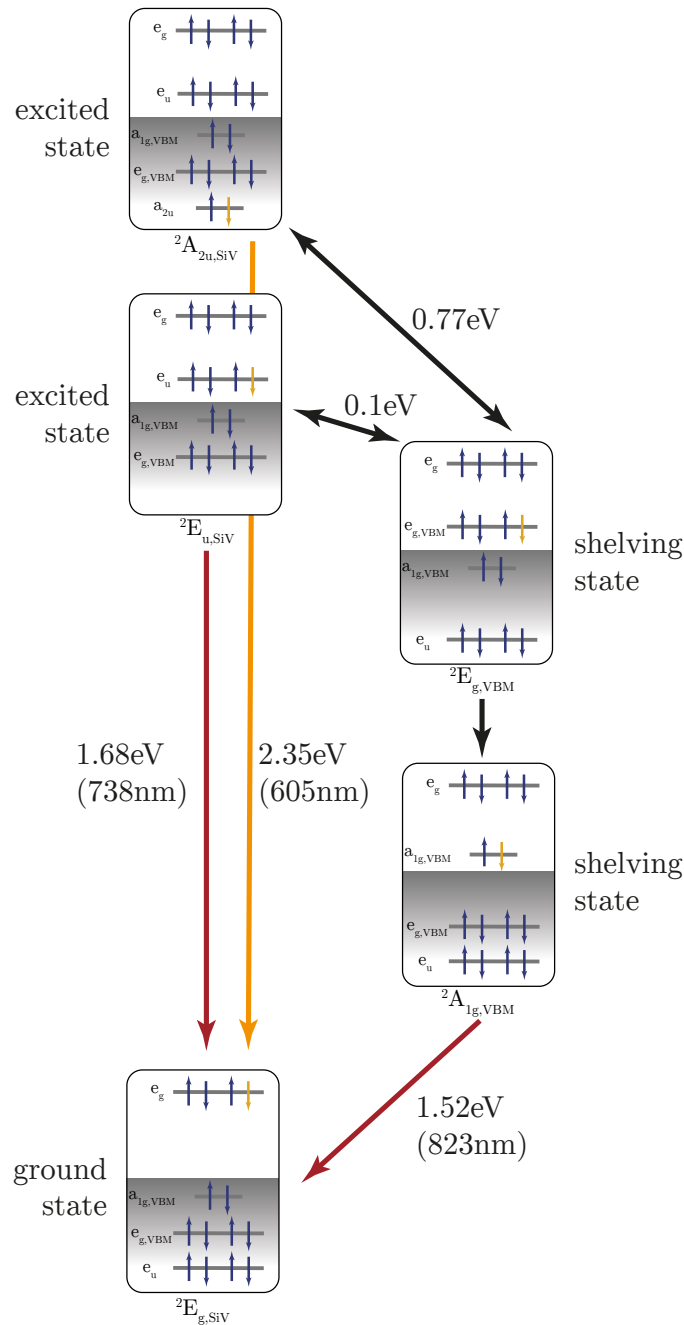


**Figure 1.6: SiV<sup>-</sup> absolute energies & shelving states according to Gali & Maze [110].** Absolute energies of the individual electronic levels relative to each other and the valence band edge (individual diagrams) as well as relative energetic ordering of the resulting electron configurations. Due to the presence of the SiV<sup>-</sup> the valence band states (VBM) are perturbed causing additional localized  $a_{1g,VBM}$  and  $e_{g,VBM}$  states. Therefore, in addition to the ground and excited states of the defect (left side of the diagram) additional excited states involving the band levels appear (right side). These levels are linked to each other and to the ground state via parity-forbidden transitions and are thus long-lived, accounting for the shelving observed in SiV<sup>-</sup> autocorrelation measurements.

strong crystal strain which perturbs the  $\text{SiV}^-$  symmetry and thus lifts the parity selection rules. This line has never been seen for the  $\text{SiV}^-$  centres investigated in this thesis and other similar centres in type IIa HPHT material, underlining its high crystal quality and low strain. Additionally, in a number of previous experiments it has been observed that for some  $\text{SiV}^-$  centres an increase in fluorescence under resonant excitation can be achieved by adding an additional repump laser. This effect is not present for all  $\text{SiV}^-$  centres and a clear correlation between this repumping and other properties of the centres such as strain so far remains elusive. We observed the repumping for a wide range of applied wavelengths from 532 nm up to 810 nm. Besides potentially influencing the charge state of the  $\text{SiV}^-$  in the presence of optical fields, based on the simulations by Gali et al. this repumping might also be explained by deshelving due to optical excitation of the parity-allowed transition from the upper shelving level  ${}^2E_{g,VB\bar{M}}$  into the about 0.77 eV (1610 nm) higher lying  ${}^2A_{2u}$  excited state followed by a direct decay back into the  ${}^2E_{g,\text{SiV}}$  ground state.

In this chapter we presented a detailed review of both the important physical properties of the diamond host lattice as well as the silicon vacancy defect. Most importantly we discussed the  $\text{SiV}^-$  centre's spectral properties and established a detailed theoretical framework describing the electronic properties of both unperturbed  $\text{SiV}^-$  centres as well as  $\text{SiV}^-$  centres subjected to external magnetic fields. In the following chapter we will now take a closer look at the coherent interaction between a multi-level system like the  $\text{SiV}^-$  and several coherent light fields. Building up on the basic electronic properties discussed here, we will then discuss a number of experimental techniques and theoretical models later used in this work utilizing light to measure the  $\text{SiV}^-$  centre's inherent coherence properties as well as to coherently control its quantum state for QIP applications.

## Chapter 2

# Light-matter interactions

As we have discussed in the introduction, a method to fully control the quantum state of qubits is a fundamental requirement for realizing a QIP system [17]. Their computational basis is a quantum mechanical two-level system and, as we will see throughout this chapter, any quantum state of this system can be represented as a vector on a unit sphere, the so-called Bloch sphere. Thus, to be able to reach an arbitrary point on the surface of this sphere (i.e. to prepare an arbitrary quantum state), rotations around two orthogonal axes are needed [128]. Moreover, although the basis of a qubit consists of only two basis states, in multi-level systems, additional levels are frequently used to aid controlling, initializing or reading out the two-level qubit. Throughout the work presented here we will use orbital as well as spin states of the  $\text{SiV}^-$  to realize a qubit basis. Due to the unique electronic structure of the  $\text{SiV}^-$ , all of them are optically addressable and therefore we will use laser pulses to control the centre. Thus, the aim of this chapter is the derivation of a fundamental theoretical background on atomic systems interacting with coherent fields of light and to introduce the techniques used to characterize and control the qubits in this work. A detailed description of the concepts and effects discussed throughout this chapter can for example be found in [129, 130]. First, we develop the most basic model of a two-level atom interacting with a single classical coherent light field, omitting any dissipative processes such as spontaneous emission. We then include these processes using the density matrix representation of the system. In Sec. 2.2 we will then extend this model to a three-level system interacting with two light fields which can be detuned independently from the atomic resonance frequencies. We also look at a minor variation of this system, a three-level system coupled to an additional, auxiliary level which is used to model branching and decoherence in multi-level systems. We will use this configuration to model the results of the coherent population trapping experiments in Chap. 4.2 and Chap. 4.3. Finally, we will derive a full four-level model appropriate to describe the population dynamics as well as coherent interactions within the orbital doublet ground and excited state manifolds of the  $\text{SiV}^-$  at zero magnetic field. This model will be used to model the results of the resonant as well as Raman-based ultrafast coherent control experiments in Chap. 4.4 and Chap. 5.

## 2.1 A two-level atom interacting with light

The most basic quantum system one could imagine to interact with light is a single atom consisting of only two energy levels, a ground state  $|1\rangle$  and an excited state  $|2\rangle$  linked by a single optical transition with transition frequency  $\omega_0$  (c.f. Fig. 2.1). This system is of course purely fictional as no real atom solely features two levels. However, in many cases more complex systems can be approximated successfully using this simple picture.

### 2.1.1 The two-level Hamiltonian

The time evolution of the system is described by the time-dependent Schrödinger equation

$$H\psi(r, t) = i\hbar \frac{d\psi(r, t)}{dt}. \quad (2.1)$$

with the Hamiltonian  $H$  and wave function  $\psi(r, t)$ . In the following we assume the system is interacting with a single coherent field of light with carrier frequency  $\omega$ . The total Hamiltonian

$$H = H_0 + H_i \quad (2.2)$$

of the system can thus be split into two components, the unperturbed Hamiltonian of the atom  $H_0$  which relates to the eigenenergies of the system as well as  $H_i$  describing the interaction of the atom with the light field. By defining the energy of the ground state to be  $E_1=0$  the atomic Hamiltonian in matrix representation can be written as

$$H_0 = \hbar \begin{pmatrix} 0 & 0 \\ 0 & \omega_0 \end{pmatrix} \quad (2.3)$$

and the most general solution of  $H$  is given by

$$\psi(r, t) = c_1(t)\psi_1(r, t) + c_2(t)\psi_2(r, t). \quad (2.4)$$

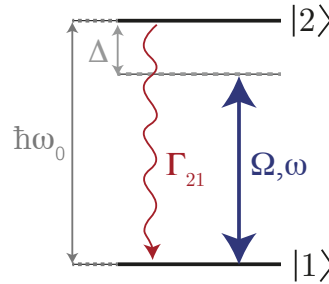


**Figure 2.1: The two-level system.** Schematic representation of a two-level atom with ground state  $|1\rangle$  and excited state  $|2\rangle$  (optical transition frequency  $\omega_0$ ) interacting with a single coherent field of light with frequency  $\omega$  and Rabi frequency  $\Omega$ . Additionally, the system can undergo spontaneous emission from  $|2\rangle$  to  $|1\rangle$ .

By inserting this expression in 2.1 we obtain the following set of coupled differential equations:

$$c_2(t)\exp(-i\omega_0 t)M_{12} = i\frac{dc_1(t)}{dt} \quad (2.5)$$

$$c_1(t)\exp(i\omega_0 t)M_{21} = i\frac{dc_2(t)}{dt} \quad (2.6)$$

$M_{ij}$  hereby represents the transition matrix element with

$$M_{ij} = \frac{1}{\hbar} \langle \psi_i | H_i | \psi_j \rangle \quad (2.7)$$

with

$$H_i = PE_0 \cos(\omega t). \quad (2.8)$$

Here, we made use of the so called *dipole approximation* [131] which assumes that the length scale of the system is significantly smaller than the wavelength of the interacting field. For optical fields ( $\lambda = 300 - 800$  nm) and atoms ( $r_{atom} \approx 10^{-10}$  m) or colour centres ( $r_{cc} \approx 10^{-9}$  m = a few lattice constants) this assumption is almost perfectly fulfilled and thus  $kr \ll 1$  holds. Under this approximation we can assume the coupling between atom and field to be solely of dipolar character with the dipole operator

$$P = e \sum_i r_i \quad (2.9)$$

with position operators  $r_i$  and no spatial dependence of the electric field. With this we define the Rabi frequency

$$\Omega = \frac{1}{\hbar} E_0 \langle \psi_i | P | \psi_j \rangle = \frac{e}{\hbar} E_0 \langle \psi_i | r | \psi_j \rangle. \quad (2.10)$$

The Rabi frequency can be interpreted as a measure of the interaction strength between atom and light field. Using this expression, we can rephrase the interaction Hamiltonian in matrix representation as

$$H_i = \hbar \begin{pmatrix} 0 & \Omega \cos(\omega t) \\ \Omega \cos(\omega t) & 0 \end{pmatrix} = \hbar \begin{pmatrix} 0 & \frac{\Omega}{2}(e^{i\omega t} + e^{-i\omega t}) \\ \frac{\Omega}{2}(e^{i\omega t} + e^{-i\omega t}) & 0 \end{pmatrix} \quad (2.11)$$

and the total Hamiltonian  $H$  thus is given by

$$H = H_0 + H_i = \hbar \begin{pmatrix} 0 & \frac{\Omega}{2}(e^{i\omega t} + e^{-i\omega t}) \\ \frac{\Omega}{2}(e^{i\omega t} + e^{-i\omega t}) & \omega_0 \end{pmatrix}. \quad (2.12)$$

To simplify simulating the time-dependent interaction of the atom with the field it is convenient to transform  $H$  into a rotating frame. This allows modelling the atom-light interaction on a relative frequency scale with respect to the laser frequency instead of having to treat the system using absolute (optical) frequencies. We transform  $H$  into the interaction picture according to  $U^\dagger H U - iU^\dagger \dot{U}$  with the unitary transformation matrix

$$U = \begin{pmatrix} 1 & 0 \\ 0 & e^{i\omega t} \end{pmatrix}. \quad (2.13)$$

This transformation corresponds to a change into a new frame of reference rotating with the optical frequency  $\omega$  leading to a new Hamiltonian  $H'$  of the form

$$H' = \hbar \begin{pmatrix} 0 & \frac{\Omega}{2}(1 + e^{-2i\omega t}) \\ \frac{\Omega}{2}(1 + e^{2i\omega t}) & \omega - \omega_0 \end{pmatrix}. \quad (2.14)$$

Now, we apply the so-called *rotating wave approximation* (RWA) which assumes that the terms oscillating at  $2\omega$  average out on the time scale of the system dynamics and can be neglected [129]. Furthermore, we define the detuning  $\Delta = \omega - \omega_0$  between atomic resonance and field carrier frequency. The Hamiltonian  $H'$  can thus be written as

$$H' = \frac{\hbar}{2} \begin{pmatrix} 0 & \Omega \\ \Omega & \Delta \end{pmatrix}. \quad (2.15)$$

Due to its simplicity, from now on, we will solely use this interaction picture to represent the more complex Hamiltonians in the following sections. Moreover, by inserting the matrix elements 2.7 into 2.5 and 2.6 and again performing the RWA we obtain the following differential equations:

$$\frac{\Omega}{2} c_2(t) \exp(-i\Delta t) = i \frac{dc_1(t)}{dt} \quad (2.16)$$

$$\frac{\Omega}{2} c_1(t) \exp(i\Delta t) = i \frac{dc_2(t)}{dt} \quad (2.17)$$

Solving these expressions with the initial conditions  $|c_1|^2(t=0) = 1$  and  $|c_2|^2(t=0) = 0$  as well as  $\Delta = 0$  leads to the following simple terms for the probabilities  $|c_i|^2$  to find the system in  $|g\rangle$  or  $|e\rangle$  at a certain point in time:

$$|c_1|^2(t) = \cos^2(\Omega t) \quad (2.18)$$

$$|c_2|^2(t) = \sin^2(\Omega t) \quad (2.19)$$

These equations represent a time-dependent oscillation of the excitation probability of the atom, the well-known Rabi oscillations [132]. Figure 2.2 shows the calculated populations of the ground (blue) and excited state (red) using the equations above, assuming a Rabi frequency of  $\Omega=1$  MHz. Here the atom is in perfect resonance with the light field and no dissipative processes are destroying the coherence of the system. Thus, the observed oscillations show perfect visibility and are completely undamped. Note that under coherent excitation of the system the excitation probability can reach unity while the probability to find the system in its excited state under incoherent excitation is always less than or equal to 0.5 [129]. In reality, the condition of no dissipation is usually not fulfilled as e.g. optically excited systems spontaneously decay back into their ground state or external fields such as phonon- or nuclear spin-baths induce additional decoherence. In the following section we thus strive to incorporate these effects into the theoretical framework of light-matter interactions.

### 2.1.2 Optical Bloch equations and the density matrix

To describe the effects of spontaneous emission and other decoherence processes on our two-level atom we now use a density matrix representation of our system. From equations

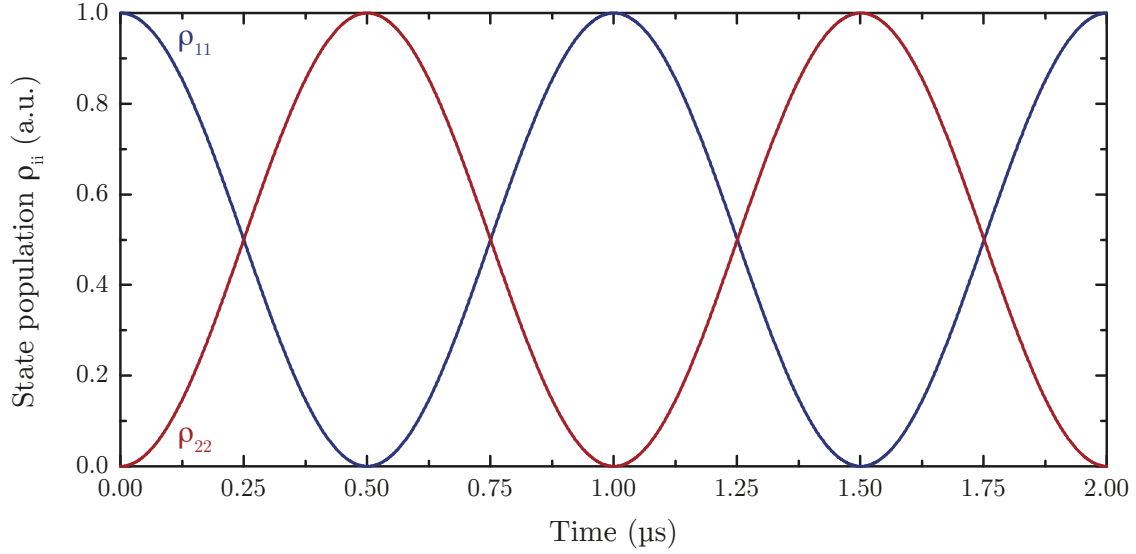


**Figure 2.2: Rabi oscillations.** Simulated Rabi oscillations ( $\Omega=1$  MHz) of a two-level system assuming no spontaneous emission and no detuning. The system undergoes undamped oscillations of the excitation probability for an infinite period of time and with a visibility of 1.

2.18 and 2.19 it is apparent that the quantities of interest to represent the state of the system are the expectation values given by  $c_i c_j^*$ . Using these products, we define the density matrix  $\rho$  with its matrix elements

$$\rho_{ii} = |c_i|^2 \quad (2.20)$$

and

$$\rho_{ij} = c_i c_j^* \quad (2.21)$$

The diagonal elements  $\rho_{ii}$  hereby represent the populations in states  $|i\rangle$  and are real numbers while the off-diagonal elements  $\rho_{ij}$  are called coherences as they introduce coupling between the states and are in general complex. Moreover, for the populations

$$\sum_i \rho_{ii} = 1 \quad (2.22)$$

holds. For a pure state (i.e. a well-defined superposition of basis states)  $Tr(\rho^2)$  equals unity, while for a mixed state (i.e. a statistical mixture of basis states without defined phase relations)  $Tr(\rho^2)$  is less than one. In analogy to the time-dependent Schrödinger equation which defines the evolution of the wave function  $\psi$  the time-dependence of the density matrix is defined by the quantum mechanical master equation for open quantum systems:

$$\dot{\rho} = \frac{i}{\hbar}[H, \rho] + \mathcal{L}(\rho) + \sum \mathcal{D}_i(\rho) \quad (2.23)$$

Here, the coherent evolution of the system is included in the commutator of the Hamiltonian  $H$  with  $\rho$  while decoherence is added via the Lindblad superoperator  $\mathcal{L}(\rho)$  and the dephasing

operators  $\mathcal{D}_i(\rho)$ . The Lindblad operators hereby model decoherence due to dissipation, i.e. incoherent transfer of population between different states due to e.g. spontaneous emission. Additional decoherence due to pure dephasing of the energy levels, i.e. without population transfer, (e.g. due to phonon scattering) or limited laser coherence is included via the operators  $\mathcal{D}_i(\rho)$ . Initially we assume these to be zero but we will briefly discuss their form later on. To incorporate spontaneous decay from  $|2\rangle$  into  $|1\rangle$  we first define the Lindblad superoperator

$$\mathcal{L}(\rho) = \sum \mathcal{L}_{ij} = -\frac{1}{2} \sum (C_{ij}^\dagger C_{ij} \rho + \rho C_{ij}^\dagger C_{ij}) + \sum C_{ij} \rho C_{ij}^\dagger \quad (2.24)$$

with the collapse operators

$$C_{ij} = \sqrt{\Gamma_{ij}} |j\rangle \langle i|. \quad (2.25)$$

The constant  $\Gamma_{ij}$  hereby is the spontaneous emission rate between the two states. For the simple two-level system we can thus write

$$\mathcal{L}_{21} = \hbar \begin{pmatrix} \Gamma_{21} \rho_{22} & -\frac{\Gamma_{21}}{2} \rho_{12} \\ -\frac{\Gamma_{21}}{2} \rho_{21} & -\Gamma_{21} \rho_{22} \end{pmatrix}. \quad (2.26)$$

Inserting this expression and 2.15 into 2.23 then leaves us with the following equations of motion:

$$\dot{\rho}_{11} = \frac{i\hbar\Omega}{2} (\rho_{12} - \rho_{21}) + \hbar\Gamma_{21}\rho_{22} \quad (2.27)$$

$$\dot{\rho}_{12} = \frac{i\hbar}{2} (\Omega\rho_{11} - \Omega\rho_{22} + 2\Delta\rho_{12}) - \frac{\hbar\Gamma_{21}}{2} \rho_{12} \quad (2.28)$$

$$\dot{\rho}_{21} = \frac{i\hbar}{2} (\Omega\rho_{22} - \Omega\rho_{11} - 2\Delta\rho_{21}) - \frac{\hbar\Gamma_{21}}{2} \rho_{21} \quad (2.29)$$

$$\dot{\rho}_{22} = \frac{i\hbar\Omega}{2} (\rho_{21} - \rho_{12}) - \hbar\Gamma_{12}\rho_{22} \quad (2.30)$$

These are the so-called *optical Bloch equations* (OBE) for the two-level system, including spontaneous decay. Additionally, we define the so-called *Bloch vector* according to

$$\begin{pmatrix} u \\ v \\ w \end{pmatrix} = \begin{pmatrix} \rho_{21} + \rho_{12} \\ i(\rho_{12} - \rho_{21}) \\ \rho_{11} - \rho_{22} \end{pmatrix} = \begin{pmatrix} 2\text{Re}(\rho_{12}) \\ 2\text{Im}(\rho_{21}) \\ \rho_{11} - \rho_{22} \end{pmatrix} = \begin{pmatrix} r \sin \theta \cos \phi \\ r \sin \theta \sin \phi \\ r \cos \theta \end{pmatrix}. \quad (2.31)$$

Using this expression we can represent every state of the two-level system as a three-dimensional vector on (or within) a unit sphere featuring  $|1\rangle$  and  $|2\rangle$  as north and south pole, respectively. We can thus characterise a certain state of the system by the polar angle  $\theta$  (with  $0 \leq \theta \leq \pi$ ) representing the distribution of population, the azimuthal angle  $\phi$  (with  $0 \leq \phi \leq 2\pi$ ) representing a phase and  $r = \text{Tr}(\rho^2)$  ( $r \in [0, 1]$ ) as a measure for the "purity" of the state. In the following chapters, we will frequently make use of this representation to refer to optical pulses inducing a certain rotation of our qubit. For example, a pulse of area  $\pi$  (also called  $\pi$ -pulse) brings the qubit from  $|1\rangle$  to  $|2\rangle$  ( $\theta = \pi$ ) while a  $\frac{\pi}{2}$ -pulse prepares the qubit in an equal superposition  $\frac{1}{\sqrt{2}}(|1\rangle + i|2\rangle)$  (this operation is also called the Hadamard gate).

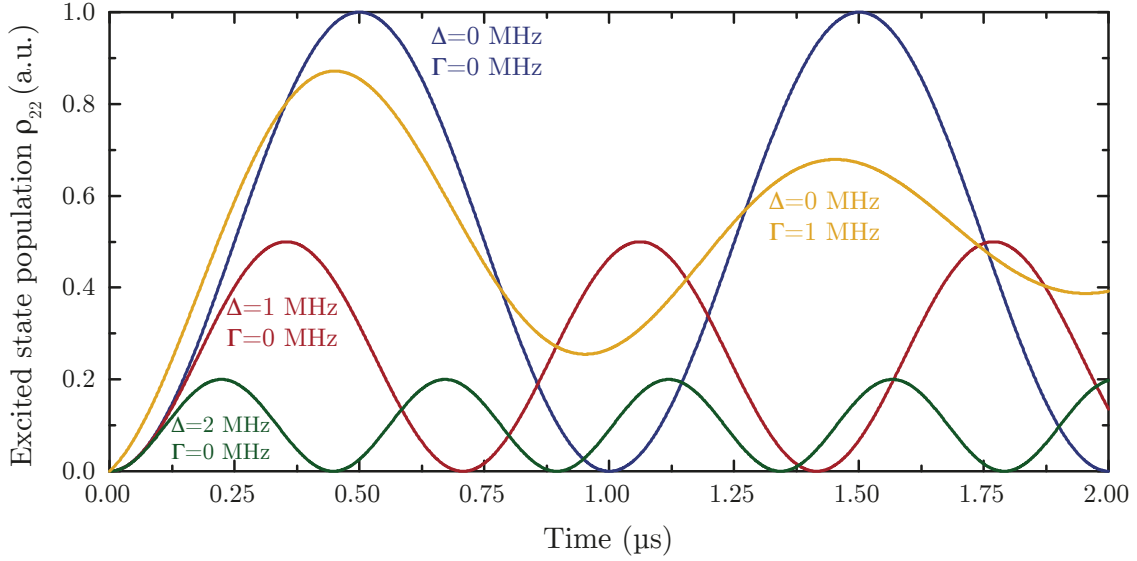


**Figure 2.3: Rabi oscillations - detuning & decoherence.** Simulation of the excited state population  $\rho_{22}$  of a two-level system interacting with a coherent light field. A density-matrix approach is used and the resulting OBEs have been numerically solved for different values of the detuning  $\Delta$  and the spontaneous decay rate  $\Gamma_{21}$ .

### 2.1.3 Rabi oscillations, Ramsey interference and Hahn echo

While for the simple case of a two-level system analytical solutions of the OBEs can be found (at least for a number of trivial cases such as  $\Delta = \Gamma = 0$ ), they have to be solved numerically for more complex systems. Using the density matrix approach we now have means to analyse the influence of the detuning  $\Delta$  and the spontaneous emission rate  $\Gamma_{21}$  on the Rabi oscillations. Figure 2.3 shows simulated Rabi oscillations using the above described density matrix model of the two-level system. The OBEs have been solved numerically (MATLAB-solver: ODE45) using a Runge-Kutta-approach [133]. This solver will also be used in the following chapters to numerically solve the OBEs for the more complex models used to evaluate the experimental data. The blue curve in Fig. 2.3 reproduces again the undamped oscillations we already observed in Fig. 2.2 for a vanishing spontaneous decay rate and detuning. Increasing the detuning  $\Delta$  (red and green curves) leads to an increase in oscillation frequency while the maximum excitation probability decreases. Additionally, including a spontaneous emission of the excited state level (yellow curve) leads to an exponential decrease of the oscillation amplitude over time as this process is incoherent (it does not preserve a fixed phase relation), leading to a randomization of the state vector in the  $xz$ -plane (i.e. its length shrinks). The fluorescence level thus decreases to half of the maximum value corresponding to a statistical mixture of ground and excited state with a probability of 0.5 to find the system excited. We name the relaxation time constant originating from this decay of population the spontaneous emission time  $T_1$  (also called longitudinal coherence time or spin lattice time). In addition to a decay of population, the coherence of a system can also be destroyed by dephasing i.e. by a

randomization of the phase of a quantum state which corresponds to a random orientation of the state vector within the equatorial plane of the system. This process does not change the population distribution in the system (i.e. it leaves the diagonal elements of the density matrix unchanged). In case of solid state quantum systems, this can on the one hand be caused by intrinsic sources such as fluctuating external electric or magnetic fields due to e.g. a nuclear or electron spin bath in the environment of the observed quantum system. On the other hand, external sources such as limited laser coherence can also lead to such a dephasing. In the density matrix formalism we account for these processes using the operators  $\mathcal{D}_i(\rho)$  in equation 2.23 which take on the form

$$\mathcal{D}_i(\rho) = d_i(\rho_{ii} |i\rangle \langle i| - \frac{1}{2}|i\rangle \langle i|, \rho_{ii}) \quad (2.32)$$

with the dephasing rates  $d_i$ . The coherence times associated with these types of processes are commonly called homogeneous phase coherence time  $T_2$  (also called transverse coherence time) containing homogeneous as well as inhomogeneous contributions. With it we define a total coherence time (or free induction decay time)  $T_2^*$  [134] according to

$$\frac{1}{T_2^*} = \frac{1}{2T_1} + \frac{1}{T_2} \quad (2.33)$$

that combines the above-mentioned decoherence mechanisms. Thus for vanishing dephasing, the ultimate limit to the coherence of a qubit is given by the relaxation processes according to [130]

$$T_2^* \leq 2T_1. \quad (2.34)$$

Moreover, in ensembles of qubits an additional decoherence time constant  $T_2'$  is introduced accounting for inhomogeneous effects making the total coherence time

$$\frac{1}{T_2^*} = \frac{1}{2T_1} + \frac{1}{T_2} + \frac{1}{T_2'} \quad (2.35)$$

The same time-constant  $T_2'$  can also be used to model trial-to-trial variations in repetitive experimental scheme using single qubits [33]. Note that attention has to be paid as many different notations for the above mentioned coherence times are used in literature such as the exchanged meanings of  $T_2$  and  $T_2^*$ .

The Rabi oscillations discussed above allow for a defined rotation of a qubit state about an arbitrary angle  $\theta$  around the x-axis of the Bloch sphere. With this technique, all possible qubit operations are given by a set of  $1 \times 1$  matrices forming a Lie group  $U(1)$ , thus this control is frequently called  $U(1)$ - or angular control [25]. To realize a complete set of single-qubit gates a rotation around a second axis on the Bloch sphere is needed. This can be accomplished by harnessing the natural free precession of the state vector in the xy-plane of the sphere (around the z-axis) at  $\omega$ . This technique is called *Ramsey interferometry* and consists of a two-pulse sequence [135]. Starting in the ground state  $|1\rangle$ , in the Bloch sphere picture introduced above, we first apply a pulse to rotate the system around  $\theta = \frac{\pi}{2}$ , leaving the system in an equal superposition (c.f. Fig. 2.4)

$$|\psi_{\frac{\pi}{2}}\rangle = \frac{1}{\sqrt{2}}(|1\rangle + i|2\rangle). \quad (2.36)$$

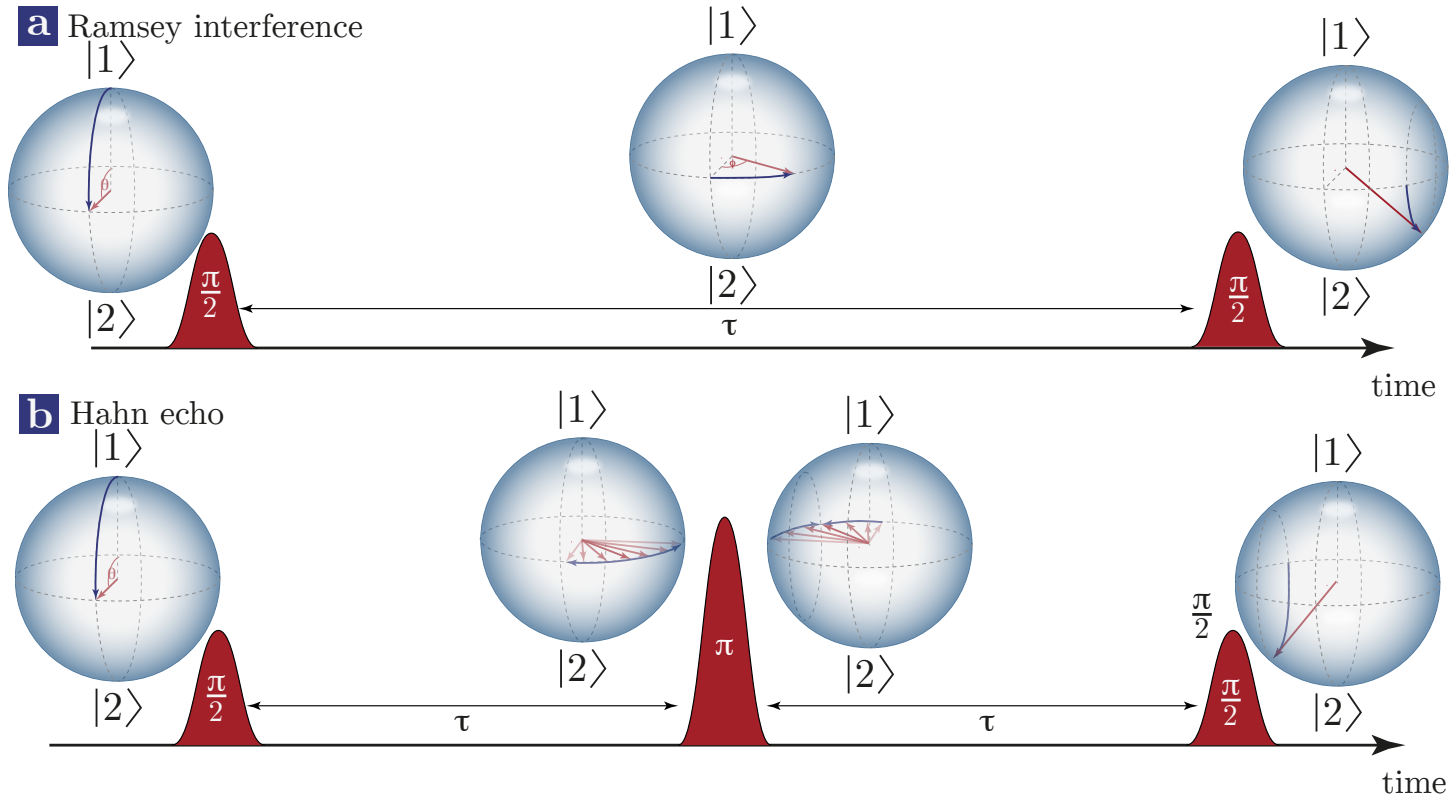


**Figure 2.4: Pulse sequences.** Bloch sphere representations for (a) a Ramsey interference pulse sequence featuring two subsequent  $\frac{\pi}{2}$ -pulses and (b) a Hahn echo sequence consisting of two  $\frac{\pi}{2}$ -pulses with an additional  $\pi$ -pulse in the centre. The multiple arrows in this representation can either be understood as different phase evolutions of individual quantum systems in an ensemble or as different evolutions of a single system during repetitive experimental sequences.

Due to the difference in energy, both states will accumulate phase at different rates and the system is then allowed to freely evolve for a certain time  $\tau$ . The resulting rotation angle within the xy-plane is given by  $\phi(\tau) = \omega_0 \cdot \tau$ . We can thus rewrite the state as

$$|\psi_{\frac{\pi}{2} \rightarrow \tau}\rangle = \frac{1}{\sqrt{2}}(|1\rangle + ie^{-i\omega_0\tau}|2\rangle) = \frac{1}{\sqrt{2}}(|1\rangle + ie^{-i\phi(\tau)}|2\rangle). \quad (2.37)$$

After  $\tau$  a second  $\frac{\pi}{2}$ -pulse now rotates the system around  $\theta$ . This leaves the system in another superposition state of  $|1\rangle$  and  $|2\rangle$  in which their ratios now depend on the accumulated phase. This state can be written as

$$|\psi_{\frac{\pi}{2} \rightarrow \tau \rightarrow \frac{\pi}{2}}\rangle = \frac{1}{2}(1 - e^{-i\phi(\tau)})|1\rangle + \frac{i}{2}(1 + e^{-i\phi(\tau)})|2\rangle \quad (2.38)$$

Experimentally we will e.g. detect the fluorescence of the system resulting from an excitation to  $|2\rangle$  and thus the fluorescence level is proportional to the excitation probability. If  $\tau$  is chosen such that the resulting angle is  $\phi = 2n\pi$  ( $n \in \mathbb{N}$ ), a second  $\frac{\pi}{2}$ -pulse applied after  $\tau$  will bring the system to its excited state  $|2\rangle$  (the two pulses act constructively on  $\theta$ ) and the maximum signal is detected. On the contrary, a rotation by  $\phi = (2n + 1)\pi$  followed by a  $\frac{\pi}{2}$ -pulse thus brings the system back to its ground state and no fluorescence is measured. For all intermediate cases, the excitation probability is proportional to  $\phi$  obeying

$$|\langle 2|\psi_{\frac{\pi}{2} \rightarrow \tau \rightarrow \frac{\pi}{2}}\rangle|^2 = \frac{1}{2}(1 + \cos(\phi(\tau))) \quad (2.39)$$

and resulting in a pattern of fringes for varying values of  $\tau$ . To harness this technique for full coherent control of the qubit, the pulse area  $\theta$  of the two pulses as well as  $\tau$  can be adjusted to reach an arbitrary point on the Bloch sphere. This allows to access a full set of single-qubit operations and we call the technique the so-called axis or SU(2) control [25]. Moreover, while the simple picture of the state transformations above does not include any decoherence terms, in the presence of decoherence, the fringe amplitude decays exponentially for increasing pulse delays with a rate  $\frac{1}{T_2^*}$ . We can thus modify Eq. 2.39 to

$$|\langle 2|\psi_{\frac{\pi}{2} \rightarrow \tau \rightarrow \frac{\pi}{2}}\rangle|^2 = \frac{1}{2}(1 + \cos(\phi(\tau))) \cdot e^{-\frac{\tau}{T_2^*}} \quad (2.40)$$

by including an additional exponential damping term. We will utilize this decay in Chaps. 4.4.1 and 4.3 for a precise measurement of the ground and excited state coherence times of the SiV<sup>-</sup>.

By extending the Ramsey pulse sequence using an additional  $\pi$ -pulse centered in between the two  $\frac{\pi}{2}$ -pulses we obtain the so-called Hahn echo (or spin echo) pulse sequence [136]. In the case of single quantum systems this technique can be used to counteract slow environmental effects obscuring the measurement during temporal averaging (this is the inhomogeneous contribution in  $T_2'$ ) [137]. In Chap. 5 we will also look at the coherence of ensembles of SiV<sup>-</sup> centres. In this case the Hahn echo technique can counteract the effect of inhomogeneous broadening (in our case caused by static crystal strain) causing different emitters in the ensemble to have slightly different energy levels and thus, according to

Eq. 2.37, accumulate phase at different rates. To remedy this we start with the state given by Eq. 2.37 (after the application of a first  $\frac{\pi}{2}$ -pulse) and after a first delay time  $\tau$  apply a  $\pi$ -pulse, leaving the system in the state

$$|\psi_{\frac{\pi}{2} \rightarrow \tau \rightarrow \pi}\rangle = \frac{1}{\sqrt{2}}(|2\rangle + e^{-i\phi(\tau)} |1\rangle) \quad (2.41)$$

in which the phase is flipped between  $|2\rangle$  and  $|1\rangle$  with regard to state  $\psi_{\frac{\pi}{2} \rightarrow \tau}$ . After another period  $\tau$  during which the excited state again acquires phase relative to the ground state due to their difference in energy the system eventually reaches the state

$$|\psi_{\frac{\pi}{2} \rightarrow \tau \rightarrow \pi \rightarrow \tau}\rangle = \frac{1}{\sqrt{2}}(e^{-i\phi(\tau)} |2\rangle + e^{-i\phi(\tau)} |1\rangle) \quad (2.42)$$

in which both basis states are completely in phase. This leads to a rephasing of the collective state of an ensemble of emitters and thus improves the coherence time scale. This simple picture assumes the absence fast decoherence processes. However, using this technique, only non-Markovian effects i.e. processes which are essentially steady on the time-scale of the echo sequence can be reverted. Thus faster dephasing processes e.g. due to rapid phonon scattering will again lead to an exponential decay of the system at a rate  $\frac{1}{T_2}$ . Besides improving coherence times, this method therefore allows for a measurement of the remaining homogeneous phase coherence time  $T_2$  (also called Hahn echo time) by recording the decay of the Hahn echo signal with increasing pulse delays  $\tau$ , providing valuable information about the environmental noise spectrum in a sample.

Moreover, to reduce the decoherence rate of a qubit and thus to extend its lifetime, so-called *dynamical decoupling* techniques can be employed [138]. The most simple scheme for such a technique has been introduced by Carr and Purcell and can be derived from the above discussed Hahn echo by replacing the single  $\pi$ -pulse by a series of  $\pi$ -pulses with a delay shorter than the correlation time of the environment [139]. While this scheme is susceptible to pulse area errors more complex decoupling schemes employing  $\pi$ -pulses with different phases such as the widely used Carr-Purcell-Meiboom-Gill (CPMG) sequence [140] have been developed to correct for these types of experimental errors [141].

## 2.2 Coherence in three-level systems

In the previous section we investigated the coherent interaction of a light field with a simple two-level atom. While this concept is mostly artificial, this simple model allows for a study of several coherence-related phenomena and, in many cases, is even a good approximation to describe the dynamics of subsystems of multilevel quantum systems. However, most of the quantum systems known today (such as the  $\text{SiV}^-$  discussed throughout this thesis) feature several electronic states leading to a number of additional coherent phenomena which are not governed by a two-level model. Therefore, to explore some of these effects, such as coherent population trapping (CPT) and stimulated Raman adiabatic passage (STIRAP), both of which are of importance for the experiments presented in this work, we will now look at the coherent dynamics of three-level systems. In general there are three different types of three-level systems, the  $\Lambda$ -type scheme (two ground states coupled

to a common excited state), the ladder system (three states stacked in energy) and the V-type scheme (one ground state coupled to two different excited states). Here, we will solely discuss the  $\Lambda$ -system as the  $\text{SiV}^-$  electronic level structure allows for the realization of multiple of those schemes and many of the experimental methods used throughout this thesis utilize this level configuration.

### 2.2.1 Autler-Townes splitting, coherent population trapping and electromagnetically induced transparency

We now consider a three-level  $\Lambda$ -system with two non-degenerate ground states  $|1\rangle$  and  $|2\rangle$  coupled to a common excited state  $|3\rangle$  as it is depicted in Fig. 2.5. The transition frequencies of the  $|3\rangle \rightarrow |1\rangle$  and  $|3\rangle \rightarrow |2\rangle$  transitions are  $\omega_1$  and  $\omega_2$ , respectively. Moreover, we couple the two ground states to the excited state via two coherent light fields. Transition  $|1\rangle$  to  $|3\rangle$  is coupled via a field with frequency  $\omega_1$  and Rabi frequency  $\Omega_1$ , transition  $|2\rangle$  to  $|3\rangle$  via a field with frequency  $\omega_2$  and Rabi frequency  $\Omega_2$ . The interaction Hamiltonian of this system can be written as

$$H = \frac{\hbar}{2} \begin{pmatrix} 0 & \Omega_1 & 0 \\ \Omega_1 & -2\Delta_1 & \Omega_2 \\ 0 & \Omega_2 & -2(\Delta_1 - \Delta_2) \end{pmatrix} \quad (2.43)$$

with the detunings  $\Delta_{1,2} = \omega_{01,2} - \omega_{1,2}$  of the two fields and again making use of the rotating wave approximation [142]. Assuming two-photon resonance, i.e.  $\Delta_1 = \Delta_2$  but allowing for a common two-photon detuning  $\Delta = \Delta_1 - \Delta_2$  the eigenstates of this Hamiltonian can be written as

$$|\psi_+\rangle = \sin\theta \sin\phi |1\rangle + \cos\phi |3\rangle + \cos\theta \sin\phi |2\rangle \quad (2.44)$$

$$|\psi_-\rangle = \sin\theta \cos\phi |1\rangle - \sin\phi |3\rangle + \cos\theta \cos\phi |2\rangle \quad (2.45)$$

$$|\psi_0\rangle = \cos\theta |1\rangle - \sin\theta |2\rangle \quad (2.46)$$

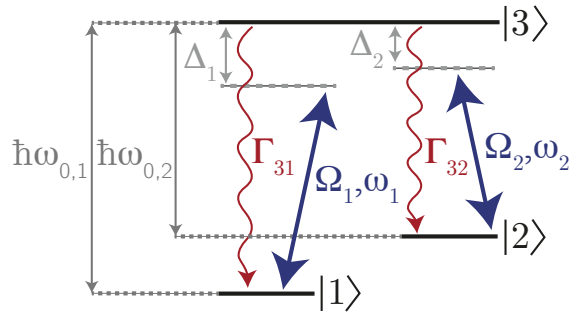


**Figure 2.5: The  $\Lambda$ -scheme.** Schematic representation of a three-level  $\Lambda$ -type atom with non-degenerate ground states  $|1\rangle$ ,  $|2\rangle$  and excited state  $|3\rangle$  (optical transition frequencies  $\omega_{0,1/2}$ ) interacting with two coherent fields of light with frequencies  $\omega_{1,2}$  and Rabi frequencies  $\Omega_{31,32}$ . Additionally, the system can undergo spontaneous emission from  $|3\rangle$  into  $|1\rangle$ ,  $|2\rangle$  with rates  $\Gamma_1$ ,  $\Gamma_2$ .

utilizing the mixing angles  $\theta$  and  $\phi$  obeying the relations

$$\tan \theta = \frac{\Omega_1}{\Omega_2} \quad (2.47)$$

$$\tan 2\phi = \frac{\sqrt{\Omega_1^2 + \Omega_2^2}}{\Delta}. \quad (2.48)$$

The resulting states called *dressed states* turn out to be superpositions of the bare atomic states [143]. Let us first look at the states  $|\psi_+\rangle$  and  $|\psi_-\rangle$ . Both states contain contributions from the excited state. Moreover, both states have the energy eigenvalues

$$E_{\pm} = \frac{\hbar}{2}(\Delta \pm \sqrt{(\Delta^2 + \Omega_1^2 + \Omega_2^2)}) \quad (2.49)$$

leading to an upwards shift of  $|\psi_+\rangle$  and a downwards shift of  $|\psi_-\rangle$  with respect to the bare excited state  $|3\rangle$ . The resulting splitting is proportional to the effective driving strength  $\tilde{\Omega} = \sqrt{\Omega_1^2 + \Omega_2^2}$  of the system and is called *Autler-Townes splitting* [144]. This splitting can also be interpreted as an AC Stark-shift of the excited state. In the presence of a strong field, this splitting can be wider than the optical linewidth. Hence, a second laser shone in on the frequency of the original resonance will exhibit a significantly reduced absorption, giving rise to a phenomenon called electromagnetically induced transparency (EIT) [64].

Let us now take a closer look at the remaining dressed state  $|\psi_0\rangle$ . This state contains no contribution from the excited state and hence does not interact with light. Therefore, this state is called a *dark state* and population that is transferred into this state is decoupled from the exciting laser. If both lasers meet the two-photon resonance condition so that the dressed states can efficiently form and the system is excited continuously, population will eventually be optically pumped into this state and the system will turn dark. Experimentally, if one laser is kept on resonance and the second one is scanned across the resonance, this manifests as a very sharp dip in the fluorescence response of the system as soon as both fields hit two-photon resonance. This phenomenon is called *coherent population trapping* (CPT) and can also be interpreted as a destructive quantum interference of both excitation pathways leading to a direct transfer of population between the two ground states [145, 146]. As this transition under normal conditions is electric dipole forbidden, its linewidth can be very narrow. Processes affecting the coherence of the ground states such as phonon-induced population transfers or spin flips (as it is the case for the SiV<sup>-</sup>) thus lead to a decoherence of the dark state  $|\psi_0\rangle$  which broadens the observed CPT-dip. Therefore, CPT is an extremely sensitive probe to measure the ground state coherence time of a quantum system. Hence, we will use this technique in Chap. 4.2 to measure the ground state spin coherence time of the SiV<sup>-</sup>. In this context we will use a slight extension of the three-level model described here, which is a  $\Lambda$ -system coupled to an additional state being is not coherently addressed and only populated and depopulated via spontaneous emission processes. We use this auxiliary state  $|aux\rangle$  to model the influence of all the additional excited and ground state spin levels of the SiV<sup>-</sup> (while keeping the numeric complexity at a minimum). These levels are not part of the  $\Lambda$ -system, however, due to phonon-mediated relaxation and thermalization within the excited and ground state

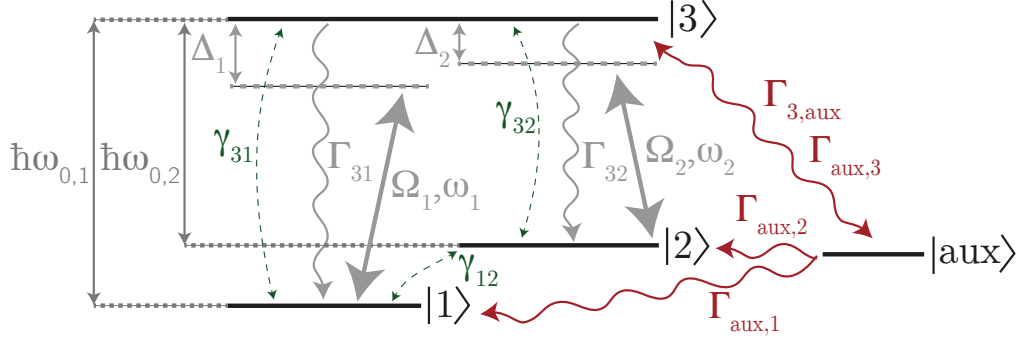


**Figure 2.6:**  $\Lambda$ -scheme with auxiliary state. Schematic representation of a  $\Lambda$ -system coupled to an auxiliary state  $|aux\rangle$  which is only interacting with the  $\Lambda$ -system via spontaneous emission. Additionally, pure dephasing rates  $\gamma_{31,31,12}$  have been introduced. To enhance comprehensibility, only newly introduced rates in comparison with Fig. 2.5 have been coloured.

manifold of the  $\text{SiV}^-$ , their presence leads to additional decoherence. The Hamiltonian for this system can therefore be written as [147]

$$H = \frac{\hbar}{2} \begin{pmatrix} 0 & \Omega_1 & 0 & 0 \\ \Omega_1 & -2\Delta_1 & \Omega_2 & 0 \\ 0 & \Omega_2 & -2(\Delta_1 - \Delta_2) & 0 \\ 0 & 0 & 0 & 0 \end{pmatrix} \quad (2.50)$$

with no coherent coupling of the additional state to any field and the interaction with the  $\Lambda$ -system occurs solely via the inclusion of Lindblad operators accounting for spontaneous emission rates  $\Gamma_{3,aux}$ ,  $\Gamma_{aux,3}$ ,  $\Gamma_{aux,1}$  and  $\Gamma_{aux,2}$  according to Eq. 2.24. Additionally, obeying Eq. 2.32, we introduce the pure dephasing rates  $\gamma_{31}$ ,  $\gamma_{32}$  between the ground and excited states as well as  $\gamma_{12}$  between the ground states to account for additional dephasing without population transfer. Figure 2.6 shows a schematic representation of the above described system as it is used to model the results in Chaps. 4.2 and 4.3. To simulate the results of these experiments, this reduced model with only a simple  $\Lambda$ -system, an additional auxiliary state  $|aux\rangle$  and only an effective ground state dephasing rate  $\gamma_{12}$  is sufficient and in the case of the Zeeman-split  $\text{SiV}^-$  significantly reduces the computational complexity as we do not have to solve a full 8-level system. For all other experiments (at zero magnetic field) we will use a more complete level including the four orbital states of the  $\text{SiV}^-$  as well as relaxations within the ground and excited state manifolds which we will discuss in the following sections.

## 2.2.2 Stimulated Raman adiabatic passage

Let us now return to the simple  $\Lambda$ -system depicted in Fig. 2.5 with its dressed states Eq. 2.44-2.46. In addition to CPT, which populated the dark state  $|\psi_0\rangle$  via optical pumping, we will now look at an adiabatic way to address this state which also allows for population transfer between the ground states in a coherent fashion without ever populating the excited state [148]. A schematic representation of the process discussed below can be found

in Fig. 5.4. At the beginning ( $t_0$ ), let us assume the system is fully initialized in state  $|1\rangle$ . Hence, the application of a weak field  $\Omega_2$  on the  $|2\rangle \rightarrow |3\rangle$  transition does not lead to a population of the excited state. Moreover, according to Eq. 2.47, for  $\Omega_1 = \Omega_b = 0$  we find  $\theta = 0$  and thus  $|\psi_0\rangle = |1\rangle$ , meaning that the ground state  $|1\rangle$  is aligned with the dark state. Let us now apply a sequence of two optical pulses (e.g. of Gaussian shape), a first pulse on the  $|2\rangle \rightarrow |3\rangle$  transition and a slightly delayed second pulse on the  $|1\rangle \rightarrow |3\rangle$  transition: In the beginning of this process  $|\psi_0\rangle \approx |1\rangle$  still holds as long as  $\Omega_2 \gg \Omega_1$  is fulfilled. Under these conditions  $\Omega_1$  can be considered off-resonant due to the Autler-Townes splitting created by  $\Omega_2$ . For  $t_1 < t < t_2$  the ratio  $\frac{\Omega_1}{\Omega_2}$  now becomes larger as the field  $\Omega_1$  increases while  $\Omega_2$  ramps down. Under uncontrolled conditions this would now lead to an excitation of the system into  $|3\rangle$  and decoherence due to spontaneous emission. However, by carefully limiting the rate of change in the Rabi frequencies, this process can be made adiabatic, i.e. it is possible to evolve the mixing angles  $\theta$  and  $\phi$  in a way that keeps the system aligned with the dark state. To realize this state evolution, we have to introduce adiabaticity criteria [130]. Using the transformation matrix

$$U = \begin{pmatrix} \sin \theta(t) \sin \phi(t) & \sin \theta(t) \cos \phi(t) & \cos \theta(t) \\ \cos \theta(t) \sin \phi(t) & \cos \theta(t) \cos \phi(t) & -\sin \theta(t) \\ \cos \phi(t) & -\sin \phi(t) & 0 \end{pmatrix} \quad (2.51)$$

we first have a look at the Hamiltonian  $\tilde{H}$  in the dressed basis which we can write as

$$\tilde{H} = U^\dagger H U - iU^\dagger \dot{U} = \begin{pmatrix} \lambda_+ & i\dot{\phi} & i\dot{\theta} \sin \phi(t) \\ -i\dot{\phi} & \lambda_- & i\dot{\theta} \cos \phi(t) \\ -i\dot{\theta} \sin \phi(t) & -i\dot{\theta} \cos \phi(t) & 0 \end{pmatrix} \quad (2.52)$$

with its three eigenvalues

$$\lambda_0 = 0 \quad (2.53)$$

$$\lambda_+ = \frac{\sqrt{\Omega_1^2 + \Omega_2^2}}{2} \tan \phi(t) \quad (2.54)$$

$$\lambda_- = -\frac{\sqrt{\Omega_1^2 + \Omega_2^2}}{2} \cot \phi(t). \quad (2.55)$$

If the system is prepared in a defined superposition of the eigenstates of  $\tilde{H}$  it will stay in this state if the off-diagonal elements of  $\tilde{H}$  are small. A more precise condition is that the absolute values of the off-diagonal elements of  $\tilde{H}$  have to be much smaller than the smallest difference between two eigenvalues which is given by

$$|\lambda_{\pm}(t) - \lambda_0| = \frac{1}{2} |\Delta(t) \pm \sqrt{\Delta^2(t) + \Omega_1^2(t) + \Omega_2^2(t)}|. \quad (2.56)$$

Using the time derivatives of the mixing angles

$$\dot{\theta}(t) = \frac{\dot{\Omega}_1(t)\Omega_2(t) - \Omega_1(t)\dot{\Omega}_2(t)}{\Omega_1^2(t) + \Omega_2^2(t)} \quad (2.57)$$

$$\dot{\phi}(t) = \frac{\frac{d}{dt} \sqrt{\Omega_1^2(t) + \Omega_2^2(t)} \Delta(t) - \sqrt{\Omega_1^2(t) + \Omega_2^2(t)} \dot{\Delta}(t)}{\Omega_1^2(t) + \Omega_2^2(t) + \Delta^2(t)} \quad (2.58)$$

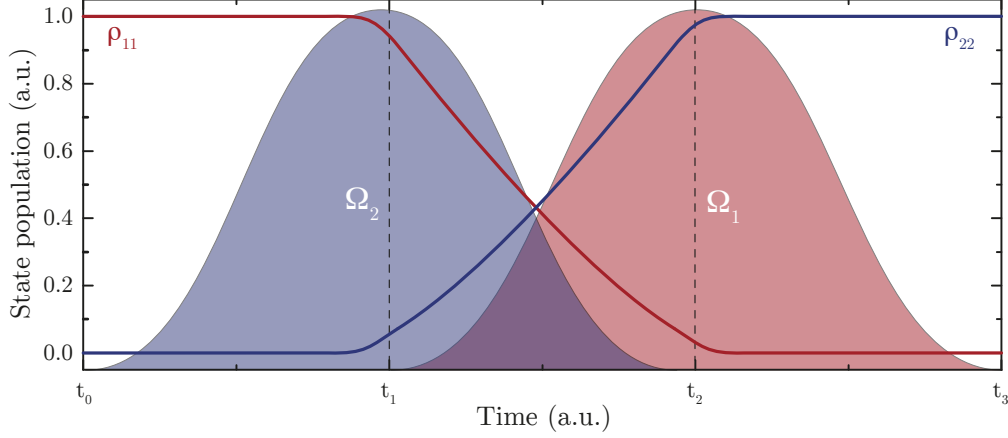


**Figure 2.7: Stimulated Raman adiabatic passage.** Simplified and idealized scheme of STIRAP. The system is initialized in the ground state  $|1\rangle$ . The graph displays the time evolution of the ground state populations  $\rho_{11}$  (red) and  $\rho_{22}$  (blue) during STIRAP transfer. The transfer is induced by two optical pulses (background) applied in a counter-intuitive sequence on both transitions of the  $\Lambda$ -scheme.

we can then finally derive

$$|\dot{\theta}(t)| \ll |\lambda_{\pm}| \quad (2.59)$$

$$|\dot{\phi}(t)| \ll |\lambda_{\pm}| \quad (2.60)$$

as local conditions for adiabaticity which by integration can be converted into the following global conditions:

$$\pi = \int_{-\infty}^{\infty} dt |\dot{\theta}(t)| \ll \int_{-\infty}^{\infty} dt |\Delta \pm \sqrt{\Delta^2 + \Omega_1^2(t) + \Omega_2^2(t)}| \quad (2.61)$$

$$\frac{\pi}{2} = \int_{-\infty}^{\infty} dt |\dot{\phi}(t)| \ll \int_{-\infty}^{\infty} dt |\Delta \pm \sqrt{\Delta^2 + \Omega_1^2(t) + \Omega_2^2(t)}| \quad (2.62)$$

Both conditions can be fulfilled for sufficiently high two-photon detunings  $\Delta$  and pulse areas. Hence, at the end of this phase the system is still in the dark state, however now the contribution of the bare state  $|2\rangle$  is maximized. In the final phase, the remaining field  $\Omega_1$  is then slowly ramped down leading to  $\frac{\Omega_1}{\Omega_2} \rightarrow \infty$  and thus  $\theta \rightarrow \frac{\pi}{2}$ . At the end of the process, this leads to an alignment of the dark state parallel to the final bare atomic state  $|2\rangle$  and completes the process termed *stimulated Raman adiabatic passage (STIRAP)*. Moreover, because the first pulse in the STIRAP scheme addresses an empty state this sequence is often referred to as being counter-intuitive.

In Chap. 4.4.3 we will use two-photon Raman-transitions to realize a full coherent control of a qubit based on the ground state orbital levels of the  $\text{SiV}^-$ . This is a very similar process to the above described STIRAP scheme with the distinct difference that time inversion symmetry is preserved by applying both Raman pulses simultaneously. In this scheme, a large two-photon detuning  $\Delta$  is used to minimize the population of the excited state

(while STIRAP can work both on resonance or detuned). Under this condition, population is coherently transferred within the ground state manifold as long as two-photon resonance is maintained. The two-photon Rabi frequency  $\Omega$  is given by [149]

$$\Omega = \frac{\Omega_1 \Omega_2}{2\Delta} \quad (2.63)$$

while the population in the excited states scales with [150]

$$\rho_{33} = \frac{\Omega_{1,2}}{(2\Delta)^2}. \quad (2.64)$$

Therefore, by detuning the lasers from resonance population of the excited state can efficiently be avoided ( $\rho_{33}$  drops quadratically with  $\Delta$ ) at the cost of control speed ( $\Omega$  drops linearly with  $\Delta$ ). We will use this technique to demonstrate two-photon Raman-Rabi oscillations and Raman-Ramsey interference in Chap. 4.3 using pulses from cw lasers modulated in length and in Chap. 4.4 using amplitude-modulated ultrafast laser pulses. Note that, due to the large detuning in this scheme, the excited state level is often times "adiabatically eliminated" in literature and the system is then treated as an effective two-level system with the two states linked via the two-photon transition [151]. In this work we won't make this simplification as experimentally perfect adiabaticity cannot be realized and a partial population of the excited state occurs which our theory has to account for to accurately reproduce the experimental results. In addition, if more than one excited state level is present, the system can couple to several  $\Lambda$ -schemes at once leading to additional transfer pathways, an effect that we will briefly discuss in the next section.

## 2.3 The double- $\Lambda$ system

As discussed in Chap. 1.2.4, the electronic structure of the  $\text{SiV}^-$  consists of an orbital doublet ground and excited state split by a spin-orbit interaction and a Jahn-Teller effect. This level arrangement can also be interpreted as two separate  $\Lambda$ -systems formed between the two ground states and the lower and upper excited state, respectively. In Chap. 4.4 we will present results on coherent manipulation of the orbital ground states of the  $\text{SiV}^-$  using Raman transitions as we have discussed them in the previous section. There we use fields detuned far from resonance to minimize optical excitation and, as briefly mentioned before, under these conditions the fields can couple the ground states via both  $\Lambda$ -schemes leading to two separate transfer pathways with different effective Rabi frequencies due to the different detuning of the lasers relative to both excited states. As we will see, this then e.g. causes additional oscillatory components in the observed two-photon Ramsey interference and thus, to ensure accurate state preparation of a certain ground state superposition, these effects have to be accounted for [152]. A schematic representation of the four-level double- $\Lambda$ -type system is depicted in Fig. 2.8. To include the additional  $\Lambda$ -system into our theoretical framework, we use the four-level Hamiltonian

$$H = \frac{\hbar}{2} \begin{pmatrix} 0 & 0 & \Omega_{1,3} & \Omega_{1,4} \\ 0 & 2(\Delta_2 - \Delta_1) & \Omega_{2,3} & \Omega_{2,4} \\ \Omega_{1,3} & \Omega_{2,3} & 2\Delta_1 & 0 \\ \Omega_{1,4} & \Omega_{2,4} & 0 & 2(\Delta_1 + \delta_e) \end{pmatrix} \quad (2.65)$$

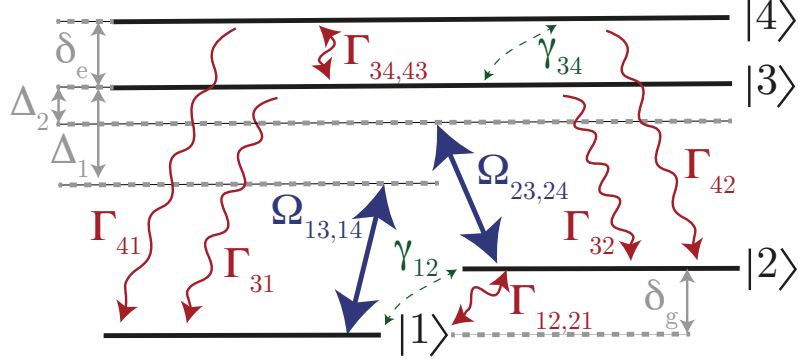


**Figure 2.8: Double- $\Lambda$ -scheme** Schematic representation of a double- $\Lambda$ -type system resembling the orbital electronic structure of the  $\text{SiV}^-$ . In a Raman-based experiment, the two fields (blue) can couple the two ground states  $|1\rangle$  and  $|2\rangle$  via both excited states  $|3\rangle$  and  $|4\rangle$  with different detunings. Additionally, the system undergoes a number of spontaneous decay processes (red) and pure dephasing processes (green).

with the excited state splitting  $\delta_e$  and the Rabi frequencies

$$\Omega_{1,j} = \frac{\mu_{1,j} E_1}{\hbar} \quad (2.66)$$

$$\Omega_{2,j} = \frac{\mu_{2,j} E_2}{\hbar} \quad (2.67)$$

to account for different effective coupling strengths of the two fields  $E_1$  and  $E_2$  originating from different transition dipole moments  $\mu_{i,j}$  of the four optical transitions. All decoherence effects have been included as presented in the previous chapters with one minor alteration: We included additional spontaneous decay rates  $\Gamma_{12,21}$  and  $\Gamma_{34,43}$  between the sublevels of the ground and the excited state manifold, respectively as phonon-mediated thermalization and relaxation between the orbital states is a significant source of decoherence. Moreover, the thermalization rates  $\Gamma_{12}$  and  $\Gamma_{34}$  are coupled to their respective relaxation rates via a Boltzmann-factor

$$\Gamma_{ij} = \Gamma_{ji} e^{-\frac{\delta_{e,g}}{k_B T}} \quad (2.68)$$

with the ground and excited state splittings  $\delta_{e,g}$ . Using this model we analyze the results from the resonant as well as Raman-based optical control experiments in Chap. 4.4. Moreover, to more accurately describe the Hahn-echo, Ramsey and STIRAP results obtained in  $\text{SiV}^-$  ensembles in Chap. 5 we expand this model in the following way: We expand the Hamiltonian from Eq. 2.65 into a three-dimensional array  $H_n$  where  $n$  represents the  $n$ -th  $\text{SiV}^-$  in the ensemble. To simulate the inhomogeneous broadening  $\Delta\nu_{inh}$  of the ensemble we define the detunings  $\Delta_{1,2}^n$  by equally distributing them over a Gaussian distribution with full width of half maximum  $\Delta\nu_{inh}$ . This resembles the fact that each  $\text{SiV}^-$  in the ensemble experiences a slightly different detuning relative to the applied laser fields. After solving the OBEs, the resulting density matrix elements  $\rho_{ij}^n$  for the individual centres are then averaged and weighted with a scaling factor for each  $\text{SiV}^-$  corresponding to the

amplitude of the Gaussian distribution. This simulates the abundance of each individual frequency class of  $\text{SiV}^-$  centres in the ensemble.

A number of MATLAB scripts have been written implementing the theoretical framework presented throughout this chapter. These scripts can be found in Appendix A. In particular, Appendix A.1 contains scripts implementing the model discussed in Sec. 2.2.1. We will use this model to analyse the CPT results in Chap. 4.2 and 4.3. To describe the coherent control experiments of single  $\text{SiV}^-$  centres in Chap. 4.4 as well as ensembles in Chap. 5 we will then use the MATLAB scripts from Appendix A.2 which implement the model presented in Sec. 2.3 of this chapter.

The theoretical concepts to realize optical control of qubits laid out throughout this chapter highly rely on the optical and electronic properties of the  $\text{SiV}^-$  centres employed for the experiments as e.g. broadened optical lines inhibit addressing individual levels and decoherence highly depends on crystal strain. Moreover, the techniques presented here require the generation of sequences of optical pulses with defined delays, bandwidths and repetition rates. Therefore, we will now take a closer look at the fabrication of high-quality  $\text{SiV}^-$  centres as well as at the optical setups used to obtain the experimental results of this thesis which will then be presented in Chap. 4 and Chap. 5.



## Chapter 3

# Sample preparation & optical setups

*Pre-selection of diamond substrates (provided by Element Six) for the fabrication of a single emitter sample has been conducted by Jonas N. Becker (J.N.B.) using a polarization microscope in the group of Prof. F. Mücklich at Saarland University. Simulations of ion implantations have been performed by J.N.B. Ion implantations have been carried out at the RUBION facility of the Ruhr University Bochum by J.N.B. with technical assistance by Dr. Detlef Rogalla. Milling of solid immersion lenses has been performed in the group of Prof. F. Mücklich at Saarland University by J.N.B and Christoph Pauly. Chemical cleaning and annealing after implantation and ion beam milling as well as Cr sputtering of diamond samples have been performed by J.N.B. (using a sputtering system at the Nano Structuring Center of the Technical University Kaiserslautern).*

*The ensemble samples have been fabricated by Dr. Hadwig Sternschulte and Element Six, respectively.*

*The confocal microscope used for sample characterization has originally been set up and modified by several former members of the group of Prof. Christoph Becher and has been described extensively in former theses [58, 119].*

*The setup for the coherent population trapping experiment has been set up in the laboratory of Professor Mete Atatüre (Cavendish Laboratory, University of Cambridge) by J.N.B and Benjamin Pingault (B.P., University of Cambridge) with technical advice from Carsten Schulte and Jack Hansom (both University of Cambridge).*

*The confocal microscope for the refrigerator has been designed by J.N.B with technical advice from Jun.-Prof. Pavel Bushev (P.B.). The parts of the setup have been fabricated by the mechanical workshop of the physics department at Saarland University following the technical drawings provided by J.N.B. Installation of optical fibre links between different laboratories has been performed by J.N.B and Matthias Bock. The optical setup has been designed and set up by J.N.B with help from David Groß, B.P. and Dr. Mustafa Gündogan (University of Cambridge). The dilution refrigerator has been operated by P.B. and Dr. Nadezhda Kukharchyk.*

*The optical setup for the coherent control experiments with single emitters has been designed and set up by J.N.B and later modified to perform experiments using emitter ensembles by J.N.B, Johannes Görlitz and Christian Weinzettl (University of Oxford).*

In this chapter we will briefly review the experimental techniques utilized throughout this work. In the first part we will discuss the fabrication of diamond samples containing single  $\text{SiV}^-$  centres as well as ensembles of emitters as they were used for the experiments in Chap. 4 and Chap. 5, respectively. In the second part of this chapter we will then focus on the optical setups used to conduct the experiments presented later in this thesis and provide selected fundamentals on some of the key devices used to conduct the experiments.

### 3.1 Fabrication of single-emitter samples

The availability of samples containing  $\text{SiV}^-$  centres with good spectral properties as well as reasonably high count rates is a fundamental requirement for the experiments presented in this thesis. Hence, in the following sections we will cover the fabrication process of a high-quality sample containing single  $\text{SiV}^-$  centres including diamond pre-selection, ion implantation as well as fabrication of all-diamond solid immersion lenses.

#### 3.1.1 Diamond substrate pre-selection

Although its inversion symmetry, to some extent, protects the  $\text{SiV}^-$  against external perturbations, previous work already indicated that the electronic and spin properties of the  $\text{SiV}^-$  can be significantly altered in the presence of strong crystal strain [58, 62]. Therefore, in previous experiments we used commercially available (Element Six, "electronic grade") CVD diamond plates featuring high purity ( $<5$  ppb  $[\text{N}_s^0]$  and  $<1$  ppb  $[\text{B}_s]$ ) and moderate strain levels. However, very frequently,  $\text{SiV}^-$  centres in these plates still exhibit significant crystal strain, most likely caused by high growth rates of the commercial material making the search for unstrained emitters a long and tedious process and limiting usability in QIP applications. In this work we therefore use a type IIa HPHT diamond substrate (Element Six, material not commercially available). Due to the high temperatures and pressures during their fabrication, the dislocation density in these types of diamond, in general, is much lower as e.g. vacancies can easily diffuse out of the material during growth. Moreover, while most commercially available HPHT diamonds are yellow stones of type Ib, containing several ppm of  $[\text{N}_s^0]$ , the material used throughout this work has been grown in presence of a nitrogen getter such as Al or Ti, allegedly reducing the  $[\text{N}_s^0]$  content to below 0.1ppm and leaving a colourless plate, well-suited for optical experiments [86]. To verify that the plate indeed experiences a reduced crystal strain compared to electronic grade CVD plates, we pre-characterized the sample using polarization microscopy. For this, we place the diamond plates in an optical microscope in between two crossed linear polarisers. An ideal diamond single crystal, as a cubic material, is not birefringent and thus, a completely unstrained sample would not cause any light to pass through the second polariser. However, if linearly polarized light passes through a strained region with two orthogonal stress components  $\sigma_1$  and  $\sigma_2$ , the components of its electric field projected onto the principal stress directions experience different refractive indices, leading to a phase difference  $\delta$  between both components according to

$$\delta = \frac{2C\pi d}{\lambda}(\sigma_1 - \sigma_2). \quad (3.1)$$

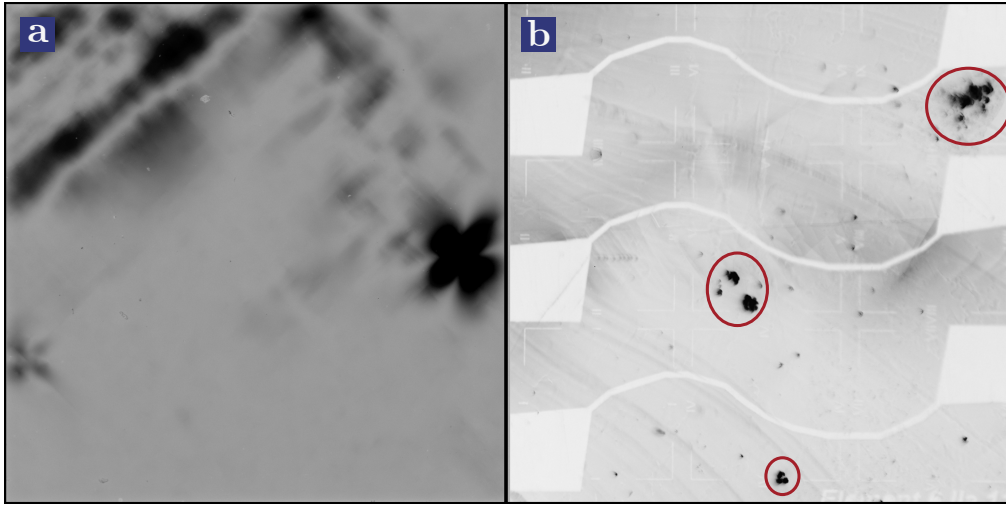


**Figure 3.1: Polarization microscopy.** Images of (a) a commercially available CVD-grown and polished diamond plate (Element Six, "electronic grade") and (b) a type IIa HPHT diamond plate (Element Six, cleaved but unpolished) taken with a polarization microscope. Red circles indicate surface damage.

with sample thickness  $d$ , wavelength  $\lambda$  and a material-dependent scaling coefficient  $C$  [153]. This strain-dependent retardation leads to a change in the polarization properties of the light transmitted through the sample which can therefore pass through the second polariser and can be observed. This technique is also useful to identify small inclusions in the diamond as they create localized strain fields enhancing their visibility [154].

In Fig. 3.1(a) a polarization microscopic image of a standard electronic grade CVD diamond plate is shown while Fig. 3.1(b) displays an image of the HPHT plate used in this thesis. Both images have been obtained using equal light and camera settings to ensure optimal comparability. Moreover, for better visibility the images have been inverted, i.e. dark areas correspond to strained regions. It is apparent that the entire image of the electronic grade plate is significantly darker compared to the HPHT plate, indicating a stronger overall strain in the plate. Previous work using Raman spectroscopy indicates that strain in this type of material typically is on the order of  $\sim 0.7\text{-}2$  GPa [155]. Additionally, several extended, very dark regions mostly in the upper half of the electronic grade image are visible, indicating regions with even higher strain, spanning over significant areas of the plate. In contrast, the HPHT plate only shows extremely faint signs of strain, mostly in the central regions of the plate. Note, that the white wave-like structures and pads are gold microwave strip lines which have been removed prior to implantation. Moreover, the localized dark spots (marked by red circles) are related to surface damage. In contrast to the electronic grade plate, this sample has only been cleaved but not polished, leaving a rougher surface with a terrace-like structure and, occasionally, deeper holes, both also showing up in the polarization images. Because sample polishing can be an additional source of strain [156] we decided not to polish the sample as the surface roughness was within acceptable limits for optical experiments. The polarization microscopy confirms that the type IIa HPHT plate indeed provides a significantly less strained environment

for the  $\text{SiV}^-$  compared to the previously used electronic grade plates. Additionally, the plate has carefully been checked for  $\text{SiV}^-$  fluorescence prior to implantation to rule out any unwanted initial contamination of the sample. The image in Fig. 3.1(b) has then been used to identify sample regions of particularly low strain (mainly around the edges) in which silicon has then deliberately been implanted to form  $\text{SiV}^-$  centres with low enough density so that individual emitters can be addressed optically. These ion implantations will be discussed in greater detail in the next section.

### 3.1.2 Silicon ion implantations

Ion implantation is a technique in which charged ions are accelerated in an electrical field of a particle accelerator and the ion beam is directed onto a host material. Due to their high kinetic energy the ions can then penetrate into the material and change its physical properties. This is e.g. frequently used to introduce dopants like boron into silicon wafers. For the purpose of colour centre fabrication this technique is extremely well-suited as it allows precise control over the implantation depth of the ion by adjusting its energy as well as the emitter density by changing the implanted ion dose. Alternatively, as we will briefly discuss in Sec. 3.2, the dopant can be introduced during diamond growth, e.g. in a CVD process. However, this generally does not allow for precise control over the colour centre concentration and thus the fabrication of single-emitter samples using this technique is extremely challenging. Moreover, using ion implantation, even more "exotic" ions can be introduced into the diamond which cannot easily be incorporated during growth. Eventually, the generation of vacancy-related complexes is enhanced as the implanted ion itself, on its way through the material, creates vacancies which then subsequently can participate in colour centre formation. This defect creation simultaneously is one of the main limitations of this method. Especially the use of high ion doses or heavy ions can cause persistent damage to the diamond lattice, even after high temperature annealing, and hence causes stress which can deteriorate colour centre properties. To simulate the depth and distribution of ions as well as the vacancies created with a certain set of implantation parameters we perform Monte-Carlo simulations using the open-source code "Stopping and Range for Ions in Matter (SRIM)" [157] which utilizes the so-called binary collision approximation (BCA) [158]. Within the BCA only binary collisions between the implanted ions and host atoms as well as between host atoms are considered. Moreover, the trajectory of an ion or atom between two scattering events is approximated by a straight line. The impact parameter, defining whether an atom is hit by an ion head-on or under streaking incidence is chosen randomly for each ion. In Fig. 3.2 a SRIM simulation for the implantation of 20000  $^{28}\text{Si}^+$ -ions in a diamond (111) surface is shown, assuming an ion energy of 900 keV and a diamond density of  $\rho_{dia} = 3.52 \frac{g}{cm^3}$ . Additionally, we adjusted the displacement energy  $E_d$  to account for varying material parameters along different crystal directions. According to [159] we used a displacement energy of  $E_d^{(111)} = 45 \text{ eV}$  for the (111) direction of type IIa diamond. This is the amount of energy needed to push a carbon atom out of a lattice site along a certain crystal direction. The energies for the (100) and (110) directions are  $E_d^{(100)} = 37.5 \text{ eV}$  and  $E_d^{(110)} = 47.6 \text{ eV}$ , respectively. At the ion energies used here, these displacement energies do not influence the axial or radial ion distribution. However, the vacancy creation efficiency and thus the colour centre formation

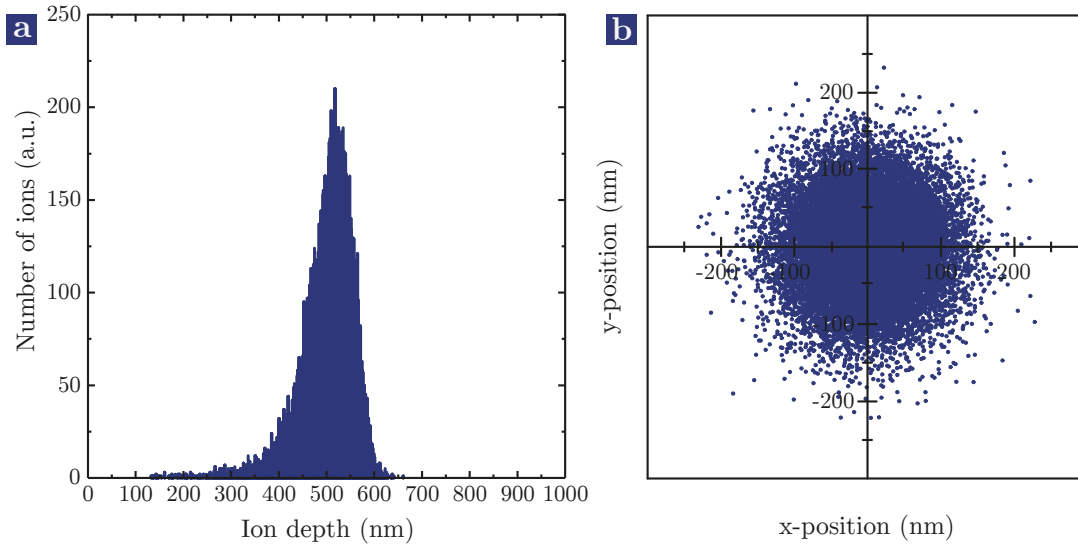


**Figure 3.2: SRIM simulations.** Simulated ion implantation of  $^{28}\text{Si}^+$  into a [111] diamond surface at an energy of 900 keV using the SRIM software [157]. In (a) the depth profile of the implantation is shown while (b) displays the radial ion distribution.

efficiency is significantly different for the three crystal directions. While along (111) a mean number of 828 vacancies are formed per ion, while along the (110) direction 782 and along the (100) directions 999 vacancies are formed. In Figure 3.2(a) the depth profile of the implantation is displayed, indicating a mean implantation depth of  $501 \pm 56 \mu\text{m}$  at 900 keV. Moreover, in Fig. 3.2(b) the radial distribution of ions (parallel to the surface) starting from a collimated ion beam with zero diameter is displayed. At 900 keV the radial spread of the ions amounts to  $r = 70 \pm 37 \mu\text{m}$ . This spread is a strongly depth and energy dependent parameter and, while it is not interfering with the fabrication process presented here, defines a limit for spatially resolved ion implantations as they are e.g. relevant for creating colour centres in nanostructures [160]. In the simulations presented here, so-called channeling effects which modify the lateral and axial ion distribution by guiding the ions through channels along certain directions of the host crystal structure are not considered but can be treated using more sophisticated molecular dynamics simulations [161].

All ion implantations in this thesis have been performed using a 4 MeV Tandem Dynamitron accelerator (Radiation Dynamics Inc.) [162] at the RUBION facility of the Ruhr-University Bochum. Figure 3.3 shows a schematic overview over the accelerator complex. To create a beam of Si-ions, the facility possesses a Cs-sputter source (1) capable of creating a beam of negatively charged ions at an energy of 20 keV [163]. The ions are then guided towards the Dynamitron (2) which consists of two end-cap electrodes at ground potential and a central electrode kept at a positive potential. Thus, the ions are accelerated towards the central electrode where they pass through a stream of gas, stripping off two electrons and leaving them with a positive charge. Hence, the ions are repelled from the central electrode and accelerated a second time towards the accelerator output. The beam then

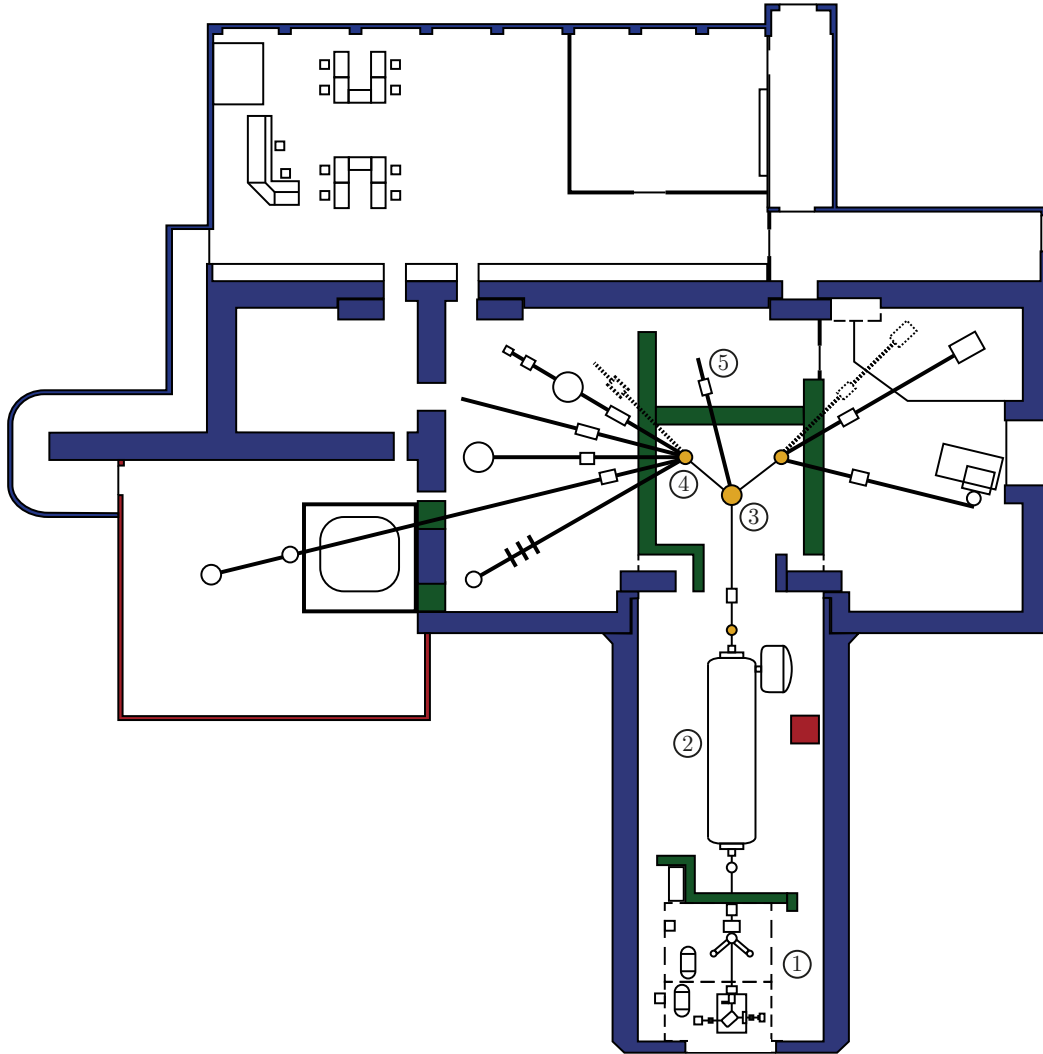


**Figure 3.3: RUBION facility.** Overview over the Tandem Dynamitron accelerator complex at the RUBION, Bochum featuring (1) a Cs-sputter ion source, (2) the Tandem Dynamitron accelerator, (3) an analyser magnet, (4) bending magnets and (5) the heavy ion beam line used throughout this work (picture adapted from [112] and [www.rubion.rub.de](http://www.rubion.rub.de)).

passes an analyser magnet (3) to select a specific isotope and is then distributed to various beam lines via bending magnets (4). The beam line used to perform the implantations presented here is the heavy ion beam line (5) which is directly attached to the analyser magnet.

The ion implantations carried out throughout this work have been performed at an ion energy of 900 keV, aiming for an implantation depth of 500 nm (cf. simulations in Fig.3.2) and at a small angle of  $8^\circ$  between target and beam to prevent channeling [58]. As the optimal ion dose to create individually resolvable  $\text{SiV}^-$  centres was not known prior to the implantations, several implantation areas have been implanted on the same diamond substrate using varying ion fluences in the range of  $10^9 - 10^{12} \frac{\text{ions}}{\text{cm}^2}$ . During the implantation, the sample has been masked using a 1 mm thick aluminium mask featuring a single hole with a diameter of 1 mm defining the implantation area. The mask has been translated between each implantation step to create several non-overlapping, adjacent implantation areas. The ion fluence of the beam has been measured prior to each implantation using a Faraday cup connected to a picoampere-metre.

As mentioned earlier, an ion travelling through the diamond creates a significant amount of vacancies (and corresponding interstitial carbon atoms) thus creating radiation damage. To restore a pristine diamond lattice and to help colour centre formation, a thermal treatment following the ion implantation is therefore necessary. To ensure a good vacancy mobility (vacancies in diamond become mobile above  $\sim 800^\circ\text{C}$  [58]) while preventing the diamond from oxidation, the sample was heated to  $1000^\circ\text{C}$  for 3 h in a vacuum of approximately  $10^{-6}$  mbar. Even in vacuum, a certain amount of graphite is formed because of radiation damage. According to [164], irreversible damage occurs above ion fluences of  $10^{15} \frac{\text{ions}}{\text{cm}^2}$ . However, all fluences used here were significantly below this limit. To remove the small amount of graphite created during annealing, the sample was chemically cleaned in peroxy-monosulfuric acid ("piranha solution", three parts of conc. sulfuric acid mixed with one part of hydrogen peroxide) for 30 min and subsequently oxidized at  $420^\circ\text{C}$  in air for 2 h. At this temperature graphite is oxidized to  $\text{CO}_2$  while diamond is preserved [165]. This results in a fully transparent diamond sample without signs of residual graphite contaminations.

### 3.1.3 Fabrication of solid immersion lenses

In the previous section we discussed the fabrication of  $\text{SiV}^-$  centres in diamond substrates. However, when performing optical experiments in diamond, the efficient extraction of light from the material is extremely challenging owing to its very high refractive index of  $n_d = 2.42$ . At a diamond/air interface, according to Snell's law, this leads to a very small critical angle  $\theta_{crit}$  for total internal reflection of only

$$\theta_{crit} = \arcsin\left(\frac{\sin(\theta_{air})}{n_d}\right) = \arcsin\left(\frac{\sin(90^\circ)}{2.42}\right) = 24.4^\circ. \quad (3.2)$$

In Fig. 3.4(a) a schematic representation of a diamond/air interface is shown. The centre of the red circle of 1  $\mu\text{m}$  diameter marks the position of an emitter. The light cone corresponding to an opening angle of  $2\theta_{crit}$  is displayed in yellow. Light outside this cone cannot pass through the diamond/air interface and is reflected back into the diamond.

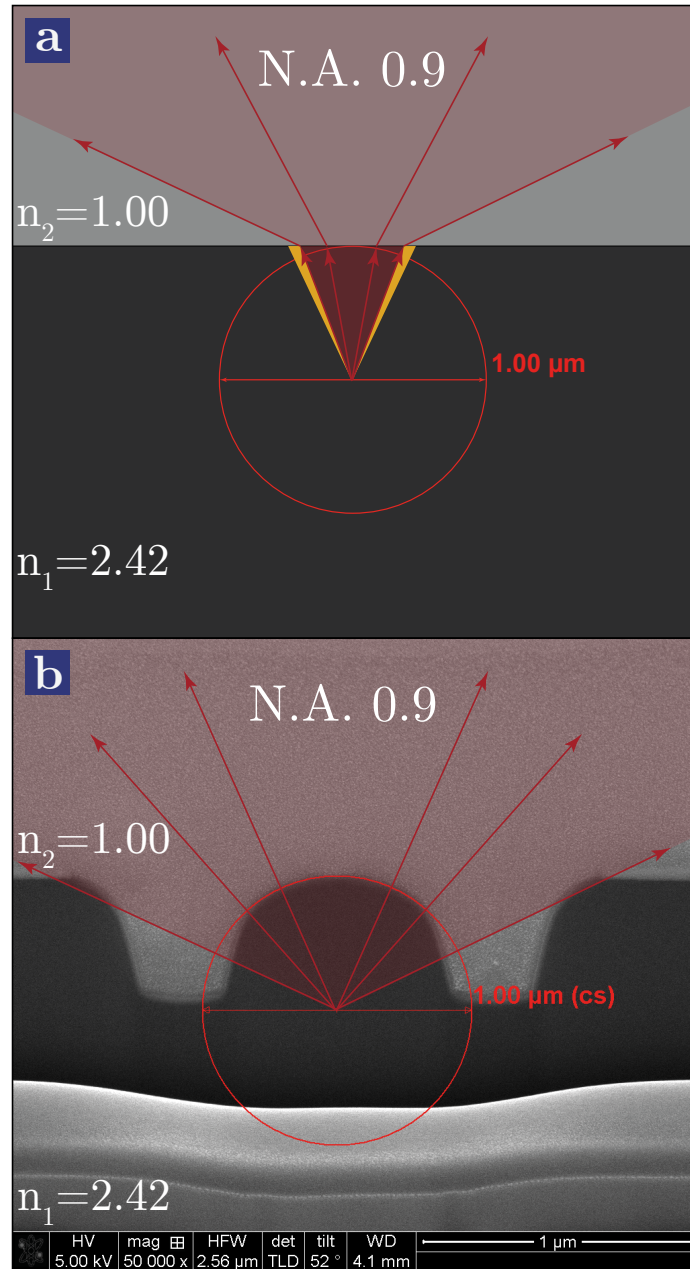


**Figure 3.4: Light outcoupling.** (a) Schematic representation of a planar diamond/air interface with refractive indices  $n_d$  and  $n_{air}$ . The centre of the red circle marks the emitter position. The yellow cone corresponds to the critical angle for total internal reflection while the red cone corresponds to an angle of emission which can be collected using a N.A. 0.9 objective. Red arrows indicate light rays as guide to the eye. (b) Scanning electron microscopy image of a cut through a solid immersion lens as they have been fabricated for this thesis. The red cone corresponds to a collection angle of a N.A. 0.9 objective. Red arrows indicate light rays as guide to the eye.

However, it turns out that even with a microscope objective featuring a numerical aperture (N.A.) of 0.9, as it has frequently been used throughout this work,  $\theta_{crit}$  is not the limiting angle. Instead, the maximally detectable emission angle of light is limited by the collection angle of the objective, due to refraction at the diamond/air interface. For a N.A. 0.9 objective, the collection angle is given by

$$\theta_{Obj} = \arcsin\left(\frac{N.A.}{n_{air}}\right) = \arcsin\left(\frac{0.9}{1.00}\right) = 64^\circ. \quad (3.3)$$

A light cone with an opening angle of  $2\theta_{Obj}$  is depicted by the red cones in the upper part (light grey) of Fig. 3.4(a) corresponding to an objective lens placed in air. For light to end up inside this cone after having passed through the interface it needs to be emitted within an angle of

$$\theta_d = \arcsin\left(\frac{N.A.}{n_d}\right) = \arcsin\left(\frac{0.9}{2.42}\right) = 21.83^\circ \quad (3.4)$$

corresponding to the red cone of light with an opening angle of  $2\theta_d$  in the lower (dark grey) part of Fig. 3.4(a). Assuming a fictional colour centre emitting light isotropically into a sphere this angle would thus correspond to a collection efficiency  $\eta_{planar}$  of

$$\eta_{planar} = \sin^2\left(\frac{\theta_d}{2}\right) = \sin^2\left(\frac{21.83^\circ}{2}\right) = 0.036. \quad (3.5)$$

However, colour centres do not radiate isotropically but in a pattern defined by single or even multiple dipoles. For the  $\text{SiV}^-$  the radiation pattern can be approximated well by a single dominant z-dipole aligned along its high symmetry axis [57]. For an optical dipole emitting perpendicularly to its axis, this efficiency can only be reached if the dipole is aligned parallel to the diamond surface. On the contrary, a dipole oriented perpendicularly to the surface experiences a roughly ten times reduced collection efficiency [166]. Note that this is another significant advantage of the (111)-oriented diamond plate used throughout this work compared to the previously used commercial (100)-oriented electronic grade plates. In the (111)-oriented material, three of the four equivalent main-dipole orientations of the  $\text{SiV}^-$  enclose an angle of only  $19.5^\circ$  with respect to the surface while in the (100)-oriented material all dipoles are oriented under an angle of  $54.7^\circ$  with respect to the surface. This results in an about 30% increased collection efficiency  $\eta$  of the  $\text{SiV}^-$  main dipole in the (111)-oriented material ( $\eta = 3.76\%$ ) compared to a (100) diamond ( $\eta = 2.93\%$ ) assuming a  $\text{SiV}^-$  500 nm below the surface. The values in brackets correspond to efficiencies calculated using finite difference time domain (FDTD) simulations (FDTD Solutions, Lumerical Solutions, Inc.) of a single optical dipole in diamond performed in collaboration with P. Fuchs according to the methods presented in [167].

To remedy the reduction of collection efficiency caused by refraction at the diamond/air interface and to collect light from a cone inside the diamond corresponding to the full N.A. of the objective lens, a hemispherical lens shape of the interface can be employed (c.f. Fig.3.4(b)). Oftentimes, this is achieved by placing a macroscopic hemispherical or super-hemispherical lens, a so-called solid immersion lens (SIL), made out of a high-refractive index material such as zirconia onto the planar substrate [168]. However, realizing an ideal

interface free of refraction between a diamond sample and a SIL is challenging and for most optical materials a certain refractive index mismatch will remain, both leading to a reduced collection efficiency. To circumvent these problems, we here fabricate hemispherical SILs directly into the surface of the diamond sample [169, 170]. This technique also allows for an exact adjustment of the SIL dimensions to match the depth of the SiV<sup>-</sup> centres as defined by the energies in the ion implantation. Using such a SIL, light emitted from the SiV<sup>-</sup> always impinges on the surface under a 0° angle, thus no refraction occurs making  $2\theta_{Obj}$  the effective collection angle. Consequently this leads to a theoretical collection efficiency of

$$\eta_{SIL} = \sin^2\left(\frac{\theta_{Obj}}{2}\right) = \sin^2\left(\frac{64^\circ}{2}\right) = 0.304, \quad (3.6)$$

about ten times higher compared to the planar diamond surface. While this is a simplified estimation as it for example does not take into account dipole orientations, SIL positioning or changes in the photonic density of states, Marseglia *et al.* demonstrated an 8-times enhancement using SILs with a diameter of 8 μm fabricated on top of NV centres deeply implanted into the diamond [171]. We here employ SiV<sup>-</sup> centres 500 nm below the diamond surface and thus the SILs have to be of this radius. This has two important consequences: First, due to the significantly smaller lens, the system is much more susceptible to misorientation of the SIL with respect to the emitter. Secondly, in contrast to [171], due to limited positioning accuracies in nanofabrication it is very challenging to fabricate SILs of such a small diameter on top of pre-characterized emitters. Hence, we here follow a probabilistic approach by fabricating several arrays with hundreds of SILs in an implanted area and post-selecting the ones showing efficient coupling to a SiV<sup>-</sup>.

To fabricate the SILs we employ a focused ion beam (FIB) milling technique using a FEI Helios Nanolab 600. The system possesses an electron beam for imaging as well as a 30 keV Ga<sup>3+</sup> beam for structuring purposes, enabling structure sizes down to 6 nm. Prior to FIB milling, the sample has been covered with a 70 nm thick Cr layer deposited via magnetron sputtering. This metallic layer prevents the build-up of charge during the milling process and thus avoids deflections of the ion beam and distortions of the fabricated structures. To mill the lenses we create a doughnut-shaped beam with a beam current of about 300 pA. The beam was slightly defocussed to facilitate the fabrication of smooth, rounded lens structures. The scanning electron microscopy (SEM) image in Fig. 3.4(b) shows a vertical cross section through one of the fabricated SILs, confirming the attempted diameter of 1 μm corresponding to an emitter depth of 500 nm. Note that in contrast to the SILs presented in an earlier work [58], the beam parameters used here have been optimized further to allow the fabrication of SILs with a truly circular top (c.f. Fig. 3.4(b)) instead of the truncated or flat-top profile fabricated before. After the milling process, the metal layer was removed using a Cr etchant (Diammonium cerium(IV) nitrate, acetic acid, water in a mass ratio of 8.75 mg : 240 mg : 50 g) and the sample was cleaned in deionized water. To remove Ga ions which have been implanted into the diamond during milling (the penetration depth of 30 keV Ga ions in diamond is about 15 nm) and to cure radiation damage caused by the Ga ion beam, the sample was subjected to the same annealing and chemical cleaning process used after ion implantation, leaving a clean, graphite-free sample ready for optical experiments.

### 3.2 Fabrication of ensemble samples

While the goal of the fabrication process described in the previous section was to realize a diamond sample featuring individually addressable  $\text{SiV}^-$  centres, the scope of this work is also to investigate the coherence properties of dense  $\text{SiV}^-$  ensembles and their potential applications in QIP. As we have discussed earlier, the symmetry properties of the  $\text{SiV}^-$  render the centre robust against perturbations such as crystal strain which leads to a shift of electronic states and thus to an inhomogeneous broadening of the spectral lines of the ensemble. Therefore, it is possible to fabricate dense ensembles of  $\text{SiV}^-$  centres with inhomogeneous broadenings well below the ground state splitting of the  $\text{SiV}^-$ . Hence, individual electronic transitions can still be addressed in such an ensemble, rendering coherent manipulation feasible.

To fabricate a dense ensemble of  $\text{SiV}^-$  centres with optimal spectral properties, ion implantation cannot be used as the ion beam causes a significant amount of damage to the host material for high fluences (irreversible damage occurs above ion fluences of  $10^{15} \frac{\text{ions}}{\text{cm}^2}$  [164]). Moreover, the fabrication of thicker ensemble layers of several  $\mu\text{m}$  or even mm thickness would not be feasible without elaborate and time-consuming ion beam energy sweeps. Therefore, it is more practical to grow such an ensemble using CVD techniques as they have been discussed in Chap. 1.1.3. To fabricate a low-strain ensemble heteroepitaxial growth, i.e. growth on top of a non-diamond substrate is not suitable because the remaining lattice constant mismatch between substrate and diamond always leads to a considerable amount of strain in the sample. Therefore, a homoepitaxial growth technique must be used, starting from a strain-free high quality diamond substrate which then can be overgrown with a layer of Si-doped diamond. To achieve a high-quality layer two requirements have to be fulfilled: First, a careful pre-selection of a suitable substrate is important as e.g. strain or polishing damage of the substrate will directly be transferred into the newly-grown diamond layer [172, 173]. Secondly, it has been demonstrated that slow growth with a small methane to hydrogen ratio in the CVD chamber is advantageous [174]. This can be explained by an increased etching rate of  $\text{sp}^2$  carbons via the hydrogen species in the plasma compared to the much slower carbon ( $\text{sp}^2$  and  $\text{sp}^3$ ) deposition. This allows for the formation of a diamond layer free of graphite inclusions and lattice defects giving rise to a very low-strain diamond host lattice for the grown-in colour centres. Depending on the desired  $\text{SiV}^-$  density in the ensemble either the inevitable etching of glass parts of the CVD reactor itself by the growth plasma (this is also what makes exact dopant level control and thus fabrication of single emitter samples via this technique challenging) [114] or additional Si or SiC plates [115, 175] in the chamber can serve as Si sources in such a process. Alternatively, also the use of gaseous silane precursors has recently been demonstrated [176]. This method offers a much more precise control over the Si concentration and therefore potentially enables the growth of samples with very well defined  $\text{SiV}^-$  densities, even down to the single emitter level. Moreover it offers the possibility for  $\delta$ -doping i.e. the growth of a thin doped layer in between layers of intrinsic diamond.

To obtain the results presented in Chap. 5 two different ensemble samples have been used: The first sample is an ensemble homoepitaxially grown on top of a HPHT substrate. The sample was grown by H. Sternschulte and we will therefore refer to it as the "Sternschulte

ensemble" (sample identifier: HaStP070) for the rest of this work. This sample has already been used extensively in previous studies [57, 58, 120] and a detailed discussion of the sample properties can be found therein. Here, we will briefly review the growth conditions of the Sternschulte ensemble: The substrate for the sample is a commercially available nitrogen-rich type Ib HPHT diamond (Sumitomo) which has been pre-selected for low strain and good surface quality. On top of this substrate, an approximately 300 nm thick layer of diamond has been grown in a hot-fillament CVD reactor not exceeding a growth rate of 10 nm/h and methane to hydrogen ratios of 0.26%. No additional Si source has been added to the growth chamber as the reactor itself contained significant amounts of Si. This, on the other hand does not allow to draw any conclusion on the exact dopant level in the sample. The diamond quality of this sample has been characterized in [119] using Raman spectroscopy of the first-order diamond Raman line ( $1332.5 \text{ cm}^{-1}$ ). This line results from an excitation of a zone centre optical phonon by the laser which loses energy in this process and consequently is red-shifted by the phonon frequency. The linewidth of this Raman line is strongly influenced by the diamond quality as e.g. dislocations in the crystal cause homogeneous broadening of this line by influencing the phonon lifetime whereas strain locally alters phonon energies causing an inhomogeneous broadening [177]. For high-quality natural diamond Raman linewidths between  $1.8 \text{ cm}^{-1}$  and  $2.2 \text{ cm}^{-1}$  have been observed [178]. The value reported in [119] for the Sternschulte ensemble is  $2.6 \text{ cm}^{-1}$ , only slightly above this range, indicating a very high quality of the homoepitaxially grown layer. Moreover, no signs of additional Raman signals related to graphite contaminations ( $\sim 1600 \text{ cm}^{-1}$ ) have been observed.

The second sample, which we will only briefly use in Chap. 5.4 to measure its Raman absorption as an outlook on future experiments is a colourless type IIa CVD diamond with (001) orientation and a thickness of about  $300 \mu\text{m}$ , containing a  $150 \mu\text{m}$  layer highly doped with silicon. The sample has been provided by Element Six, however the growth conditions have not been disclosed to us by the manufacturer. We will refer to this sample as the "Element Six ensemble" (sample identifier: E6CVDSi001).

### 3.3 Optical setups

In this section we will give an overview over the experimental setups used to conduct the experiments in the following chapters. While the setups vastly differ in components due to significantly different needs of the particular experiments, the key component of all of them is a confocal fluorescence microscope. Therefore, before we look at the three different optical setups used to perform the quantum optical experiments we will briefly discuss the fundamental working principle and basic setup of a confocal microscope and we will take this opportunity to look at the setup used for sample characterization throughout this work. Moreover, in Chap. 3.3.3 we will discuss the working principle of a  $^3\text{He}/^4\text{He}$  dilution refrigerator as it is key to the experiments in Chap. 4.3 and is not yet commonly used for optical experiments.

### 3.3.1 The confocal microscope

To understand the working principle of a confocal fluorescence microscope we first have to look at how a conventional fluorescence microscope works: In a conventional (widefield) fluorescence microscope the entire sample is simultaneously illuminated with excitation light which is focused onto the sample using an objective lens. Hence, all parts of the sample emit fluorescence at once which is, usually utilizing the same objective lens, mapped onto an ocular or a camera. We call the focal plane inside the sample the object plane and the respective focal plane on the camera the image plane. The key drawback of such a conventional microscope is the fact that also excitation light in the defocused light cones above and below the object plane can excite fluorescence which then in turn is mapped onto planes above and below the image plane, creating a blurred fluorescence background. To overcome this limitation, in a confocal microscope only one point of the sample at a time is excited and a spatial filtering using a pinhole in the image plane is employed. In this configuration, only light that originates from the object plane and which has a focal spot in the image plane can pass through the pinhole while the defocused contributions from other planes in the sample are strongly suppressed. In this configuration, the point-like excitation source, the excitation volume inside the sample and the pinhole are confocal i.e. they have common focal spots. Moreover, as only one spot of the sample can be imaged at a time, the sample (or the beam) has to be scanned giving the microscope the name *confocal laser scanning microscope (CLSM)*. While we here only give a brief introduction to this technique a more detailed discussion can for example be found in [179] or [180]. The spatial resolution of such a system can be described using the so-called point spread function (PSF) which mathematically describes the broadening of the image of a point-like object acquired with an optical system. A detailed discussion of the mathematical framework of PSFs can e.g. be found in [58, 180]. Here, we only review the most important results of this description: Let us first look at the lateral resolution  $\Delta r_{lat}^{conf}$  of the confocal microscope which according to [181] is given by

$$\Delta r_{lat}^{conf} = 0.37 \frac{\lambda}{N.A.} \quad (3.7)$$

assuming equal excitation and fluorescence wavelengths, equal excitation and detection path optics and a sufficiently small pinhole. This lateral resolution is slightly higher compared to the one of a widefield microscope which according to Rayleigh's criterion

$$\Delta r_{lat}^{wf} = 0.61 \frac{\lambda}{N.A.} \quad (3.8)$$

is given by the diameter of the so-called Airy disk. This improved lateral resolution is a direct result from the point-like illumination in a confocal microscope. Under these conditions, the total PSF of the system is the product of the excitation and the detection PSF. Assuming identical excitation and detection optics it can be written as the square of the PSF of a widefield microscope leading to an improved suppression of higher-order oscillations in the psf (c.f. [58]) and thus to an improved lateral resolution. The true power of a confocal microscope however lies in the improved axial resolution given by

$$\Delta z_{ax}^{conf} = 1.5 \frac{n\lambda}{N.A.} \quad (3.9)$$

much higher than the axial resolution

$$\Delta z_{ax}^{wf} = 2 \frac{n\lambda}{N.A.^2} \quad (3.10)$$

of a widefield microscope. As described above, this is a direct consequence of the spatial filtering suppressing light from non-focal planes. Moreover, in a confocal microscope, light that does not originate from the focal plane is truly suppressed and does not lead to an increased background noise level. In contrast, Eq. 3.10 for the widefield microscope is called the depth of focus, i.e. it defines an axial range in which a sharp image is created while objects outside this range still contribute to the picture.

One of the most basic realizations of a confocal fluorescence microscope (with some minor extensions) is depicted in Fig. 3.5. This is also the setup which has been used for the characterization of samples throughout this and previous theses [58, 119].

**Excitation laser** The microscope consists of an excitation light source (1), in our case a continuously tunable continuous wave (cw) titanium sapphire (Ti:sapph) laser (Sirah Matisse TX). The laser is pumped by a diode-pumped and frequency-doubled neodymium doped yttrium orthovanadate (Nd:YVO4) solid state laser capable of producing 15 W of optical power at 532 nm (Newport Spectra Physics Millennia eV 15). The Ti:sapph laser is usually pumped with 10 W and (with mirror exchanges) is capable of producing light in the range from 690 nm-1100 nm and output powers of up to 2 W. The laser is usually operated at 695 nm for non-resonant or at 737 nm for resonant excitation of SiV<sup>-</sup> centres. The laser can be frequency-stabilized in a Pound-Drever-Hall scheme [182] using a Fabry-Pérot reference cell and can reach linewidths down to  $\sim 35$  kHz. The laser passes through a neutral density filter wheel (2), a half wave plate (3, HWP) and a polarizing beam splitter cube (4, PBS) for coarse and fine power adjustment, is guided by mirrors (5) and coupled into a single mode optical fibre (6) with a core diameter of about 5  $\mu\text{m}$  using a  $f=11.0$  mm aspheric lens. On the one hand, this guarantees high flexibility as the laser can easily be plugged to other experiments. On the other hand we use the fibre for spatial mode clean-up.

**The confocal microscope** The output of the fibre is then plugged to the excitation arm of the confocal microscope. The light coming out of the small fibre core, in very good approximation, can be treated as a point-source. The light is then collimated using a  $f=13.86$  mm aspheric lens, passes through another HWP and PBS for power adjustment and polarization clean-up as well as through an optical clean-up (bandpass  $695.5 \pm 5$  nm or bandpass  $740 \pm 6$  nm) filter (7) to suppress Raman-noise from the optical fibre [183]. The laser then hits a beam splitter (8) which can either be a simple glass plate, reflecting about 10% of the laser or a dichroic mirror which efficiently reflects the excitation laser and is transparent for the fluorescence (types and transmission curves for available dichroic beam splitters can be found in [119]). The excitation laser is then focused onto the sample using a planar semi-apochromatic objective with a 100x magnification (9) and corrected for chromatic aberration (Olympus MPLFLN100x). The objective features a working distance (W.D.) of 1.0 mm and a high N.A. of 0.9. The sample and the objective are mounted inside a liquid helium flow cryostat (10, Janis Research ST-500LN), allowing to cool the samples

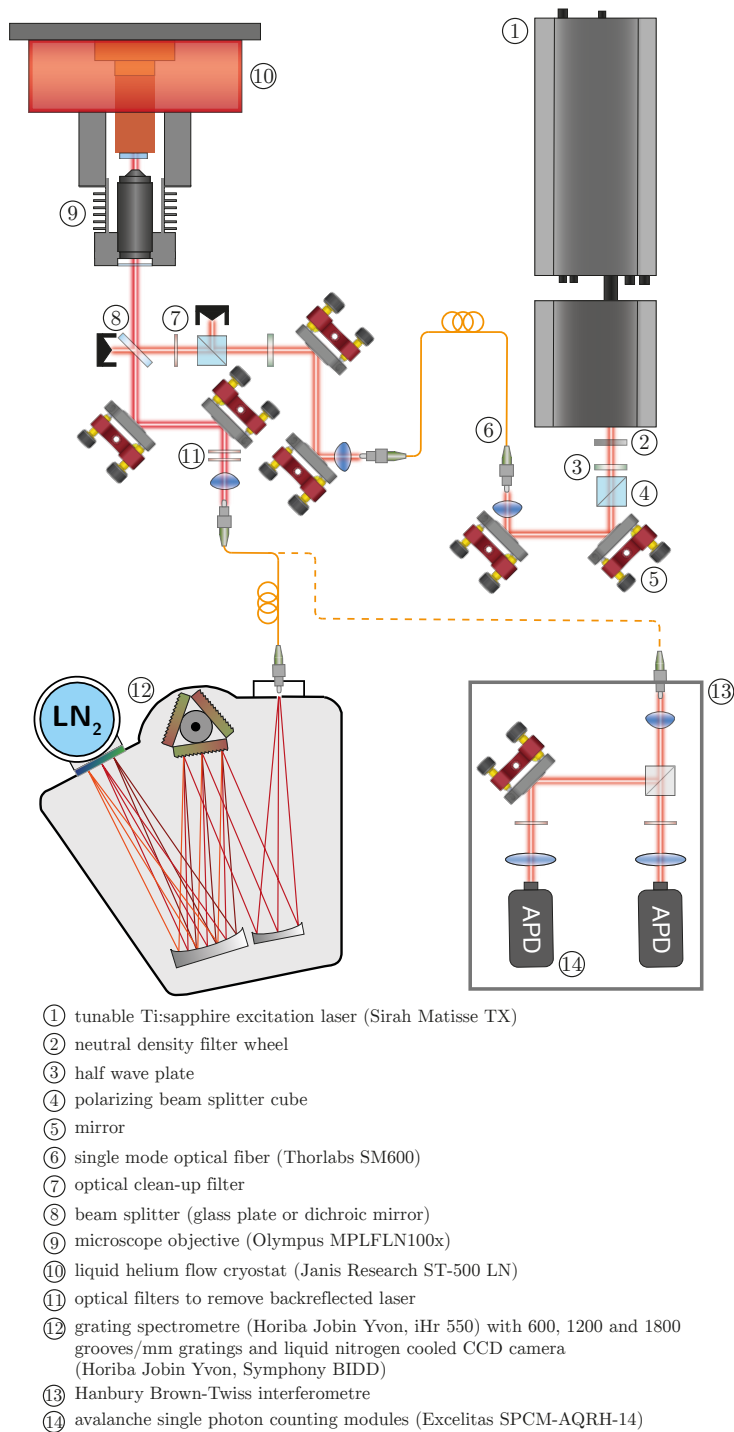


**Figure 3.5: The confocal microscope.** Schematic representation of the confocal laser scanning microscope used throughout this thesis to perform spectroscopic investigations of diamond samples. A detailed explanation of the system can be found in the main text.

down to temperatures of 4.2 K. To scan the sample in front of the fixed objective lens, the cryostat is mounted on top of two perpendicular linear translation stages (Newport, M-UMR8.25) with stepper motors (Newport LTA-HL) and the connection between cryostat and objective lens mount is kept flexible using a vacuum baffle. The objective lens mount can be translated back and forth for focusing using another, identical motorized translation stage. Fluorescence light is collected by the same objective, passes through the beam splitter and two stacked optical filters (11, longpass 730 nm or longpass 750 nm) to remove excitation light backreflected at the surface. The fluorescence is coupled into another single mode fibre using a  $f=13.86$  mm aspheric lens. The core of this fibre serves as a pinhole to realize confocal operation. The resolution of this setup has been characterized in [58] revealing a lateral resolution of about  $\Delta r_{lat}^{exp}=400$  nm as well as an axial resolution of  $\Delta z_{ax}^{exp}=1.48\mu\text{m}$ .

**Fluorescence analysis** For light analysis the setup includes a fibre-coupled grating spectrometre (12) as well as a Hanbury Brown-Twiss (HBT) interferometre (13) for photon statistics measurements [184]. The spectrometer (Horiba Jobin Yvon iHr 550) features three different gratings with 600 (0.22 nm resolution), 1200 (0.1 nm resolution) and 1800 grooves/mm (0.04 nm resolution). The detector is a liquid nitrogen cooled CCD camera with 1024x256 pixels (Horiba Jobin Yvon Sympony BIDD) with a quantum efficiency of up to 90% at 737 nm [119].

The HBT setup consists of a non-polarizing 50:50 beam splitter splitting the light into two beams which are then focussed onto two avalanche single photon counting modules (14, Excelitas, SPCM-AQRH-14, APD) featuring an active chip area of  $180\mu\text{m}$  diameter, a quantum efficiency of  $\sim 65\%$  at 737 nm and a timing resolution of  $\sim 350$  ps. In front of both APDs additional optical filters are installed to avoid cross-talk between both detectors. The APDs are connected to a counting electronics (PicoQuant PicoHarp 300) with a timing resolution of 4 ps. This allows for the measurement of exact photon arrival times on both APDs and thus the calculation of the intensity autocorrelation function  $g^{(2)}(\tau)$  which is a measure for the probability to detect two photons within a certain time interval  $\tau$  [10]. For a single quantum system the probability to detect two photons simultaneously should vanish as the system can only emit one photon at a time. Therefore, the  $g^{(2)}$ -function at  $\tau = 0$  is less than one, also referred to as *photon antibunching* (sub-Poissonian statistics) and, for ideal and background-free single photon sources even drops to zero.

The experimental apparatus discussed so far is a rather simple realization of a confocal microscope suitable to perform routine spectroscopic investigations. While all of the experiments presented in the following chapters utilize the fundamental working principle of a CLSM, they require more sophisticated optical setups featuring multiple excitation sources, beam shaping optics and different types of cryostats which we will take a closer look at in the following sections.

### 3.3.2 The coherent population trapping experiment

The setup described here is located at the Cavendish Laboratory of the University of Cambridge (group of Professor Mete Atatüre). It has been used to acquire the experimental data on coherent population trapping between the  $\text{SiV}^-$  spin states presented in Chap. 4.2,

requiring high and variable magnetic field strengths as well as two independent cw excitation sources. A schematic representation of the setup is displayed in Fig. 3.6 the components of which we will discuss in the following paragraphs.

**Excitation lasers** The excitation sources used are a diode pumped solid state laser at 660 nm (LaserQuantum GEM 660) for off-resonant excitation (1) and two external cavity diode lasers (ECDL) in Littrow geometry (Toptica DL Pro Design) with a centre wavelength of 737 nm and a linewidth  $< 300$  kHz for resonant excitation (2). The ECDLs can be tuned in frequency by either manually changing the angle of the external cavity grating using a setscrew or by an automated feed-forward tuning mechanism employing a piezo actuator at the grating combined with a change of the laser diode current. The latter technique allows for a mode-hop-free tuning over  $\sim 20$  GHz. Each laser then passes an acousto-optic modulator (3, AOM) which in combination with a photodiode (4) and a 100 kHz analog proportional-integral-differential (PID) controller (5, Stanford Research Systems SIM960) is used for intensity stabilization. To do so, a small percentage of the light is split off the main beam using a glass plate (6) and sent to the photodiode. The diode signal corresponding to the laser intensity is sent to the PID controller comparing the signal against a pre-selected setpoint and generates an error signal which is then sent to the AOM to close the control loop. Moreover, another portion of the beam is fibre-coupled and sent to a wavelength meter (7, HighFinesse WSU-10) with a frequency resolution of 2 MHz and an absolute accuracy of 10 MHz. The measured wavelength is read out using the LABVIEW measurement control software (National Instruments) and an error signal is generated using a LABVIEW software PID module. The error signal is then converted into an analog voltage using a data acquisition (DAQ) interface (National Instruments) and fed back to the laser controller. The 660 nm laser is combined with one of the ECDLs using a dichroic mirror (8) and both beams are combined with the remaining ECDL using a non-polarizing beam splitter cube. The combined lasers are then fibre-coupled to send them to the confocal part of the setup which is located on a breadboard on top of the cryostat. Moreover, the fibre ensures an ideal mode-overlap of the two resonant lasers.

**The microscope & cryostat** The sample is mounted on top of a non-magnetic xyz-piezo slip-stick positioner stack (9, Attocube ANPx101, ANPz101) made from titanium [185] and placed inside a tube containing an optical cage system to hold the objective lens as well as the positioners. As an objective lens (10) a simple aspheric lens (Thorlabs C330TME-B,  $f=3.1$  mm, N.A. 0.68) has been used as in this configuration the lens is cooled to cryogenic temperatures. Standard microscope objectives usually do not survive these conditions as they contain glued lens multiplets which are likely to crack during cooldown or warmup. Moreover, no microscope objectives certified for cryogenic operation were available at the time of this experiment. The tube is closed, evacuated and filled with about 30 mbar of helium gas for thermal coupling to the cryostat. The cryostat (11) is a liquid helium bath cryostat operating at 4.2 K, equipped with a superconducting NbTi magnet (12). The magnet is mounted in Faraday configuration, i.e. parallel to the optical axis and the magnet can be tuned continuously between 0 T and 7 T. The light coming out of the cryostat is then coupled into another single mode fibre and sent to the detection part of

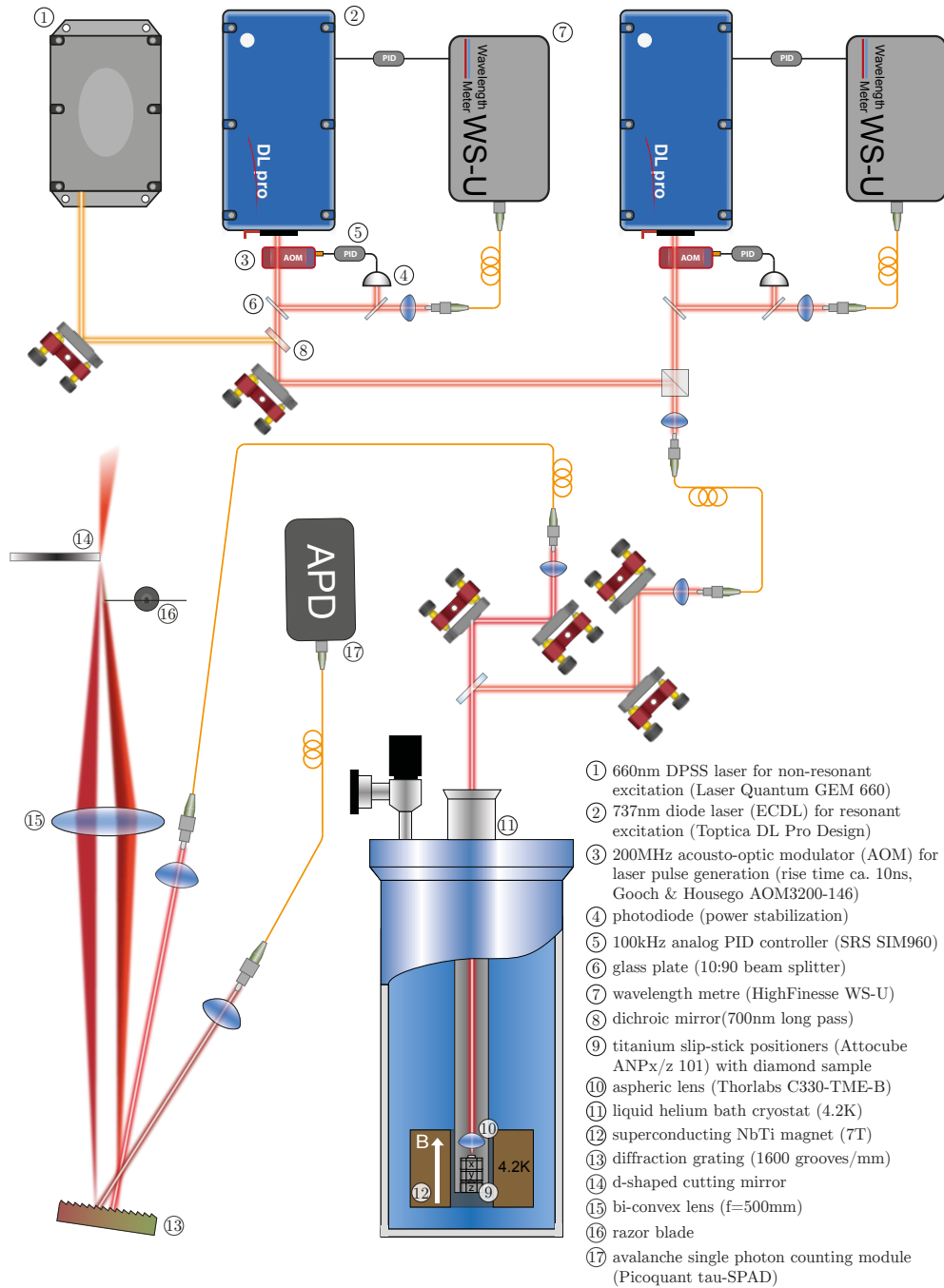


**Figure 3.6: The coherent population trapping setup.** Schematic representation of the optical setup used to perform coherent population trapping experiments on single  $\text{SiV}^-$  centres. The experiment has been set up at the University of Cambridge and its key components are discussed in the main text.

the setup.

**Quasi-resonant detection** In this experiment a quasi-resonant detection scheme is used. The coherent population trapping is performed on a  $\Lambda$ -scheme of the D-branch (c.f. Fig. 1.4) and photons emitted on the lower energy branches (due to branching in the excited state) of the ZPL are detected. To do so, a grating filter setup in a folded 4f-geometry is employed to separate the fluorescence from the excitation lasers which are only a few GHz apart. In the setup, the light is coupled out of the fibre and spectrally dispersed using a diffraction grating (13, 1600 grooves/mm). The first order diffraction is then focused onto the sharp edge of a D-shaped cutting mirror (14), using a two inch bi-convex lens (15) ( $f=500$  mm). While the excitation laser does not hit the mirror, the fluorescence is back reflected. An additional razor blade (16) in the back-reflected beam aids the filtering. By translating the d-shaped mirror and the blade in and out of the beam the filter window can then be fine-tuned. The back-reflected light again passes the two inch lens and the grating for a second time, increasing the laser suppression, is then coupled into another fibre and finally sent to an APD (17, PicoQuant  $\tau$ -SPAD) with  $\sim 70\%$  detection efficiency at 737 nm.

### 3.3.3 The dilution refrigerator experiment

This experiment aims at measuring the coherence properties of the  $\text{SiV}^-$  at temperatures in the millikelvin range. Its key component is a  $^3\text{He}/^4\text{He}$  dilution refrigerator recently installed in the laboratory of Jun-Prof. Pavel Bushev at Saarland University, the working principle of which we will discuss in greater detail in this section.

**Excitation lasers** The excitation sources for this experiment are located in the laboratory of the group of Professor Christoph Becher in the basement of the physics building at Saarland University. We here use the same cw Ti:sapph laser (1) as described in Sec. 3.3.1 as well as a self-built ECDL (2) comprised of the following components: A 737 nm laser diode (Eagleyard EYP-RWE-0740-02000-1500-SOT02-0000), a 1800 grooves/mm grating, an aspheric lens for collimation (Thorlabs C220TME-B,  $f=11$  mm), a temperature stabilized diode mount (Thorlabs TCLDM9), a temperature controller (Thorlabs TED200C) and a diode current controller (Thorlabs LDC210C). Small portions of the outputs of both lasers are fibre-coupled and sent to a micro-electromechanical systems (MEMS) switch (3) which in turn is connected to a wavelength metre (4, HighFinesse WS6-200). The MEMS switch is used to constantly switch the wavelength metre measurement between both lasers with a period of about 100 ms allowing for an (almost) continuous readout of both laser wavelengths. The switch control as well as the wavelength readout is implemented using LABVIEW. Subsequently, error signals are generated via software-PID which are then sent back to piezoelectric actuators in both lasers for frequency stabilization. To reach the dilution refrigerator which is located in the laboratory of Jun-Prof. Pavel Bushev on the first floor of the same building, we installed two 150 m long single mode fibres in the maintenance shafts of the building and both lasers are then coupled into these fibres. In the refrigerator lab, the light from the Ti:sapph is sent through a 0-10 GHz electrooptic amplitude modulator (5, Photline NIR-MX-800-LN, EOM) connected to a

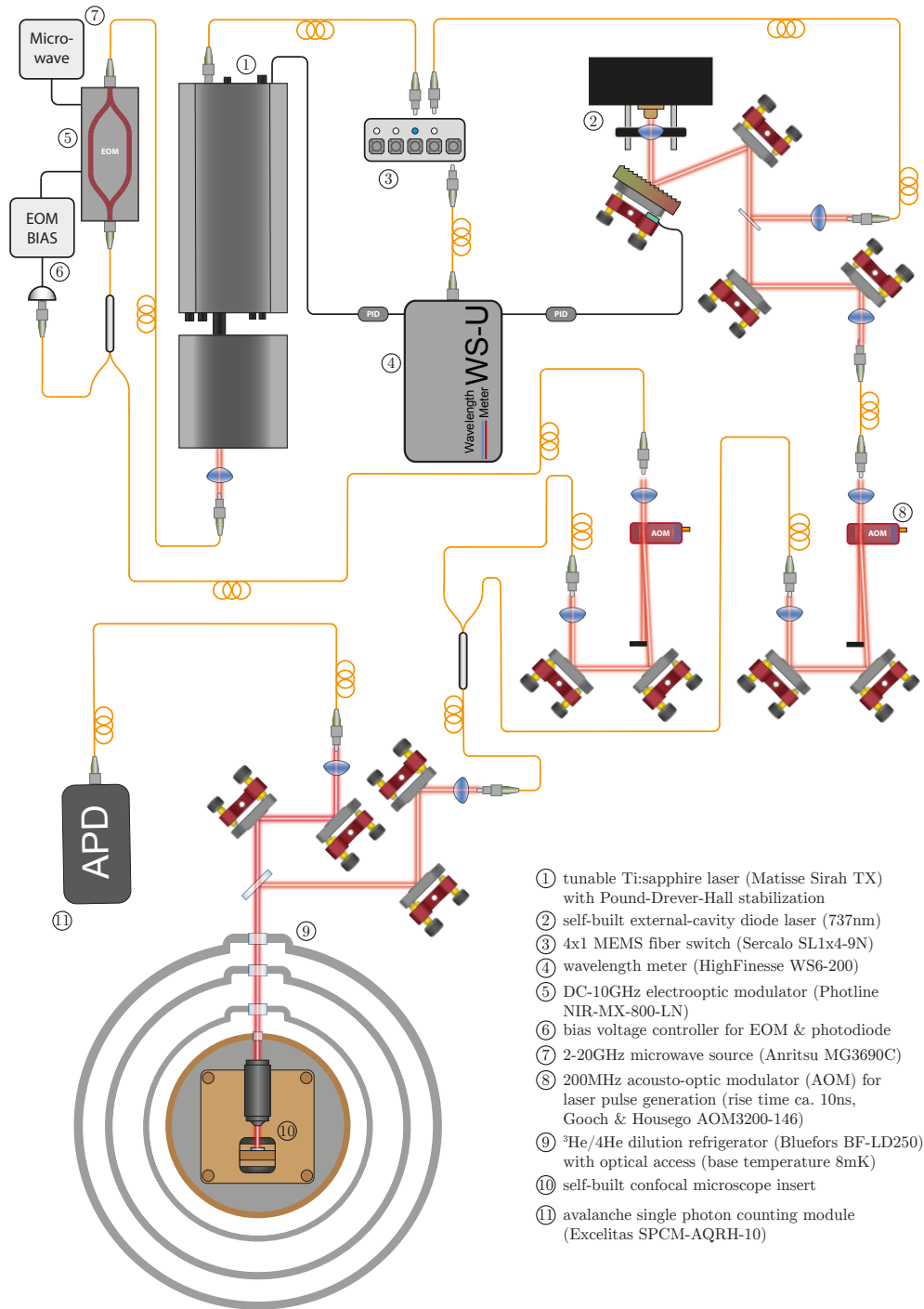


**Figure 3.7: Dilution refrigerator setup.** Schematic picture of the optical setup used to explore the properties of  $\text{SiV}^-$  centres at millikelvin temperatures. The key components as well as the dilution refrigerator are discussed in the main text.

bias controller (6, Photline MBC-DG-board) for working point selection and a 2-20 GHz microwave generator (7, Anritsu MG3690C) for driving. The EOM consists of a fibre-coupled lithium niobate chip featuring two integrated waveguides which are evanescently coupled to each other at two points, forming a Mach-Zehnder interferometer [186]. As the refractive index of lithium niobate depends on the value of an applied electric field, a pair of electrodes with an applied DC voltage in one arm of the interferometer can be used to introduce a phase shift and thus to control the output intensity of the interferometer. By changing the amplitude of the applied voltage the modulator can then be set to an arbitrary transmission value between 0% and 100%. Moreover, in lithium niobate, the application of light and electric fields leads to a slow migration of charge carriers in the material, causing a slow drift of the selected working point. To compensate for this effect the output intensity of the modulator can be constantly measured using a fibre beam splitter and a photodiode and the diode signal can be processed by the bias controller which then dynamically adjusts the amplitude of the bias voltage. Additionally, a second pair of electrodes connected to a fast signal generator can then be used to control the EOM transmission on very short time scales (rise time 300 ps) to e.g produce optical pulses from a cw laser. Here, we use the modulator to generate frequency sidebands on top of the laser carrier frequency defined by the Ti:sapph laser. To do so, we stabilize the modulator at a transmission level of 50% using the bias controller and drive it with a sinusoidal signal from the microwave generator. This creates sidebands with frequency difference to the carrier wave corresponding to the microwave frequency. Depending on the quality of the signal generator used, these sidebands can feature almost perfect phase coherence relative to the carrier wave with beat carrier-sideband beat frequencies commonly being on the order of 100 Hz-1 kHz. Moreover, by sweeping the microwave the sideband frequency can also be scanned with high precision. To select the optimal microwave power to ensure that only first-order sidebands are created, the output of the EOM is connected to a fast 0-25 GHz photodiode (Newport 1414) with traveling wave amplifier (Newport 1422) which is attached to a spectrum analyser (Anritsu MS2840A).

The modulated Ti:sapph as well as the diode laser are then sent through individual 200 MHz AOMs (8, Crystal Technologies AOM3200-146) for amplitude modulation to create optical pulses. The modulators feature rise and fall times of about 10 ns. The lasers are then combined using a fibre beam splitter and sent to the microscope. The input signals for the modulators as well as a trigger for the time tagging electronics used in the detection is generated using a four-channel delay generator (Highland Technology T560) triggered by a signal generator (Tektronix AFG3000C).

**The dilution refrigerator** To cool the diamond sample down to temperatures in the millikelvin range we use a  $^3\text{He}/^4\text{He}$  dilution refrigerator. As this is not a device commonly used for spectroscopic investigations and quantum optical experiments, we will briefly discuss the working principle of this cryostat and we will mainly follow the description in [188] and [187]: To understand how a dilution refrigerator works, we first have to take a look at the  $^3\text{He}/^4\text{He}$  phase system, described by the schematic phase diagram displayed in Fig. 3.8(a). Let us assume we start out at 1.5 K with a mixture of both He isotopes with a 1:1 composition (A). If we cool down this mixture to  $T \approx 1.2$  K it becomes superfluid (B)

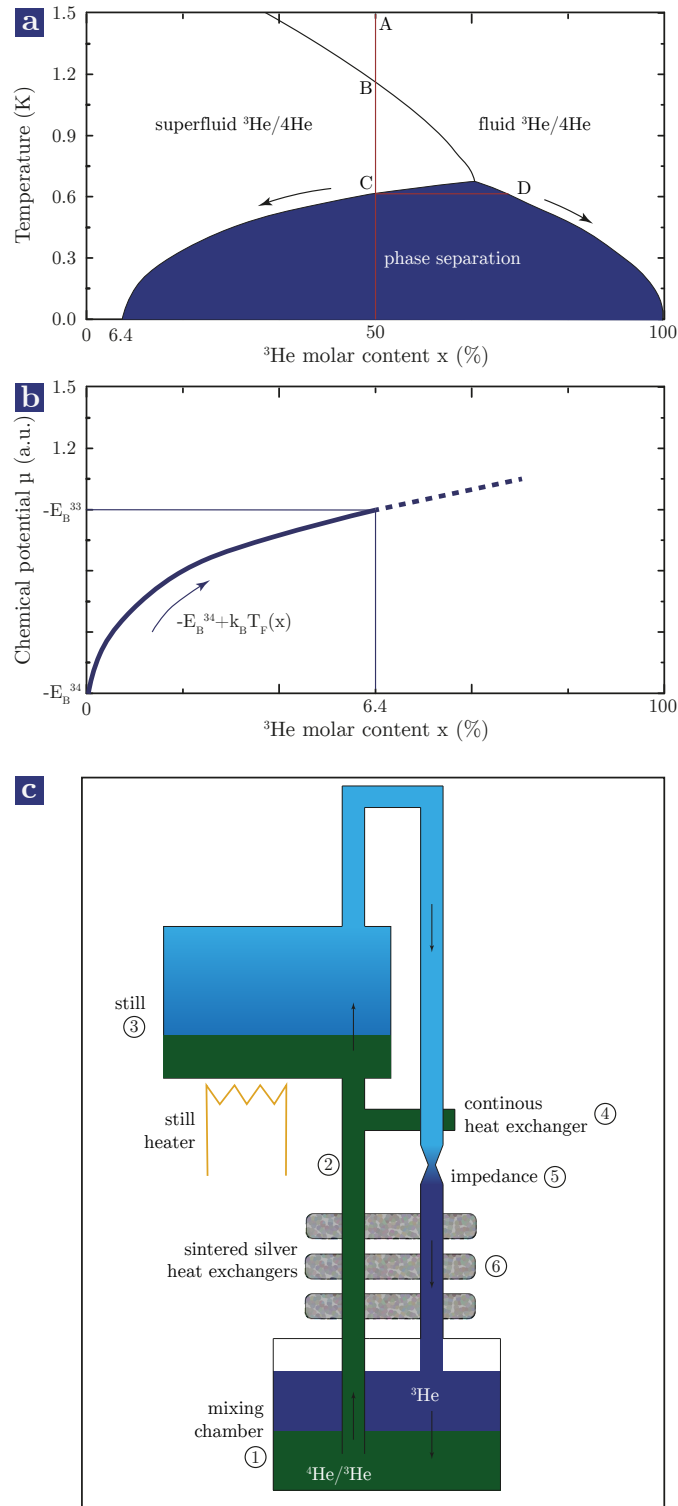


**Figure 3.8: Dilution refrigeration** (a) simplified phase diagram of the  $^3\text{He}/^4\text{He}$  phase system at temperatures below 1.5 K. (b) Dependence of the chemical potential  $\mu$  of  $^3\text{He}$  in  $^4\text{He}$  on the  $^3\text{He}$  molar content  $x$ . (c) Schematic representation of a dilution unit of a dry dilution refrigerator (all figures have been adapted from [187]).

and we can continue to cool it down without further phase transitions to  $T \approx 0.75$  K at which point we hit the phase-separation line (C). At this point the mixture separates into two phases, a  $^3\text{He}$ -rich (D) and a  $^3\text{He}$ -poor phase (C). The exact composition of these two phases strongly depends on temperature and at  $T=0$  K the solubility of  $^4\text{He}$  in the  $^3\text{He}$ -rich phase vanishes. On the other hand, even at  $T=0$  K there is always a finite solubility of  $^3\text{He}$  in  $^4\text{He}$ , leading to a minimum molar fraction of  $x=6.4\%$  of  $^3\text{He}$  in the  $^3\text{He}$ -poor phase. This finite solubility is very important for the process of dilution refrigeration and is a result of the lower weight of  $^3\text{He}$  compared to  $^4\text{He}$ . The lower weight leads to a larger zero-point motion and thus a  $^3\text{He}$  atom occupies a larger volume than a  $^4\text{He}$  atom i.e. that it is closer to  $^4\text{He}$  atoms than to other  $^3\text{He}$  atoms. As the interaction between the atoms is due to van-der-Waals forces ( $F_{vdw} \propto r^{-6}$ )  $^3\text{He}$  is more strongly bound in a  $^4\text{He}$  environment than in  $^3\text{He}$ , leading to the finite solubility at  $T=0$  K. Furthermore, to understand why the solubility amounts to exactly  $6.4\%$  we have to take a closer look at the chemical potential  $\mu$  of  $^3\text{He}$  in  $^4\text{He}$  which is given by

$$\mu = -E_B^{34} + k_B T_F(x) \quad (3.11)$$

with the binding energy  $E_B^{34}$  of  $^3\text{He}$  in  $^4\text{He}$  and the Fermi temperature  $T_F$ . In Fig. 3.8(b) the chemical potential, which is a function of the molar fraction  $x$  is shown. The observed dependence of  $\mu$  on  $x$  can be explained by the fact that  $^3\text{He}$  is a fermion (it contains three nucleons) whereas  $^4\text{He}$  is a boson (four nucleons). Therefore, in analogy to particles in a box, several  $^3\text{He}$  atoms in  $^4\text{He}$  have to occupy increasingly higher energy levels. Hence, the process of dissolving further  $^3\text{He}$  atoms becomes energetically decreasingly favourable and stops as soon as  $E_B^{34}$  equals  $E_B^{33}$  at  $x=6.4\%$ .

The cooling can now be achieved by continuously removing  $^3\text{He}$  atoms from the mixture and thus forcing new atoms from the pure  $^3\text{He}$  phase to diffuse into it. As  $^3\text{He}$  in  $^4\text{He}$  behaves like a Fermi gas its enthalpy will be higher compared to the  $^3\text{He}$  liquid phase and the enthalpy difference  $\Delta H$  causes cooling (in a simplified picture this can be described as a cooling due to the "evaporation" of a Fermi-liquid).

In Fig. 3.8(c) a schematic representation of a "dry" dilution refrigerator, as it has been used in this work, is shown. The term "dry" hereby refers to the fact that the system, which needs to be pre-cooled to at least  $4.2$  K to start operation in dilution-mode, does not contain a reservoir of liquid helium which needs regular refills. Instead, pre-cooling is achieved using a pulse tube cooler [189] (based on the working principle of a Stirling engine) and the cryostat can therefore be operated continuously without the need to refill any coolants. This is cost effective as liquid helium becomes increasingly expensive and avoids misalignments of the experiment which can easily occur during refills due to vibrations or temperature variations. Fundamentally, the dilution unit consists of two reservoirs linked by a series of tubes. The lower reservoir, the so called mixing chamber (1) contains the two helium phases (the lighter, pure  $^3\text{He}$  phase is floating on top of the heavier mixed phase). This is where the cooling process takes place and the chamber is connected to the cold plate of the cryostat. Using a tube (2) reaching through the  $^3\text{He}$  phase into the mixed phase, a portion of this phase is now transported into a second chamber, the so-called "still" (3). There, by reducing the pressure over the mixture  $^3\text{He}$  is distilled off (the vapour pressure of  $^3\text{He}$  is higher than of  $^4\text{He}$ ) allowing new  $^3\text{He}$  to diffuse into the mixture down in the mixing chamber. The still is constantly kept at a temperature of

about 0.8 K by heating it to ensure a high enough vapour pressure to retain high  $^3\text{He}$  removal rates. Moreover, the concentration gradient of  $^3\text{He}$  between mixing chamber and still creates an osmotic pressure that automatically sucks fresh  $^3\text{He}$ -rich mixture into the still [190]. The gaseous  $^3\text{He}$  is then again cooled down. In a classical dilution refrigerator containing liquid helium this pre-cooling is achieved by thermalizing it against a 1 K pot generated by pumping on liquid helium from the reservoir. In a dry refrigerator this is not possible. Instead, the cooling is achieved using the pulse-tube and additional continuous heat exchangers (4) to thermalize the gas against the cold liquid rising up from the mixing chamber to the still. An impedance (5) in the tube pressurizes the gas up to 2.5 bar. After the impedance the  $^3\text{He}$  expands and liquifies again. Before returning it to the  $^3\text{He}$ -rich phase of the mixing chamber the  $^3\text{He}$  has to be cooled even further. This is achieved by sending it again through a series of heat exchangers (6) and thermalizing it against the dilute  $^3\text{He}/^4\text{He}$  mixture rising up to the still. This final heat exchange is non-trivial due to the so-called *Kapitza resistance*, a thermal boundary resistance between the liquid helium and the solid metal of the heat exchanger [191]. This thermal resistance is proportional to  $T^{-3}$  and is caused by the scattering of phonons at the liquid/metal interface at very low temperatures. This inefficient heat exchange can only be counteracted by making the interaction area in the heat exchanger very large and thus, to reach temperatures below a few tens of millikelvin the use of several cascaded sintered silver (surface area  $\sim 1\text{m}^2/\text{g}$ ) heat exchangers is required, making these systems complex and costly. After this last cooling step, the liquid  $^3\text{He}$  is then fed back to the mixing chamber, completing the closed helium circuit of the dilution unit which therefore does not use up any coolant and can be operated continuously.

The dilution refrigerator used throughout this work (BlueFors LD250) has been installed in 2015 and is a dry refrigerator featuring a pulse tube cooler to bring the system down to 3.7 K. The base temperature of the cryostat is 8 mK achieved by a dilution unit containing about 18 L of  $^3\text{He}$  and featuring sintered silver heat exchangers. The cooling powers are  $14\ \mu\text{W}$  at 20 mK and  $0.4\ \text{mW}$  at 120 mK. The system cools down from room temperature to 3.7 K in about 48 h and, after starting the dilution unit, from there to base temperature in about 6 h. It can be run fully automated via a software interface. Moreover, as a rather special feature for dilution refrigerators, the system allows for optical access to the large sample space ( $d=290\ \text{mm}$ ) via two line-of-sight ports (LOS), each of them consisting of four windows installed in the different heat-shielding layers of the cryostat (c.f. Fig. 3.7). For the work presented here only one of those LOS ports has been used and four UV-fused silica windows with a custom-made anti-reflective coating (EKSMA Optics, surface finish  $\lambda/4$  at 633 nm) from 650-800 nm on both sides have been installed, each of them featuring a reflectivity  $<0.5\%$  at 737 nm to minimize signal and laser losses and avoid etaloning. With the windows installed, the base temperature has been measured to be 11 mK, slightly above the original value, most likely due to stray light (or black body radiation from the outer heat shields) entering and heating the sample space (temperatures are measured at the mixing chamber plate). Moreover, the vibrations at the mixing chamber plate caused by the pulse tube cooler are well below 100 nm, enabling high-resolution optical experiments.

To enable spectroscopy and quantum optical experiments of single emitters at millikelvin temperatures, in this work we designed and built a confocal microscope capable of operating

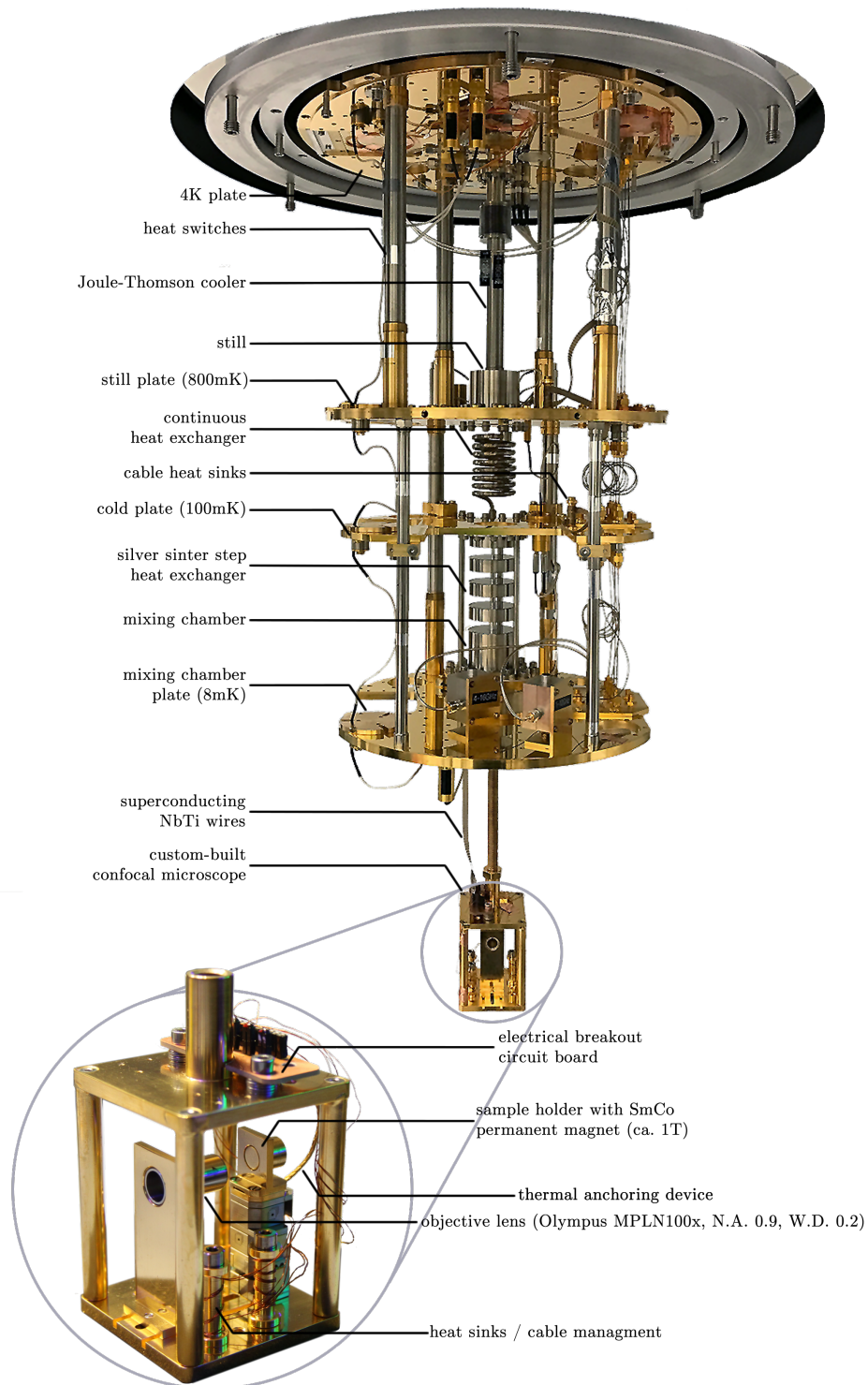


**Figure 3.9: Dilution refrigerator and confocal inset.** Picture of the inner cage of the dilution refrigerator used throughout this work, including the self-build confocal microscope (insert). The key components of the refrigerator and the confocal setup are labelled and further discussed in the main text.

inside the cryostat described above. An image of the opened cryostat with the installed confocal setup (upper part) and a magnified picture of the confocal setup (insert) is shown in Fig. 3.9. The key components of fridge and microscope have been labelled. The confocal microscope consists of a copper cage attached to the mixing chamber plate via a M10 threaded copper rod. The individual parts (thread, top plate, support rods, base plate) of the cage have been first screwed and later brazed together using a copper/silver solder to ensure ideal thermal conductivity. A copper objective lens holder hosting an achromatic, high-N.A. microscope objective (Olympus MPLN100x, N.A. 0.9, W.D. 0.2 mm), a xyz-stack of titanium slip-stick piezo positioners with resistive position encoders (Attocube ANPx51, ANPz51) as well as a number of copper wire heat sinks are attached to the base plate of the cage using non-magnetic titanium screws. A copper sample holder is mounted on top of the positioner stack and a 8x8 mm cylindrical permanent SmCo magnet (<http://www.magnet-shop.net>, SM-08x08-SC-N) capable of producing a magnetic field of  $\sim 0.2$  T in 1 mm distance from its surface in Faraday configuration is embedded into the holder. Note that, although NdFeB magnets are in principle stronger than SmCo magnets at room temperature, they undergo a spin-reorientation transition at 135 K leading to a sudden drop in field strength [192] and a change of the field orientation from a single axis towards a cone. Therefore, at low temperatures NdFeB is in fact outperformed by SmCo [193]. The sample is mounted to the holder using conductive silver paint with high silver content (RS Pro 186-3600) and baked at 120°C for 5 min to improve electrical and thermal conductivity. Moreover, the positioner stack is a poor thermal conductor and Ti becomes superconducting at about 400 mK, causing the thermal conductivity to drop to zero. To still ensure good thermal coupling of the sample to the cryostat, a thermal coupling device (Attocube ATC50) made from gold-plated copper plates and copper braids is directly connecting the sample holder to the top plate of the confocal cage while ensuring enough mechanical flexibility for the positioners to move. Finally, the positioners are connected to a home-made electrical breakout board bundling up the electrical connections of all three positioners and combining them into a single connector. Here, we also reduce the number of electrical lines from 15 to 11 by combining grounds and supply voltages of the encoders of the three stages [194]. To connect the positioners to the controller outside the cryostat, low-resistive wiring has to be used to allow the slip-stick moving mechanism to work properly [195]. Since the use of copper wiring would impose an intolerable heat load to the mixing chamber plate, a 12-pair superconducting NbTi cable has been installed between the 4 K stage and the mixing chamber plate and has been carefully heatsunk at the 4 K plate, the still, the 100 mK plate and the mixing chamber using copper heatsinks. From the 4 K stage on, copper wiring is then used to connect the positioners to the controllers outside the cryostat.

**Fluorescence detection** In this experiment we detect fluorescence using a single APD (Excelitas SPCM AQRH-14) fibre-coupled to the microscope. Detection of the ZPL under non-resonant detection is carried out using a  $695 \pm 5$  nm bandpass filter for excitation clean-up, two stacked 730 nm longpass filters in front of the detection fibre and a single  $740 \pm 13$  nm bandpass filter in front of the APD. Detection under resonant excitation is achieved by detecting the phonon sideband of the  $\text{SiV}^-$  using a  $740 \pm 13$  nm bandpass for

excitation cleanup, two stacked 750 nm longpass filters in front of the detection fibre and a  $780\pm 20$  nm bandpass in front of the APD. We here use this scheme instead of the grating filter discussed in the previous section as, in this experiment, we utilize transitions from the lowest excited state level and thus no additional ZPL transitions are available for detection. Moreover, this scheme allows for scanning the excitation laser frequency over several GHz without risking leakage into the detection channel. The APD is connected to a counting electronics (PicoQuant PicoHarp 300) which also receives a trigger from the delay generator for time-correlated measurements. Alternatively, the fluorescence can be analyzed using the grating spectrometre discussed in Sec. 3.3.1.

### 3.3.4 The coherent control experiment

This experiment has been set up to study the optical coherent control of single as well as ensembles of  $\text{SiV}^-$  centres. These experiments require the use of ultrafast lasers and a number of special optical setups to manipulate the length and spacing of their pulses. Moreover, additional modulated cw sources are necessary for initialization and readout purposes. Therefore, in the following paragraph we will take an extensive look at the excitation sources and their related optics. Moreover, for the investigation of the coherence properties of  $\text{SiV}^-$  ensembles, the flow cryostat introduced in Sec. 3.3.1 has been modified to allow for measurements in transmission geometry and we will briefly discuss these modifications. A simplified schematic view of the setup can be found in Fig. 3.10. For the sake of clarity, a number of optical elements not essential for the functionality of the setup (mirrors, polarization optics, filters etc.) have been omitted to make the figure more accessible.

**Excitation sources** To create ultrafast pulses we here employ a tunable, mode locked Ti:sapph laser (1, SpectraPhysics Tsunami) continuously pumped by a frequency doubled Nd:YAG DPSS laser (Coherent Verdi V10) at 532 nm, using a typical pump power of about 7 W. The mode locking in the Ti:sapph laser is achieved by an intra-cavity AOM generating frequency sidebands on top of the carrier frequency at a frequency corresponding to the mode spacing of the resonator and thus phase-locking several resonator modes. The laser uses a so-called *regenerative mode locking* scheme in which the round trip time of the cavity is constantly measured using a photodiode and the AOM frequency is adjusted accordingly [196]. Moreover, a Gires-Tournois interferometre (GTI) replacing one cavity mirror is used to induce a frequency-dependent phase shift to compensate for group velocity dispersion inside the cavity and hence to ensure short-pulse operation [197]. A GTI is closely related to a Fabry-Pérot interferometre (FPI) but uses a low-reflective entrance mirror, making it suitable for broadband applications. The GTI can be tuned by changing the mirror spacing using a piezoelectric actuator. The laser can be manually tuned in frequency from 720 nm to 850 nm using an intra-cavity birefringent etalon and generates pulses with a length of 1 ps at a repetition rate of 80 MHz. In the experiment, the repetition rate has to be reduced down to 1 MHz to allow for the application of cw pump and readout pulses in between the ultrafast pulses. To realize this, the pulses are sent through a pulse picker cell (2, electronics: Bergmann Messgeräte Entwicklung KG, Pockels cell: Leysop Ltd.) consisting of a Pockels cell in between two Glan-Taylor prisms. The first prism

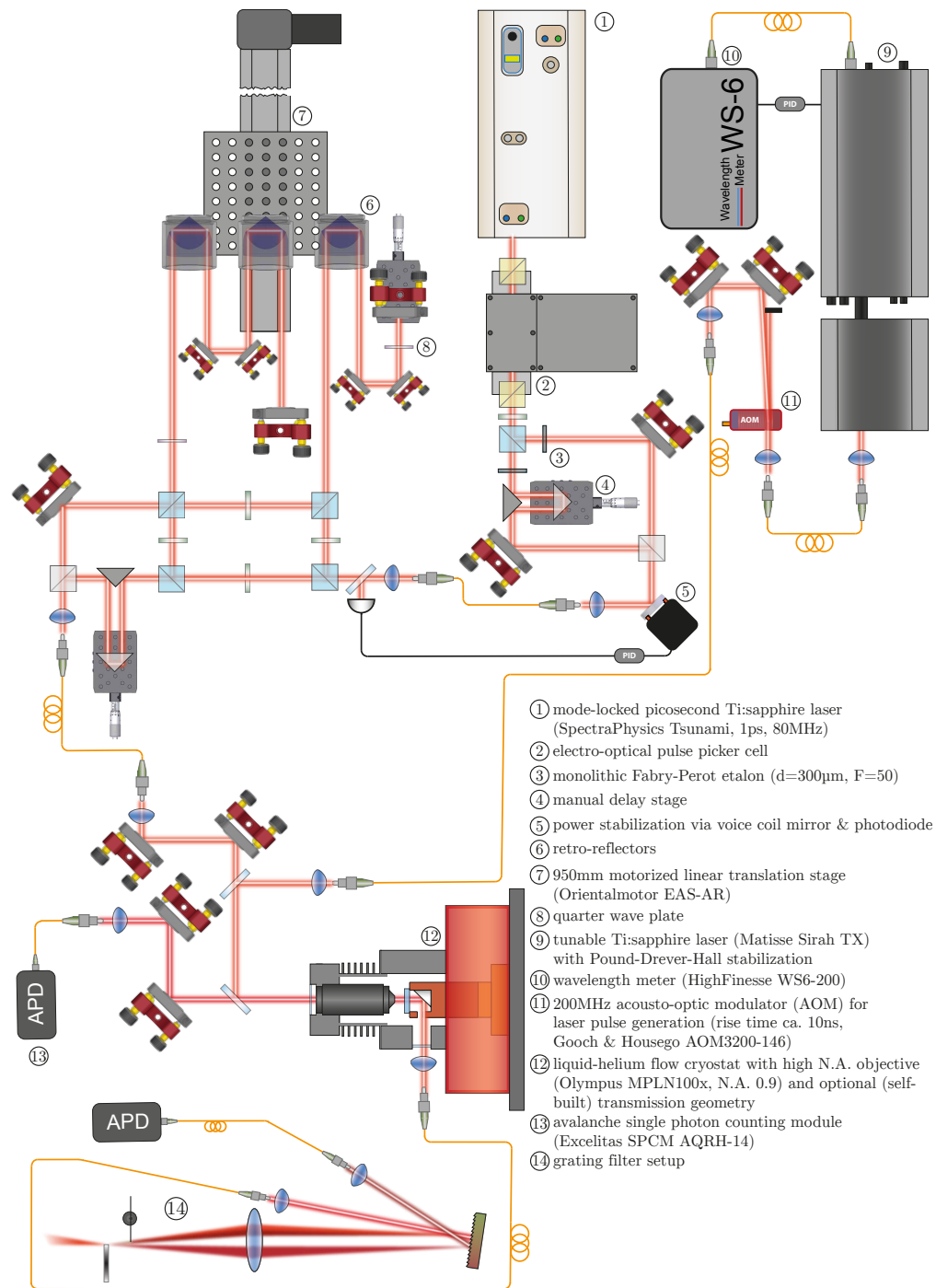


**Figure 3.10: Coherent control setup.** Schematic picture of the optical setup used to perform coherent control experiments of single  $\text{SiV}^-$  centres as well as ensembles using ultrafast laser pulses. Further details is given in the main text.

defines the input polarization of the cell and the second one is aligned such that if the Pockels cell is switched off all light is blocked. If a high voltage is applied to the Pockels cell, the polarization is rotated and light can pass through the second prism. To control the cell, the trigger signal provided by the photodiode of the laser is sent to two delay generator PCI cards which in turn generate the appropriate 1 MHz pulses for the pulse picker. These signals are then fed into a high-voltage generator and sent to the pulse picker. After the pulse picker, the laser is split into two beams using a HWP and a PBS and each beam is sent through an individual monolithic Fabry-Pérot etalon (3, Layertec, Finesse  $F=50$ , thickness  $d=50, 100, 300, 500 \mu\text{m}$ ). For the experiments in Chap. 4.4 only one of these arms is used whereas the experiments in Chap. 5.3 require two pulses at different frequencies. The etalons are thin glass substrates with a mirror coating on both sides. By tilting the etalons in the beam the effective path length of the light through the plate and thus the frequency of the transmitted light can be changed. We use these etalons to reduce the initial pulse bandwidth of about 300 GHz down to values suitable for experiments with the  $\text{SiV}^-$ . With the available etalons we can reach bandwidths of 4 GHz ( $d=500 \mu\text{m}$ ), 7 GHz ( $d=300 \mu\text{m}$ ), 20 GHz ( $d=100 \mu\text{m}$ ) and 40 GHz ( $d=50 \mu\text{m}$ ) with a two-sided exponential pulse shape in time domain (Lorentzian in frequency domain) due to the transmission function of the etalons. The two path lengths of both arms are kept equal by a delay stage (4) in one arm and the two arms are then recombined with another PBS and coupled into a fibre. One mirror in front of the fibre has been replaced by a voice-coil steering mirror (5, Optics in Motion) which, in combination with a photodiode after the fibre and a PID controller (TEM Messtechnik, Laselock), has been used for intensity stabilization by deliberately misaligning the fibre coupling. We used a voice coil mirror in combination with a fibre coupling for intensity stabilization of the laser instead of an AOM as the high peak powers of ultrafast laser pulses can easily damage AOMs at the intensities necessary for the experiments. The light is then sent to a delay stage setup capable of producing Ramsey and Hahn echo pulse sequences. To do so, the laser is coupled out of the fibre and a part of it is split off by a first PBS. The polarization of the light is then rotated such that it is transmitted through a second PBS. Subsequently, the laser is reflected by a retro-reflector (6) mounted on a 950 mm motorized translation stage (7), sent through a quarter wave plate (8, QWP) set under  $45^\circ$ , reflected by a fixed mirror mounted on a translation stage (for delay adjustments), sent through the same QWP for a second time, again reflected at the retro-reflector and finally reflected at the PBS (because the QWP in double-pass configuration rotated the polarization). The use of the retro-reflectors in combination with the QWP and a fixed mirror (instead of just regular mirrors on a stage) hereby ensures that instabilities and irregularities of the stage do not lead to a change of the direction of the output beam. The remaining part of the laser input which has been transmitted at the first PBS is then split again at a second PBS and the reflected part is sent to another delay stage twice as long as the first stage. The output of this second stage is then overlapped with the output of the first stage using a PBS and the resulting beam is combined with the undelayed laser which has been transmitted at all beam splitters using a non-polarizing beam splitter. An additional manual delay stage in the undelayed path allows for a fine tuning of the pulse separation. In a Hahn echo sequence consisting of a  $\pi$  pulse in between two  $\pi/2$  pulses, the first  $\pi/2$  pulse would be created by the undelayed laser, the  $\pi$  pulse by the laser propagating along the first (shorter) delay arm and the second  $\pi/2$

pulse via the second (longer) delay arm. Scanning the motorized stage then leads to a symmetric and perfectly coupled change of the delays between the  $\pi$  pulse and the first and the last  $\pi/2$  pulse, respectively. Finally, the combined output beam is then coupled into another fibre and sent to the microscope.

To create the pump and readout pulses a tunable cw Ti:sapph laser (9, Sirah Matisse TX), frequency stabilized to a wavelength meter (10, HighFinesse WS-6 200) is used. The output of the laser is fibre coupled, sent through an AOM for pulse generation, again fibre coupled and sent to the microscope. The AOM is controlled using a delay generator (Highland Technology T560) receiving a trigger signal from the pulse picker electronics (which in turn is triggered by the pulsed laser) to ensure synchronization with the ultrafast laser.

**The microscope** In the confocal microscope part of the setup both lasers are coupled out of their respective fibres and overlapped using a simple glass plate. The microscope is most widely identical with the setup presented in Sec. 3.3.1 with the exception that, in addition to standard operation in reflection geometry, the flow cryostat (12) has been modified to also allow for measurements in transmission. To accomplish this, a cold finger extension made from copper with a right angle prism mirror glued into it has been designed and fabricated. Moreover an aluminium tube with a window to extend the vacuum baffle has been built and installed. In this setup, the sample is glued onto the cold finger extension. The laser coupled out of the objective lens can now be transmitted through the sample, is reflected at the prism mirror and can leave the cryostat through the window in the vacuum baffle. The light is recollimated and coupled into a fibre. This setup allows for laser absorption measurements as they have been performed in Chap. 5.4 and [198].

**Fluorescence detection** The signal in reflection geometry is detected using a single APD (13, Excelitas SPCM AQRH-14) connected to a counting electronics (PicoQuant PicoHarp 300). For time-correlated experiments, the counting electronics receives a trigger generated by the delay generator mentioned above. Alternatively, the fluorescence can be analysed using the grating spectrometre described in Sec. 3.3.1. In transmission the fluorescence can either be directly analyzed using the APD or the spectrometre or it can be fibre-coupled to a 4f grating-filter setup featuring a 2400 <sup>grooves</sup>/mm grating and a resolution of  $\sim 5.5$  GHz [198]. The output of the filter setup is then again fibre-coupled (with the fibre core acting as a spatial filter for frequency selection) and sent to the APD.

## Chapter 4

# Experimental results I: Single SiV<sup>-</sup> centres

*Sample characterization and spectroscopic investigation of suitable SiV<sup>-</sup> centres for the experiments presented below have been performed by Jonas Nils Becker (J.N.B.) and Carsten Arend at Saarland University.*

*The experimental results in Sec. 4.2 have been obtained in the Cavendish Laboratory at the University of Cambridge. The experiments have been performed by Jonas Nils Becker (J.N.B.) and Benjamin Pingault (B.P., University of Cambridge) with technical assistance from Jack Hansom and Carsten Schulte (both University of Cambridge). The simulations of these experimental results have been developed by J.N.B. and the model reverts back to the group theoretical model developed by Dr. Christian Hepp in an earlier work [58]. The experiments have been supervised jointly by Prof. Mete Atatüre (University of Cambridge) and Prof. Christoph Becher (C.B.) and have been published in [199].*

*The experiments at millikelvin temperatures presented in Sec. 4.3 have been carried out at Saarland University using a cryostat in the group of Jun.-Prof. Pavel Bushev (P.B.). The optical experiments have been performed by J.N.B. with help from B.P., David Groß (as part of his Master's thesis) and Dr. Mustafa Gündogan (University of Cambridge). P.B. and Dr. Nadedzhda Kukharchyk aided in the operation of the cryostat. The analysis of these results utilizes the same model as the CPT experiments. The experiments have been supervised jointly by C.B. and P.B.*

*The coherent control experiments in Sec. 4.4 have been performed by J.N.B. at Saarland University. The theoretical model used to analyse the experimental data has been developed by J.N.B. and Johannes Görlitz (as part of his Master's thesis). The experiments have been supervised by C.B. and published in [200].*

In this chapter the experimental results obtained using single  $\text{SiV}^-$  centres in bulk diamond will be presented and discussed. In Sec. 4.1 we will start with a discussion of the properties of the sample the fabrication process of which we have discussed in the previous chapter. We will take a look at the spectral properties of two  $\text{SiV}^-$  centres in this sample, which have been used to obtain the results in the following sections. In Sec. 4.2 we will then discuss the results of the CPT experiments which, in combination with the theoretical model discussed in Sec. 2.2.1 have been used to determine the ground state spin coherence time of the  $\text{SiV}^-$ . The discussion of these results will directly point us towards the necessity of performing similar experiments at even lower temperatures to be able to explore different possible decoherence processes. Therefore, in Sec. 4.3 we will look at measurements performed using the dilution refrigerator setup discussed in Sec. 3.3.3. Finally, in Sec. 4.4 we make use of the advantageous electronic structure of the  $\text{SiV}^-$  to demonstrate full coherent control of its orbital state using ultrafast laser pulses. This allows for a large number of single qubit gates even in the presence of fast decoherence processes.

## 4.1 Sample & emitter properties

The sample used for the experiments in the following sections consists of  $\text{SiV}^-$  centres implanted in the (111) main surface of a HPHT type IIa diamond plate and has been prepared according to the methods discussed in the previous chapter. The sample has been implanted with Si, creating four different regions with  $10^9$ ,  $10^{10}$ ,  $10^{11}$  and  $10^{12}$  ions/cm<sup>2</sup>, respectively and SIL arrays have been fabricated in the  $10^9$  and  $10^{10}$  ions/cm<sup>2</sup> regions. We were able to address individual  $\text{SiV}^-$  centres in the  $10^9$  ions/cm<sup>2</sup> region, while higher ion doses led to ensembles of emitters. The dose to obtain single emitters is consistent with the implantations performed in [35, 201] by Wang *et al.* but an order of magnitude lower compared to the implantations performed in [58] by Hepp *et al.* Therein, the higher ion dose necessary to create single centres has been attributed to a lower vacancy creation efficiency when implanting Si with 1 MeV compared to the 10 MeV implantation performed by Wang *et al.* This explanation, however, is contradictory to the results obtained here as the 900 keV implantations performed in this work still yield single centres in the  $10^9$  ions/cm<sup>2</sup> region, even though, due to a higher displacement energy, the implantation into the (111) surface reduces the vacancy yield by another  $\sim 20\%$  compared to the implantations into (100) surfaces performed by Hepp *et al.* Thus the number of available vacancies, most likely, is not the limiting factor for the formation of  $\text{SiV}^-$  centres. Comparing the three implantations reveals that the implantations in this thesis and by Wang *et al.* have been performed using type IIa substrates (HPHT diamond in this work and natural diamond in [35, 201]) while Hepp *et al.* used an electronic grade CVD substrate. While this electronic grade material is specified to contain less than 5 ppb of substitutional nitrogen impurities ( $[N_s^0]$ ), the  $[N_s^0]$  content in "standard" type IIa material is significantly higher (typically on the order of  $\sim 100$  ppb [86]). This  $[N_s^0]$  can act as an electron donor for the negatively charged  $\text{SiV}^-$ , stabilizing its charge state and thus aiding its efficient formation (note that also other impurities might act as electron donors for the  $\text{SiV}^-$ ). This picture is also consistent with e.g. reports of  $\text{SiV}^-$  containing nanodiamonds showing increased  $\text{SiV}^-$  fluorescence levels when doped with additional nitrogen [202]. From the observed emitter

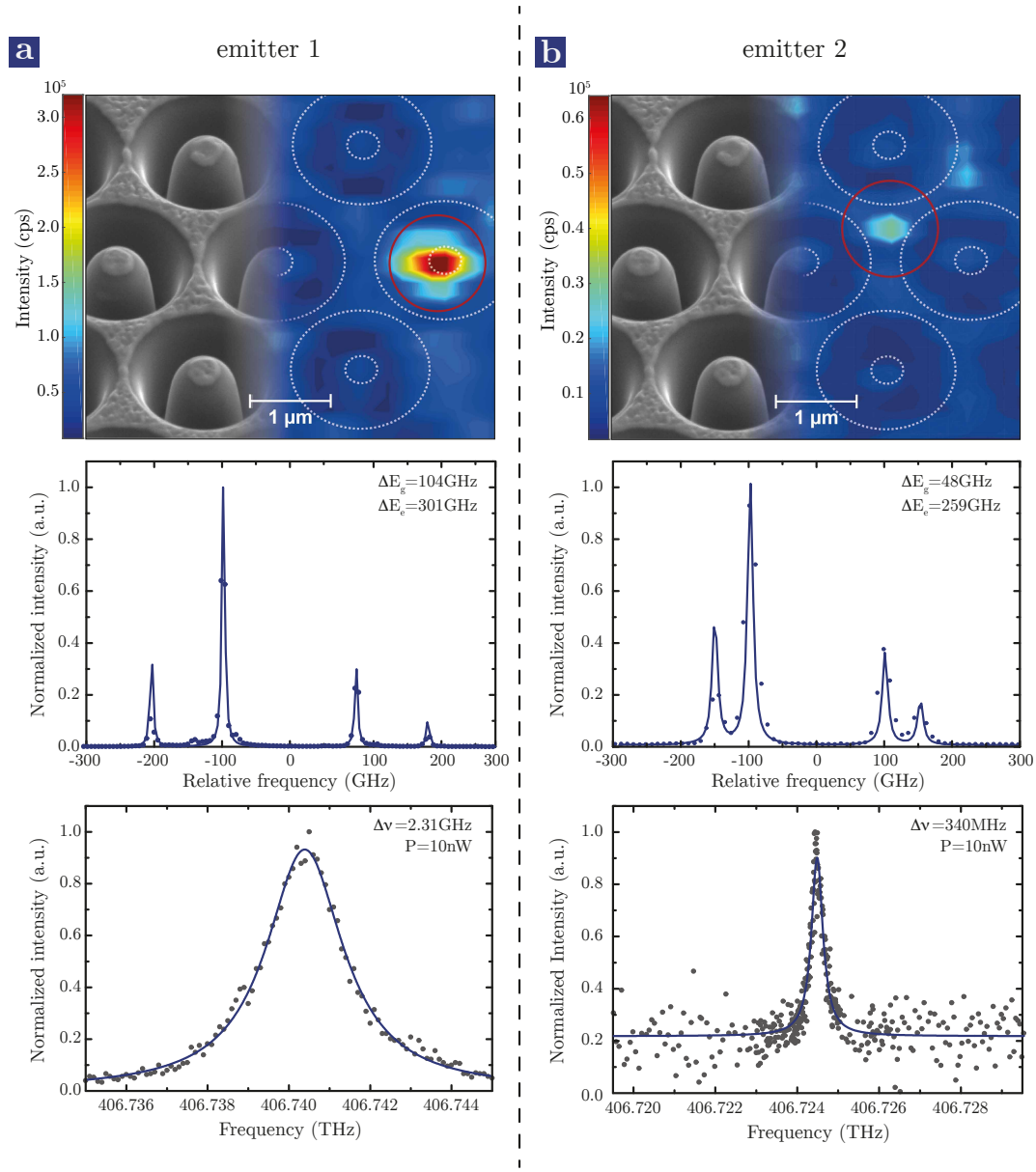


**Figure 4.1: Properties of investigated emitters.** Merged SEM and confocal images for the two  $\text{SiV}^-$  centres (a,b) used for the experiments in the following chapters (top row), their fluorescence spectrum (middle row) as well as a PLE scan across their  $C$  transition (bottom row). Further explanations can be found in the main text.

density in the confocal scans of about  $0.5\text{-}1\ \mu\text{m}^{-2}$  we estimate a yield of about 5-10%, significantly higher than the reports of [58] and on the same order of magnitude of what has been reported in e.g. [203, 204].

Most of the investigated sites on the sample showed clear signs of the characteristic SiV<sup>-</sup> fine structure with ground state splittings varying between ideal values of  $\Delta E_g=48$  GHz up to  $\Delta E_g \approx 600$  GHz in extreme cases, indicating sample regions free of crystal strain as well as more strained regions, possibly caused by FIB milling of the SILs. Moreover, the sample still shows a significant amount of background fluorescence caused by the FIB milling. This could most likely be improved by annealing the sample a third time. However, due to the good spectral properties of the SiV<sup>-</sup> centres after the second annealing and cleaning step, it has been decided not to perform an additional annealing to avoid the risk of annealing out pre-characterized sites. One additional outstanding feature of this sample is the significantly increased brightness of SiV<sup>-</sup> compared to emitters in previous samples. While e.g. the SiV<sup>-</sup> centres in the electronic grade samples used in [58] showed count rates of only a few thousand counts per second (with SIL enhancement), for the centres in this new sample count rates of  $3\text{-}5 \cdot 10^4$  cps have been measured on a regular basis, even without the enhancement by a SIL. In parts, this is due to the samples (111) orientation, which, as we have mentioned in Sec. 3.1.3, increases the collection efficiency by about 30%. However, this does not fully account for the fluorescence enhancement by more than one order of magnitude. The additional enhancement might again be caused by the increased nitrogen content of the substrate material. Emitters in electronic grade diamond might be susceptible to photoionization i.e. changes in their charge state during optical excitation, leaving the centre in a non-fluorescent state until it can regain its original charge. This leads to blinking and, if this process occurs on relatively fast timescales, to a reduced average count rate. A high nitrogen content of the host material might therefore accelerate the recovery of the centre's original charge state by providing an increased amount of available negative charges. However, while blinking of SiV<sup>-</sup> centres has been confirmed in nanodiamonds [126, 205] and evidences of it have also been reported in bulk diamond [201] no systematic study of this phenomenon in bulk diamond and its dependence on the nitrogen content have been performed so far. For this work we examined the photon arrival time histograms for blinking down to a bin size of  $10\ \mu\text{s}$  (limited by the maximum count rate of the emitters) and no sign of blinking has been observed down to these time scales. Moreover, for emitters perfectly centred below a SIL an enhancement of about a factor of 8-10 has been measured, in very good agreement with previously reported values [171]. This enhancement yields count rates of  $\sim 3 \cdot 10^5$  cps enabling the demanding experiments presented in the following chapters.

To perform these experiments two different SiV<sup>-</sup> centres, from here on termed "emitter 1" and "emitter 2", have been selected and we will now briefly discuss their fundamental properties:

**Emitter 1** In Fig. 4.1(a) a confocal scan (upper graph), a photoluminescence spectrum (middle graph) and a photoluminescence excitation (PLE) scan across line C at 0 T (bottom graph) are shown for emitter 1. To better emphasize the positioning of the emitter relative to the SILs, the confocal scan has been overlaid with a SEM image of the SIL

array. As apparent from this scan, the emitter is almost perfectly centred below a lens, enabling efficient excitation and photon extraction from the diamond. This leads to high count rates of about  $3 \cdot 10^5$  cps under non-resonant excitation at 690 nm with 7 mW of excitation power. The measured emission spectrum (blue dots) of this emitter at 10 K reveals the characteristic four-line fine structure of the  $\text{SiV}^-$  with a ground state splitting of  $\Delta E_g=104$  GHz and an excited state splitting of  $\Delta E_e=301$  GHz. We modelled this spectrum (solid line) using the group theoretical model developed and discussed in [58] yielding the following set of parameters:

**Table 4.1:** Resulting parameters for emitter 1 obtained from the group theoretical model presented in [58].

$\Delta E_g$	$\Delta E_e$	$\lambda_g$	$\lambda_e$	$\Upsilon_g$	$\Upsilon_e$	$\zeta_{g,e}$
		(GHz)				(GPa)
104	301	39	244	9	19	0.12

The parameters  $\lambda_{g,e}$  and  $\Upsilon_{g,e}$  hereby represent the strengths of spin-orbit coupling and Jahn-Teller effect in the ground or excited state, respectively. Moreover, the model indicates  $\zeta_{g,e}=0.12$  GPa of uniaxial strain leading to about 50 GHz of additional splitting in the ground and excited state compared to the ideal splitting [62, 114]. Moreover, the PLE scan at only 10 nW of resonant excitation power (fluorescence detection on the PSB) reveals a linewidth of  $\Delta\nu=2.31$  GHz, significantly above the lifetime-limited linewidth of  $\Delta\nu_{min} \sim 100$  MHz. This broadening is most-likely caused by the strain increasing phononic dephasing rates. Moreover, strong crystal strain can potentially lift the inversion symmetry of the  $\text{SiV}^-$  making it susceptible to external perturbations by e.g. fluctuating electric fields and thus causing spectral diffusion. This leads to spectral line shapes with a Gaussian contribution which however has not been observed for emitter 1. Although, the analysis of this emitter revealed a considerable amount of crystal strain, this emitter has been used for the coherent population trapping experiments presented in Sec. 4.2 because there collection efficiency was significantly limited by the cryogenic confocal microscope setup and thus a superior count rate of the emitter was of essence to successfully perform the measurements.

**Emitter 2** In contrast to the first  $\text{SiV}^-$ , confocal scans reveal that emitter 2 in fact is not centred below a SIL but rather positioned in between lenses. The centre shows count rates of about  $4 \cdot 10^4$  cps under non-resonant excitation with 7 mW of excitation power at 690 nm. The fluorescence spectrum reveals that this emitter is essentially free of crystal strain and modelling the spectrum using the group theoretical model (solid line) reveals the following set of parameters:

PLE scans of this emitter reveal very narrow optical transitions down to  $\Delta\nu=340$  MHz, close to the ideal linewidth. Due to its almost ideal properties, this emitter has been used to obtain the results presented in Sec. 4.3 and Sec. 4.4 as the fluorescence detection in these setups was efficient enough to tolerate lower emitter count rates. In the following sections we will now use these two emitters to first investigate the coherence properties of

**Table 4.2:** Resulting parameters for emitter 2 obtained from the group theoretical model presented in [58].

$\Delta E_g$	$\Delta E_e$	$\lambda_g$ (GHz)	$\lambda_e$	$\Upsilon_g$	$\Upsilon_e$	$\zeta_{g,e}$ (GPa)
48	259	40	254	8	19	0

the  $\text{SiV}^-$  at liquid helium and millikelvin temperatures and then subsequently to control the quantum state of the  $\text{SiV}^-$  using ultrafast optical pulses.

## 4.2 Coherent population trapping

**Zeeman spectra** The aim of this section is to explore the ground state spin coherence time of single  $\text{SiV}^-$  centres using coherent population trapping. Using the theoretical framework presented in Chap. 2.2.1 the width of the fluorescence dip created by pumping into the dark state can directly be related to the coherence time of the two ground states involved in this state. In general, a long coherence time scale is desirable in QIP applications to allow for a large number of gate operations. Therefore, we here look at the coherence time of the potentially long-lived electron spin degree of freedom of the  $\text{SiV}^-$  which requires working in external magnetic fields to split the spin sublevels via Zeeman interactions. As discussed above, emitter 1 has been used for these experiments. To identify the resonance frequencies of all 16 optical transitions between the spin sublevels and to find a suitable magnetic field strength we first measured fluorescence spectra at several magnetic fields represented as a spectral map displayed in Fig. 4.2(a). Note that all transitions (also the spin-flipping ones) are visible in this map because of a misalignment of the magnetic field from the high symmetry axis of the emitter of about  $70.5^\circ$ . The field hereby constitutes an external quantization axis competing with the internal one of the  $\text{SiV}^-$  which is defined by the spin-orbit interaction and aligned along the emitter's high symmetry axis. As the spin-orbit interaction strength is different in the ground and excited state, the resulting effective quantization axes in both states also differ, resulting in a finite overlap between ground and excited state sublevels of similar spin projection [57]. This overlap relaxes the optical selection rules and causes all transitions to appear in the optical spectrum. Moreover, these finite transition dipole moments are a fundamental prerequisite for optical control and CPT experiments with the  $\text{SiV}^-$  as they allow to efficiently drive  $\Lambda$ -schemes between states of different spin projection. To gain further insight into the electronic level structure and interactions between the levels we used the group theoretical model from [58] to simulate the spectral map using the parameters presented in Tab. 4.1. The white lines in Fig. 4.2(b) represent the calculated transition frequencies and Fig. 4.2(c) shows a full simulation of the spectral map, both being in excellent agreement with our experimental data. For the CPT measurement we drive a  $\Lambda$ -scheme using transitions D1 and D2 which originate from the same orbital branch but have ground states of opposite spin and share a common excited state spin level. Moreover, as we employ a quasi resonant detection scheme for this experiment, working with the upper most excited state ensures an efficient branching of population into the other excited states and especially into the strong B-multiplet. The fluorescence of these transitions is then detected to read out the

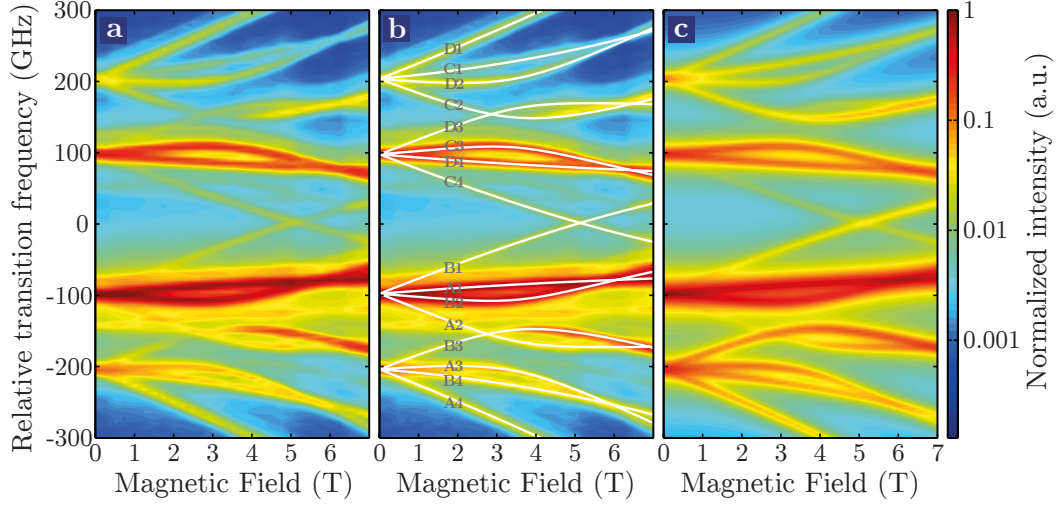


**Figure 4.2: Measured and simulated spectral map of emitter 1.** Photoluminescence spectra in dependence of the applied magnetic field for emitter 1 displayed as a colour map (a,b). The white lines in (b) represent the optical transitions as calculated from the group theoretical model presented in [58]. The colour map in (c) shows a full simulation of the magnetic field map using the same model. For these simulations, the parameters presented in Tab. 4.1 have been used.

amount of excited state population. A schematic representation of the  $\Lambda$ -scheme driven for the CPT as well as of the transitions used for detection is depicted in Fig. 4.3(a). For a first CPT measurement we chose a magnetic field strength of  $B=0.7$  T. On the one hand, this ensures a large enough Zeeman splitting so that individual transitions can be addressed. On the other hand, working close to the avoided level crossings between 3-5 T has to be avoided. These avoided crossings or anticrossings are caused by the strong spin orbit interaction in the  $\text{SiV}^-$  and induce a spin mixing [57]. Therefore, working close to these avoided crossings will shorten the ground state coherence as additional cross relaxation between the ground state spin levels occurs owing to the finite overlap between both states.

**Coherent population trapping** The CPT measurement is carried out by driving D1 with a weak probe and D2 with a stronger pump laser. A two-dimensional CPT scan at relatively high powers ( $P^{D1}=2.5 \mu\text{W}$ ,  $P^{D2}=1.5 \mu\text{W}$  while  $P_{sat}^{D1}=0.33 \mu\text{W}$ ,  $P_{sat}^{D2}=0.66 \mu\text{W}$ ) in which both the pump and the probe frequencies are varied is shown in Fig. 4.3(b). A clear dip in fluorescence is apparent in this scan, indicating the formation of the dark state. This dip follows the pump laser detuning as the two-photon resonance condition needs to stay fulfilled. Figure 4.4(a) represents a cut along the white dashed line in Fig. 4.3(b) showing a single CPT scan for zero pump detuning, emphasizing the narrow width of the pronounced CPT dip. To analyse the ground state spin coherence in greater detail, we performed further CPT scans at low excitation power to minimize power broadening as much as possible while maintaining reasonable signal to noise ratios. Contributions

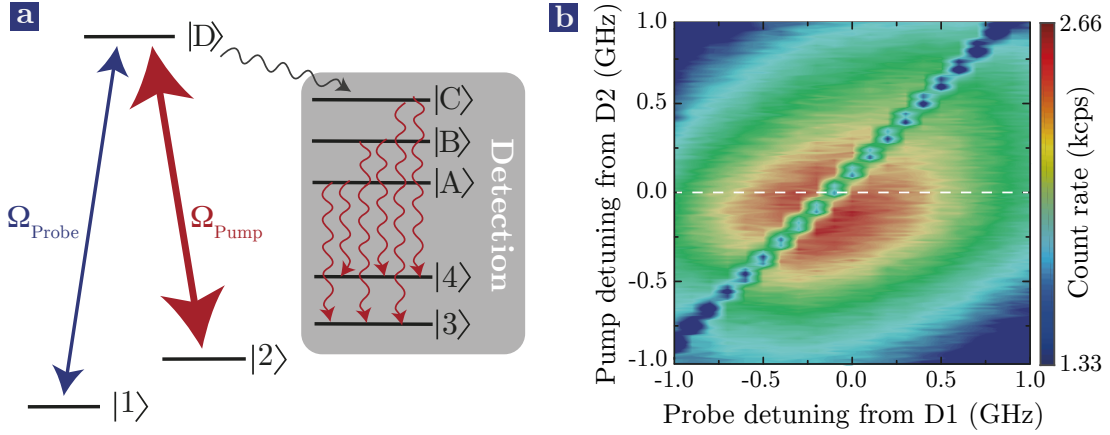


**Figure 4.3: Coherent population trapping.** A schematic representation showing the  $\Lambda$ -scheme driven as well as the optical transitions used for detection in the CPT experiments (a) and a two dimensional CPT scan (b) in which both pump and probe detuning are scanned ( $P^{D1}=2.5\ \mu\text{W}$ ,  $P^{D2}=1.5\ \mu\text{W}$  while ( $P_{\text{sat}}^{D1}=0.33\ \mu\text{W}$ ,  $P_{\text{sat}}^{D2}=0.66\ \mu\text{W}$ ).

of the remaining power broadening to the total dip width were then analyzed using the theoretical model as discussed below. A zoomed-in measurement of the dip region (grey dots) for a power of  $P^{D1} = P^{D2} = 0.33\ \mu\text{W}$  is shown in Fig. 4.4(b). To obtain this scan, 70 individual measurements have been taken and averaged. Using a Lorentzian fit we find a lowest measured full width at half maximum of the dip of  $\Delta\nu_{\text{CPT}}^{0.7T, 4.2K} = 12.1\ \text{MHz}$  and a contrast of about 16%. While the coherence time of the system is reflected in the width of the CPT resonance, it does not alter the depth of the dip. This contrast is related to the time the system spends in the dark state relative to the bright state and is thus mainly influenced by the driving field powers which define the optical pumping rates into the dark state. To extract the free induction decay time  $T_2^*$  of the ground state spin from this value, we simulate the dip using the four-level master equation model introduced in Chap. 2.2.1, featuring the three levels of the  $\Lambda$ -scheme as well as an auxiliary state to model the branching and decays via the additional ground and excited states. This model takes into account contributions from residual power broadening as well as decoherence caused by spontaneous decay, pure dephasing and limited relative laser coherence. For this simulation (solid blue line in Fig. 4.4(b)) only the ground state decoherence rate has been used as a free parameter as all spontaneous decay rates have been calculated from the measured excited state lifetime ( $\tau = 1.662(6)\ \text{ns}$ ) in combination with relative transition dipole moments extracted from the group theoretical simulation of the magnetic field map discussed above. The dip width contributions of the individual processes are indicated by the coloured Lorentzian dip insets in Fig. 4.4(b). The simulation indicates a residual power broadening of the dip of 3.6 MHz (green Lorentzian). Moreover, the relative coherence of the lasers has been measured using a homodyne detection scheme i.e. both lasers have been overlapped at a beam splitter and their beat frequency has been measured at the output port using a fast photodiode. This measurement reveals a relative laser coherence of 5.5 MHz (green Lorentzian) at an integration time of 500 ms, identical to the one used

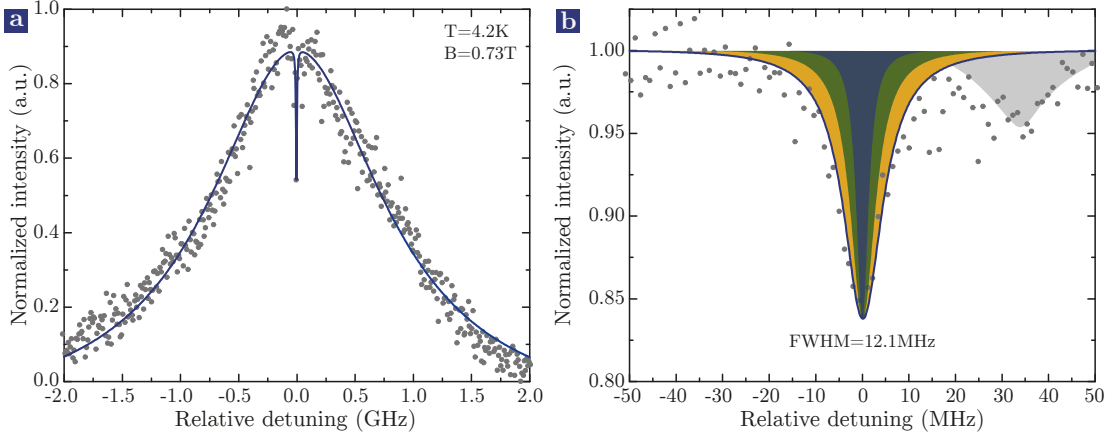


**Figure 4.4: CPT line scan and simulation.** (a) CPT scan for zero pump detuning across the entire D1 transition and (b) zoomed-in low-power scan of the CPT-dip region. Coloured Lorentzian insets in (b) represent different dip-broadening contributions and are further discussed in the main text. The grey side-dip suggests the presence of an additional emitter with strong spectral and spatial overlap.

in the CPT measurement. The remaining contribution is the decoherence of the ground state spin levels and amounts to  $\Delta\nu_{CPT}^{spin}=3.5(2)$  MHz giving rise to a free induction decay time of

$$T_2^* = \frac{1}{2\pi \cdot \Delta\nu_{CPT}^{spin}} = \frac{1}{2\pi \cdot 3.5 \text{ MHz}} = 45(3) \text{ ns} \quad (4.1)$$

This value is also in good agreement with the coherence time found in a complementary study by L. Rogers *et al.* who reported  $T_2^*=35(3)$  ns, also measured via CPT [206]. The following table summarizes all rates used in or obtained by the model:

**Table 4.3:** Transition and dephasing rates in the Master equation model used to simulate the CPT measurement.

$\Gamma_{D,1} = 2\pi \cdot 3.0 \text{ MHz}$	$\Gamma_{D,2} = 2\pi \cdot 4.7 \text{ MHz}$
$\Gamma_{D,Aux} = 2\pi \cdot 88.1 \text{ MHz}$	$\Gamma_{Aux,D} = 2\pi \cdot 40.5 \text{ MHz}$
$\Gamma_{Aux,1} = 2\pi \cdot 19.3 \text{ MHz}$	$\Gamma_{Aux,2} = 2\pi \cdot 20.9 \text{ MHz}$
$\gamma_{D,1} = \gamma_{D,2} = 2\pi \cdot 3250 \text{ MHz}$	$\gamma_{2,1} = 2\pi \cdot 3.5 \text{ MHz}$

**Number of emitters** The CPT scan also revealed the presence of a second emitter with high spectral and spatial overlap with the main emitter examined here. This side emitter shows up as a dimmer CPT dip (grey Lorentzian) detuned by about 35 MHz from the main dip. This emitter did not show up in cw  $g^{(2)}$  autocorrelation measurements, due to the low intensity relative to the main emitter. We confirmed the presence of this second emitter using pulsed  $g^{(2)}(\tau)$  measurements (Fig. 4.5(a)) in which the high peak

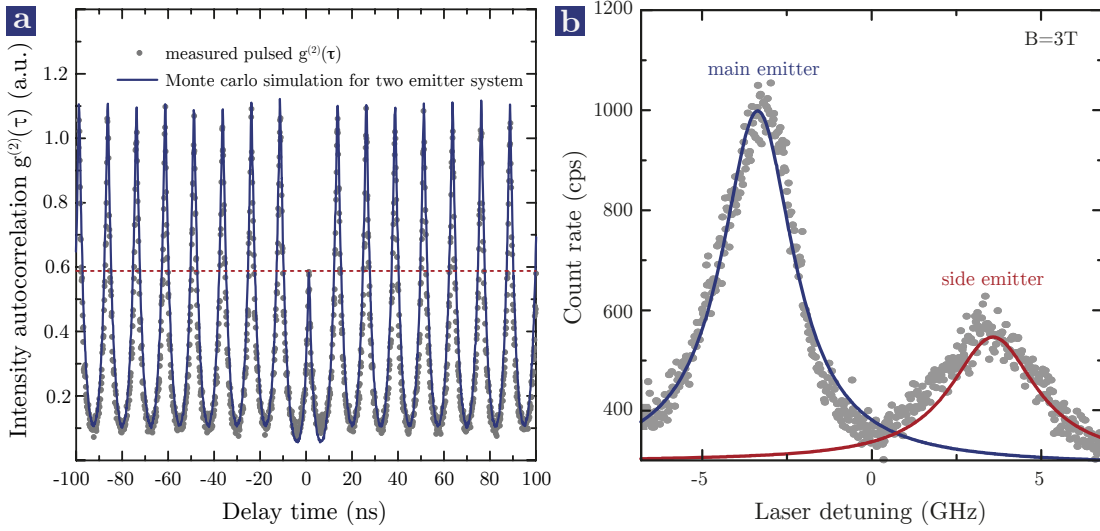


**Figure 4.5: Autocorrelation and PLE measurement of emitter 1.** In (a) a pulsed  $g^{(2)}(\tau)$  autocorrelation measurement (grey dots) and Monte Carlo simulation (blue solid line) is shown. The value  $g^{(2)}(0)=0.6$  suggests the presence of a second emitter. This is supported by the Monte Carlo simulation as well as a PLE scan at 3T shown in (b).

intensity of the pulses aids in exciting the weak  $\text{SiV}^-$  more efficiently as well as PLE scans at higher magnetic fields (Fig. 4.5(b)). In this measurement we obtain a value of  $g^{(2)}(0)=0.6$  which in fact suggests the presence of a second quantum system. Moreover, to confirm that this measured  $g^{(2)}(\tau)$  is consistent with a second emitter being present, we modelled the measurement using a Monte Carlo simulation similar to the ones performed in [207] (assisted by A. Lenhard). To do so, we considered two independent two-level systems, each with an excited state lifetime  $\tau_0=1.66$  ns. We then used a series of randomized processes to determine the change of state of both systems from each time step to the next. First, in every excitation cycle we randomly decide if the systems are excited and we scale the excitation probabilities of both emitters to account for their different strengths in the CPT measurements. If a system is excited, we then again insert a random number into an exponential decay function with a decay time  $\tau_0$  to simulate the spontaneous decay of the system. If one of the two systems decays, a click is written to a list, similar to a real detection event in a real measurement. Additionally, we add a Poisson-distributed timing jitter of 350 ps to these clicks to simulate the jitter of the detectors used to measure the  $g^{(2)}(\tau)$ . Finally we randomly separate the file into two lists to simulate an HBT setup and then correlate them to obtain the simulated  $g^{(2)}(\tau)$ . We obtain a good agreement between the measured and the simulated  $g^{(2)}(\tau)$  by assuming a ratio of both emitters of 2:1. This value is also consistent with the measured PLE scan in Fig. 4.5 as well as the observed side dip in the CPT measurement. From the magnetic field dependence of the splitting between both emitters we estimate a difference in crystal strain of about 2%. However, note that the presence of this second  $\text{SiV}^-$  does not interfere with the analysis presented here as we can clearly distinguish both emitters in the CPT scans.

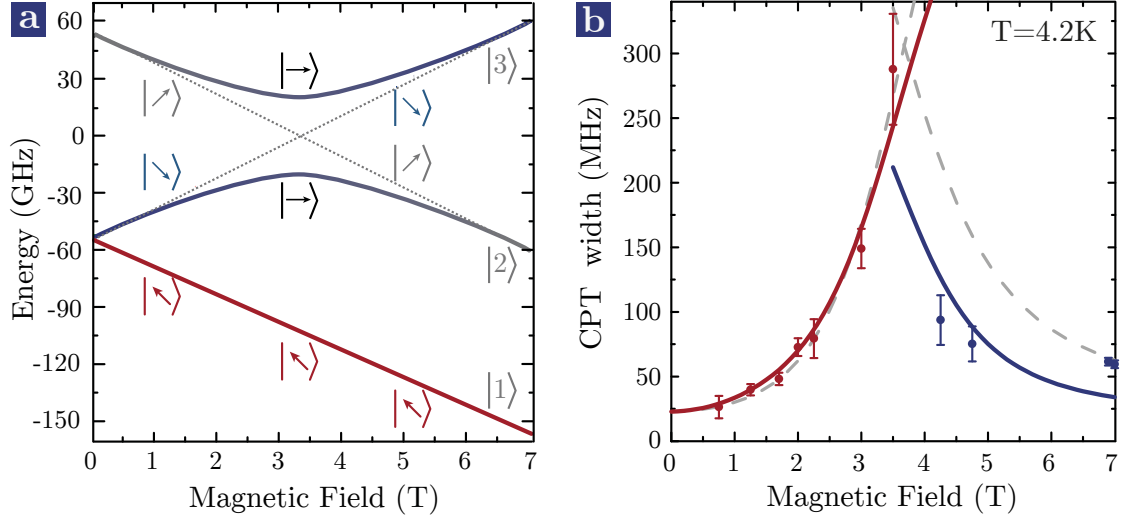


**Figure 4.6: Magnetic field dependence of CPT.** (a) Simulated ground state level scheme for varying magnetic fields. The simulation is based on the group theoretical model from [58]. Tilted arrows indicate spin orientations due to changing effective quantization axes. (b) Linewidth of the CPT dip in dependence of the applied magnetic field. As the spin projections of states  $|2\rangle$  and  $|3\rangle$  exchange signs, we create CPT between  $|1\rangle$  and  $|2\rangle$  before the avoided crossing (red dots) and  $|1\rangle$  and  $|3\rangle$  after it (blue dots). The dashed grey lines indicate the spin overlap between  $|1\rangle$  and  $|2\rangle$  /  $|3\rangle$  calculated from the group theoretical model. Red and blue solid lines represent this overlap multiplied by an additional Boltzmann factor. Error bars represent curve fitting errors of the CPT dip width with a Lorentzian function.

**Decoherence mechanisms** Let us now return to the coherence properties of the  $\text{SiV}^-$  and explore possible explanations for its surprisingly short ground state coherence time: To understand this phenomenon, it is of great importance to recall that the states in the  $\text{SiV}^-$  are not clean spin levels but also contain an orbital contribution. This, in combination with the competition of internal and external quantization axes as well as fluctuating spin baths in the environment of the  $\text{SiV}^-$  opens the door for a large number of possible decoherence mechanisms which we will further discuss here and in the following section. First, we investigate the role of direct phonon-mediated transitions [121] between the two spin levels of the  $\Lambda$ -system. We expect this rate to be strongly dependent on the applied magnetic field due to the presence of avoided crossings between 3-5 T during which the orthogonality of the involved spin levels is lifted. Using the model from [58] we simulated the ground state level scheme for varying magnetic field strengths. This is shown in Fig. 4.6(a). The orientation of the spin states of the individual levels in the frame of a "pure" spin up/spin down basis is indicated by tilted arrows. This rotation of spin quantization axes for individual states is a direct result of the complex interplay between spin-orbit and Zeeman interactions in the  $\text{SiV}^-$  in the presence of off-axis magnetic fields. As the spin orientations of states  $|2\rangle$  and  $|3\rangle$  are exchanged at the avoided crossing we

perform the CPT measurement between states  $|1\rangle$  and  $|2\rangle$  before and  $|1\rangle$  and  $|3\rangle$  after the avoided crossing. In Fig. 4.6(b) the measured CPT dip width (red and blue dots) for several magnetic fields are shown (error bars represent fit errors in the individual Lorentzian fits). As we have discussed above, this width is directly proportional to the decoherence rate between the two levels and, as expected, increases rapidly when approaching the avoided crossing. To further analyse this broadening we employ the following simple model: The eigenstates of the SiV<sup>-</sup> as extracted from the group theoretical model [58] can be written as

$$|\Psi_k\rangle = \alpha |e_+ \uparrow\rangle + \beta |e_+ \downarrow\rangle + \gamma |e_- \uparrow\rangle + \delta |e_- \downarrow\rangle \quad (4.2)$$

with the orbital components  $e_{+,-}$ , the  $S_z$  spin component  $\uparrow, \downarrow$  (in the frame of the internal quantization axis of the SiV<sup>-</sup>) and the complex expansion coefficients  $\alpha, \beta, \gamma$  and  $\delta$  for the ground states  $k=1\dots 4$ , respectively. To project these states onto the  $\uparrow, \downarrow$  spin subspace and to determine the  $S_z$  component of each individual eigenstate we can thus use the projector

$$P = |\uparrow\rangle \langle \uparrow| + |\downarrow\rangle \langle \downarrow|. \quad (4.3)$$

Moreover, to determine the spin overlap of the two ground states involved in the CPT we can calculate their squared scalar product  $|\langle \Psi_1 | P^\dagger P | \Psi_{2,3} \rangle|^2$  (grey dashed lines). Especially for the low-field branch this simple quantity (with a constant y-offset to account for other decoherence process not directly related to the spin overlap) already results in a very good agreement with the measured CPT dip widths (red dots) whereas after the avoided crossing the dip width recovers faster than predicted by the pure spin overlap. This deviation most likely results from the phonon population decreasing for higher magnetic fields due to larger Zeeman splitting and the fact that, after the avoided crossing, we drive the  $\Lambda$ -scheme using the higher lying state  $|3\rangle$ . To account for this change we therefore multiply the spin overlap by a Boltzmann factor taking into account the field dependent level splitting  $\Delta E_{1,2/3}(B)$ . For the low-field regime this quantity results in almost the same curve (red solid line) as the pure spin overlap but additionally resembles the measurements in the high field regime significantly better. Moreover, from Fig. 4.6(b) it is apparent that both in the low and the high field limit the CPT dip width saturates at the observed values. In these regions, far away from any avoided crossing, the direct relaxation between the two spin sublevels is most likely not the coherence limiting process and another source of decoherence, here included in the offset, presumably dominates.

In addition to this direct relaxation between both states there are two other possible decoherence processes involving thermalization to the upper orbital branch of the SiV<sup>-</sup> ground state: First, absorption of a phonon with  $E_p \approx 48$  GHz can lead to a thermalization of the state prepared in the spin doublet of the lowest orbital state into the spin sublevels of the upper orbital branch. This process is followed by a relaxation back into the lower spin sublevels under phonon emission. This excitation and de-excitation in general only flips the orbital degree of freedom while being spin-conserving. In the SiV<sup>-</sup>, in the presence of off-axis magnetic fields, the two orbital branches also exhibit slightly different quantization axes and thus, in analogy to the spin-flip via optical excitation discussed above, with a small but finite probability this process can also induce a spin-flip. In the following, we characterize the time scale of this indirect spin-flip as well as the above-mentioned direct process by a common spin-relaxation time  $T_1^{spin}$ . Using optical

pumping experiments at  $T \approx 5\text{K}$ , Rogers *et al.* measured  $T_1^{spin} = 2.4\text{ ms}$  for magnetic fields aligned with the SiV<sup>-</sup> high symmetry axis, while a field misaligned by only  $20^\circ$  already leads to a drastic reduction down to  $T_1^{spin} = 3.4\ \mu\text{s}$  [206]. Moreover, recently we measured  $T_1^{spin} = 350(11)\text{ ns}$  for a field off-axis by  $70.5^\circ$  at  $3.5\text{ K}$  using the same technique [208]. This strong angular dependence is a direct consequence of the competition process between internal and external quantization axes. Moreover, even if the thermalization does not introduce a spin flip it still leads to decoherence as the spin splitting in both orbital branches differs by about 20% [57, 58, 122]. This means that a superposition prepared in the lower spin doublet undergoes a different phase evolution when transferred to the upper spin levels and, as this transfer process occurs randomly, this leads to the acquisition of random phase causing decoherence. Again, using optical pumping experiments at zero magnetic field, Jahnke *et al.* determined this purely orbital relaxation rate to be  $T_1^{orbit} = 39(1)\text{ ns}$  at  $5\text{ K}$  [121]. As already briefly discussed in Chap. 1.2.4, they identify a linear electron-phonon interaction with a single E-symmetric phonon mode as the driving force for the spin as well as the orbital relaxation with thermalization rate

$$\gamma_+ = 2\pi\chi\rho\Delta E_{g,e}^3 n(\Delta E_{g,e}, T) \quad (4.4)$$

and relaxation rate

$$\gamma_- = 2\pi\chi\rho\Delta E_{g,e}^3 [n(\Delta E_{g,e}, T) + 1] \quad (4.5)$$

with proportionality constants  $\chi$ ,  $\rho$  as well as ground and excited state splittings  $\Delta E_{g,e}$ . The term  $n(\Delta E_{g,e}, T)$  refers to the phonon number

$$n(\Delta E_{g,e}, T) = \frac{1}{\exp(\frac{\hbar\Delta E_{g,e}}{k_B T}) - 1} \quad (4.6)$$

given by a Boltzmann distribution [122]. For temperatures  $T \gg \hbar\Delta E_{g,e}/k_B$  the rates can then be approximated as

$$\gamma_+ \approx \gamma_- \approx 2\pi\chi\rho\Delta E_{g,e}^2 k_B T. \quad (4.7)$$

Moreover, due to the close match of their measured  $T_1^{orbit} = 39(1)\text{ ns}$  and  $T_2^* = 35(3)\text{ ns}$  Jahnke *et al.* claim that the orbital relaxation is the spin coherence limiting process at liquid helium temperatures. Therefore, the coherence time of the SiV<sup>-</sup> might be improved in future devices by engineering the phonon environment of the diamond host lattice to eliminate phonons with an energy of  $E_p \approx 48\text{ GHz}$  so that ground state thermalization cannot take place any more. This can either be achieved by cooling the sample well below  $2.3\text{ K}$  or by fabricating small nanostructures with a confinement for phonons of that frequency [209]. This might for example be achieved by creating a phononic band gap by patterning a diamond membrane to fabricate a so-called phononic crystals (in analogy to photonic crystals in which a band gap for photons is created) [210]. First simulations show that, while in principle being possible, these structures will be very challenging to fabricate as a full phononic band gap at  $50\text{ GHz}$  requires e.g. a  $120\text{ nm}$  spaced grid of holes with a diameter of  $90\text{ nm}$  in a  $60\text{ nm}$  thick membrane. Thus, a more feasible approach might be the growth of nanodiamonds with a diameter smaller than  $120\text{ nm}$  to eliminate the respective phonons [121]. While the fabrication of such nanodiamonds is easily possible with current diamond growth techniques, they currently still provide

rather strained crystal environments leading to alterations of the electronic properties of the SiV<sup>-</sup> beyond acceptable margins for QIP applications. Alternatively, also the strain itself can be used to manipulate the phonon-mediated transition rates. As discussed in [58], crystal strain is a purely orbital perturbation and like the JT effect increases the ground and excited state splittings of an SiV<sup>-</sup> if present. From Eq. 4.4 and Eq. 4.5 it is now evident that the phononic rates consist of terms being cubic (due to the phonon density of states  $\rho(\omega)$  increasing quadratically and the interaction density  $\chi(\omega)$  increasing linearly with  $\omega$ ) and inverse exponentially dependent (due to the decreasing excitation probability) on the ground state splitting. Hence, while for  $\Delta E_g$  of up to 300 GHz the cubic term dominates, for even higher splittings the phononic rates start to drop again. In [211] we measured this trend by selecting SiV<sup>-</sup> centres experiencing different crystal strain due to their local environment and measuring their linewidth, depending on the ground and excited state decoherence rates, using PLE. A more controlled approach to use strain to improve the SiV<sup>-</sup> coherence has recently been presented by Sohn *et al.* The authors used a diamond nano-electro-mechanical system (NEMS) to apply strain in a nanobeam and to create ground state splittings of up to  $\Delta E_g \approx 500$  GHz, resulting in spin coherence times of  $T_2^* = 250$  ns [212]. Furthermore, it is important to point out that, while it is reasonable to assume that the phonon-mediated orbital rate is the dominant source of decoherence at 4 K and above, the fundamental limit of  $T_2^*$  is given by  $T_2^* \leq 2T_1$  and thus  $T_2^{*,max} = 2 \cdot 39 = 78$  ns in the experiments presented in [206]. The  $T_2^*$  measured there however is about a factor of two lower than this limit, suggesting the presence of additional decoherence processes. For example, besides the  $T_1$ -related relaxation processes discussed so far also other processes directly affecting the phase coherence time  $T_2$  of the system can be sources of additional decoherence. This can e.g. be caused by a nuclear or electron spin bath in the environment of the SiV<sup>-</sup> causing magnetic field noise. The presence of these spin baths is a reasonable assumption for the sample used in our CPT experiments as it contains <sup>13</sup>C (I=1/2) in its natural abundance of 1.1%. Moreover, the vacancies created during the ion implantation led to the creation of a dense ensemble of NV centres (S=1) suggesting the presence of a considerable amount of  $[N_s^0]$  (S=1/2) in the sample. Additionally, the inclusion of other impurities during HPHT growth is not unlikely as e.g. Ti (I=-5/2, -7/2) is used as a nitrogen getter in these processes. Fluctuations in such a spin bath, to some extent, can be counteracted using Hahn-echo [136] or more elaborate dynamical decoupling sequences [213] as the decoherence due to the bath is a non-Markovian process (i.e. it has a "memory") on the time scale of the decoupling sequence. The phonon-mediated  $T_1$  processes described above, however, are fast and memoryless and thus Markovian in nature. This means that these processes cannot be dynamically decoupled. Moreover, in principle the spin bath could also lead to a direct spin-flip if the SiV<sup>-</sup> spin resonantly exchanges energy with spins from the bath. In the following chapter we will further explore the role of the phonon-mediated  $T_1$  processes with respect to the spin coherence of the SiV<sup>-</sup> and its counter-play with possible  $T_2$  processes using optical pumping and CPT experiments at millikelvin temperatures. Before we proceed to these experiments, we will briefly summarize the main results from the experiments presented in this section:

- We here demonstrated, for the first time, that optical access to the coherence of the

ground state electron spin degree of freedom of the  $\text{SiV}^-$  is feasible using coherent population trapping in external magnetic fields and we determined the ground state free induction decay time to be  $T_2^* = 45(3)$  ns.

- Using magnetic field dependent CPT measurements, we investigated the role of a direct relaxation between the two spin states involved in the CPT dark state. These experiments reveal a drastic increase of decoherence when tuning the spin states into a level anti-crossing as spin selection rules are relaxed. Moreover, these measurements suggest that decoherence in the low and the high field limit (away from the avoided crossings) is dominated by other processes such as phonon-mediated thermalization between the different orbital branches of the ground state or magnetic field noise caused by an impurity spin bath. These effects will be investigated in further detail in the following section.

### 4.3 Millikelvin experiments

#### 4.3.1 Measurement of orbital and spin relaxation rates

In this section we will now try to deepen the understanding of the spectral and coherence properties of the  $\text{SiV}^-$  by performing additional experiments at temperatures in the millikelvin range. To do so, we use the confocal microscope and dilution refrigerator setup discussed in Chap. 3.3.3. As this setup includes a high N.A. objective and thus is more efficient than the setup used for the initial CPT experiments in the previous chapter, we decided to use the dimmer but less strained emitter 2 for the following experiments as it resembles "the ideal  $\text{SiV}^-$ " more closely.

**PLEs, light narrowing & orbital relaxation** To identify the frequencies of the relevant optical transitions at 3.7 K (which is the base temperature of the pulse-tube pre-cooler) as well as 12 mK base temperature, we first performed PLE scans as well as a measurement of the orbital relaxation time  $T_1^{\text{orbit}}$  at 3.7 K: In this setup, the sample is directly mounted to a SmCo permanent magnet providing a magnetic field just strong enough to enable addressing of individual transitions between spin sublevels. In Fig. 4.7(a) three different PLE scans at an excitation power of only  $P=5$  nW (with detection on the PSB) are shown. The scans reveal the four transitions between the spin sublevels 1, 2, A and B (cf. inserted level scheme) with very narrow linewidths down to 314 MHz for transition A1 at 3.7 K (upper graph). At 12 mK, an additional pump laser on the transitions A2 or B2 and B1 or A1 needs to be applied to avoid fast spin initialization and thus loosing the PLE signal during the scan. At low pump laser powers of  $P_{\text{pump}}=2$  nW a broadening of the transitions (middle graph) by about 250 MHz compared to 3.7 K is observed while the linewidth recovers for higher powers of  $P_{\text{pump}}=50$  nW, slowly approaching the values measured at 3.7 K (lower graph). This, at first unintuitive, change in linewidth is an initial hint for an alteration in the internal dynamics of the  $\text{SiV}^-$  upon cooling below temperatures of  $2.3 \text{ K} = 48 \text{ GHz}/k_B$ , corresponding to the orbital splitting. We can reproduce this phenomenon using a simple four-level OBE model similar to the one described in Sec. 2.2.1, including two ground and excited state levels. Each excited state can hereby spontaneously decay into both ground states with transition strengths extracted from the group theoretical model above [58] and lifetimes  $\tau_{A,B}$ . Moreover, ground state  $|2\rangle$  can decay into  $|1\rangle$  with a rate  $1/T_1^{\text{spin}}$ . Additionally, we employ the power ratios for pump and probe lasers given in Fig. 4.7(a) and we use in advance the relaxation times  $T_1^{\text{spin},3.7\text{K}} = 303 \text{ ns}$  and  $T_1^{\text{spin},12\text{mK}} = 108 \mu\text{s}$  at 3.7 K and 12 mK measured later in this section. Using this simplified model, the linewidth change can then be illustrated as follows: Let us for example look at transition A1 between the lowest ground  $|1\rangle$  and excited state  $|A\rangle$  spin levels. Population excited into  $|A\rangle$  has a finite chance to undergo a spin flip and decay into state  $|2\rangle$  instead of returning to  $|1\rangle$ , due to the tilted quantization axes of ground and excited state mentioned above (red wavy arrow in Fig. 4.8(a)). However, as also discussed above, at 3.7 K the two ground state spin levels  $|1\rangle$  and  $|2\rangle$  can also decay into each other without optical excitation via phonon-mediated thermalization to the upper orbital branch which likewise possesses a slightly tilted axis of quantization compared with the lowest orbital branch (blue arrow in Fig. 4.8(a)). Thus population pumped into  $|2\rangle$  will eventually

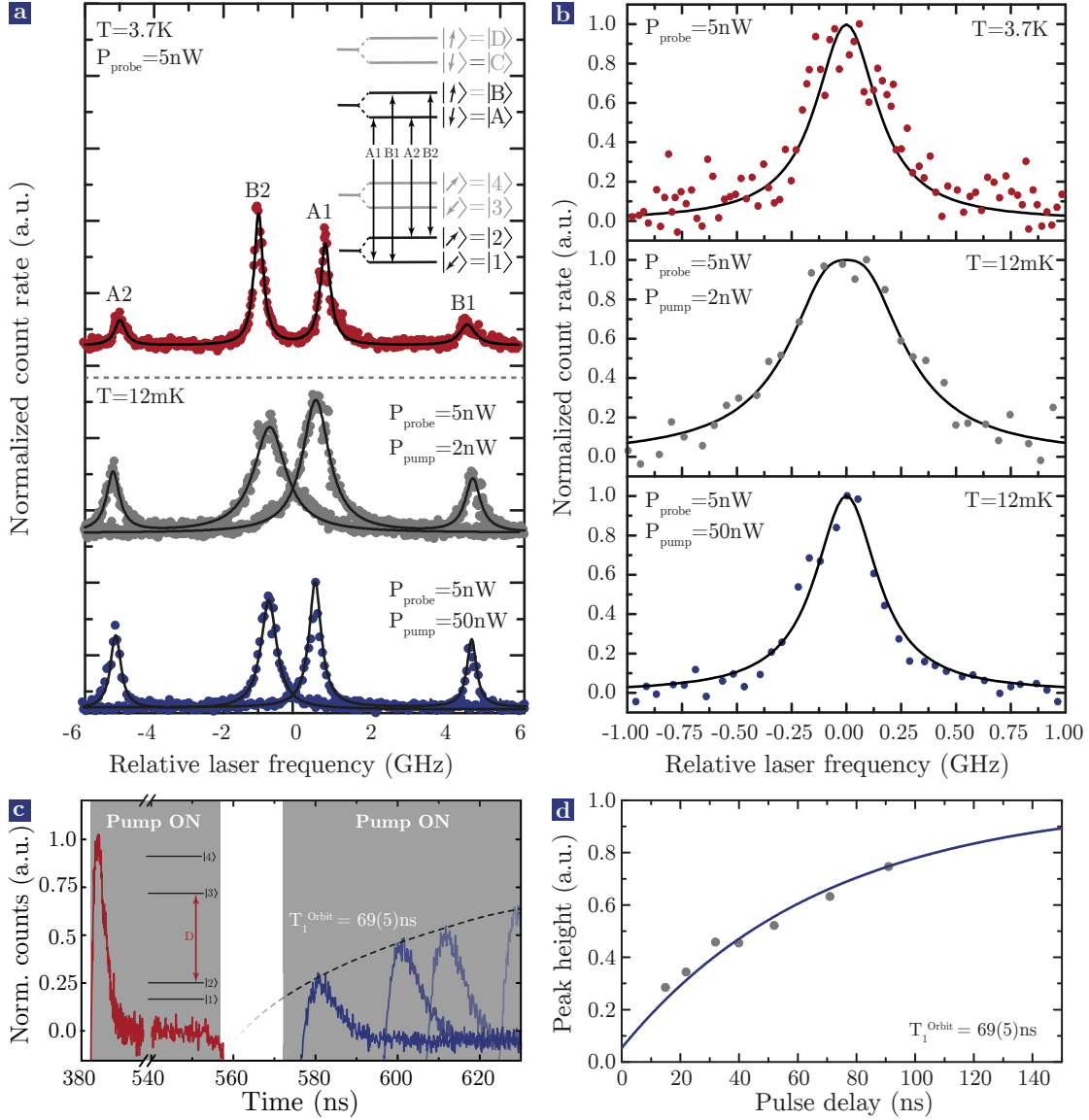


**Figure 4.7: Spin-sublevel spectrum and orbital relaxation rate.** (a) PLE scans across the spin sublevel transitions of the lowest orbital branch of the SiV<sup>-</sup> ground and excited states (black states and transitions in inserted level scheme) for 3.7 K (upper graph, red dots) and 12 mK (middle and lower graph, grey and blue dots). At 12 mK, an additional pump laser applied to the spin flipping transitions A2 and B1 is used to avoid fast spin initialization. At low pump powers a broadening of the lines is observed (middle graph) which again vanishes for increasing pump powers (lower graph), approaching the linewidths at 3.7 K. (b) PLE scans of A1 resonances only (coloured dots) and simulations (black lines) using a four-level OBE model including two ground and two excited states. The model reproduces the observed line broadening effect. Further details are given in the main text. (c) Pulse sequence and resulting fluorescence signal of optical pumping scheme used to measure  $T_1^{\text{Orbit}}$ . The equilibrium fluorescence level during the pulses has been set to zero. (d) Recovery of readout peak height for different delays between initialization and readout pulse in orbital optical pumping experiment. The recovery rate resembles  $T_1^{\text{Orbit}}$ .

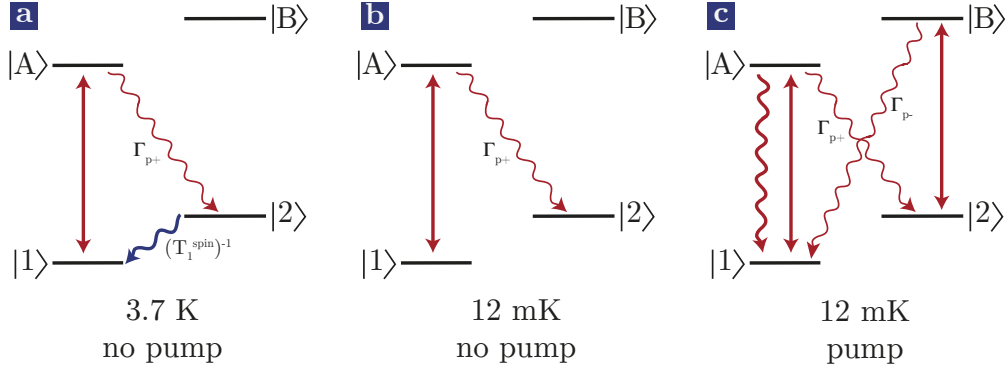


**Figure 4.8: Light narrowing.** Schematic level scheme including the two lowest ground state spin sublevels  $|1\rangle$  and  $|2\rangle$  as well as the lowest excited state spin sublevels  $|A\rangle$  and  $|B\rangle$ . (a) Optical driving transition A1 at 3.7K leads to an optical spin pumping (red wavy arrow) with rate  $\Gamma_{p+}$  which is counteracted by phonon mediated decays between the ground state spin sublevels (blue arrow). (b) At 12 mK the ground state decay vanishes leading to a considerable spin pumping by  $\Gamma_{p+}$ . (c) Adding a second laser on transition B2 at 12 mK leads to a spin pumping back into  $|1\rangle$  via the rate  $\Gamma_{p-}$ , effectively compensating  $\Gamma_{p+}$ .

return to  $|1\rangle$  at a rate  $1/T_1^{spin,3.7K}$  and we can define an effective spin pumping rate

$$\frac{1}{T_1^{eff}} = \Gamma_{p+} - \frac{1}{T_1^{spin,3.7K}} \quad (4.8)$$

of  $|1\rangle$  as the difference of the optical spin pumping rate  $\Gamma_{p+}$  and the ground state spin relaxation  $1/T_1^{spin,3.7K}$ . Since the optical linewidth  $\Delta\nu$  of the transition A1 is given by

$$\Delta\nu = \frac{1}{2\pi\tau_A} + \frac{1}{2\pi T_1^{eff}}, \quad (4.9)$$

with the excited state lifetime  $\tau_A$ , the effective relaxation time  $T_1^{eff}$  of  $|1\rangle$  contributes to the linewidth. However, due to the relatively fast thermalization processes, at 3.7 K, the optical linewidth is dominated solely by the excited state dynamics while  $T_1^{eff}$  plays a negligible role. This leads to the PLEs displayed in the upper panel of Fig. 4.7(a) with linewidths reaching down to 314 MHz. In Fig. 4.7(b) we exemplarily show the simulations using the OBEs (solid lines) overlaid on top of PLE scans of transition A1 only (dots) with the upper panel corresponding to the above described case at 3.7 K. Assuming the above mentioned powers and rates, the model reproduces the measured PLE very well. When cooling down to 12 mK the linewidth drastically increases in the absence of a second laser. The reason for this is that the ground state thermalization and thus the spin flipping process relaxing population from  $|2\rangle$  back into  $|1\rangle$  after optical pumping is essentially frozen out (cf. Fig. 4.8(b)). Therefore, the effective spin pumping rate  $1/T_1^{eff}$  from  $|1\rangle$  into  $|2\rangle$  significantly increases as it is now solely governed by  $\Gamma_{p+}$ . Hence, while the excited state lifetime stays constant (verified by time correlated single photon counting experiments identical to the ones presented in Sec. 4.4 for the same emitter)  $T_1^{eff}$  now

becomes a significant additional contribution to the optical linewidth. The middle panel in Fig. 4.7(b) shows the simulation for the reduced ground state spin relaxation, again nicely reproducing the PLE data. By applying an additional laser, capable of optically pumping population from  $|2\rangle$  back into  $|1\rangle$  via a rate  $\Gamma_{p-}$  (cf. Fig. 4.8(c)), the effective spin pumping rate  $1/T_1^{eff}$  can be artificially reduced. Consequently, for increasing pump powers  $T_1^{eff}$  again becomes a negligible contribution compared to  $\tau_A$  and the optical linewidth again approaches the values measured at 3.7 K. This can be seen from the simulation in the lower panel of Fig. 4.7(b). Similar "light narrowing" effects have e.g. been observed in alkali vapours [214, 215] and for magnetic resonances in NV centres [216]. Moreover, from the PLE scans above we can extract the Zeeman splittings in the ground and excited state, which amount to  $\Delta E_g^{Zeeman} = 5.881(9)$  GHz and  $\Delta E_e^{Zeeman} = 4.001(7)$  GHz, indicating a magnetic field of about  $B = 0.21$  T. Additionally, to characterize the relaxation between the orbital sublevels, which supposedly is the main source of spin decoherence, we measured  $T_1^{orbit}$  using optical pumping of transition D (between the upper orbital ground and lower orbital excited state) at zero magnetic field. The pulse sequence consisting of a pump and a readout pulse as well as the resulting fluorescence response is depicted in Fig. 4.7(c). After exciting the SiV<sup>-</sup> on transition D, the system can decay into both orbital ground states and thus, continuously driving D will eventually pump the majority of the population into the lower ground state. Therefore, starting from a thermal population of about 40% the population, and thus the fluorescence, decays at the beginning of the initialization pulse as the upper orbital ground state is emptied out. Due to the thermalization between the orbital states which continuously counteracts this process, the fluorescence does not decay to zero but saturates at a finite equilibrium level (set to zero in Fig. 4.7(c)). The population in this steady state is eventually given by the ratio of the excited state decay rate and  $T_1^{orbit}$ . After switching off the initialization pulse, the thermalization then again starts to equilibrate the population in the two ground state orbital levels and the population in the upper ground state level starts to increase. To read out the recovery of this population we then apply a second pulse with a certain delay and the height of its rising edge peak normalized to the peak in the initialization pulse corresponds to the recovered population. From the measured peak heights for different delays we can then extract  $T_1^{orbit}$  using an exponential fit. This measurement is shown in Fig. 4.7(d), revealing  $T_1^{orbit} = 69(5)$  ns at 3.7 K. This value also is in excellent agreement with  $T_1^{orbit} = 67(2)$  ns which we measured in a similar sample in [208].

**Spin relaxation** While cooling down, the occupation of phonons with an energy of  $48 \text{ GHz} = k_B \cdot 2.3 \text{ K}$  (corresponding to the orbital splitting) drops drastically. Thus the orbital relaxation time increases rapidly and becomes immeasurably long. From Eq. 4.4 and [122] we estimate  $T_1^{orbit} = 1 \text{ ms}$  at 300 mK and several hours at the base temperature of 12 mK used to conduct the experiments. At these temperatures, the lowest spin doublet is shielded from the detrimental effects of orbital thermalization. Note that this is not the case for the spin states of the upper orbital ground state branch as they will rapidly decay into their respective spin counterparts of the lower orbital state under phonon emission. Therefore, all of the following experiments are performed on the spin levels

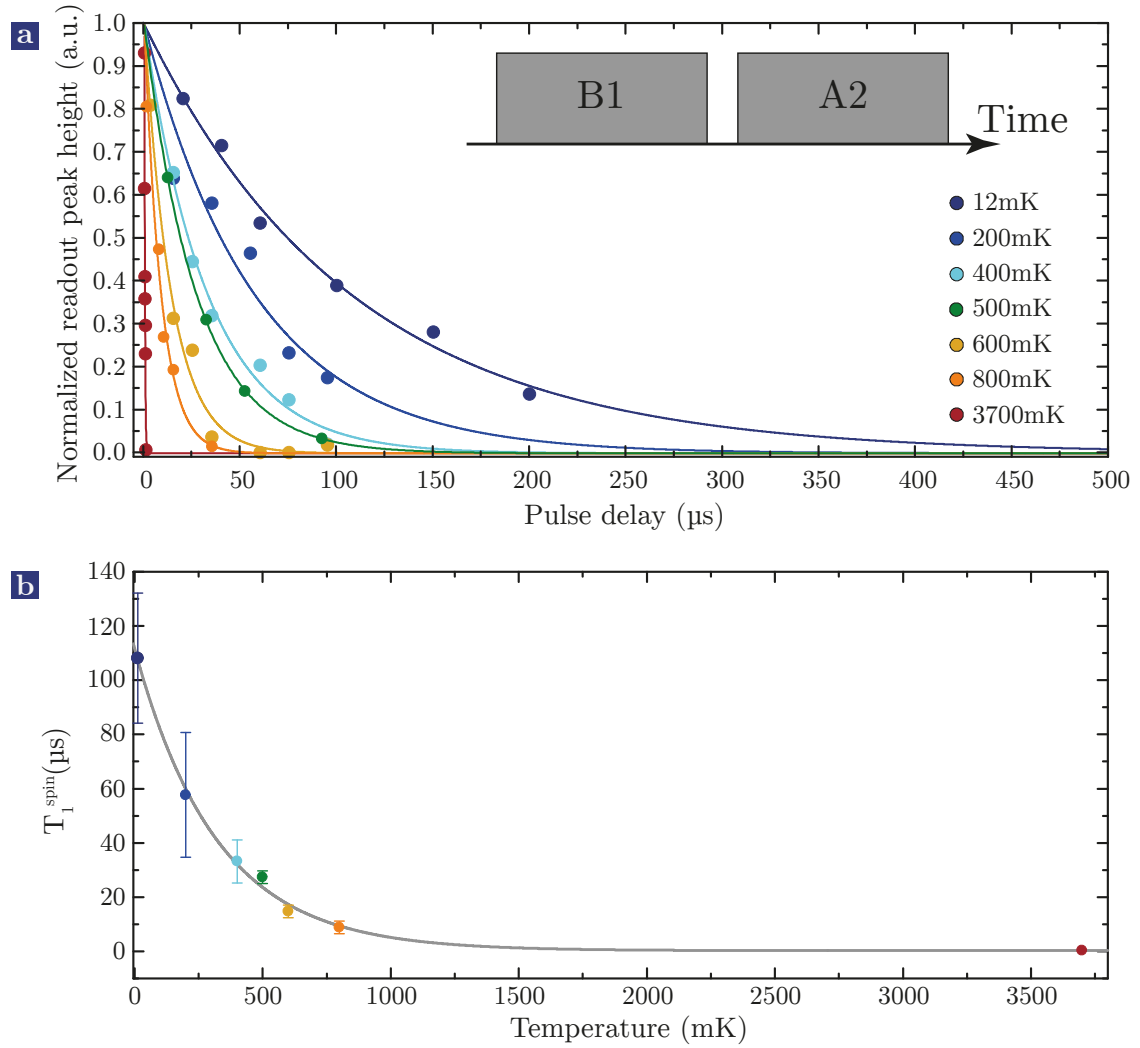


**Figure 4.9: Spin relaxation rates.** (a) Measurement of  $T_1^{spin}$  using an optical pumping sequence consisting of an initialization pulse resonant with the spin-flipping transition B1, pumping population into state  $|2\rangle$  and a readout pulse on the strong spin-allowed transition B2 providing a strong signal. (a) Individual decays of the rising edge peak height of the readout pulse for varying pulse delays at different temperatures. (b) Temperature-dependant decay of  $T_1^{spin}$ . The grey line only serves as a guide to the eye.

|1⟩ and |2⟩ using the optical transitions shown in the PLE scan in Fig. 4.7(a). While the orbital thermalization is strongly quenched at low temperatures, the relaxation of the spin itself can cause decoherence. To estimate this effect we measured  $T_1^{spin}$  at 3.7 K and various temperatures between 1 K and 12 mK. To do so, we again used an optical pumping sequence consisting of two pulses. However, for this measurement two different transitions have been addressed by both pulses. The first pulse is resonant with the spin flipping transition B1. This pulse does not produce noticeable fluorescence as the spin-forbidden transition is weak but efficiently pumps the spin into level |2⟩. We then use a second pulse on the allowed transition B2 to produce a strong fluorescence signal to read out the population of state |2⟩ after a certain delay. Again, we use the ratio of the decay of the rising edge peak of the readout pulse as a measure for the population in this state and its decay over time represents  $T_1^{spin}$ . The resulting curves for various temperatures are shown in Fig. 4.9(a) and the corresponding  $T_1^{spin}$  times are displayed in Fig. 4.9(b). Therein, while the variation of  $T_1^{spin}$  with temperature, at first glance, appears to drop off exponentially, we would like to emphasize that the grey line in Fig. 4.9(b) only serves as a guide to the eye and, as we will see below, the variation of the spin relaxation rate with temperature is more complex than suggested by this representation. Due to the strongly misaligned magnetic field, the spin relaxation time at 3.7 K amounts to 303(9) ns, in good agreement with values measured in [208] for similar field angles. While lowering the temperature,  $T_1^{spin}$  increases rapidly by almost three orders of magnitude and reaches 108(24)  $\mu$ s at 12 mK base temperature. At these temperatures, the spin-flip via the above mentioned excitation to the upper orbital ground state branch, just like  $T_1^{orbit}$ , is completely frozen out. Therefore, to analyse the nature of the spin relaxation mechanism we now take a closer look at the temperature dependence of the spin relaxation rate  $1/T_1^{spin}$  displayed in Fig. 4.10. For temperatures between 12 mK and approximately 500 mK the measured relaxation rate (blue dots) scales approximately linearly with temperature and finally saturates for temperatures below approximately 50 mK. This linear scaling indicates a so-called direct spin-flip process involving single phonons disturbing the lattice and thus creating magnetic field fluctuations which can couple to the SiV<sup>-</sup> spin and induce a spin flip [217]. This process can be fit by a function of the form [218]

$$\frac{1}{T_1} = \coth \left( \frac{g\mu_B B}{k_B(T + T_0)} \right). \quad (4.10)$$

and can be used to determine the effective temperature  $T_{eff} = T + T_0$  of the SiV<sup>-</sup>. With  $g \approx 2$  and  $B=0.21$  T we obtain a good fit of the data (blue dashed line in insert) indicating  $T_{eff} = 41(3)$  mK at a total optical power of about 50 nW. Moreover, we expect the direct spin-flip rate to further decrease when aligning the magnetic field with the axis of the SiV<sup>-</sup> as the state tomographies calculated with our group theoretical model [58] indicate that even between the two spin sublevels the misaligned field causes a finite overlap (of about 2% at 70.5°) which further facilitates the spin decay. The model indicates that this overlap appears to be caused by the small contribution of the JT effect and vanishes for magnetic fields aligned with the high symmetry axis of the SiV<sup>-</sup>. If the temperature significantly exceeds the phonon-temperature corresponding to the spin splitting (here  $5.881$  GHz/ $k_B = 282$  mK) also higher order phonon processes like the Raman (the system undergoes a two-phonon transition via a virtual level) or Orbach process (the system is

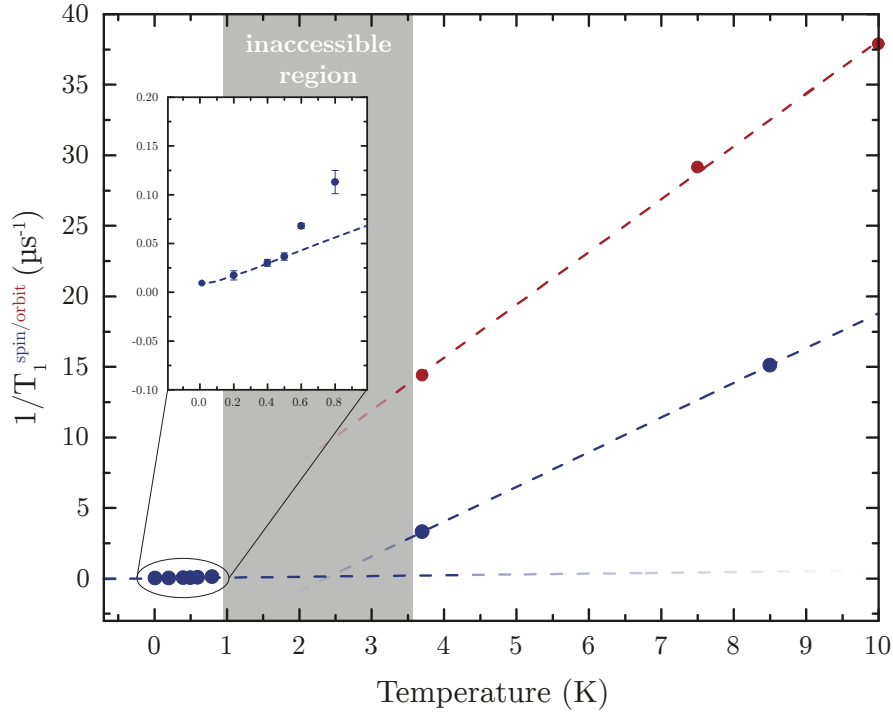


**Figure 4.10: Temperature dependence of spin relaxation.** Temperature dependence of the measured spin-lattice relaxation rate  $T_1^{\text{spin}}$  (blue dots): At temperatures  $\leq \Delta_z/k_B$ , with  $\Delta_z$  being the Zeeman splitting of the spin sublevels, a temperature dependence following a hyperbolic cotangent is observed, corresponding to a phonon-mediated direct spin-flip process (lower blue dashed line in main figure and inset) whereas the rate deviates for higher temperatures due to multi-phonon processes (see inset). At  $T > 2.3$  K a single-phonon process involving excitation to the upper orbital ground state starts to dominate the spin relaxation. Moreover, at  $T > 2.3$  K the decoherence of the  $\text{SiV}^-$  is dominated by the much faster orbital relaxation (red dots and red dashed line). The grey shaded temperature region is inaccessible with the dilution refrigerator used to perform the measurements.

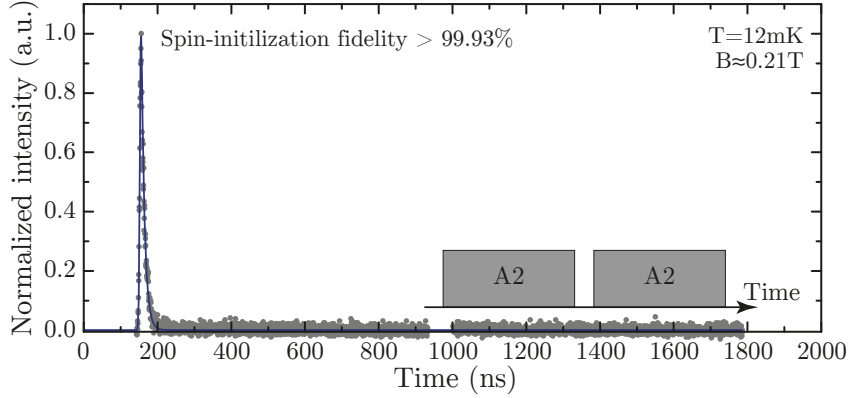


**Figure 4.11: Spin initialization at millikelvin temperatures.** Measurement (grey dots) and exponential fit (blue line) of spin initialization fidelity using optical pumping on the spin flipping transition A2 at 12 mK and  $B \approx 0.4$  T.

excited into a higher vibrational mode by one-phonon absorption and subsequently relaxes into the other spin state by emission of a second phonon) [217, 219] become relevant. This results in a deviation from the linear temperature dependence. For  $T > 2.3$  K the above discussed single-phonon-induced spin flip via thermalization to the second orbital branch then again leads to a linear scaling at higher temperatures [121, 208]. As discussed above, this might also be further suppressed by aligning the magnetic field with the  $\text{SiV}^-$  high symmetry axis to minimize the spin overlap between the individual spin sublevels of the ground state manifold. However, as previously reported in [121, 199, 206], at  $T > 2.3$  K the spin relaxation is not the decoherence determining rate of the system as it is outperformed by the orbital relaxation rate (red dots and lines), which in this region also scales linearly with temperature indicating a single-phonon process but increases steeper than  $T_1^{\text{spin}}$  (The data points at 8.5 K for  $T_1^{\text{spin}}$  as well as 7.5 K and 10 K for  $T_1^{\text{orbit}}$  have been measured using the flow cryostat setup discussed in Sec. 4.2 and have been included in this graph to provide a more complete picture). A more detailed analysis of the spin relaxation processes in the non-linear regime, however, requires additional data at temperatures between 1 K and 3.7 K. Unfortunately, this temperature region is not accessible with the dilution refrigerator used in this work but might be explored in future studies using a recently ordered 1.5 K cryostat.

Due to the very slow  $T_1^{\text{spin}}$  at 12 mK we can achieve a very good initialization fidelity of the spin in the lowest spin level using optical pumping. The corresponding pumping curve is displayed in Fig. 4.11. After a very steep decrease of the fluorescence at the beginning of the initialization pulse caused by pumping the spin from the upper to the lower spin sublevel) no considerable revival of fluorescence has been detected in the rising edge of the 70 ns delayed readout pulse. From the ratio of the first peak to the equilibrium level of the readout pulse we estimate a spin initialization fidelity of at least  $F=99.93\%$ , limited by detector dark counts in this measurement.

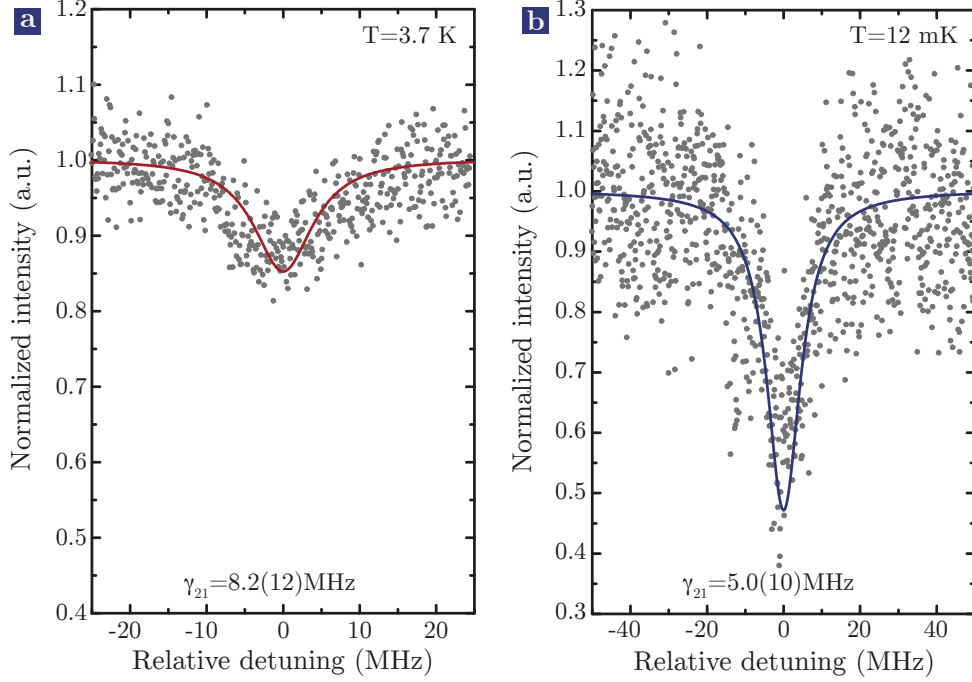


**Figure 4.12: Coherent population trapping in dilution refrigerator.** CPT measurements (grey dots) and simulations using a four-level Master equation model (red and blue lines) for emitter 2 at (a) 3.7 K and (b) 12 mK.

### 4.3.2 Measurement of ground state spin coherence

**Coherent population trapping** After having measured the relaxation rate contributions to the spin decoherence at low temperatures, we now proceed to a direct measurement of the ground state spin coherence time and to do so, we again use CPT. Assuming  $T_2^* = 2T_1^{spin}$  is the time scale of the dominating decoherence process at base temperature we would estimate a CPT dip width of  $\Delta\nu_{CPT} = 1/(2\pi \cdot T_2^*) = 1/(2\pi \cdot 2T_1^{spin}) = 1/(2\pi \cdot 2 \cdot 108\mu s) = 0.74 kHz$  in the absence of any other broadening mechanisms. The measured change in CPT linewidth, however, is much more moderate than expected. In Fig. 4.12(a) and (b) the CPT measurements of emitter 2 at 3.7 K and 12 mK are shown, respectively. Grey dots hereby represent experimental data whereas the red and blue solid lines are simulations using the four-level Master equation model also used to analyse the CPT measurements in the previous section. For the CPT dip at 3.7 K the model indicates a ground state decoherence rate  $\gamma_{2,1}^{3.7K} = 1/2\pi \cdot T_2^* = 8.2(12) MHz$  (cf. model in Chap. 2.2.1). This is significantly larger than what we would expect from only the orbital and spin relaxation processes at these temperatures. Taking only the measured  $T_1$  processes into account, i.e. assuming pure dephasing, the CPT dip width would amount to

$$\frac{1}{2\pi \cdot T_2^*} = \frac{1}{2\pi \cdot 2T_1} = (4\pi \cdot 55.4 ns)^{-1} = 1.44 MHz \quad (4.11)$$

with

$$T_1 = \left( \frac{1}{T_1^{orbit}} + \frac{1}{T_1^{spin}} \right)^{-1} = \left( \frac{1}{69 \text{ ns}} + \frac{1}{303 \text{ ns}} \right)^{-1} = 55.4 \text{ ns} \quad (4.12)$$

The deviation of this value by about 6.8 MHz from the measured ground state decoherence rate already indicates that another mechanism is dominating the spin decoherence in this sample. This decoherence is most likely caused by a spin bath in the environment of the SiV<sup>-</sup>. From the measured ground state decoherence rate we estimate the time scale of this process to be

$$\left( \frac{1}{T_2} + \frac{1}{T_2'} \right)^{-1} = \left( \frac{1}{T_2^*} - \frac{1}{2T_1} \right)^{-1} = \left( \frac{1}{19.4 \text{ ns}} - \frac{1}{2 \cdot 55.4 \text{ ns}} \right)^{-1} = 24 \text{ ns} \quad (4.13)$$

at 3.7 K. When cooling down to 12 mK, the ground state decoherence rate drops to  $\gamma_{1,2}^{12mK} = 5.0(10)$  MHz. While the contrast of the CPT dip significantly increases, the change in the dip width is less apparent. Therefore, in Fig. 4.12(c) we normalized and compared both simulated signals, illustrating the narrowing of the CPT dip at 12 mK. This dip can be fit well with the model by assuming  $T_1 = T_1^{spin} = 108 \mu\text{s}$  (the orbital rate vanishes at these temperatures) and an almost constant contribution of transverse relaxations of  $\left( \frac{1}{T_2} + \frac{1}{T_2'} \right)^{-1} = 32 \text{ ns}$ . We attribute this surprisingly short coherence time at low temperatures as well as the only minor temperature dependence of  $T_2^*$  to a strong resonant interaction with an electron spin bath mainly consisting of  $[N_s^0]$  (also called P1 centres), a common impurity in type IIa diamond [86] which is a S=1/2 system with  $g \approx 2$ .

**Raman-Rabi oscillations, Ramsey interference & Spin echo** In addition to the measurement of the total coherence time  $T_2^*$  a direct measurement of the homogeneous phase coherence time  $T_2$  at millikelvin temperatures can give further insights into the nature and timescales of the involved decoherence mechanisms via the spin bath. This can be accomplished e.g. by a spin echo measurement. Since microwave-based control of the SiV<sup>-</sup> requires high intensity pulses which might lead to a heating of the sample and thus to an alteration of the SiV<sup>-</sup> centre's coherence properties, we here attempt an all-optical echo measurement. To realize this, we first demonstrate two-photon Rabi oscillations between the two ground state spin sublevels using a cw laser and two cascaded Mach-Zehnder-based EOMs. The first EOM is used to modulate a sideband at 5.881 GHz onto the carrier frequency while the second EOM is used to cut pulses out of the bichromatic field (in the following called "Raman pulses"). Since this EOM setup imposes severe limitations to the total optical power, we decided to employ a resonant Raman scheme in which both fields fulfil both one- and two-photon resonance. According to Eq. 2.63 this maximizes the Raman Rabi frequency at the cost of adiabaticity. Thus a small amount of fluorescence, corresponding to a finite population of the excited state, can be observed during the pulses. While this can be further optimized in future experimental setups by using detuned pulses with higher powers (e.g. created by two phase-locked lasers), we here utilize the finite fluorescence (which primarily originates from the cycling transition A1) of the pulses as a direct method to read out the state of the SiV<sup>-</sup>. The following measurements primarily focus on the investigation of the coherence properties of the SiV<sup>-</sup> but, at the same time, demonstrate all-optical coherent control over the SiV<sup>-</sup> ground state spin qubit.

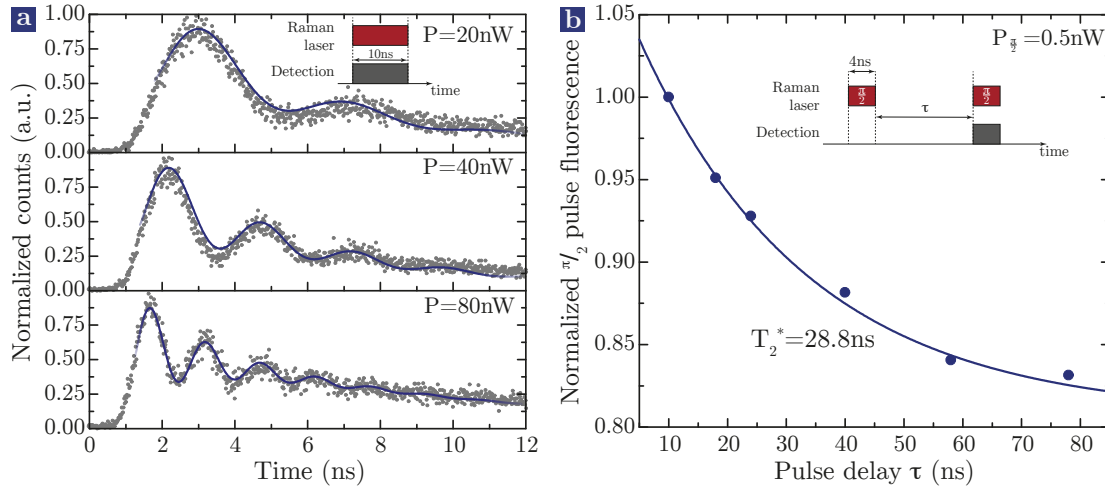


**Figure 4.13: Raman Rabi oscillations & Ramsey interference of the  $\text{SiV}^-$  spin.** (a) All-optical Rabi oscillations and (b) Ramsey interference of the ground state electronic spin of the  $\text{SiV}^-$  using Raman pulses created via sideband modulation of a single cw laser at 12 mK. No one-photon detuning has been employed. Further details are given in the main text.

To verify the coherence of the ground state transfer, we first apply 10 ns pulses with different powers and detect the time-resolved fluorescence during the pulse. The corresponding count rate histograms are shown in Fig. 4.13(a). The presence of Rabi oscillations is clearly evident in the fluorescence traces, confirming coherent rotations. As expected for two-photon oscillations, the Rabi frequency scales roughly linearly with the applied laser power ( $\Omega(20 \text{ nW})=1.54 \text{ MHz}$ ,  $\Omega(40 \text{ nW})=2.48 \text{ MHz}$ ,  $\Omega(80 \text{ nW})=4.13 \text{ MHz}$ ). Moreover, to further verify that the observed Rabi oscillations originate from a two-photon process, the sideband has been detuned away from two-photon resonance by about 100 MHz leading to a rapid disappearance of the Rabi oscillations. The blue solid lines in Fig. 4.13(a) (and in all following figures of this section) represent simulations using the density matrix model discussed in Chap. 2.2.1. Besides a global scaling parameter, only the ratio of the powers of both fields has been used as a free parameter. On the one hand, the model indicates that the damping in the Rabi oscillations is caused by the spin decoherence and on the other hand by a slight non-adiabaticity of the process, i.e. by excitation to and spontaneous emission from the excited state. The non-adiabaticity is caused by two factors: First, an imbalanced driving of the  $\Lambda$ -scheme occurs as the power of the sideband could not be controlled arbitrarily. Secondly, both fields are on one-photon resonance and therefore lead to a finite excited state population. These limitations are of purely technical nature and can be overcome in future experiments. Moreover, since we employed significantly shorter pulses and lower powers in the following measurements, these excitation induced decoherence effects are negligible. Using the smallest possible pulse width of 4 ns we adjusted the pulse amplitude to  $P=0.5 \text{ nW}$  such that a rotation angle of  $\Theta = \pi/2$  per pulse is achieved. With these pulses we performed a Ramsey-interference experiment as it has been introduced in Chap. 2.1.3. The resulting data (dots) and simulation (solid line) are shown in Fig. 4.13(b). Here, due to experimental time constraints only the upper envelope

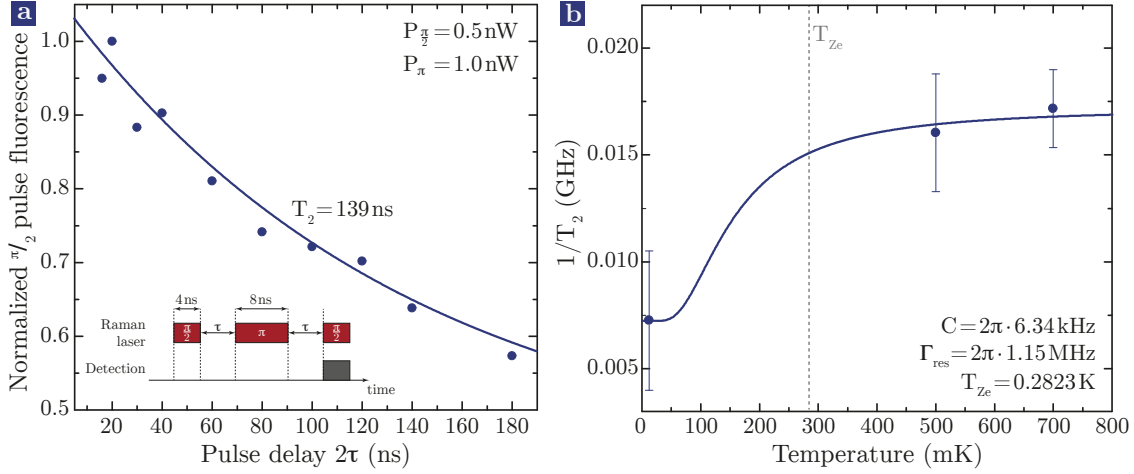


**Figure 4.14: All-optical Spin echo.** (a) Measured decay (dots) and density-matrix simulation (line) of spin-echo amplitude at base temperature of 12 mK. (b) Temperature dependence of  $T_2$ . Dots correspond to measurements and solid line represents model of bath-spin flip-flop rate according to [220, 221].

of the Ramsey signal instead of individual fringes has been measured by fine tuning the temporal spacing of the two  $\pi/2$  pulses to maximize the fluorescence for a number of fixed delays. However, in this context we are mainly interested in the coherence properties of the  $\text{SiV}^-$  and hence a measurement of the envelope decay is sufficient to extract  $T_2^*$ . Individual Ramsey fringes have been resolved in the ultrafast control experiments presented in the following section and can be found in Fig. 4.17. The measured decay time of the Ramsey signal of  $T_2^* = 28.8$  ns again corresponds to the total spin coherence of the  $\text{SiV}^-$  and closely matches the value measured via CPT. This corresponds to a ground state decoherence rate of  $\gamma_{21} = 5.5$  MHz extracted from the theoretical model (blue line) as the only free parameter.

By adding a central  $\pi$ -pulse with twice the length of the  $\pi/2$ -pulses we finally generate a classical spin-echo sequence. The theoretical concept of this echo technique has been introduced in Chap. 2.1.3. In Fig. 4.14(a) the measured (dots) and simulated (line) decay of the echo signal at 12 mK are shown, indicating a phase coherence time of  $T_2 = 139$  ns, about 5 times longer than  $T_2^*$ . This drastic improvement indicates a significant contribution of slow noise induced by the spin bath, the influences of which can be very well rephased by the echo sequence. Moreover, even better values for  $T_2$  might be reached in future experiments by applying dynamic decoupling sequences utilizing multiple  $\pi$ -pulses at short delays [138]. Especially for such techniques the all-optical nature of the scheme presented here in combination with the extraordinarily low power levels are extremely favourable as they minimize thermal effects as opposed to microwave-based control techniques.

While the improvement of  $T_2$  in comparison to  $T_2^*$  is significant, its absolute value is still low in comparison to its ultimate limit of  $2T_1 = 2 \cdot 108 \mu\text{s}$ . For a more detailed analysis of the limiting decoherence processes we performed spin echo measurements at 500 mK and 700 mK showing a significant drop of the phase coherence time to  $T_2 = 62.3$  ns and  $T_2 = 58.2$  ns, respectively. The resulting data is shown in Fig. 4.14(b) and the change in  $T_2$

is very well fit by a model for the probability of flip-flop processes, i.e. energy-conserving exchanges of spin orientations between bath spins which has already successfully been applied to the NV centre [220, 221]. The model is of the form

$$\frac{1}{T_2} = \frac{C}{(1 + \exp(\frac{T_{Ze}}{T}))(1 + \exp(-\frac{T_{Ze}}{T}))} + \Gamma_{res}. \quad (4.14)$$

Here the first factor represents a decoherence rate caused by magnetic field fluctuations created by spin flip-flop processes in a bath. These fluctuations increase with rising temperature due to thermal excitation and decrease with increasing magnetic field strength (here expressed by the Zeeman temperature  $T_{Ze} = g\mu_B B/k_B$ ) as the splitting between the spin levels and therefore the polarization of the bath increases. Hence, for temperatures close to absolute zero or for very high magnetic fields this noise contribution vanishes as all bath spins are in their ground state and thus no flip-flops occur [221]. The second term,  $\Gamma_{res}$ , then accounts for residual decoherence sources other than spin flip-flops. To further understand this large residual rate, we now make a small excursus and take a closer look at the decoherence effects on the intensively investigated NV centre in comparison to the SiV<sup>-</sup>: In the NV the flip-flop processes discussed above are the main source of dephasing, causing  $T_2$  on the order of several  $\mu\text{s}$  at  $T \geq 4\text{ K}$  and approaching several hundreds of  $\mu\text{s}$  for temperatures below 4 K even in nitrogen-rich diamonds. However, in the NV, a second, much more severe, decoherence process can be observed at a specific magnetic field strength of 0.514 T. At this point the  $|m_s = -1\rangle \rightarrow |m_s = 0\rangle$  transition of the NV is tuned into resonance with the  $|m_s = -1/2\rangle \rightarrow |m_s = 1/2\rangle$  transition of the bath. The resulting dipolar magnetic coupling then leads to resonant spin exchange, causing a tremendously enhanced decoherence rate of  $> 4\text{ MHz}$  in type Ib diamond [222]. In the NV this effect is limited to a specific magnetic field strength as the zero field splitting between  $|m_s = \pm 1\rangle$  and  $|m_s = 0\rangle$  and the different g-factor ( $g \neq 2$ ) of the  $|m_s = -1\rangle \rightarrow |m_s = 0\rangle$  transition assures that the system is off-resonant with the bath for all other field strength.

Let us now compare this situation to the one of the SiV<sup>-</sup> centre: In the experiments presented here, the Zeeman temperature amounts to  $T_{Ze} = 5.881\text{ GHz}/k_B = 282\text{ mK}$ . From Fig. 4.14(b) it is evident that, as expected, a significant increase of the decoherence rate for temperatures close to the Zeeman temperature occurs as the rate of flip-flop processes in the bath increases, causing more magnetic field noise. The resulting temperature-dependent flip-flop rate can be well fit with a scaling rate  $C = 2\pi \cdot 6.34\text{ kHz}$ . However, for temperatures much lower than  $T_{Ze}$  the spin echo time saturates at the observed value of  $T_2 = 139\text{ ns}$ , corresponding to a considerable residual dephasing rate of  $\Gamma_{res} = 2\pi \cdot 1.15\text{ MHz}$ , much higher than what has been observed for NV centres. This strong residual dephasing is a direct consequence of the SiV<sup>-</sup> centre's electronic structure. Much like the bath spins, the SiV<sup>-</sup> is a  $S=1/2$  system with a g-factor of  $g \approx 2$ . Therefore, independent of the applied magnetic field, the SiV<sup>-</sup> is always fully resonant with the P1 spin bath and we therefore attribute the severe  $T_2$ -limit persisting down to temperatures as low as 12 mK to a resonant magnetic dipolar coupling to the bath, leading to direct spin flip-flop processes between the SiV<sup>-</sup> spin and the bath spins. This resonant process cannot be counteracted with a spin echo or dynamical decoupling sequence. In the limit of high flip-flop rates (strong

coupling to the bath spins) we can calculate the limit for  $T_2$  according to [223] as

$$T_2 = \frac{1}{4\pi\Delta\omega_d} \quad (4.15)$$

with the so-called dipolar broadening rate

$$\Delta\omega_d = \frac{\mu_0 g^2 \mu_B^2 \rho}{\hbar} \cdot \frac{1}{N} \sum_{k=1}^N \left| \frac{3 \cos(\theta_k)^2 - 1}{2} \right| \quad (4.16)$$

with vacuum permeability  $\mu_0$ , electron g-factor  $g$  ( $g \approx 2$ ), Bohr magneton  $\mu_B$  and spin bath density  $\rho$ . The angle  $\theta_k$  hereby reflects the angle between the external magnetic field and the conduit between the  $\text{SiV}^-$  as well as the  $k$ -th P1 centre in the bath. After integration over all  $\theta_k$  this yields

$$\rho = \frac{9\sqrt{3}\hbar}{4\pi^2 \mu_0 g^2 \mu_B T_2} = \frac{9\sqrt{3}\hbar}{4\pi^2 \mu_0 g^2 \mu_B \cdot 139 \text{ ns}} = 6.8 \cdot 10^{17} \text{ cm}^{-3} \quad (4.17)$$

for the spin bath density, corresponding to a concentration of about 3.8 ppm. This is about one to two orders of magnitude higher than what is expected for high-quality type IIa diamond [86]. However, we would like to clarify that the spin density calculated here is most likely not the average spin density across the entire sample but rather an average local value which, might additionally be experimentally biased for the following reasons: To perform the measurements presented here, exceptionally bright  $\text{SiV}^-$  centres had to be selected. As already mentioned above, our data, as well as additional diamond growth experiments [202] suggest that a correlation between brightness, stability of the  $\text{SiV}^-$  emission and the abundance of electron donors such as  $[\text{N}_s^0]$  is likely. Thus by selecting exceptionally bright emitters we might undeliberately limit our attention to  $\text{SiV}^-$  centres which are located in sample regions with a locally increased spin density, e.g. due to growth inhomogeneities [224]. These local variations also account for the severe difference in coherence times observed for (bright) colour centres in different locations of the sample (e.g.  $T_2^* = 45 \text{ ns}$  for emitter 1 and  $T_2^* = 19.5 \text{ ns}$  for emitter 2 at 3.7 K). This fluctuation is unlikely to arise from variations of  $T_1$ -related phenomena as they mainly depend on the phonon-environment of the diamond host lattice and are thus not expected to vary significantly within a high-quality single crystal diamond plate. Thus, these fluctuations are likely to be caused by local variations in the dipolar coupling of the  $\text{SiV}^-$  centres to their local bath. To further validate this, we attempted measuring the coherence time of a  $\text{SiV}^-$  in an electronic grade diamond sample. This however was not successful as the significantly lower count rates for  $\text{SiV}^-$  centres in these samples prevented any experiments under resonant excitation [58, 225]. Thus we conclude that electron donor impurities like the P1 on the one hand severely affect the spin coherence time of the  $\text{SiV}^-$  but might on the other hand be responsible for the significant fluorescence enhancement observed for  $\text{SiV}^-$  centres examined in type IIa HPHT material compared to centres in the much purer electronic grade CVD diamond. This hypothesis is further supported by another  $\text{SiV}^-$  in identical type IIa HPHT material which we recently used in another work [208]. For this  $\text{SiV}^-$  practically identical  $T_1$  times to the ones obtained here for emitter 2 have been measured

but a spin coherence nicely matching  $T_2^* = 2T_1 = 134(4) \text{ ns}$  has been observed at 3.5 K, suggesting that the SiV<sup>-</sup> is located in a relatively pure region of the sample. Moreover, for this SiV<sup>-</sup> much lower count rates of only about 500 cps under resonant excitation as well as fluorescence blinking have been observed, indicating potential charge state issues. While these count rates were sufficient for the microwave-based experiments presented in [208], they would however not suffice for the experiments presented here. For the sake of completeness, in addition to decoherence induced by the electron spin bath, the sample also contains a nuclear spin bath consisting of <sup>13</sup>C, <sup>14</sup>N, <sup>15</sup>N and possibly other nuclei incorporated during HPHT growth. The contributions of this slow and far-off-resonant bath have been neglected here as they are typically several orders of magnitudes lower compared to the fast decoherence rates discussed here. To further investigate the coherence properties and to engineer SiV<sup>-</sup> samples that show both, high fluorescence intensities as well as decent spin coherence times, a comprehensive diamond growth study exploring different types and concentrations of electron donors and other impurities will be necessary which, however, is beyond the scope of this work. In particular, electron donor systems with  $S \neq 1/2$  need to be identified to avoid the creation of a spin bath resonant with the SiV<sup>-</sup>. For this, substitutional oxygen and sulfur defects might be interesting candidates which recently have both been identified as potential donor systems in diamond with  $S=1$  using density functional theory [226, 227].

To conclude this section we would now like to summarize the main results from the experiments at millikelvin temperatures:

- For the first time, we here successfully investigated single SiV<sup>-</sup> centres at temperatures as low as 12 mK using a home-built confocal microscope insert designed to operate in a dilution refrigerator.
- The measurements reveal a substantial increase in spin relaxation time  $T_1^{spin}$  from 303 ns at 3.7 K to 108  $\mu$ s at 12 mK. A phonon-assisted direct spin flip has been identified as the limiting process at temperatures below  $\approx 500 \text{ mK}$  whereas a multi-phonon process plays an increasing role at temperatures between 500 mK and 2.3 K. At even higher temperatures a single-phonon process including thermalization to the upper orbital ground state level then determines the spin relaxation. The long spin relaxation time also facilitates a high spin initialization fidelity of at least 99.93% at 12 mK.
- The increase in spin coherence for low temperatures by about 40% is less drastic. We attribute this moderate change to a significant contribution of an almost temperature-independent spin dephasing process on a time scale  $(\frac{1}{T_2} + \frac{1}{T_2'})^{-1} = 24 \text{ ns}$  at 3.7 K and  $(\frac{1}{T_2} + \frac{1}{T_2'})^{-1} = 32 \text{ ns}$  at 12 mK. Using all-optical Raman-based spin echo measurements we identified two decoherence processes limiting the phase coherence: First, a temperature- and magnetic field-dependent flip-flop process of the bath spins causing magnetic field noise. Secondly, a temperature- and field-independent resonant coupling of the SiV<sup>-</sup> to the P1 bath. Especially this last process is detrimental to the SiV<sup>-</sup> spin coherence as it can neither be suppressed by changing the temperature or magnetic field nor by applying dynamic decoupling sequences and can only be reduced by lowering the spin bath density in future samples.

## 4.4 Ultrafast all-optical coherent control

The previous sections focused on investigating the coherence properties of the  $\text{SiV}^-$  at liquid helium and millikelvin temperatures. These investigations indicate a fundamental limit of the coherence time of about  $2T_1=140$  ns at 4 K. In current samples, even lower values below 50 ns have been found to persist down to temperatures of 12 mK, presumably due to coupling to a strong spin bath. While this might be overcome in future devices by careful sample engineering, even in the limit of such short coherence times the  $\text{SiV}^-$  still is a very interesting candidate for QIP applications due to its unique electronic properties. In this section we will thus go one important step further and focus on manipulating the state of the  $\text{SiV}^-$  to deliberately prepare arbitrary quantum superpositions. As we have seen in the introduction, the relevant benchmark of a quantum system to be useful for (local) QIP applications is the number of possible state rotations per coherence time interval rather than the total coherence time. Thus, if the system can be manipulated fast enough, short coherence times are tolerable. The  $\text{SiV}^-$  is an ideal candidate for such ultrafast control schemes for two reasons: First, already at zero magnetic field, the  $\text{SiV}^-$  offers four narrow optical transitions forming two optically accessible  $\Lambda$ -schemes between the two orbital ground state levels and the lower and upper orbital excited state level, respectively. Moreover, this optical accessibility also extends to the spin degree of freedom (depending on the magnetic field angle) as the counter-play of internal and external quantization axes allows for driving of spin-flipping transitions. This optical controllability enables a spatially selective manipulation of individual sites in multi-qubit systems (a laser can e.g. be very well focused onto a specific qubit) without addressing qubits in the vicinity. Secondly, the large splitting between the orbital branches of the  $\text{SiV}^-$  allows for the use of extremely short, and thus broadband, laser pulses while minimizing unwanted cross-excitations of electronic states. This brings the speed-up advantage over microwave-based techniques which usually rely on pulses of at least nanosecond duration. These two features enable ultrafast all-optical control of the quantum state of  $\text{SiV}^-$  centres. Note that we recently also demonstrated full coherent control of the  $\text{SiV}^-$  electronic spin using microwave-based methods, which however shall not form a part of this thesis [208]. As using the spin degree of freedom of the  $\text{SiV}^-$  in current samples brings no significant advantage, we restricted ourselves to controlling its orbital state in the following experiments. This, on the one hand, eliminates the need for an external magnetic field (which was not available in Saarbrücken at the time of the experiments) and thus simplifies technological implementation, on the other hand it allows utilizing the large orbital level splitting and thus the application of very short pulses (48 GHz  $\approx$  9 ps). However, we would like to note that an extension of the experiments presented in the following to the magnetic sublevels using the very same techniques is easily possible.

We will divide this section into three main parts. First, we will demonstrate full coherent control of the  $\text{SiV}^-$  orbital state via Rabi oscillations and Ramsey interference using optical pulses resonant with one of the four optical ZPL transitions (Sec. 4.4.1). In Sec. 4.4.2, we then also utilize the observed one-photon Rabi oscillations in conjunction with finite difference time domain (FDTD) simulations to calculate the transition dipole moment and quantum efficiency of the  $\text{SiV}^-$ . Finally, to harness the full coherence time of the  $\text{SiV}^-$  we demonstrate an off-resonant Raman-based control of the centre's ground state in Sec. 4.4.3.

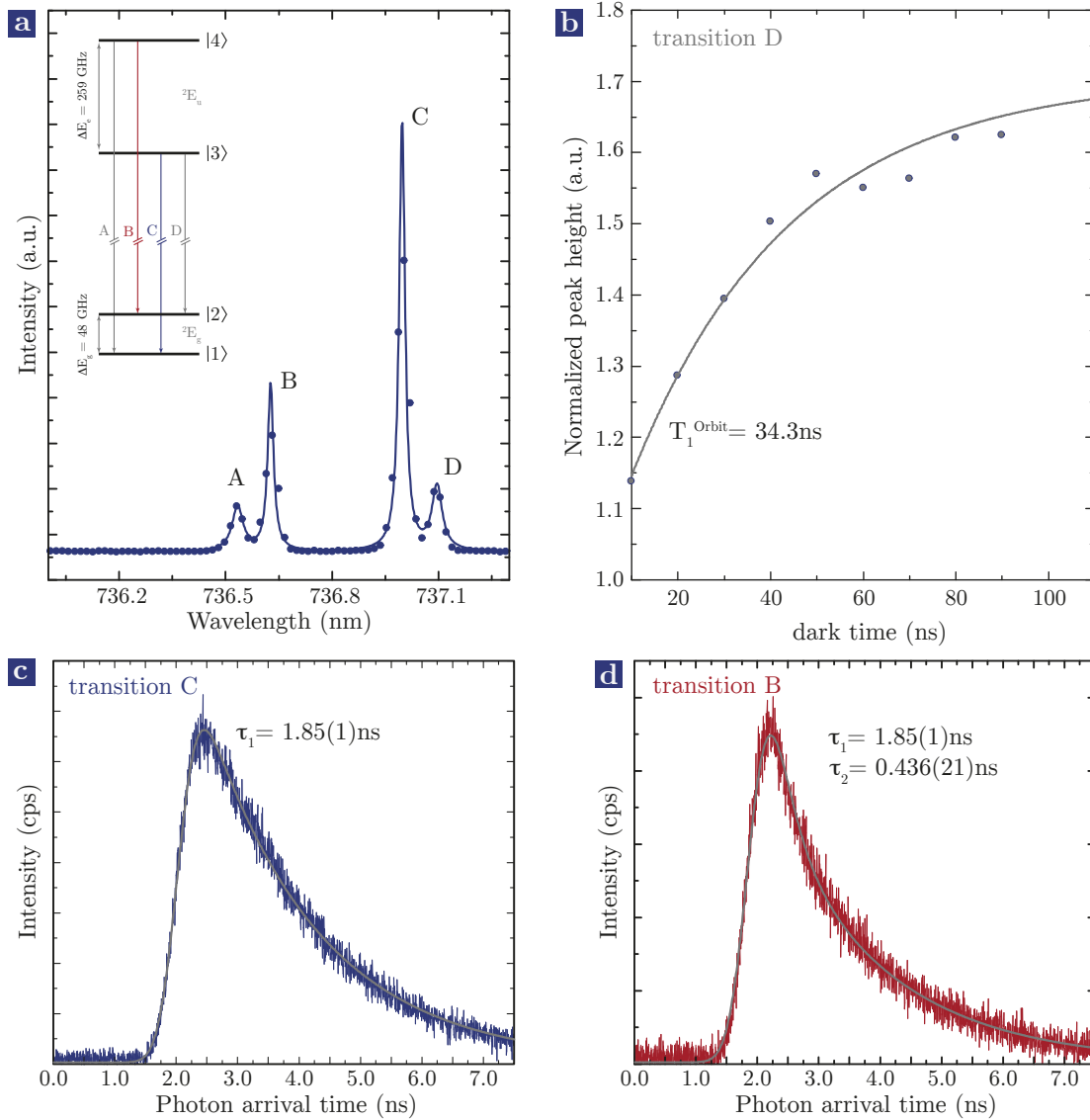


**Figure 4.15: Fluorescence spectrum, TCSPC and orbital relaxation of emitter 2.** (a) Fluorescence spectrum of emitter 2 at 5 K under non-resonant excitation at 690 nm (blue dots) and simulation with group theoretical model (blue solid line). The inset shows the SiV<sup>-</sup> level structure at 0 T. (b) Measurement of ground state orbital relaxation time  $T_1^{\text{Orbit}}$  (grey dots) using the optical pumping on transition D and exponential fit (grey solid line). The scheme is discussed above. (c), (d) TCSPC measurements on C and B (blue and red), respectively using resonant excitation of these levels. The grey lines are a fit with a single-exponential convoluted with a Gaussian instrument response function (IRF) in (c) and a bi-exponential decay convoluted with the IRF in (d).

Before we discuss the results of these control experiments we will briefly discuss a number of additional characterization measurements carried out for emitter 2. These measurements have been used to determine all the internal rates within the four-level orbital fine structure and have been used in the model presented in Chap. 2.3 to simulate all of the Rabi oscillation and Ramsey interference experiments discussed below. In Fig. 4.15(a) a fluorescence spectrum of emitter 2 under non-resonant excitation is shown (blue dots: measurement, solid line: group theoretical model). The inset again shows the level scheme for the  $\text{SiV}^-$  at zero field and we here use the terminology A, B, C, D for the four optical transitions between the orbital states  $|1\rangle$ ,  $|2\rangle$ ,  $|3\rangle$ ,  $|4\rangle$  for the states in ascending order of energy. From the model we determine the relative transition strengths  $\eta$  of the four transitions, corrected by the out-coupling efficiency of the respective dipoles (transitions A, D correspond to the XY-dipole of the  $\text{SiV}^-$  whereas B, C originate from the z-dipole) calculated using a numerical algorithm discussed in [126], revealing a ratio of 1:0.4 for the Z- compared to the XY-dipole 500 nm below a (flat) diamond surface. From this we obtain  $\eta_A : \eta_B : \eta_C : \eta_D = 0.19 : 0.4 : 1 : 0.6$  for the individual transition strengths. Note that in the (111) sample transition A and D are only weakly observed in the spectrum as the XY-dipole is almost aligned with the optical axis, although their real transition strength is much larger. In Fig. 4.15(b) a measurement of the ground state thermalization rate  $T_1^{\text{orbit}} = 34.3 \text{ ns}$  is shown. This has been measured using the same optical pumping sequence as discussed in the previous section on transition D. The obtained value at about 5 K is consistent with what has been measured at 3.7 K ( $T_1^{\text{orbit}} = 69 \text{ ns}$ ), indicating a temperature mismatch between actual and measured temperature of about 2.5 K (as  $1/T_1^{\text{orbit}}$  scales linearly in this temperature range) [121]. Moreover, to measure the excited state decay and thermalization rates we performed time-correlated single photon counting (TCSPC) measurements under resonant excitation of transition C (Fig. 4.15(c)) and transition B (Fig. 4.15(d)) using 12 ps laser pulses. The obtained histogram for transition C can be very well fit by a single exponential decay with time constant  $\tau_1 = 1.85(1) \text{ ns}$  convoluted with a Gaussian instrument response function with a width of 357(3) ps, nicely matching the timing jitter of the detectors. The same measurement on transition B shows that a single exponential decay does not suffice to achieve a good fit of the histogram but a second exponential with a short time constant  $\tau_2 = 0.436(21) \text{ ns}$  has to be included. We attribute this fast process to the decay of the upper into the lower excited state. This fast branching has also been observed for the spin-dependent fluorescence observed in [125]. With these excited state lifetimes and the relative transition strengths from above we can thus calculate the individual rates

$$\Gamma_{31} = \frac{\eta_C}{\eta_C + \eta_D} \cdot \frac{1}{\tau_1} = \frac{1}{1 + 0.6} \cdot \frac{1}{1.85 \text{ ns}} = 338 \text{ MHz} \quad (4.18)$$

$$\Gamma_{32} = \frac{\eta_D}{\eta_C + \eta_D} \cdot \frac{1}{\tau_1} = \frac{0.6}{1 + 0.6} \cdot \frac{1}{1.85 \text{ ns}} = 203 \text{ MHz} \quad (4.19)$$

$$\Gamma_{41} = \frac{\eta_A}{\eta_A + \eta_B} \cdot \frac{1}{\tau_1} = \frac{0.19}{0.19 + 0.4} \cdot \frac{1}{1.85 \text{ ns}} = 174 \text{ MHz} \quad (4.20)$$

$$\Gamma_{42} = \frac{\eta_C}{\eta_C + \eta_D} \cdot \frac{1}{\tau_1} = \frac{0.19}{0.19 + 0.4} \cdot \frac{1}{1.85 \text{ ns}} = 366 \text{ MHz} \quad (4.21)$$

for the optical transitions. Moreover, we can calculate the thermalization and relaxation rates within the ground and excited state manifolds according to

$$\Gamma_{43} = \frac{1}{\tau_2} = \frac{1}{0.436 \text{ ns}} = 2.29 \text{ GHz} \quad (4.22)$$

$$\Gamma_{34} = \Gamma_{43} \cdot \exp\left(-\frac{259 \text{ GHz}}{20.83 \frac{\text{GHz}}{\text{K}} \cdot 5 \text{ K}}\right) = 0.19 \text{ GHz} \quad (4.23)$$

for the excited states and

$$\Gamma_{12} = \frac{1}{\tau_2} = \frac{1}{34.3 \text{ ns}} = 29.2 \text{ MHz} \quad (4.24)$$

$$\Gamma_{21} = \Gamma_{43} \cdot \exp\left(\frac{48 \text{ GHz}}{20.83 \frac{\text{GHz}}{\text{K}} \cdot 5 \text{ K}}\right) = 46.3 \text{ MHz} \quad (4.25)$$

for the ground states. We use these rates to simulate all of the following experimental results in the resonant as well as the Raman-based control experiments which we will now discuss further.

#### 4.4.1 Resonant coherent control

**Rabi oscillations** To realise a universal single-qubit gate it is necessary to rotate the state vector of the qubit around two different axes of the Bloch sphere. Rotation around a horizontal x or y axis is usually achieved by driving Rabi oscillations while the rotation around the vertical z axis is achieved by utilizing a Ramsey interference sequence. Further theoretical details on these methods can be found in Chap. 2. In this first series of control experiments we construct the qubit basis out of an orbital ground and excited state of the SiV<sup>-</sup> and control the qubit via the resonant optical transition linking both states. This type of control can be considered as the ultimate speed test as in this scheme the control does not only need to be faster than the ground state decoherence but also faster than the decoherence of the excited state. In Fig. 4.16(a) and (b) the measured one-photon Rabi oscillations for the transitions C and B are shown, respectively. In this measurement we used 12 ps long resonant pulses, obtained by filtering a 1 ps long fundamental pulse using monolithic Fabry P erot etalons (the etalon characteristics are given in appendix B). The excited state population of the SiV<sup>-</sup> has been read out via detecting the fluorescence on the PSB. Diamond background fluorescence, mainly caused by the FIB milling process, has been subtracted from both curves and the slight upwards slope in both measurements is caused by residual background. A plot of the PSB fluorescence against the square root of average laser power, which is proportional to the Rabi frequency  $\Omega$ , reveals Rabi oscillations for both transitions with contrasts exceeding 90% (red and blue dots). We attribute the minor deformation of the curve in Fig. 4.16(b) around  $2\pi$  to a marginal drift of the cryostat, slightly changing the alignment and thus the effective Rabi frequency. We observe coherent rotations of up to  $\Theta=6\pi$  for transition B and even  $\Theta=10\pi$  for transition C, both solely limited by the available laser power (approximately  $100\mu\text{W}$ , after etalon filtering ( $\sim 1\%$  transmission) and setup losses). In this representation the Rabi frequency increases for higher laser powers (as the pulse length stays constant). We therefore achieve a maximum

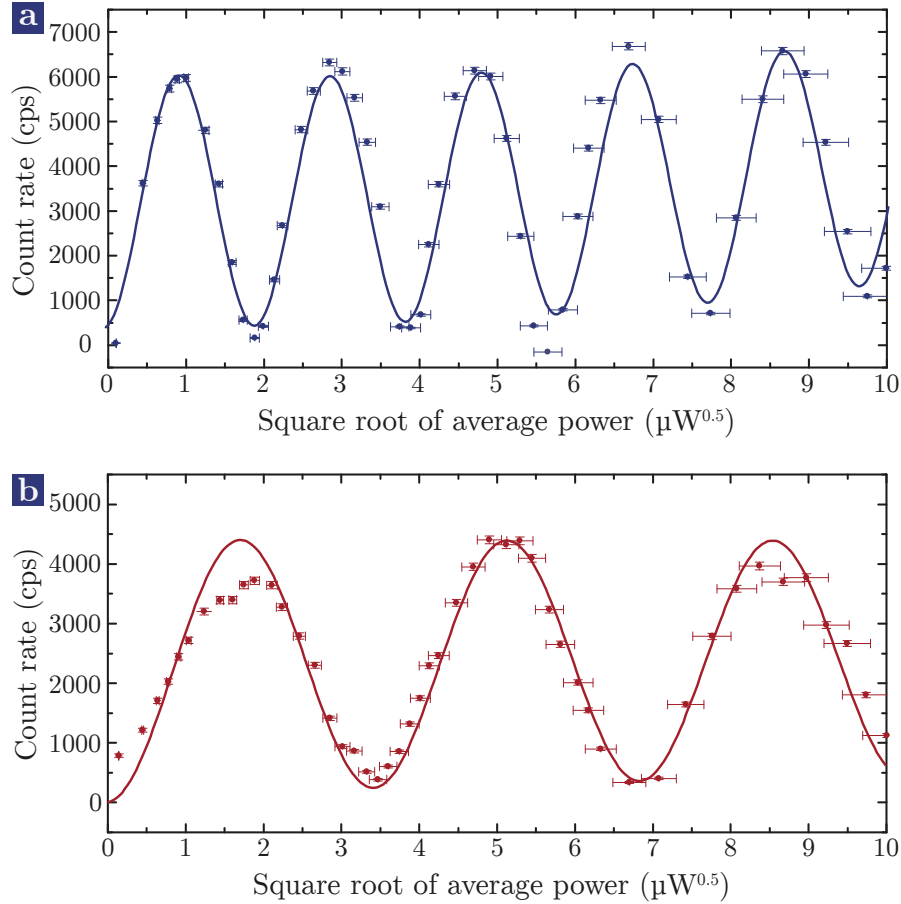


**Figure 4.16: Optical one-photon Rabi oscillations.** Measured PSB photon count rate (red and blue dots) as a function of average laser power (after subtraction of fluorescence background caused by the FIB milling process) for picosecond laser pulses resonant with (a) transition C between the lower ground and excited state and (b) transition B between the upper ground and excited state. The pulse length was set to 12 ps ( $\sim 20$  GHz) using a monolithic Fabry P rot etalon. x-errors (standard deviations): measured relative laser power stability, y-errors (standard deviations): Poisson-distributed count rate errors  $\sqrt{N}$ . Both data sets are modelled using a four-level Master equation model (solid lines). Further details are given in the main text.

Rabi frequency of  $\Omega_B = \frac{6\pi}{12\text{ps}} = 1.57\text{ THz}$  for transition B and even  $\Omega_C = \frac{10\pi}{12\text{ps}} = 2.62\text{ THz}$  for transition C, emphasizing the high control speed. Furthermore, no sign of damping can be observed in both curves, even at high rotation angles. This indicates that on the time scale of the pulse length no ultrafast decoherence processes such as photoionization take place as it is e.g. observed for the NV centre [60]. Because for the SiV<sup>-</sup> no state detection technique like e.g. shelving to a long-lived metastable state as it is done in trapped ions [228] has been implemented so far, we estimate the  $\pi$ -pulse fidelity from the simulation using the Master equation model. The blue and red solid lines in Fig. 4.16(a) and (b) show the simulated Rabi oscillations. To obtain these curves only the above calculated rates and no other free parameters other than a simple scaling factor have been used and the resulting Rabi oscillations closely match the measured data points. From this simulation we estimate a  $\pi$ -pulse fidelity of at least 95%. Our model indicates that this is limited by a slight cross-excitation of the neighbouring optical transitions with the tails of the optical pulse and can be avoided in future experiments by using slightly narrower pulses.

**Ramsey interference** To rotate the qubit state around a second axis we utilize a Ramsey interference pulse sequence in which we exploit the natural Larmor precession of the state during a defined free evolution time in between two  $\pi/2$ -pulses. The respective powers of the  $\pi/2$ -pulses have been determined from the above Rabi curves and amount to  $P_{\pi/2}^C = 0.16\mu\text{W}$  and  $P_{\pi/2}^B = 0.24\mu\text{W}$ . The resulting measured upper and lower envelopes of the Ramsey interference curves for transitions C (blue dots) and B (red dots) are shown in Fig. 4.17(a). Because the resonance frequency of the optical transition is about 406.8 THz, the interference pattern oscillates with a period of about 2.4 fs and therefore individual fringes have only been measured for a short delay interval (inset in Fig. 4.17(a)). However, by fine-tuning the temporal spacing of the pulses for a number of fixed delays, the maximum and minimum count rate at each fixed delay point and thus the upper and lower envelopes of the Ramsey curves have been measured. The exponential decays of the fringe amplitudes are shown in Fig. 4.17(b). The time constants of these decays represent the excited state coherence times. Using transition C, a coherence time of  $T_2^* = 1044\text{ ps}$  for the lower excited state  $|3\rangle$  has been obtained. The solid lines in both figures again represent density matrix simulations and the model indicates two main processes for the amplitude decay: First, the spontaneous decay of  $|3\rangle$  into the ground states as well as some thermalization into  $|4\rangle$  are responsible for the majority of the observed decoherence. Secondly, our model indicates that about  $\gamma/2\pi = 160\text{ MHz}$  of pure dephasing have to be added to make the decay fit and we attribute this to phonon broadening, most likely caused by a slight heating of the sample with the laser pulses. For the upper excited state  $|4\rangle$  a much shorter coherence time  $T_2^* = 398\text{ ps}$  has been measured, caused by the very fast decay into the lower excited state.

#### 4.4.2 Transition dipole moments & quantum efficiency

In addition to its purpose in controlling the qubit state we can also utilize the one-photon Rabi oscillation to calculate the quantum efficiency  $\Phi$  and the transition dipole moment  $\mu$  for the bulk SiV<sup>-</sup>. To do so, we calculate the electric field at the coordinates of the emitter:

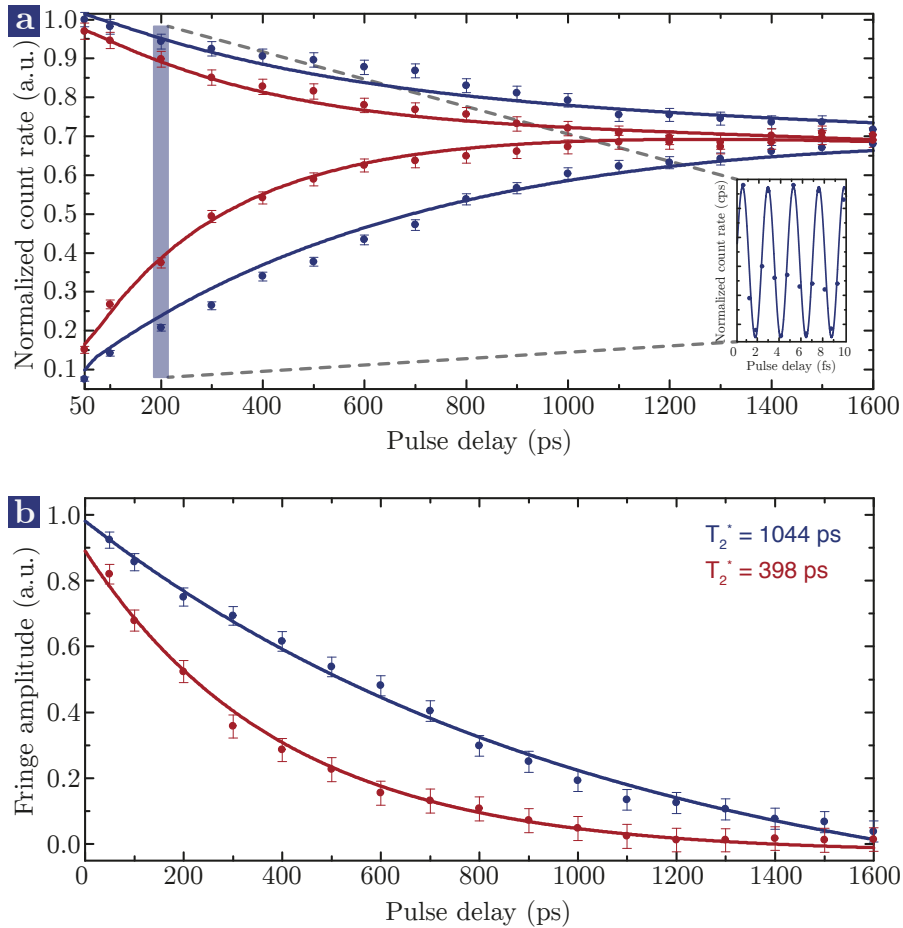


**Figure 4.17: Resonant Ramsey interference.** By applying a sequence of two subsequent  $\pi/2$ -pulses with variable delay, Ramsey interference fringes can be observed. In (a) the measured upper and lower envelopes of the interference pattern for transition C (blue dots) and B (red dots) are shown together with the simulated envelopes using a four-level Master equation model (blue and red lines). The inset shows a series of individual Ramsey fringes. The measured (dots) and simulated (lines) decays of the interference fringe amplitudes for both transitions is depicted in (b). x-errors (standard deviations): measured relative laser power stability, y-errors (standard deviations): Poisson-distributed count rate errors  $\sqrt{N}$ .

Starting from a beam with a Gaussian spatial distribution

$$I(r) = P_0 \frac{1}{2\pi\sigma_r^2} e^{-\frac{r^2}{2\sigma_r^2}} \quad (4.26)$$

with  $\sigma_r = \frac{d_{focus}}{2\sqrt{2\ln(2)}}$ , focal diameter  $d_{focus}$  and average beam power  $P_0$ . By assuming that, after careful alignment of the setup, the emitter is centred in the focal spot this simplifies to

$$I(r=0) = \frac{P_0}{2\pi\sigma_r^2} \quad (4.27)$$

and with this expression we can write

$$\begin{aligned} \int E(t)dt &= \sqrt{\frac{P_0\tau TS^2}{\pi\epsilon_0 cn\sigma_r^2} \int_{-\infty}^{\infty} e^{-\frac{2\ln(2)}{w_{pulse}}|t|} dt} \\ &= \sqrt{\frac{P_0\tau TS^2}{\pi\epsilon_0 cn\sigma_r^2} 2 \int_0^{\infty} e^{-\frac{2\ln(2)}{w_{pulse}}t} dt} = \sqrt{\frac{P_0\tau TS^2 w_{pulse}}{\pi\epsilon_0 cn\sigma_r^2 \ln(2)}} \end{aligned} \quad (4.28)$$

for the time-integrated electric field of a single excitation pulse with repetition rate  $\tau$  and pulse width  $w_{pulse}$ , assuming a two-sided exponential temporal intensity distribution after filtering by the monolithic Fabry-Pérot etalons for pulse length adjustment [229]. In this expression we additionally introduce a measured correction factor  $T=0.68$  that includes the limited transmission of the microscope objective and cryostat window as well as the back reflection of light at the diamond surface. This value has been measured by determining the back reflected laser power behind the confocal beam splitter. Moreover, as the equations above assume a spherical focal spot we introduce an additional correction factor  $S$ , correcting for the increased elongation of the focal spot in diamond compared to air. This elongation as well as the focal spot diameter have been extracted from finite difference time domain (FDTD) simulations. In Fig. 4.18(a) the normalized electric field distribution for a Gaussian beam with a diameter of 3 mm (corresponding to the beam diameter in the setup) focused by a N.A. 0.9 objective lens in air is shown. The resulting focal spot shows only a small elongation and a focal spot diameter of about  $d_{focus}^{air}=893(2)$  nm (FWHM). In contrast to this, Fig. 4.18(b) shows the same beam focused through a diamond/air interface. In this case, we obtain a lateral focus diameter of about  $d_{focus}^{diam}=862(3)$  nm (FWHM). Additionally, a significant axial elongation occurs, caused by spherical aberration due to refractive index mismatch [230]. This results in a noticeable drop in maximum electric field strength in the centre of the focal spot compared to the focus in air. To take this axial distortion into account we therefore use the ratio  $S=0.57$  of the electric field values in the centres of the focal spots in diamond and air as an additional correction factor. From the Rabi curve in Fig. 4.16(a) we extract a  $\pi$ -pulse power of  $P_{\pi}^C=817(16)$  nW and with Eq. 4.28 we can then calculate the respective transition dipole moment:

$$\mu_C = \frac{\pi\hbar}{\int E(t)dt} = 14.3 \text{ Debye} \quad (4.29)$$

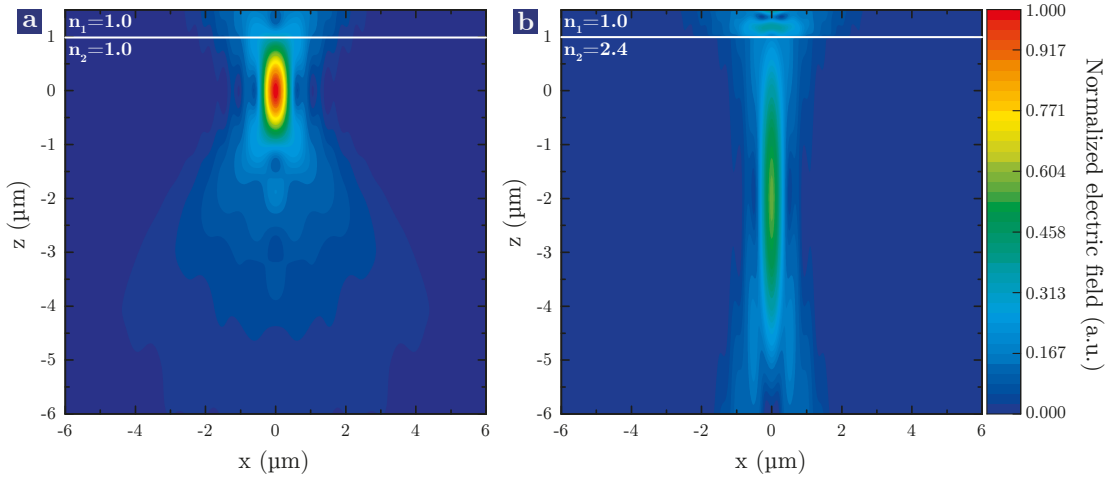


**Figure 4.18: Simulated laser foci in air and diamond.** (a) FDTD simulation of the electric field of a Gaussian beam focused by a N.A. 0.9 objective in air. (b) FDTD simulation of the same Gaussian beam focused through an air/diamond interface. While the focus diameters do not significantly differ in both cases, spherical aberration leads to an axial elongation of the focus in diamond (simulations performed in collaboration with P. Fuchs).

Using the definition of the Einstein coefficient  $A_{21}$  for spontaneous emission [231]

$$A_{21} = \frac{8\pi^2\nu^3}{3\epsilon_0\hbar c^3} \cdot \mu^2 \quad (4.30)$$

we can then calculate the natural lifetime  $\tau_0$  of the system which amounts to

$$\tau_0 = \frac{1}{A_{21}} = 6.24 \text{ ns}. \quad (4.31)$$

By comparing this lifetime to the fluorescence lifetime measured via TCSPC discussed above we can then obtain the quantum efficiency of the system which amounts to

$$\Phi = \frac{\tau_1}{\tau_0} = \frac{1.85 \text{ ns}}{5.4 \text{ ns}} = 29.6\%. \quad (4.32)$$

This value is in good agreement with theoretical and experimental quantum efficiencies previously reported by Riedrich-Möller *et al.* [232]. In there, quantum efficiencies between 15% and 67% have been reported for SiV<sup>-</sup> centres in bulk diamond. Moreover, quantum efficiencies below 10% have been reported for SiV<sup>-</sup> centres in nanodiamonds [126]. Taking the reduced photonic density of states in nanodiamonds into account, these values are consistent with the values reported here and by Riedrich-Möller *et al.* for bulk SiV<sup>-</sup> centres. We would like to note that the value of  $\Phi$  determined here can be considered a lower bound as this calculation e.g. assumes a perfect focus and an ideal placement of the emitter inside the focal spot. In reality, a slightly defocused beam or a deformation of the focal spot due to surface geometry and roughness might lead to an additional reduction of the electric field strength at the position of the emitter and thus to a higher actual quantum efficiency

than the one estimated here. While the most significant error source is the exact size and shape of the focus, which is not accessible experimentally, we can try to estimate the error as follows: The power fluctuations of the pulsed laser have been measured to be on the order of 2% leading to  $P_{\pi}^C = 817(16)$  nW. These fluctuations induce a certain fluctuation in the fluorescence count rate. Centring the emitter in the focal spot by optimizing the count rate is therefore obscured by these power fluctuations. From these fluctuations we estimate a positioning error of about  $\pm 75$  nm from the focal spot centre and an error of  $\mu_C = 14.3(2)$  Debye and  $\Phi = 29.6(7)\%$  for the transition dipole moment and quantum efficiency, respectively.

### 4.4.3 Raman-based ground state control

While control of the qubit presented in Sec. 4.4.1 is easily achieved by utilizing the ZPL transitions, its usefulness for QIP applications is limited due to its inherently short coherence time. Even in the absence of any other additional decoherence processes, the coherence time of this qubit is limited by the lifetime of the excited state of the SiV<sup>-</sup> as every superposition contains an excited state contribution. Therefore, to harness the full coherence time scale of the SiV<sup>-</sup>, a qubit solely consisting of ground state levels is desirable. In the SiV<sup>-</sup>, even at zero magnetic field, such a qubit can be controlled optically by driving a  $\Lambda$ -scheme between the two orbital ground state levels and a common excited state using ultrafast laser pulses. To minimize unwanted population of the excited states, the fields used to control the qubit are detuned from one-photon resonance while still maintaining two-photon resonance and the control thus is achieved via a Raman interaction. To further enhance the control speed we here realized a so-called sub-cycle control scheme (faster than one optical cycle of the system) by simultaneously driving both arms of the  $\Lambda$ -system using a single 1 ps pulse, red-detuned by  $\Delta = 500$  GHz from the lower excited state (red), as depicted in Fig. 4.19(a). Additionally, to initialize the qubit and to read out its state after the Raman-based state rotation, we employ 200 ns long optical pumping pulses on transition D (yellow). Pumping this transition initializes the qubit into the lowest ground state  $|1\rangle$ . The fundamental pulse sequence used in the following experiments is shown in Fig. 4.19(b). This figure also shows two fluorescence traces (blue) obtained with (top) and without (middle) a Raman-pulse in between the two resonant initialization and readout pulses. The rising edge peak of the first pulse in both traces indicates the qubit initialization into the lower state by optically pumping population of  $|2\rangle$  from an initial value of 37% (thermal equilibrium at 5 K) down to an equilibrium value defined by the ratio of the pump rate and thermalization rate between both ground states. If no Raman-pulse is present (middle trace), thermalization leads to a small but finite rising edge peak in the readout pulse as the population in  $|2\rangle$  slowly starts to increase again. On the contrary, if a Raman-pulse is applied the rising edge peak in the readout pulse is significantly enhanced as population has been transferred via the Raman process. In contrast to optical excitation followed by spontaneous emission, this process is coherent and thus can be used to control the ground state qubit. In unstrained SiV<sup>-</sup> centres such as emitter 2, the inner transitions B and C are linearly polarized while A and D are elliptical [58]. For maximum transfer efficiency in the Raman process the driving strengths of the fields in both arms of the  $\Lambda$ -scheme have to be equalized. We achieve this by rotating

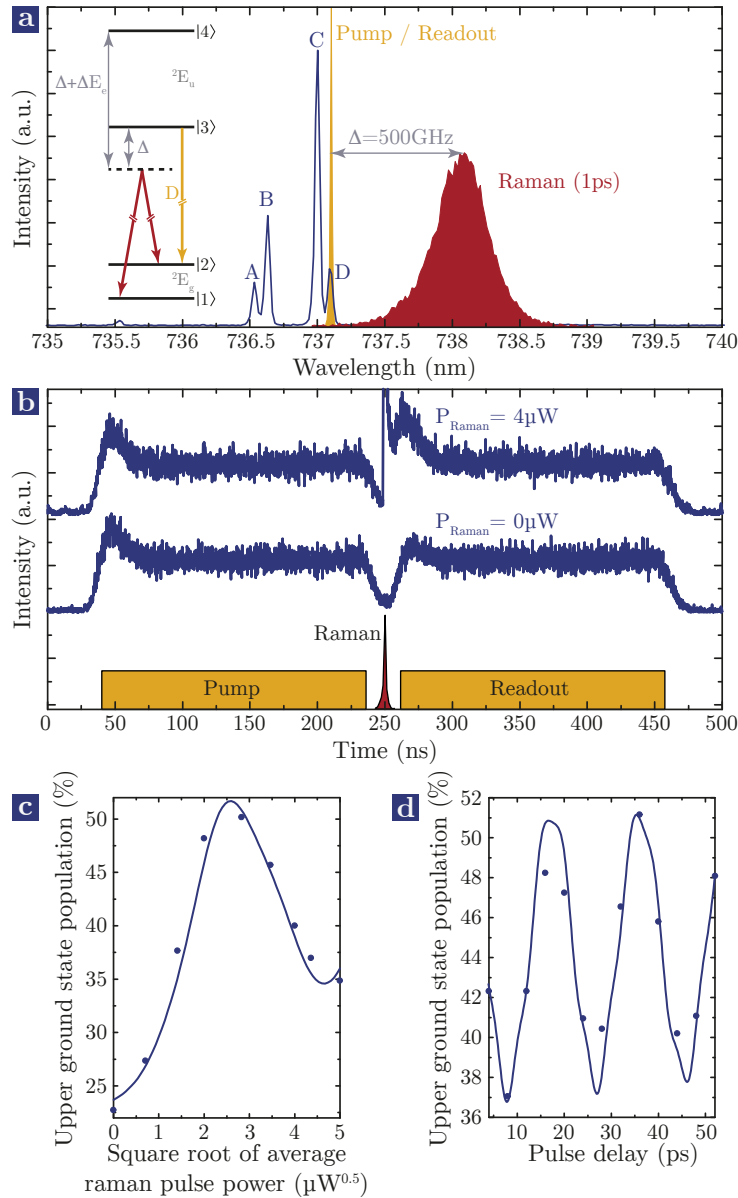


**Figure 4.19: Raman-based population transfer between ground states.** (a) Fluorescence spectrum and level scheme indicating spectral positions of lasers relative to  $\text{SiV}^-$  transitions. (b) Schematic pulse sequence (bottom) and measured fluorescence response (top) for the Raman beam switched off as well as  $P_{\text{Raman}} = 4 \mu\text{W}$  (1 MHz repetition rate). (c) Normalized upper ground state population as a function of the average Raman beam power. (d) Ramsey interference generated by two subsequent Raman pulses verifying coherent transfer. Solid lines are simulations using the four-level density matrix model with the relative driving strength of both Raman transitions as the only free parameter. The model indicates that the ratio of the driving strengths of transitions C and D in the Raman beam is about 1:0.7 after polarization optimization.

the pulse polarization. However, using a single Raman pulse makes this a challenging task. At the optimized polarization, the population in the upper ground state is measured for varying Raman pulse areas and the resulting data (blue dots) is depicted in Fig. 4.19(c). A two-photon Rabi oscillation with rotation angles of  $\Theta \approx 2\pi$  is evident in the data with the angle being solely limited by the available laser power. We again complement the data by a simulation with our four-level density matrix model, using the above discussed experimentally determined rates and the relative driving strength of the two arms of the  $\Lambda$ -system as the only free parameter. The data is fit well by the model indicating a ratio of 1:0.7 for the driving strengths of both arms detuned from C and D, respectively. Moreover, as the SiV<sup>-</sup> is a double- $\Lambda$ -system, transfer can also occur via the second  $\Lambda$ -scheme including the upper excited state  $|4\rangle$ . The Raman Rabi frequency  $\Omega_R$  of a  $\Lambda$ -system generally is given by

$$\Omega_R = \frac{\Omega_1 \Omega_2}{2\Delta} \quad (4.33)$$

with the two one-photon Rabi frequencies  $\Omega_{1,2}$  and the one-photon detuning  $\Delta$  [233]. Using this expression and the above mentioned relative transitions strengths of the four optical transitions we can estimate the ratio of the Raman Rabi frequencies of both transfer pathways according to

$$\frac{\Omega_{R1}}{\Omega_{R2}} = \frac{\frac{\Omega_C \Omega_D}{2\Delta}}{\frac{\Omega_A \Omega_B}{2(\Delta + \Delta E_e)}} = \frac{\frac{1.0 \cdot 0.6}{2 \cdot 500 \text{ GHz}}}{\frac{0.19 \cdot 0.4}{2(500 + 259 \text{ GHz})}} \approx 27 \quad (4.34)$$

To be more precise, the effects of both transfer paths do not simply add up but path interference depending on the relative phase  $\Delta\phi$  of both coupling fields can occur in such a double- $\Lambda$ -system. The total Raman Rabi frequency is then given by [152]

$$\Omega_R = \sqrt{\Omega_{R1}^2 + \Omega_{R2}^2 + 2\Omega_{R1}\Omega_{R2} \cdot \cos(\Delta\phi)}. \quad (4.35)$$

However, in the experiments presented here we used a single broadband coupling field excluding the possibility for  $\Delta\phi \neq 0$ . Under this assumption both pathways add up. We included this coupling to the second excited state into our model and investigated its effect on the two-photon Rabi oscillations. The resulting simulated oscillations without (blue) and with (red) the second  $\Lambda$ -system included is shown in Fig. 4.20(a). While the frequencies of both oscillations are essentially identical, an additional damping can be observed in the red curve. However, the model indicates that this effect is not caused by additional decoherence introduced by the presence of the second transfer pathway. Instead it is rather caused by populating the excited state  $|4\rangle$  due to resonant excitation with the high energy tail of the broad Raman pulse as we have to assume this excitation in the model to reproduce the data. The very same effect is what causes the apparent decrease in visibility for larger rotation angles and can be remedied in future experiments using narrower pulses which however requires a modification of the current laser system. In addition to the influence of the Raman pulse we also theoretically analysed the optical pumping process by fitting the measured fluorescence curves during the pump pulses with the model. The resulting data (red), simulated fluorescence curve (blue, right y axis) and resulting population of the upper ground state (green, left y axis) are displayed in Fig. 4.20(b).

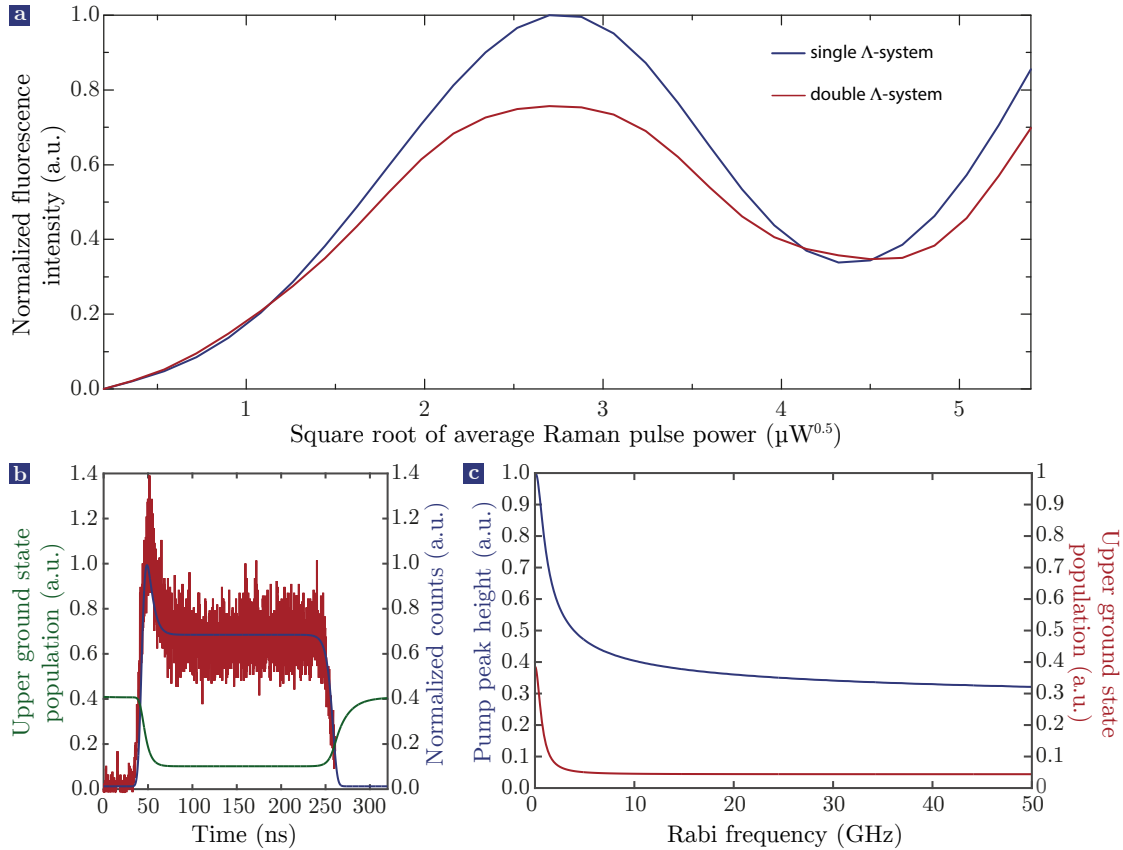


**Figure 4.20: Simulations of optical pumping efficiency and influence of double- $\Lambda$ -system.** (a) Simulations of Raman-Rabi-oscillations assuming a single  $\Lambda$ -system consisting of levels  $|1\rangle$ ,  $|2\rangle$  and  $|3\rangle$  (blue) and a double- $\Lambda$ -type scheme including the  $|1\rangle$ ,  $|2\rangle$ ,  $|3\rangle$  as well as  $|1\rangle$ ,  $|2\rangle$ ,  $|4\rangle$  subsystems (red). (b) Simulated (blue, right y-axis) and measured (red) pump pulse fluorescence as well as relative population in upper ground state (green, left y-axis). (c) Simulated pump pulse contrast (difference between rising edge peak and equilibrium value, blue, left y-axis) and upper ground state population (red, right y-axis) for different pump pulse Rabi frequencies.

During the pumping process, the population very quickly decays from its initial value of about 40% down to an equilibrium value of 10.5%, close to the theoretical minimum of  $\frac{\tau_1}{T_{1\text{orbit}}} = \frac{1.85\text{ ns}}{34.3\text{ ns}} = 5.5\%$ . Moreover, in Fig. 4.20(c) we also investigated the relation between the ground state population (red, right y axis) and the resulting fluorescence peak value in the rising edge peak of the pump pulse (blue, left y axis) for different Rabi frequencies i.e. pump powers. From these curves it is apparent that, while the population rapidly drops already with moderate powers, the fluorescence level decreases more slowly making a direct conversion of count rate into ground state population without the use of a proper model challenging. Due to the limited rise and fall time of the AOM used in the experiment to cut the pump and readout pulses from the cw laser, a minimum delay of about 15 ns had to be used between the end of the pump and the Raman pulse. During this period of time the population in the upper ground state increases rapidly due to thermalization from  $|1\rangle$  to  $|2\rangle$  and reaches a value of 22% when the Raman pulse is applied, limiting the Raman pulse fidelity. The limited initialization fidelity, in combination with the unequal driving strengths in both arms of the  $\Lambda$ -system and the about 30% reduction in fidelity due to resonant excitation, limits the  $\pi$ -pulse fidelity in this experiment to about 30%. Finally, to realize a universal gate using the two orbital ground states we demonstrate SU(2) control by realizing a Raman Ramsey interference experiment. To do so, we keep the pump and readout sequence unchanged but apply a series of two subsequent Raman  $\pi/2$  pulses with a variable delay in between both resonant pump/readout pulses. The resulting curve is shown in Fig. 4.19(d) indicating an interference fringe pattern (blue dots) with a frequency of about 48 GHz matching the ground state splitting. The data is again nicely fit by the theoretical model without any additional free parameters. The model also correctly predicts the slight distortions of the interference pattern which is again caused by resonant background processes. Moreover, the minima in the Ramsey curve do not reach the optically pumped minimum of 22%, indicating that a finite amount of incoherent transfer occurs [234]. This can be further improved in future experiments by further optimizing Raman pulse parameters such as width, shape detuning, polarization or frequency chirp. Also the initialization via optical pumping can be further improved by using faster modulators so that the delay between pump and Raman pulses can be reduced as well as working at lower temperatures to slow down ground state thermalization. This will be possible in the future using a recently ordered 1.5 K cryostat. Furthermore, more complex transfer schemes utilizing separate rotation fields for both arms of the  $\Lambda$ -system might be explored in future experiments. This gives more flexibility on the pulse parameters of the individual fields and thus allows for a more accurate optimization of the relative transition strengths. An additional time delay between the pulses in each arm might be introduced to optimize the adiabaticity of the transfer process [148]. Some of these improvements have already been realized in later experiments using colour centre ensembles which will be discussed in the following chapter.

To conclude this section we would now like to summarize the key results of the resonant and Raman-based coherent control experiments:

- For the first time, we here demonstrated coherent control of the orbital degree of freedom of a single SiV<sup>-</sup> solely relying on ultrafast optical fields.

- We realized resonant control of a qubit based on a ground and an excited state level of the  $\text{SiV}^-$  via Rabi oscillations and Ramsey interference using 12 ps laser pulses. Furthermore, from the Rabi curves we determined a transition dipole moment of  $\mu_C=14.3 \text{ D}$  and a quantum efficiency of  $\Phi=29.6\%$  for transition C.
- Finally, to utilize the full ground state coherence time of the  $\text{SiV}^-$ , we demonstrated full sub-cycle control of a qubit based solely on  $\text{SiV}^-$  ground state levels using a single 1 ps long off-resonant Raman control pulse to realize two-photon Rabi oscillations as well as Raman Ramsey interference.



## Chapter 5

# Experimental results II: ensembles of SiV<sup>-</sup> centres

*The experiments in this chapter have been designed and performed by Jonas Nils Becker (J.N.B.), Johannes Görlitz (J.G., as part of his Master's thesis) and Christian Weinzettl (C.W., University of Oxford) with advice from Prof. Christoph Becher (C.B.), Dr. Joshua Nunn (J.N., University of Oxford) and Dr. Eilon Poem (E.P., University of Oxford). The experiments have been carried out in the labs of C.B. at Saarland University. Initial theoretical work on achievable memory efficiencies and storage times has been performed by J.N.B. and E.P. during a research visit of J.N.B. to Prof. Ian Walmsley's (I.W.) group at the University of Oxford. To model the results of the experiments, a density matrix model for the ensemble has been developed by J.N.B., J.G. and C.W. based on the initial code of J.N.B. for single emitters which has been used in the previous chapter.*

While the previous chapter focused on the coherence properties and control of single  $\text{SiV}^-$  centres, we now will also investigate ensembles of emitters. The high optical densities of such ensembles allow for strong light-matter interactions (the coupling strength of an ensemble of  $N$  emitters scales as  $\sqrt{N}$ ) and thus enables the realization of e.g. single photon switches [235] or optical quantum memories [236], while we here focus on the latter one. For example, optical quantum memories allow for the storage of quantum information encoded in photons by converting them to a collective ground state excitation of the ensemble. This excitation can later be read out on demand by converting it back into the original photons. Ensembles of  $\text{SiV}^-$  centres possess a number of favourable properties for the realization of such a memory. Coherent control of ensembles, especially in the solid state, is a very challenging task due to inhomogeneous broadening caused by locally varying crystal environments. As the Rabi frequency of an individual emitter depends on the detuning, such a broadening thus leads to a distribution of Rabi frequencies and e.g. Rabi oscillations of the ensemble are quickly averaged out [237]. While inhomogeneous broadening also occurs in  $\text{SiV}^-$  ensembles, its magnitude is moderate compared to many other solid state systems such as rare-earth ions or quantum dots. This is because the inversion symmetry of the  $\text{SiV}^-$  renders it relatively insensitive against first-order Stark and strain shifts. Therefore, ensembles with inhomogeneous linewidths well below the fine structure splitting of the  $\text{SiV}^-$  can be fabricated relatively easily permitting addressing of individual optical transitions in the ensemble and thus enabling a multitude of coherent control techniques. The second strength of the  $\text{SiV}^-$  for memory applications arises from its wide ground state splitting of 48 GHz. In a Raman-based memory protocol the bandwidth of the memory is solely limited by this ground state splitting and therefore the  $\text{SiV}^-$  offers a platform to store extremely short photons. The realization of such a broadband memory, especially in conjunction with a solid-state platform, is a very desirable feature for high-speed QIP applications but is rarely possible in most other quantum systems due to narrow energy level splittings.

The experiments presented here are intended to form the foundation to realize such a quantum memory based on an ensemble of  $\text{SiV}^-$  centres. Therefore, before taking a look at the experimental results we will first discuss the fundamental working principle of such a memory based on the theoretical framework established in Chap. 2.

## 5.1 Concept of a Raman quantum memory

**Memory scheme** We here plan to implement a memory based on off-resonant Raman transitions as it has been theoretically proposed in [238] and experimentally demonstrated in caesium vapours [239]. The scheme is based on the concept of Raman transitions discussed in Sec. 2.2.2 and consists of three stages: First, the ensemble is optically pumped into one of its ground states by applying a resonant laser (Fig. 5.1(a)). Secondly, the single photon we intend to store (green wavy arrow) with Rabi frequency  $\Omega_s$  is applied off-resonantly together with a strong control field (red solid arrow) of Rabi frequency  $\Omega_c$  in a  $\Lambda$ -type configuration, both fulfilling a two-photon resonance condition (Fig. 5.1(b)). Under these conditions, a single photon is converted into a coherent collective excitation

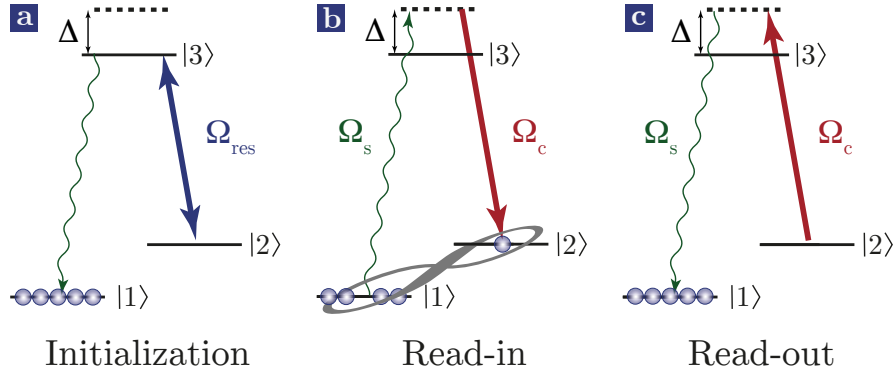


**Figure 5.1: Raman quantum memory.** (a) First the ensemble is optically pumped into state  $|1\rangle$  using a resonant pump  $\Omega_{res}$ . (b) The single photon  $\Omega_s$  is then read in using a two-photon transition aided by a strong control field  $\Omega_p$ . The grey "double loop" symbolises the formation of a coherent collective excitation. (c) The read-out is performed by again applying  $\Omega_p$  which converts the collective ensemble excitation back into the single photon.

of the ensemble of the form

$$|s\rangle = \frac{1}{\sqrt{N}} \sum_i^N c_i |1_1 1_2 \dots 2_i \dots 1_N\rangle \quad (5.1)$$

with the complex phase and amplitude factors  $c_i$  [240]. This  $N$ -particle Dicke state is also called a *spin wave* due to some similarities to the formalism used to describe the propagation of disturbances in magnetic materials. If the control field is applied a second time while a spin wave is in the memory, the excitation is converted back via the reversed read-in process (Fig. 5.1(c)). For large one-photon detunings  $\Delta$  this scheme is robust against inhomogeneous broadening and thus ideally suited for solid state systems. Moreover, as both arms of the  $\Lambda$ -scheme have to be addressed separately, the bandwidth in this protocol is effectively limited by the ground state splitting  $\Delta E_g$  of the ensemble (for  $\Delta > \Delta E_g$ ). Hence the use of spin sublevels requires relatively large magnetic fields to achieve wide Zeeman splittings and high memory bandwidths. Since no such magnet was available in Saarbrücken at the time of the experiments, in the following we again restricted ourselves to the use of orbital levels. However, we would like to stress that all of the experiments presented below can also be performed using spin sublevels. Before we discuss the achieved experimental results, we will now first perform a brief theoretical analysis of two of the key parameters of a Raman-based quantum memory based on currently available SiV<sup>-</sup> ensembles, namely its storage efficiency and storage time. This treatment largely follows the theoretical description of a similar memory proposed for NV centres by Poem *et al.* *et al.* [241] and utilizes the formalism for the electronic structure of the SiV<sup>-</sup> as well as its interplay with crystal strain derived by Hepp *et al.* [58]:

**Storage efficiency** The memory efficiency of a Raman-based memory is proportional to the square of the relative Raman coupling strength  $\mathfrak{R}^2$  which can be written as

$$\mathfrak{R} = \sqrt{\frac{n_d \rho \epsilon_c}{\epsilon_0^2 h c}} \frac{\pi^2 L}{A} R_{fi}^{\beta\alpha} \quad (5.2)$$

with refractive index of diamond  $n_d$ , vacuum permittivity  $\epsilon_0$ , Planck's constant  $h$  and speed of light  $c$ . Furthermore,  $\rho$  is the volume density of SiV<sup>-</sup> centres in the sample,  $\epsilon_c$  is the control pulse energy and  $L$  and  $A$  are length and area of the storage medium, respectively. To calculate the Raman coupling

$$R_{fi}^{\beta\alpha} = \sum_k \frac{d_{kf}^{\beta*} d_{ki}^{\alpha}}{\Delta_k} \quad (5.3)$$

of the two ground states  $|f\rangle$  and  $|i\rangle$  which are coupled via several excited states  $|k\rangle$  by two laser modes  $\alpha$  and  $\beta$  (with one-photon detuning  $\Delta_k$ ), we have to calculate the dipole matrix elements [242]

$$d_{ki}^{\alpha} = \langle k|d|i\rangle \quad (5.4)$$

with the dipole operator  $d = e \cdot r$  and  $r$  being the position operator. To do so, we need to diagonalize the Hamiltonian  $H$  of the SiV<sup>-</sup> as given in Chap. 1.2.4 and [58] including SO and JT interactions:

$$H = H_{SO} + H_{JT} = \frac{\lambda_{g,e}}{2} \begin{pmatrix} 0 & 0 & -i & 0 \\ 0 & 0 & 0 & i \\ i & 0 & 0 & 0 \\ 0 & -i & 0 & 0 \end{pmatrix} \quad (5.5)$$

$$+ \frac{\Upsilon_{xg,e}}{2} \begin{pmatrix} 1 & 0 & 0 & 0 \\ 0 & 1 & 0 & 0 \\ 0 & 0 & -1 & 0 \\ 0 & 0 & 0 & -1 \end{pmatrix} + \frac{\Upsilon_{yg,e}}{2} \begin{pmatrix} 0 & 0 & 1 & 0 \\ 0 & 0 & 0 & 1 \\ 1 & 0 & 0 & 0 \\ 0 & 1 & 0 & 0 \end{pmatrix}. \quad (5.6)$$

Moreover, to estimate the coupling strength we assume a transition dipole moment of  $\mu = 14.3$  Debye calculated in the previous chapter, a SiV<sup>-</sup> density of  $\rho_{SiV} = 10^{13} \text{cm}^{-3}$ , a length  $L=300\text{nm}$  and area  $A=0.336\mu\text{m}^2$  of the ensemble as well as a control pulse energy of  $\epsilon_c = 0.1nJ$ . For a cross-polarized signal and control field and for a blue-detuning of about  $\Delta = 100$  GHz from the upper excited state, this for example yields

$$\mathfrak{R} = 0.7 \quad (5.7)$$

for the coupling strength. While the exact calculation of the memory efficiency is complex and can for example be found in [243], a value of  $\mathfrak{R} = 1$  hereby corresponds to a read-in efficiency of 50% and thus a total memory efficiency of 25% [238, 241]. For  $\mathfrak{R} \gg 1$  the efficiency eventually saturates at unity. With the values calculated here we thus estimate a read-in efficiency slightly below 50%. This is high enough to provide a measurable signal for first proof-of-principle memory demonstrations. This value is entirely limited by the estimated optical density of the Sternschulte ensemble sample, which has not been

specifically designed for this type of experiment. The exact density of  $\text{SiV}^-$  in the ensemble is not known and not easily experimentally accessible. We here estimated the density based on the achieved fluorescence count rates in comparison with implanted ensembles in which the  $\text{SiV}^-$  concentration is roughly known. The estimated density of  $\rho_{\text{SiV}} = 10^{13} \text{cm}^{-3}$  is not very high and together with the short length of the ensemble significantly limits the efficiency. However, considering the Sternschulte ensemble has not been optimized for applications in quantum memories the efficiency estimated here already underlines the potential of the  $\text{SiV}^-$  for high-efficiency memories. Since e.g. ensembles of NV centres have successfully been created with much higher densities of  $10^{17}$ - $10^{18} \text{cm}^{-3}$  we believe that the fabrication of  $\text{SiV}^-$  ensembles with improved densities and thicknesses is feasible. Using such an ensemble, theoretical efficiencies of  $\eta = \mathfrak{R}^2 = 1$  are achievable. Later on we will briefly investigate a recently obtained ensemble sample, the Element Six ensemble, which offers a significantly larger  $\text{SiV}^-$  density compared to the Sternschulte ensemble while showing identical inhomogeneous broadenings. This demonstrates the potential for the fabrication of future ensemble samples via optimized growth processes with even more advanced spectral properties.

**Storage time** In the previous chapter the ground state coherence time of single  $\text{SiV}^-$  centres in bulk diamond at 4 K has been determined to be on the order of 45 ns, most likely limited by phonon-mediated processes. While this imposes a fundamental limit to the storage time of an  $\text{SiV}^-$  memory at liquid helium temperatures, the orbital coherence of the ensemble will be further limited by its inhomogeneous broadening caused by static random crystal strain. More precisely, to estimate the storage time we have to estimate the inhomogeneous broadening of the two-photon transition between both ground states. To theoretically estimate this from the broadening of the optical transitions (which can be obtained from PLE measurements) we first calculate the eigenenergies of the system based on the total Hamiltonian  $H = H_{SO} + H_{JT} + H_S$  including the strain Hamiltonian  $H_S$  which, according to [58], for the  $\text{SiV}^-$  can be written as

$$\mathcal{H}_S = \epsilon_{g,e} e_x + \epsilon_{g,e} e_y \quad (5.8)$$

for the ground and excited states, respectively (neglecting  $A_1$ -symmetric terms which only lead to a global energy shift). From this, we obtain the eigenenergies of the two ground states

$$\varepsilon_{1,2} = \pm \sqrt{\frac{\lambda_g^2}{4} + (\Upsilon_{x,g} + \epsilon_g e_x)^2 + (\Upsilon_{y,g} + \epsilon_g e_y)^2} \quad (5.9)$$

The corresponding two-photon transition  $S$  between the ground states can therefore be expressed as

$$S = \varepsilon_2 - \varepsilon_1 = 2 \sqrt{\frac{\lambda_g^2}{4} + (\Upsilon_{x,g} + \epsilon_g e_x)^2 + (\Upsilon_{y,g} + \epsilon_g e_y)^2} \quad (5.10)$$

By performing a Gaussian error propagation up to the second order we can then calculate the width of the distribution  $\delta S$  of two-photon transition frequencies with respect to a

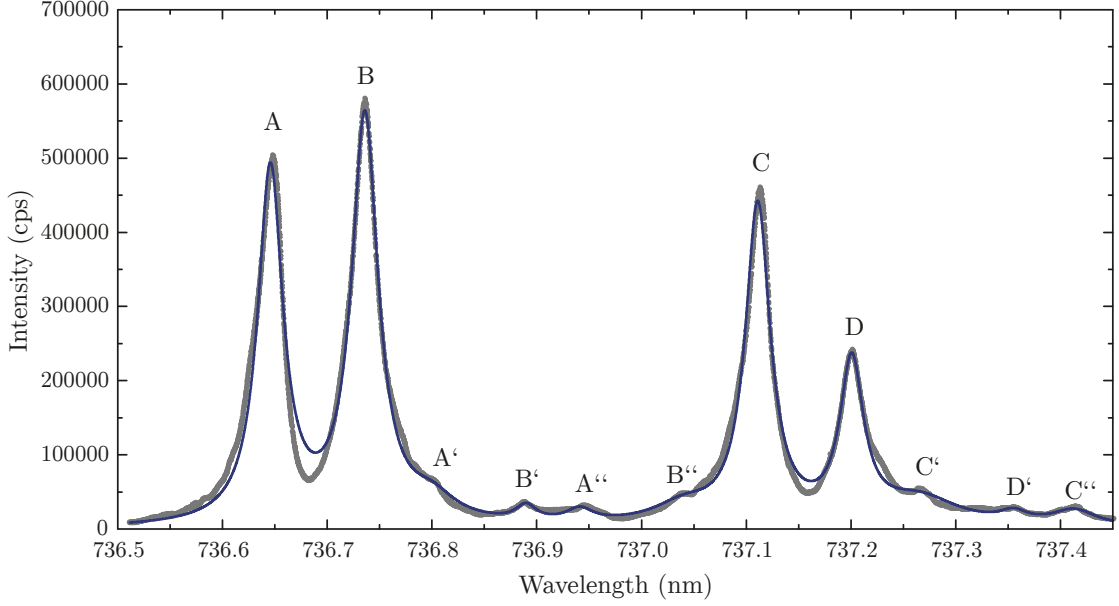


**Figure 5.2: Ensemble PLE measurement.** A PLE scan across the entire ZPL spectral region of the Sternschulte ensemble is shown. Fluorescence is detected on the PSB. The lines A, B, C, D belong to  $^{28}\text{Si}$  while the lines A', B', C', D' correspond to  $^{29}\text{Si}$  and A'', B'', C'' to  $^{30}\text{Si}$ , respectively (line D'' was out of range).

strain distribution  $\delta e_{x,y}$ . Assuming  $\delta e_x = \delta e_y = \delta e$  we obtain

$$\delta S^2 = \left( \frac{4\epsilon_g \Upsilon_{x,g} \delta e + \epsilon_g^2 \delta e^2}{\sqrt{\Upsilon_{x,g}^2 + \Upsilon_{y,g}^2 + \frac{\lambda_g^2}{4}}} - \frac{\epsilon_g^2 \Upsilon_{x,g}^2 \delta e^2}{(\Upsilon_{x,g}^2 + \Upsilon_{y,g}^2 + \frac{\lambda_g^2}{4})^{\frac{3}{2}}} \right)^2 \quad (5.11)$$

$$+ \left( \frac{4\epsilon_g \Upsilon_{y,g} \delta e + \epsilon_g^2 \delta e^2}{\sqrt{\Upsilon_{x,g}^2 + \Upsilon_{y,g}^2 + \frac{\lambda_g^2}{4}}} - \frac{\epsilon_g^2 \Upsilon_{y,g}^2 \delta e^2}{(\Upsilon_{x,g}^2 + \Upsilon_{y,g}^2 + \frac{\lambda_g^2}{4})^{\frac{3}{2}}} \right)^2 \quad (5.12)$$

for the variance of the distribution of two-photon transitions. Finally, we can relate the width of the strain distribution  $\delta e$  to the optical line width  $\delta \varepsilon = \frac{\delta \nu}{2\sqrt{2\ln(2)}}$  ( $\delta \nu$  being the FWHM of the optical line e.g. measured via PLE) via  $\delta e = \frac{\delta \varepsilon}{\epsilon_e}$  (with the excited state strain energy  $\epsilon_e$ ). Neglecting small Jahn-Teller contributions ( $\Upsilon_{x,y} = 0$ ) and defining  $\kappa = \frac{\epsilon_g}{\epsilon_e}$  as the ratio of the ground and excited state strain energies. These parameters have been determined to  $\epsilon_g = 484 \text{ GHz/GPa}$  and  $\epsilon_e = 630 \text{ GHz/GPa}$  in [58] by fitting strain-dependent SiV<sup>-</sup> spectra from [62] with a group theoretical model. Using this expression we find

$$\delta S = 2\sqrt{2}\kappa^2 \frac{\delta \varepsilon^2}{S_g} \quad (5.13)$$

for the relation between the optical line broadening and the two-photon broadening. The parameter  $S_g$  hereby represents the ground state splitting of the ensemble. To determine the optical linewidth we performed a PLE scan across the ZPL transitions of the ensemble

which is displayed in Fig. 5.2. The ensemble has been grown using a Si source with a natural isotope distribution and therefore optical lines of all three stable Si isotopes with intensity ratios matching the isotope abundances are visible in the spectrum. The lines A, B, C, D hereby belong to  $^{28}\text{Si}$ , the lines A', B', C', D' to  $^{29}\text{Si}$  and A'', B'', C'' to  $^{30}\text{Si}$  (line D'' was out of range). From this PLE we obtain an average standard deviation of linewidths of  $\delta\varepsilon \approx 10\text{ GHz}/2\sqrt{2\ln(2)} \approx 4.25\text{ GHz}$  and a ground state splitting of  $S_g = 48\text{ GHz}$  for the Sternschulte ensemble. This results in a standard deviation of the two-photon broadening of

$$\delta S = 2\sqrt{2}\kappa^2 \frac{\delta\varepsilon^2}{S_g} = 2\sqrt{2} \cdot 0.77^2 \frac{(4.25\text{ GHz})^2}{48\text{ GHz}} = 0.63\text{ GHz} \quad (5.14)$$

and a corresponding FWHM of  $2\sqrt{2\ln(2)} \cdot \delta S = 1.48\text{ GHz}$ . This value is in good agreement with CPT measurements performed on this ensemble presented in [211], directly probing the ground state coherence and revealing a width of about 1.6 GHz. The expected storage time then amounts to

$$\tau_S = \frac{1}{2\pi \cdot 1.48\text{ GHz}} \approx 100\text{ ps}. \quad (5.15)$$

Due to the still relatively large inhomogeneous broadening in this particular sample, the expected storage time is too short for technological applications and might even render the read-out of stored photons challenging. However, the experiment presented here are intended to be a proof-of-principle for the coherent manipulation of  $\text{SiV}^-$  ensembles. We believe the inhomogeneous broadening of these ensembles can be reduced significantly in future samples specifically designed for memory applications as inhomogeneous distributions with  $\delta\nu = 300\text{--}400\text{ MHz}$  have already been reported for less dense samples [59]. Furthermore, we tried fitting the lines in Fig. 5.2 using a Voigt function to determine possible contributions of Gaussian line shapes which would be a sign for time-dependent spectral diffusion processes. However, no such contribution could be identified and each line is very well fit with a single Lorentzian only. Therefore, the inhomogeneous broadening is solely caused by a temporally invariant perturbation. This means that, in principle, its effects on the decoherence of the ensemble can be reversed using Hahn echo techniques, a possibility which we will explore in the following section.

## 5.2 Ultrafast Ramsey interference and Hahn echo

As an initial experiment demonstrating coherent manipulation of a dense ensemble using pulsed optical fields we performed a resonant Ramsey interference measurement in analogy to the one presented for single emitters in Chap. 2.3 using 12 ps long laser pulses on transition C between the lowest orbital ground and excited states. We perform this measurement for several reasons: First, it offers the possibility to determine whether the available pulse powers are high enough to manipulate dense ensembles. Secondly, the resonant Ramsey interference is a relatively robust measurement and we use it to determine the excited state coherence times of the ensemble as well as to validate the four-level ensemble OBE model described in Chap. 2.3. Thirdly, the Ramsey interference forms the basis for more complex echo experiments performed later on. The red dots in Fig. 5.3(a) and (b) display the

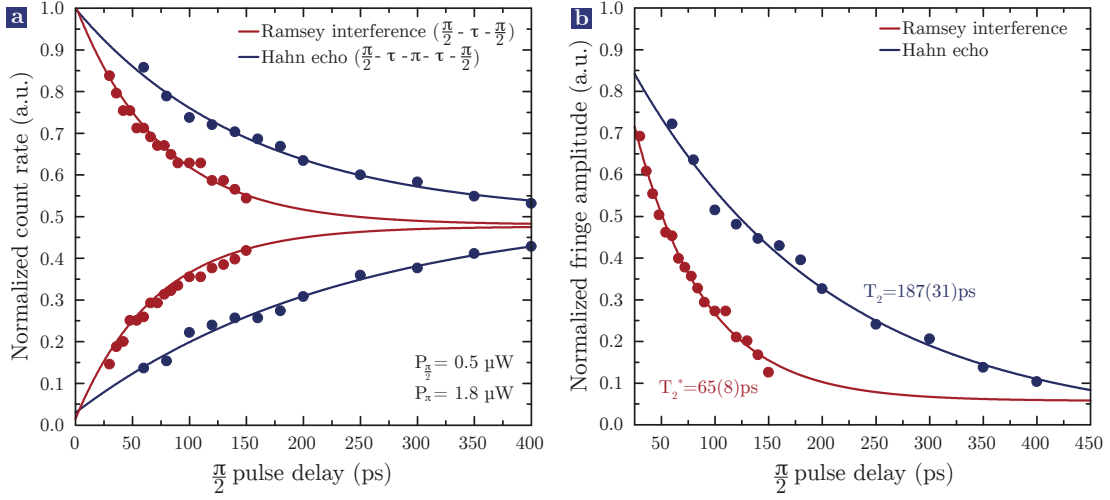


**Figure 5.3: Ramsey interference and Hahn echo in SiV<sup>-</sup> ensemble** In (a) the measured upper and lower envelopes of the Ramsey interference pattern (red dots) and Hahn echo (blue dots) on transition C are shown together with the simulated envelopes using a four-level ensemble density matrix model (blue and red lines), assuming an inhomogeneous broadening of about 10 GHz. The measured (dots) and simulated (lines) decays of the interference fringe amplitudes for both measurements are depicted in (b).

measured upper and lower envelopes of the Ramsey interference signal and the resulting decay in fringe amplitude, respectively. The data is well fit by our four-level ensemble OBE simulation (solid red line) by assuming an inhomogeneous broadening of about 10 GHz, consistent with the PLE measurements and validating the functionality of the model. The measurement yields an excited state coherence time of  $T_2^* = 65(8) \text{ps}$ , about 15 times smaller than what has been measured for a single SiV<sup>-</sup> centre in the previous chapter. This fast decay is the result of a superposition of Ramsey curves of different emitters in the ensemble experiencing different Larmor frequencies. The fringes of the individual SiV<sup>-</sup> centres average out due to their difference in Larmor frequency and thus the resulting ensemble curve decays much faster than the single-emitter Ramsey curves. Moreover, from this measurement we also determine the resonant  $\pi/2$  powers to  $P_{\pi/2} = 0.5 \mu\text{W}$ , easily reachable with the available laser sources.

To explore the possibility of reversing the decoherence induced by inhomogeneous broadening due to static crystal strain, a rephasing of the ensemble and thus an extension of its coherence time using an all-optical Hahn echo sequence has been attempted. To explore this possibility we applied a simple echo sequence similar to the one discussed in Chap. 2.1.3 consisting of the two  $\pi/2$  pulses from the Ramsey sequence above with an additional  $\pi$  pulse in between. The resulting measured envelopes (blue dots) and simulated curves (blue lines) of the Hahn echo experiment are shown in Fig. 5.3(a) and the measured (blue dots) and simulated (blue line) fringe amplitude is shown in Fig. 5.3(b). The echo signal decays significantly slower than the Ramsey fringes, giving rise to a phase coherence time of  $T_2 = 187(31) \text{ps}$ , about a factor of three longer than  $T_2^*$ . In fact, our model indicates that

perfect rephasing and a single-emitter coherence level can be reached with this technique under perfect circumstances. However, the model also shows that in the experiment presented here an additional excitation-induced dephasing of about 900 MHz occurs, most likely caused by locally heating the sample with the intense  $\pi$ -pulse. Similar effects have already been observed at lower powers for the Ramsey interference measurements of single  $\text{SiV}^-$  centres in the previous chapter. In future setups this might be improved by optimizing thermal anchoring as well as using lower sequence rates (the experiments above have been measured at 80 MHz rate while all following experiments have been measured at 1 MHz) or slightly longer pulses. The experiments presented here demonstrate the potential of echo sequences to remedy effects of inhomogeneous broadening. While the implementation of a similar Raman-based echo method for memory applications is beyond the scope of this work similar sequences acting on the two-photon transition between the ground state manifold of the  $\text{SiV}^-$  might be used in future protocols to further extend storage times.

### 5.3 Stimulated Raman Adiabatic Passage

Let us now go one step further towards a quantum memory by implementing a Raman-based technique. To realize a quantum memory we will first demonstrate a Raman-based population transfer between the orbital ground states of the ensemble using two pulsed classical light fields in a  $\Lambda$ -type arrangement. This technique is called stimulated Raman adiabatic passage (STIRAP) and its theoretical framework has been introduced in Chap. 2.2.2. For this experiment we first initialize the ensemble into the lowest orbital ground state  $|1\rangle$  by optically pumping transition D with a 100 ns long pulse from a resonant cw laser. A second, identical pulse is used to read out the population in state  $|2\rangle$  after a certain delay. For the ensemble-based experiments we made two crucial modifications to the setup presented in Chap. 3.3.4: First, we use a Mach-Zehnder-based electro-optic modulator (EOM, Jenoptik AM705b) instead of an AOM to cut the pump and read-out pulses from the cw laser. The EOM enables the generation of pulses with much faster rise and fall times ( $\approx 1$  ns) and thus enables us to apply shorter delays between the pulses without creating significant pulse overlap. Secondly, instead of using the narrowband titanium-sapphire laser (Sirah Matisse TX) to create the pump pulses we modified a pulsed Ti:sapphire laser (SpectraPhysics Tsunami X1BB) to run in a broadband cw mode. To do so, we removed all elements used for mode-locking and all frequency selective elements except the birefringent filter from the linear cavity and installed an additional Fabry Perot etalon with a free spectral range of  $\text{FSR}=250$  GHz and a finesse of  $F=0.2$  for fine wavelength selection. This arrangement enables the laser to run with a linewidth of 5-7 GHz and thus allows us to efficiently initialize the majority of the inhomogeneously broadened ensemble simultaneously, increasing its optical depth for the Raman process. We have to use this technique instead of e.g. slowly scanning the frequency of a narrowband laser across the ensemble due to the relatively fast ( $T_1 \approx 35$  ns) relaxation process within the ground state orbital manifold of the  $\text{SiV}^-$  ensemble. The resulting measured pump and read-out fluorescence histogram (grey dots) as well as four-level OBE simulations (blue line) using the ensemble model presented in Chap. 2.3 are shown in Fig. 5.4(a). These curves can be understood analogously to the optical pumping experiments in the previous chapter.

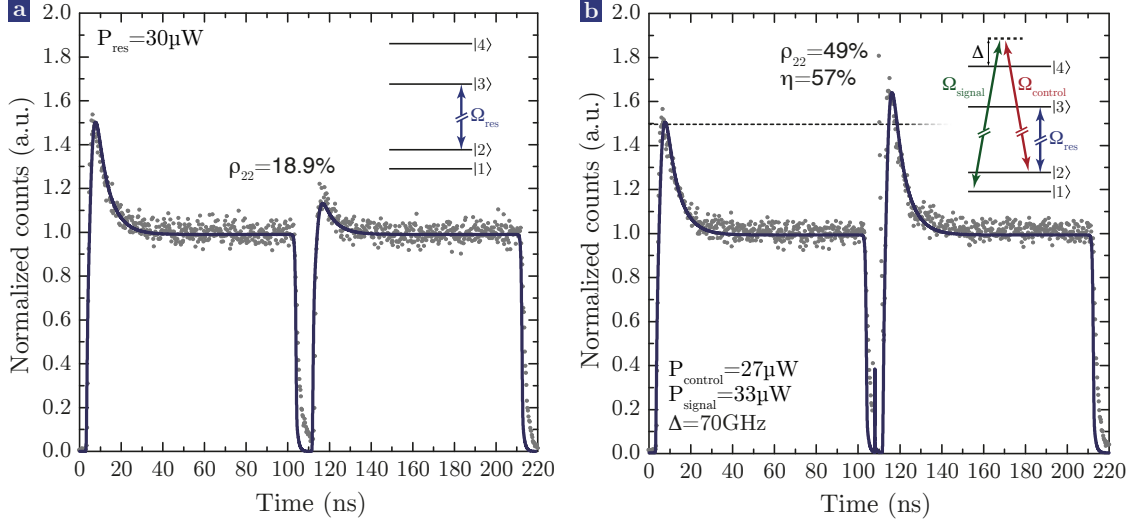


**Figure 5.4: Stimulated Raman adiabatic passage** (a) Measured sideband fluorescence (grey dots) collected during pump and readout sequence consisting of two subsequent 100 ns laser pulses on transition D as well as four-level OBE simulation (blue solid line). The model indicates a population of  $\rho_{22} = 18.9\%$  at the point in between both pulses where later the Raman pulses will be applied. (b) Same sequence including two Raman pulses in between the resonant pulses. The enhanced rising edge of the readout pulse indicates the successful Raman-based transfer. The OBE model indicates an upper ground state population of  $\rho_{22} = 49\%$  after the transfer corresponding to a transfer efficiency of  $\eta = 57\%$ .

Starting with an equilibrium population of  $\rho_{22}=37\%$ , the population is pumped into  $|1\rangle$ , leading to the rising edge fluorescence peak which rapidly decays down to an equilibrium value. This equilibrium is defined by the ratio of the ground state relaxation and the excited state decay rate. After switching off the pump, population thermalizes back into  $|2\rangle$  causing the revival of the rising edge peak in the readout pulse. With this technique we achieve a minimum population of about 14% during the pump pulse and 18.9% five nanoseconds after the pump pulse has ended. This delay allows for the application of a Raman pulse in between pump and read-out to perform the STIRAP transfer. The resulting PSB fluorescence of the sequence of resonant pulses with the additional Raman pulses in between is shown in Fig. 5.4(b). For this measurement we used the maximally available laser power and optimized the relative powers in both Raman pulses resulting in  $P_{signal}=33\mu\text{W}$  and  $P_{control}=27\mu\text{W}$ . The significantly increased rising edge peak in the read-out pulse indicates a successful transfer of population from  $|1\rangle$  back into  $|2\rangle$ . With the aid of the OBE model we can determine the population in  $|2\rangle$  after the Raman transfer to amount to  $\rho_{22} = 49\%$ . This corresponds to a transfer efficiency of  $\eta = 57\%$ . This is due to the fact that our model indicates that the maximum transferable population is limited by the initialization fidelity into state  $|1\rangle$  which only amounts to  $\rho_{11}^{max} = 81.1\%$ . Our simulation shows that the STIRAP using picosecond pulses, especially at very small pulse delays as they were used here, is not unidirectional but also transfers leftover population in  $|2\rangle$  after optical pumping into  $|1\rangle$ , hence limiting the transfer efficiency. To validate that

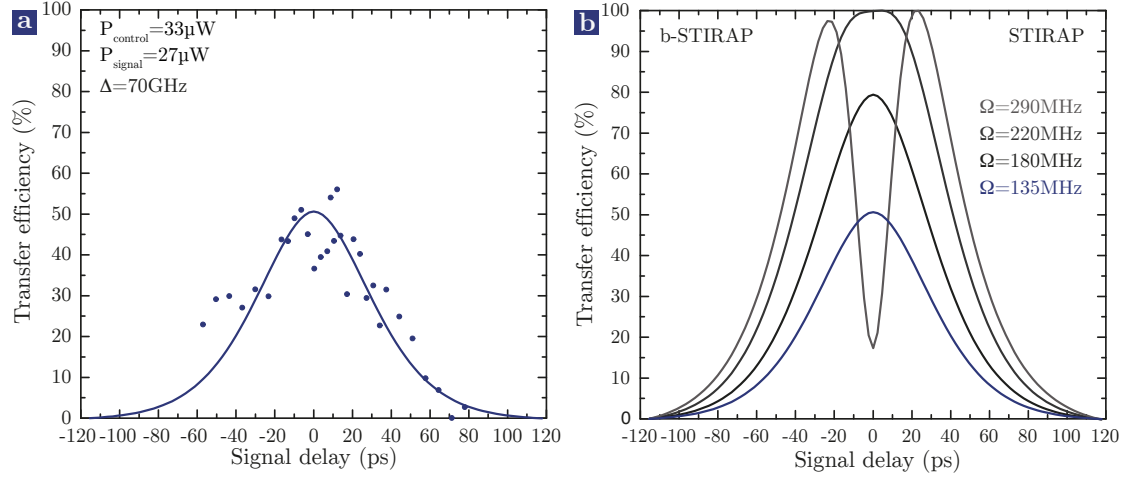


**Figure 5.5: Raman pulse delay** (a) Measured (dots) and simulated (line) scan of the pulse delay between control and signal pulse. (b) Simulated delay scans for different Rabi frequencies and a power ratio of  $P_{\text{control}}/P_{\text{signal}} = 1.2$ . The blue curve corresponds to the simulation used in (a). Further details can be found in the main text.

the population transfer is indeed caused by a two-photon transition we also performed measurements with solely the control or the signal pulse being present. The corresponding histograms did not show any significant population transfer. Moreover by tuning control and signal field out of two-photon resonance the transfer can be suppressed, validating the observed transfer is indeed STIRAP. Finally, we performed a scan of the temporal delay between control and signal pulse. The resulting measurement (blue dots) is displayed in Fig. 5.5(a) together with a simulated delay scan from our OBE model (blue line). The curve has been measured starting at a signal delay of 80 ps (control preceding) and has been measured up to -60 ps (signal preceding). At this point the flow cryostat became unstable and the measurement has been stopped. However, the covered range is large enough for a faithful analysis using the OBE model. For varying delays a near-Gaussian dependence of the transfer efficiency with a maximum at zero delay has been found. Our model indicates that this symmetric shape of the delay curve is achieved for relatively low Raman pulse powers. Moreover, in addition to the limited initialization fidelity, the model shows that the low pulse power is the second main factor limiting the transfer efficiency. The simulations in Fig. 5.5(b) indicate that the measurements presented here, in which the Raman pulse powers are limited by the available laser power, have been performed at a simulated Rabi frequency of  $\Omega = 135 \text{MHz}$ , about a factor of 1.6 below the efficiency maximum reached at  $\Omega = 220 \text{MHz}$ . For even higher pulse powers two distinct maxima form shifted away from zero delay, corresponding to two different Raman-based transfer processes. For a preceding control the classical STIRAP process transferring population via the dark state using the "counter-intuitive" pulse sequence discussed in Chap. 2.2.2 is realized. A second maximum can be found for a preceding signal field corresponding to the so-called bright-STIRAP (b-STIRAP) process. This process works analogously to the classical STIRAP but population is transferred via the bright state. The b-STIRAP can be

very efficient as long as the evolution times are much shorter than the excited state decay times of the system (as the bright state contains excited state contributions). However, even the slightest imperfections in any experimental parameters such as delays, pulse forms or pulse power ratios will leave the ensemble in a partially excited state resulting in decoherence and reduced transfer efficiencies [244]. Even for the picosecond pulses used here this difference is visible in the simulated delay scan for the highest Rabi frequency  $\Omega=290$  MHz in which both regimes, STIRAP and b-STIRAP are clearly distinguishable. There the maximum efficiency for the transfer via b-STIRAP (left peak) is slightly lower than for STIRAP (right peak).

## 5.4 Raman absorption

The above demonstrated Raman-based coherent population transfer via STIRAP is the fundamental physical process also used in the Raman quantum memory. To store weak coherent fields and ultimately single photons, the strength of the signal field is decreased while the power in the control field is increased to maximize the Raman coupling strength. Moreover, in contrast to detecting the PSB fluorescence of the ensemble we now measure the transmission of the signal field. To suppress the strong control field, we use a polarizer perpendicular to the polarization direction of the control and a subsequent grating filter setup described in Chap. 3.3.4 and [198]. In the left part of Fig. 5.6(a) the measured count rate histogram for the absorption of a weak signal field with  $P_{\text{signal}}=10$  nW, corresponding to about 37000 photons per pulse, is shown. The red line hereby corresponds to the transmitted signal in absence of the control field while the blue curve corresponds to the signal transmission with  $P_{\text{control}}=75$   $\mu\text{W}$  of applied control field. The background created by residual transmission of the control is given in green. After subtraction of this background, a maximum absorption of about 80% has been reached. This is considerably higher than what we estimated above, indicating that we underestimated the density of the Sternschulte ensemble in the theoretical treatment. As evident from the delay scan shown in Fig. 5.6(b) the maximum absorption is hereby reached for pulse delays close to zero, consistent with the simulated delay scans in the low power regime performed for STIRAP in Fig. 5.5(b). The blue dots correspond to measured values whereas the blue line represents a Gaussian fit serving as a guide to the eye. The slight asymmetry of the curve towards positive values is again caused by cryostat instabilities. For increasing control powers the signal transmission first decreases exponentially and reaches an almost constant value at the maximum available control power of  $P_{\text{control}}=75$   $\mu\text{W}$ . This power dependence is shown in the lower curve of Fig. 5.5(c) in which blue dots again correspond to measured values and the blue line represents an exponential fit. Absorption in this regime is most likely limited by the number of signal photons relative to the amount of  $\text{SiV}^-$  centres in the focal volume. Moreover, the absorption values reached in the measurements of Fig. 5.5(b) and (c) are considerably lower than the maximum value of about 80% presented above. We attribute this to a significant variation in the  $\text{SiV}^-$  density across the ensemble on the  $\mu\text{m}$  scale visible in high resolution confocal scans such as the one shown in Fig. 5.5(d). On the small and localized bright spots in this scan high absorptions of 70-80% have been measured while much lower values have been obtained from the far more extended less

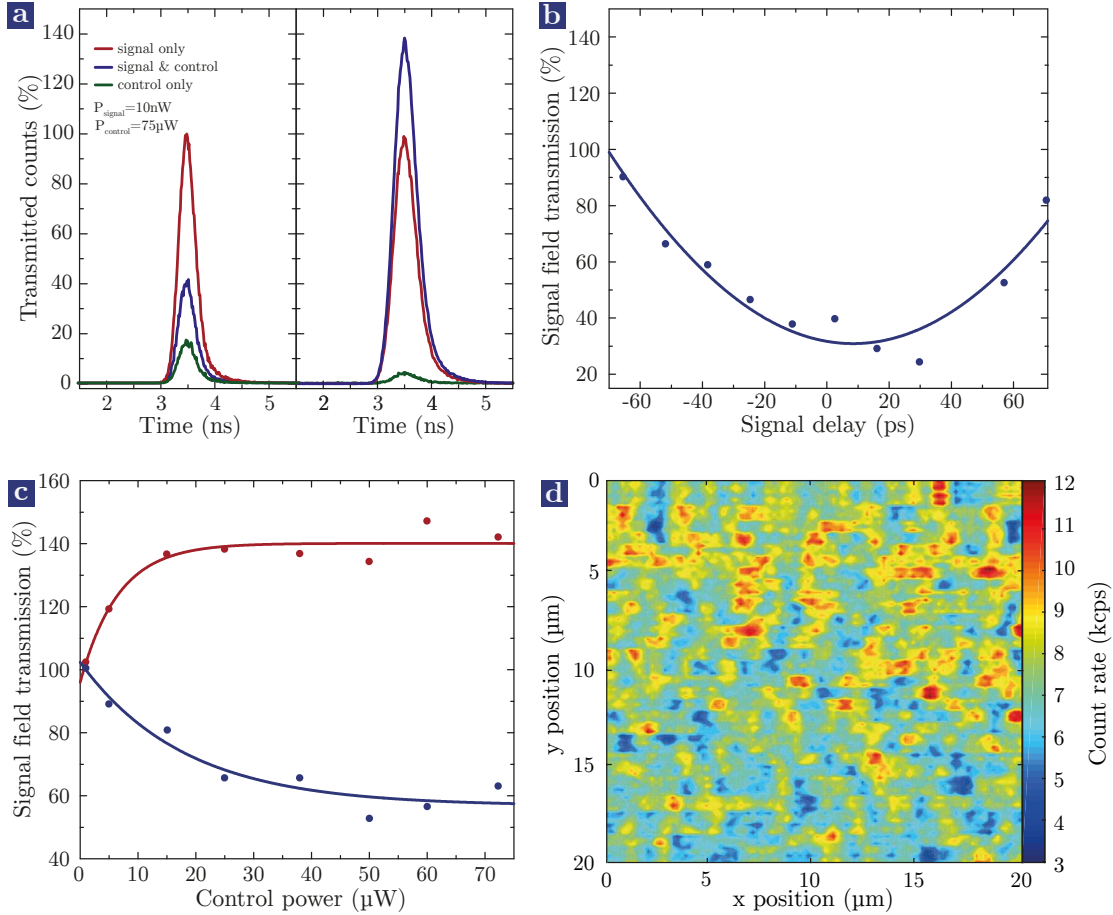


**Figure 5.6: Raman absorption** (a) Transmitted signal field without (red) and with a strong control field being present (blue) as well as the background due to the control field only (green). Depending on the relative phase of signal and control a signal absorption (left graph) as well as signal gain (right graph) can be achieved. (b) Dependence of the Raman absorption on the delay between signal and control pulse. The asymmetry is caused by cryostat drift. (c) Control power dependence of Raman absorption (blue) and gain (red). (d) Confocal scan across the Sternschulte ensemble sample with a 200 nm resolution demonstrating significant inhomogeneities in the SiV<sup>-</sup> density.

dense regions. However, due to drift of the flow cryostat it is not possible to position onto one of the localized dense regions for long-term experiments. Hence, we recently tested a new ensemble sample, the "Element Six ensemble", as a promising alternative sample for future experiments. This sample does not show significant density variations on the relevant length scales and Raman absorptions of 80% at  $P_{signal}=10$  nW of signal power have been measured, independent of the position on the sample. For lower signal powers of  $P_{signal} \approx 1$  nW even higher values of more than 90% have been measured. However, at these powers the amount of transmitted control field is significant compared to the residual signal. Hence, for a more thorough characterisation and future experiments with even lower signal field strengths the control field suppression needs to be optimized further. This can for example be realized by adding a second grating filter stage or by using volume Bragg gratings offering much better extinction ratios.

In addition to the above discussed regime in which the signal is absorbed in the presence of the control we also, in both samples, observed a signal gain regime (cf. right graph in Fig. 5.5(a)) and the amount of absorption or gain depends on the relative phase (i.e. a very short pulse delay) of signal and control field. Hence, to allow operation at the point of maximum absorption and minimum gain a phase stabilization had to be added to the setup (not displayed in Fig. 3.10 for reasons of clarity) which has been implemented as follows: Before splitting the laser into the two arms containing the signal and control etalons, a 532 nm reference laser (SpectraPhysics Millennia eV15) has been overlapped with the 737 nm laser using a dichroic mirror. After being split by a polarized beam splitter both lasers travel through the control as well as the signal arm, with the 532 nm laser being unaltered by the etalons as their coatings show  $\sim 90\%$  transmission at 532 nm (cf. Appendix B). Both arms have then been recombined at a second polarizing beam splitter and the reference laser has been separated from the 737 nm pulses using a second dichroic mirror. In the resulting 532 nm beam the two components from the signal and control arms are still cross-polarized and therefore do not interfere yet. Hence, the combined beam is sent through yet another polarizing beam splitter under  $45^\circ$  incident polarization, projecting 50% of the laser from each arm onto both ports of the beam splitter at. The temporal fluctuations in the resulting interference have then been measured using two photodiodes at the output ports. Their signals have been sent to a PID controller (TEM Messtechnik, LaseLock Digital) calculating an error signal and creating a feedback via a piezo actuator inserted into a delay stage in the control arm. With this its length relative to the signal arm can be actively stabilized and a defined path difference can be selected using the PID set-point. By deliberately selecting the point of maximum gain we were also able to perform further characterizations of this process, which for the memory corresponds to a source of undesired noise. A prominent source of noise in Raman-based quantum memories is degenerate four-wave mixing (FWM) in which the strong control field also couples to the signal transition, consequently creating spurious excitations in the storage state via spontaneous Raman scattering, which are then read out again by the very same control field causing additional signal photons [245, 246]. This process shows a quadratic dependence of the created signal photons on the control field power whereas the measurement (red dots and line in Fig. 5.5(c)) indicates a steep increase between  $P_{control}=0$   $\mu$ W and  $P_{control}=10$   $\mu$ W and a saturation for control powers greater than  $P_{control}=10$   $\mu$ W. Moreover, while FWM noise should also be created in absence of

an incident signal field we only observe gain with an applied signal field. Moreover, the amplitude of the gain depends roughly linearly on the applied signal field power with 63% at  $P_{signal}=11$  nW, 43% at  $P_{signal}=7.7$  nW and only 13% at  $P_{signal} \approx 1$  nW. Due to this scaling and the requirement that both signal and control have to be present we attribute this gain to a stimulated Raman scattering (SRS) seeded by the weak signal and pumped by the strong control laser coupling to the upper ground state level  $|2\rangle$  [247, 248]. Even at 5 K and in the presence of the above discussed optical pumping sequence, this level still has a minimum population of about 20%, allowing for a considerable scattering rate. In principle also a linear scaling of the gain amplitude with the applied control field power is expected for SRS [247] and the saturation of the gain for high control field powers observed in Fig. 5.5(c) is surprising at first. This indicates that the SRS is efficient enough to deplete the population in  $|2\rangle$  much faster than it can be restored by the phonon-assisted thermalization, hence creating a bottleneck for high control pulse energies. However, due to the presence of only very weak seeding fields this process might become negligible for signals on the single photon level as they would be applied if the system is operated as a quantum memory. Moreover, the process might be further reduced by reducing the residual population of  $|2\rangle$  which can be achieved by working at lower temperatures. This will be possible in future experiments due to a recently ordered 1.5 K cryostat. At this temperature the thermal population of  $|2\rangle$  has already reduced to 18%. In addition, the phase dependence of this process most likely is a consequence of the specific configuration of the  $\Lambda$ -scheme driven here. While SRS in a regular  $\Lambda$ -system in which the two ground states  $|1\rangle$  and  $|2\rangle$  are not directly coupled is not expected to show a phase-dependence, it has been shown theoretically that in multi-level systems with closed interaction contours a dependence of the temporary evolution of the populations and coherences on the relative phase of the applied fields occurs [152]. In the case described here, the interaction contour in the  $\Lambda$ -system is closed by the phonon-mediated transitions between the two orbital ground states, causing the phase dependence. The resulting configuration is sometimes referred to as a  $\Delta$ -system. The phase dependence is expected to weaken if the coupling of the orbital ground states to each other becomes small which again can be achieved by cooling the system to lower temperatures. Alternatively the use of spin sublevels would also suppress this effect as selection rules prohibit a direct transition between both states. This possibility, which in addition offers the advantage of potentially much larger storage times, will also be explored in future experiments. Using the above-mentioned new cryostat featuring a 9 T magnet a considerable Zeeman splitting can be created to access the spin degree of freedom of the  $\text{SiV}^-$  ensemble while maintaining decent memory bandwidths. By applying a second control pulse delayed to the first one we also attempted a read-out of the memory after a signal field has been absorbed in the presence of a first control pulse. This however was not successful so far for three main reasons: First, the read-out control pulse had to be split off the control used for read-in, limiting the available control power in both pulses to about 15  $\mu\text{W}$ . As apparent from Fig. 5.5(c) this limits the Raman absorption to about 50% of its maximum value. Consequently, a reduced stored signal is available for read-out and additionally we expect the read-out efficiency to be non-optimal as well. Secondly, the timing jitter of the APD of about 250 ps required the use of delays greater than 200 ps between read-in and read-out to be able to distinguish between both pulses. This however is already a factor of two longer than the storage

time estimated from the inhomogeneous broadening calculated above and will therefore again greatly limit the achievable read-out signal strength. Thirdly, the identification of small signals read out from the ensemble has been rendered challenging in the presence of residual control field transmitted through the filter setup. These problems might be addressed in future experiments by further minimizing power losses in the setup or ideally by using two synchronized mode-locked lasers creating pulses with about 30 ps length at the signal and control frequencies respectively to avoid the use of the extremely lossy etalons. Additionally, the use of superconducting nanowire single photon detectors with timing jitters lower than 100 ps can facilitate the temporal separation of read-in and read-out signal pulses even at small delays. Such detectors were not accessible during the experiments presented above but are available in the group for future measurements. Moreover, the control field suppression might be optimized by adding an additional grating filter stage or by replacing the current filter by volume Bragg gratings. Finally, the inhomogeneous broadening in future  $\text{SiV}^-$  ensemble samples needs to be reduced further. This is necessary to achieve technologically meaningful storage times which will also greatly simplify read-out experiments. Due to the above-derived quadratic dependence of the storage time on the inhomogeneous broadening even a moderate improvement of ensemble quality can lead to significant storage time extension. For example, a broadening with  $\delta\nu=5$  GHz, half of what is currently achieved in the samples utilized in the experiments presented above, already allows for storage times of about 1 ns.

Before we conclude this chapter we would like to briefly discuss the potential of  $\text{SiV}^-$  ensembles for the storage of single photons and quantum states based on the experimental results achieved so far: For the storage of single photons a high memory efficiency as well as a low noise level are essential. The experiments presented above demonstrate absorption of relatively strong pulses still containing several thousands of photons with an efficiency of up to 80%. To increase the control power density, in these experiments a tight focusing using a N.A. 0.9 objective lens has been used, which significantly reduces the number of addressed  $\text{SiV}^-$  centres. Hence, we believe that in the current configuration or possibly by using a larger focal spot (which consequently requires higher control powers) to address a larger sub-ensemble high enough storage efficiencies for single photon-storage can be reached. Moreover, in the experiments above we identified a phase-dependent SRS as the main noise source at the investigated signal intensities. While this process can already be efficiently suppressed by setting a correct phase between signal and control, we expect this process to further decrease for lower signal fields (due to the lack of seeding) and lower temperatures (due to a reduced population in the upper ground state). At lower signal powers FWM as an additional source of noise might become relevant as it is e.g. the case in the caesium Raman memory [249]. For the  $\text{SiV}^-$  we might be able to suppress this type of noise by carefully choosing the detuning of the fields. As depicted in the left part of Fig. 5.7(a), FWM noise is caused by the creation of spurious excitations in the upper ground state (the storage state) created by the strong control field (red) coupling to the lower ground state and spontaneously scattering Stokes Raman photons (yellow) at a frequency  $\omega_c - \Delta E_g$ . For the  $\text{SiV}^-$ , by working at a detuning of  $\Delta = 2\Delta E_g = 96$  GHz from the excited state it is possible to create a situation in which the unintentionally scattered photon (yellow) is resonant with one of the ZPL transitions as depicted in the right part of Fig. 5.7(a). The resonant absorption corresponds to a loss channel for the spontaneous

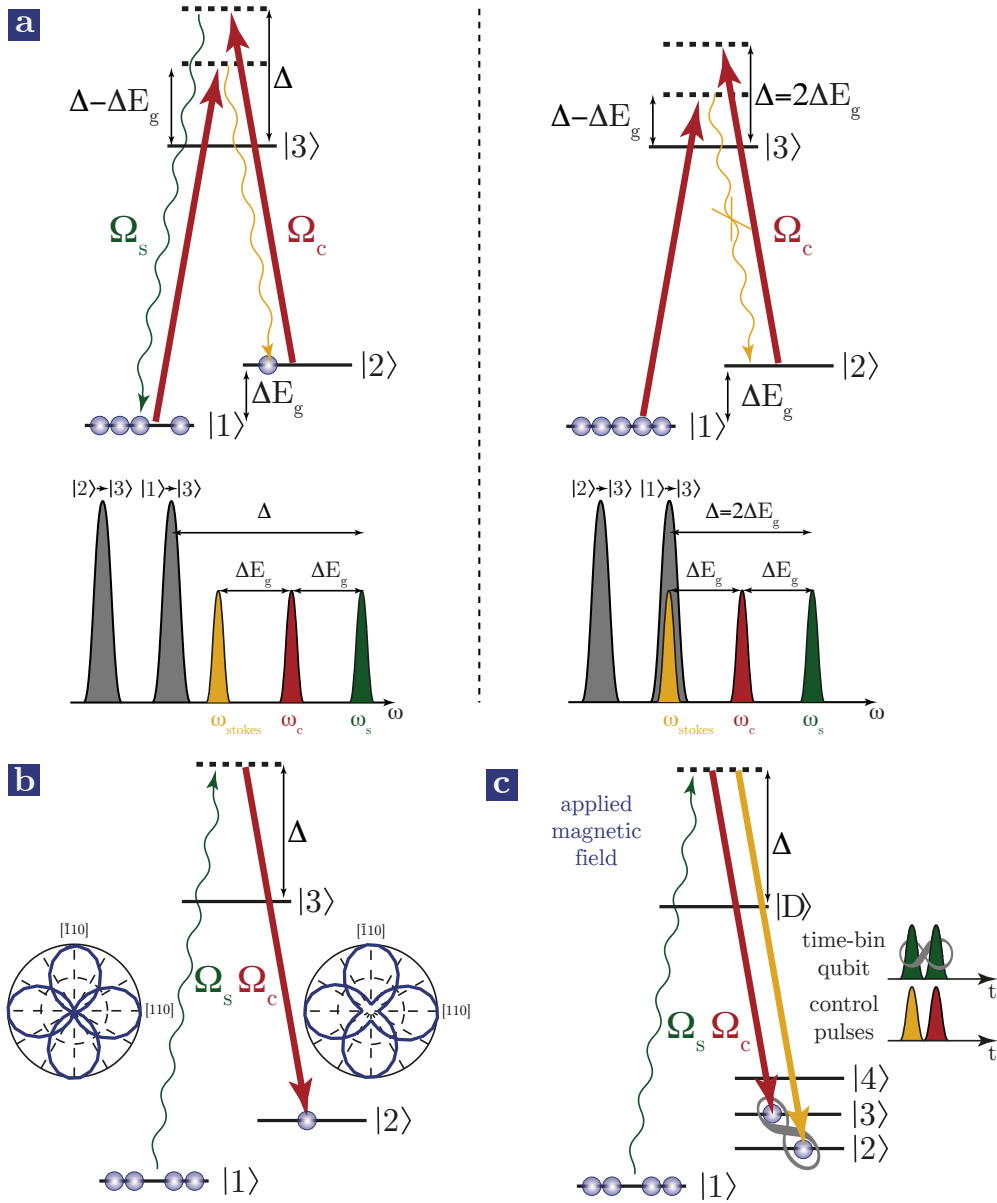


**Figure 5.7: Suppression of FWM noise & Qubit storage** (a) Left: Generation of spurious spin wave excitations by FWM process due to coupling of the strong control field (red) coupling to the lower ground state  $|1\rangle$  and scattering Stokes photons (yellow). Readout of the resulting excitations leads to unwanted photons at the signal frequency (green). In this configuration the detuning  $\Delta$  is chosen arbitrarily Right: By choosing  $\Delta = 2\Delta E_g$  the FWM process can be suppressed as the spontaneously created Stokes photon (yellow) becomes resonant with the  $|1\rangle \rightarrow |3\rangle$  transitions. This loss channel strongly suppresses the creation of spurious excitations. (b) Storage of polarization encoded photons can be achieved in an unoriented ensemble, i.e. a sample which contains SiV<sup>-</sup> ensembles along all equivalent  $\langle 111 \rangle$  directions. (c) Storage of a time-bin qubit by storing the two bins in different storage states (here magnetic sublevels) using two control fields of different frequency.

Raman scattering process and is therefore expected to significantly suppress it. Even if population is transferred via the scattering and subsequent resonant absorption of a Stokes photon, the resulting excitation (in contrast to the excitations directly created by FWM) is not phase-matched and is therefore emitted into  $4\pi$  during read-out, hence creating a negligible noise contribution.

Let us now also take a closer look at the storage of qubits encoded in photons. We here exemplarily discuss the storage of polarization- as well as time-bin-qubits [250, 251]. The storage of polarization-encoded qubits requires a polarization-independent memory. While the signal transition  $|1\rangle \rightarrow |3\rangle$  used above is linearly polarized for single  $\text{SiV}^-$  centres, it is effectively unpolarized in the ensembles used above as they contain several orthogonal sub-ensembles aligned along all equivalent  $\langle 111 \rangle$  directions (featuring optical transitions with projected polarizations along the  $\langle 110 \rangle$  directions). Hence, a polarization qubit can be stored in this type of ensemble by effectively storing its two orthogonally polarized basis states in different sub-ensembles as depicted in Fig. 5.7(b). By reading out both sub-ensembles simultaneously using an unpolarized control field, the original polarization state of the photon is then restored.

The storage of a time-bin encoded photon in the  $\text{SiV}^-$  memory is much more challenging. In a time-bin qubit the two basis states are encoded in terms of arrival times of the photon in two distinct time intervals, an early or a late time bin. Direct temporal multiplexing, i.e. reading in and out the two time bins one after each other using the same Raman-transition and storage state is not feasible in a Raman memory since the application of a readout pulse will immediately trigger the emission of a stored photon independent of when the spin wave has been created. Therefore the time-bin encoding has to be converted into an energy encoding using two subsequent control pulses of different frequency targeting different storage states for both time bins. This is shown in Fig. 5.7(c). As illustrated, in  $\text{SiV}^-$  ensembles this might be realized by using two orthogonal spin sublevels as storage states for the two bins. This scheme however has two distinct disadvantages. First, when reading out the memory there is a finite chance that the first readout control pulse also couples to the state containing the late time bin and triggers its readout. To minimize this it is advantageous to store the early bin using the higher energy field (green) as it couples to the state for the late bin with a larger detuning from resonance, hence minimizing the scattering probability. Secondly, one of the storage states has to originate from the upper orbital ground state branch. Therefore, a relaxation of population transferred into this state into the same spin sublevel of the lower orbital branch under phonon-emission might occur, destroying the stored time-bin encoded state. While this might in principle be overcome by engineering nanostructures featuring a phononic band gap at the respective phonon frequencies, such a solution might be incompatible with the requirement of a high optical density and therefore a large ensemble volume. Hence, it might be more suitable to first convert the time-bin qubit into a polarization qubit [252] before storing it in this type of memory.

To conclude this chapter on coherent manipulation of  $\text{SiV}^-$  ensembles we will now briefly summarize the main results:

- After introducing the concept of a Raman quantum memory we theoretically estimated storage efficiency and storage time of a  $\text{SiV}^-$ -based memory utilizing currently

available ensemble samples: By calculating the Raman coupling we estimated a read-in efficiency of slightly less than 50% for the Sternschulte ensemble consisting of an only about 300 nm thick homoepitaxially grown diamond layer with an estimated SiV<sup>-</sup> density of  $10^{13}$  SiV<sup>-</sup>/cm<sup>3</sup>, demonstrating the potential of SiV<sup>-</sup> ensembles for high-efficiency memories. Moreover, we estimated the storage time by relating the distribution of optical transition frequencies caused by static crystal strain to the distribution of two-photon transitions between the two orbital SiV<sup>-</sup> ground states. The calculation indicates that with the currently available samples showing an optical inhomogeneous broadening of about  $\delta\nu=10$  GHz storage times on the order of 100 ps are feasible which improve quadratically for narrower broadenings.

- As a first experiment using pulsed fields to coherently manipulate an SiV<sup>-</sup> ensemble we performed a resonant Ramsey interference experiment mainly to determine whether the available optical power suffices to manipulate the ensemble and to validate the OBE ensemble model from which we extract an excited state coherence time of  $T_2^*=65(8)$  ps. Building up on this measurement, we performed a resonant Hahn-echo experiment to explore the possibility of counteracting the dephasing induced by inhomogeneous broadening. A simple three-pulse echo sequence lead to an improvement of the coherence time by a factor of three with  $T_2=187(31)$  ps indicating the great potential of similar sequences acting on the two-photon transitions for future memory protocols.
- As a first experiment exploring the Raman-based manipulation of the ensemble we performed STIRAP utilizing a strong control as well as signal field. Transfer efficiencies of 57% from state  $|1\rangle$  into  $|2\rangle$  have been achieved, limited by the initialization fidelity and the available energy of the Raman pulses.
- Finally, we decreased the power in one of the Raman beams to the nW level and measured its absorption in the ensemble in the presence of its strong counterpart. This corresponds to the memory read-in process and absorptions of over 90% have been reached. In addition to the absorption we also found a process causing signal gain depending on the relative phase of both Raman fields. This is most likely caused by stimulated Raman scattering pumped by the strong control field. The phase dependence most likely is the result of a closed interaction contour due to phonon-assisted transitions between the ground state levels.



# Chapter 6

## Outlook & Summary

In this chapter we will start out with a short outlook on a number of interesting future experiments using the  $\text{SiV}^-$ , building up on the techniques developed earlier. Moreover, we will discuss how the investigations of the  $\text{SiV}^-$  properties, particularly in comparison with its well-investigated counterpart, the NV centre, can be used to select other colour centres in diamond for QIP applications and we will discuss two potential candidates. Finally, we will summarize the important results of the theoretical and experimental work presented earlier to conclude this thesis.

### 6.1 Outlook

The optical addressability of the  $\text{SiV}^-$  orbital and spin sublevels render the centre particularly interesting for QIP applications and the Raman-based coherent manipulation presented throughout this thesis is a powerful tool for optical coherent control. These techniques form the basis for a number of interesting future experiments. Therefore, let us now exemplarily discuss selected experiments for both, single  $\text{SiV}^-$  centres and ensembles.

**Cavity-enhanced Raman transitions** To realize a scalable QIP system based on  $\text{SiV}^-$  centres it is necessary to optically couple individual qubits. This requires the emission of Fourier-limited single photons with high rates as well as the transfer of quantum information from the  $\text{SiV}^-$  spin onto the state of a photon. Both tasks can be accomplished using cavity-enhanced Raman transitions. This requires coupling of individual  $\text{SiV}^-$  centres to optical cavities with mode volumes on the order of a single cubic ZPL wavelength to reach sufficient coupling strengths  $g$ . Assuming an orientation of the cavity field parallel to the dipole of the emitter the coupling strength is given by

$$g = \sqrt{\frac{c\lambda^2\gamma}{8\pi V}} \approx 2\pi \cdot 31 \text{ GHz} \quad (6.1)$$

with wavelength  $\lambda=737 \text{ nm}$ , bulk decay rate  $\gamma = 1/\tau_0 = 1/6.24 \text{ ns}=160 \text{ MHz}$  with natural lifetime  $\tau_0$  derived in Chap. 4.4.2 and mode volume  $V = 1(\lambda/n)^3$  with refractive index  $n=2.42$ . Moreover, we define the cavity decay rate

$$\kappa = \frac{\omega_0}{Q} \quad (6.2)$$

with quality factor  $Q$ . To achieve a strong coherent emission of the  $\text{SiV}^-$  into the cavity mode and at the same time prevent re-absorption, a cavity coupling in the Strong-Purcell regime defined by  $g^2/\kappa \gg \gamma$  as well as  $\kappa > g \gg \gamma$  is required. In this regime the coherent emission into the cavity largely dominates over spontaneous decay. For quality factors of  $Q=12000$   $\kappa$  and  $g$  then become comparable, defining an upper bound on  $Q$ . The resulting cavity linewidth of  $2\kappa/2\pi=67$  GHz would then allow for the coupling of individual spin transitions at magnetic field strengths of about 3 T. Assuming all of the parameters calculated above, a cooperativity  $C$ , i.e. ratio of cavity coupling to dissipative terms, of

$$C = \frac{g^2}{2\kappa\gamma} \approx 540 \quad (6.3)$$

can be reached, demonstrating strong coherent emitter-cavity interactions. To realize these cavity parameters, photonic crystals fabricated in thin diamond membranes can be used [41]. Using recently developed dry etching techniques, the fabrication of photonic crystals with  $Q$  factors close to the ones calculated above appears feasible [43]. Tuning of the cavities at cryogenic temperatures can then be achieved by either condensing noble gases onto the cavity surfaces or by bonding them to a piezo to apply strain.

To generate Fourier-limited photons, we again utilize a  $\Lambda$ -scheme between two spin sublevels of the  $\text{SiV}^-$  ground state and a common excited state with the cavity being resonant with one of the transitions. A strong control field  $\Omega_c$  applied to the second arm of the  $\Lambda$ -system and detuned from the excited state by  $\Delta_c$  then causes emission of Raman photons at a rate  $\Omega_{\text{eff}} = g\Omega_c/2\Delta_c$ , aided by the cavity enhanced vacuum field with an effective damping of  $\gamma_{\text{eff}} = 2\gamma(\frac{\Omega_c}{2\Delta_c})^2$ . Assuming a detuning of  $5\Omega_c$  this would e.g. allow for an emission rate of  $\Omega_{\text{eff}} = 2\pi \cdot 3.1$  GHz at an almost negligible damping rate of  $\gamma_{\text{eff}} = 3.2$  MHz.

To transfer a spin state onto a degree of freedom of a photon we can again utilize the above presented scheme for the creation of Raman photons as it has for example been demonstrated for trapped atoms [253]. To do so, an arbitrary superposition of spin states can first be prepared using the microwave-based control techniques which we recently demonstrated in [208]. The resulting state can then be mapped onto the polarization or time-bin degree of freedom by either simultaneously driving Raman transitions from both spin sublevels to a common final state (polarization encoding) or by addressing both levels successively using two individual control pulses delayed with respect to each other (time-bin encoding).

**Single photon switching with ensembles** Building up on the coherent manipulation techniques demonstrated for  $\text{SiV}^-$  ensembles, single photon switching can be realized utilizing the four orbital states of the  $\text{SiV}^-$  in a N-type level scheme [235]. Starting from some atomic ensemble with a  $\Lambda$ -type level structure, the switch is based on the concept of electromagnetically induced transparency (EIT) [64] in which a weak (single photon) field applied to one arm of a  $\Lambda$ -system is transmitted through the ensemble in the presence of a strong control field applied to the second arm due to destructive quantum interference. The application of an additional single photon-level field coupling one of the ground states to an additional level (hence the N-type configuration) then destroys the coherence in the  $\Lambda$ -system and therefore again renders the ensemble absorptive. For this scheme to be efficient, an optical density larger than one, high optical powers of the coupling field to

reach large Rabi frequencies as well as a narrow linewidth of the two-photon compared to the one-photon transition are the necessary requirements [235], all of which are satisfiable in  $\text{SiV}^-$  ensembles. Such an ensemble can then either be used to switch a single photon field with another one or as a photon number sorter since it is only transparent for one photon but not for two.

**Novel colour centres for QIP applications** Based on the experiences gathered by investigating the optical, electronic and coherence properties of the  $\text{SiV}^-$  during former works [58, 119] as well as this thesis and by comparing its advantages and disadvantages to the ones of the NV centre (the second well investigated colour centre in diamond), a targeted search for new promising colour centres for QIP applications, overcoming disadvantages of both the  $\text{SiV}^-$  and the NV, now appears feasible. In particular, while the NV centre offers good electronic spin coherence it lacks decent optical properties and robustness against external perturbations. In contrast, the  $\text{SiV}^-$  offers narrow linewidths and small phonon sidebands while its spin coherence is limited due to phonon processes within its orbital doublet states. Additionally, its inversion symmetry renders it insensitive against crystal strain and fluctuating magnetic fields, enabling unprecedented indistinguishability of individual  $\text{SiV}^-$  centres as well as fabrication of very homogeneous ensembles. Hence, a colour centre optimized for QIP applications would feature inversion symmetry but does not possess orbital multiplets so that coherence is not reduced by phonon-mediated transitions. Alternatively, the orbital splitting should be as large as possible to enable freezing out phonons with the respective frequencies at temperatures achievable with regular helium cryostats. Along this line, recently the negatively charged Germanium vacancy centre ( $\text{GeV}^-$ ) has been investigated as a potential alternative to the  $\text{SiV}^-$  [111, 254, 255]. The  $\text{GeV}^-$ , as the heavy analogon of the  $\text{SiV}^-$ , features the same basic geometric and electronic properties as its lighter counterpart with a four-line ZPL at 602 nm, a Huang-Rhys factor of  $S=0.33$  and a large ground state splitting of about 169 GHz due to an increased spin-orbit coupling caused by the heavy Ge atom. Since the  $\text{GeV}^-$  also features orbital doublets, its coherence is limited by phonon transitions as well. In fact, the coherence time of the  $\text{GeV}^-$  at 10 K is expected to be even lower than the one of the  $\text{SiV}^-$  due to an increased phonon density of states at 150 GHz. However, due to the effectively higher phonon temperature of about 8 K it should be significantly easier to freeze out these phonons and therefore an orbital coherence in the millisecond regime could be accessible at 1.5 to 2 K, temperatures reachable with regular helium cryostats. In this regime the lowest spin doublet is again protected against phononic dephasing and, by applying a magnetic field, can be used for QIP. Moreover, in the context of quantum memories, the centre's large ground state splitting potentially offers the possibility for very large storage bandwidths.

While the use of the  $\text{GeV}^-$  reduces the technological complexity in QIP applications by remedying the need for millikelvin temperatures, it does not resolve the fundamental limitations of the  $\text{SiV}^-$ . This could however be accomplished by yet another class of defects, Nickel-related centres, which have not been considered for QIP applications so far. For Ni, several interstitial as well as substitutional defects in a number of different charge states have been reported [256, 257]. For QIP applications two of these defects are of special interest, the  $\text{NiV}^+$  and the  $\text{NiV}^{2+}$ . The molecular structure of both defects

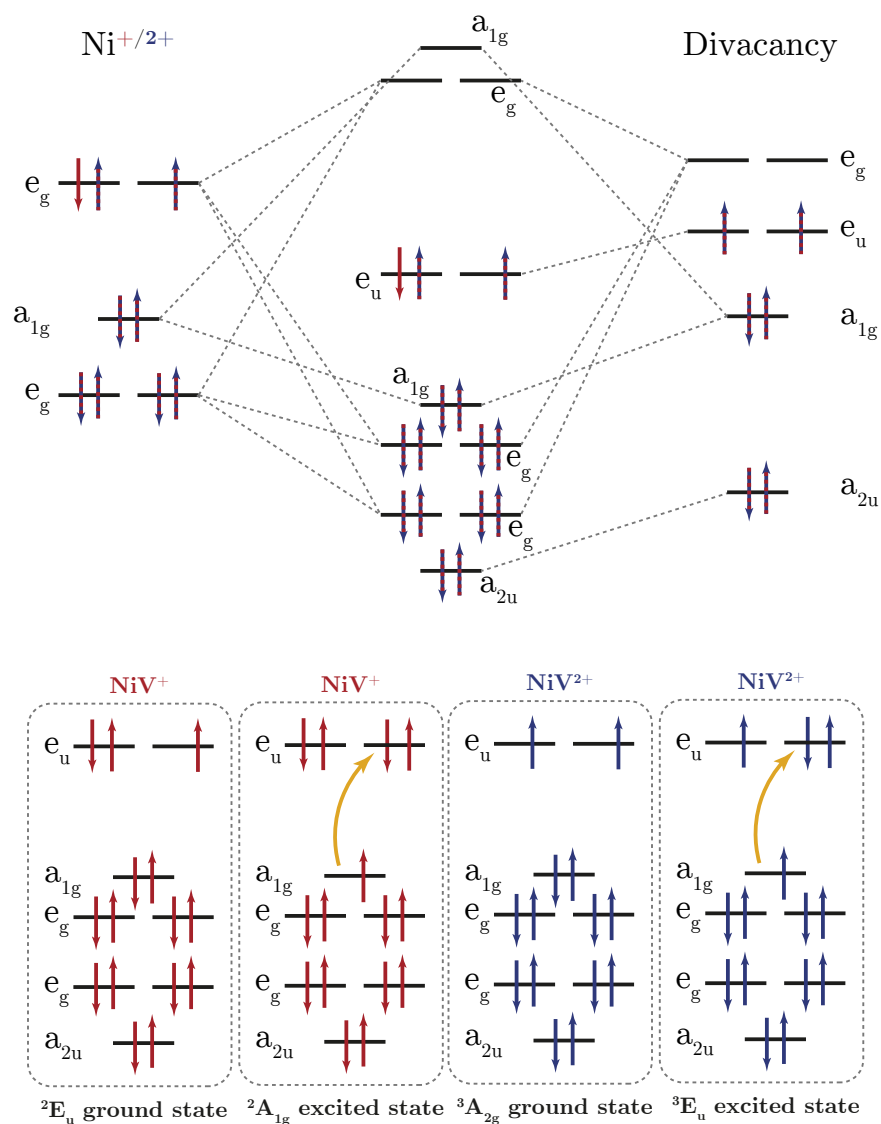


**Figure 6.1:  $\text{NiV}^{+/2+}$  orbital scheme and electron configurations.** (top) Electron orbital scheme of  $\text{NiV}^{+}$  (red) and  $\text{NiV}^{2+}$  (blue) constructed from a  $\text{Ni}^{+/2+}$  ion ( $[\text{Ar}]3d^{8/9}$ ) in a trigonal antiprismatic crystal field as well as a carbon divacancy featuring  $D_{3d}$  symmetry. (bottom) electron configurations of ground and excited states of  $\text{NiV}^{+/2+}$ .

again is a trigonal- antiprismatic split-vacancy complex with a Ni atom occupying an interstitial site [258]. However, both centres differ in their charge state and thus in their electronic structure. Using ESR measurements, the  $\text{NiV}^+$  has been determined to be a  $S=1/2$  system and has been related to a two-fold split ZPL observed at 883/885 nm, indicating a split ground or excited state splitting with a large splitting of  $\Delta=725$  GHz. Starting from a  $\text{Ni}^+$  ( $[\text{Ar}]3d^9$ ) or  $\text{Ni}^{2+}$  ( $[\text{Ar}]3d^8$ ) in a  $D_{3d}$  symmetric crystal field created by a divacancy (six electrons from carbon dangling bonds) using group theory predicts the electron orbital scheme depicted in the top part of Fig. 6.1, consistent with density functional theoretical calculations performed by Larico *et al.* [259]. We here made use of the symmetry adapted linear combinations of carbon dangling bonds under  $D_{3d}$  symmetry derived in [58]. Moreover, to explain the optical properties observed for both colour centres, we have to assume a significant admixture of Ni-related atomic orbitals (in contrast to the  $\text{SiV}^-$  in which the Si orbitals show almost no admixtures to the molecular states). Filling the resulting electron orbitals with 13 ( $\text{NiV}^+$ ) and 14 ( $\text{Ni}^{2+}$ ) electrons, we arrive at the ground and excited state level configurations depicted in the bottom part of Fig. 6.1. For the  $\text{NiV}^+$  the model indicates an  ${}^2E_u$  ground and an  ${}^2A_{1g}$  excited state. Assuming a spin-orbit interaction of  $\Delta E_g=725$  GHz acting on the orbital doublet ground state, the resulting two optical transitions correctly reproduce the observed fine structure as well as polarization properties of the 883/885 nm ZPL [260]. The corresponding level scheme is displayed in Fig. 6.2(a). While the  $\text{NiV}^+$ , like the  $\text{SiV}^-$ , again features an orbital doublet ground state, the splitting of the two orbital sublevels is large enough to potentially achieve good spin coherence times of the lowest spin doublet already at temperatures below 35 K, easily reachable with modern cryostats. Moreover, the centre again offers all the key

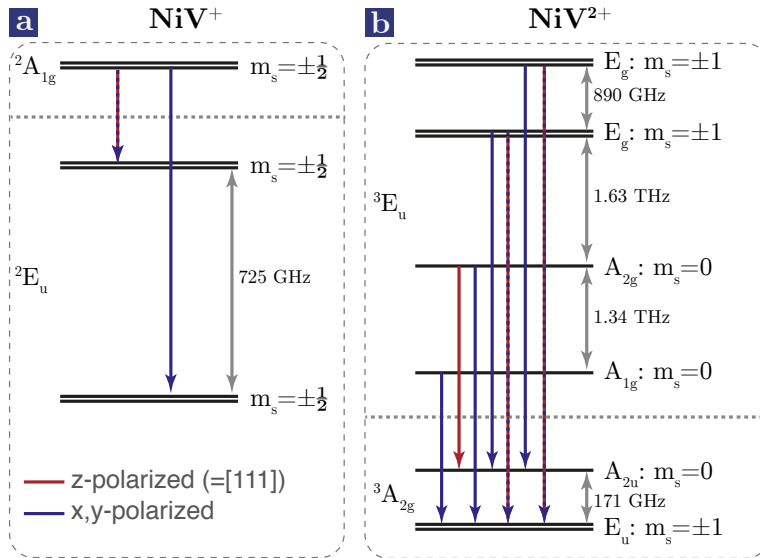


**Figure 6.2:  $\text{NiV}^{+/2+}$  level schemes.** Level schemes and optical transitions of (a)  $\text{NiV}^+$  and (b)  $\text{NiV}^{2+}$ . Transitions polarized along the (111) high symmetry axis of the centre are indicated in red, transitions polarized perpendicular to (111) are displayed in blue. Further details can be found in the main text.

ingredients to realize a broadband memory.

In contrast to all colour centres discussed so far, the electronic structure of the  $\text{NiV}^{2+}$  as predicted by group theory is not susceptible to decoherence by phonon-mediated processes as it features a  ${}^3A_{2g}$  ground state coupled to a  ${}^3E_u$  excited state (cf. 6.1). Comparing this to the optical spectra measured in [260] indicating seven individual ZPL transitions at 1016 nm shows that the degeneracies between the  $|m_s = 0\rangle$  and the  $|m_s = \pm 1\rangle$  sublevels in ground and excited state are lifted by strong spin-spin interactions, similar to the NV ground state [45]. Under this assumption we can then derive the level scheme displayed in Fig. 6.2(b). One particularly interesting feature is that the spectra measured by Lawson *et al.* display a significant transition strength of two cross-polarized optical transitions linking the  $|m_s = 0\rangle$  and  $|m_s = \pm 1\rangle$  ground state spin levels to a common  $A_{1g}$  excited state. This allows for optical ground state spin control without the need of applying additional strain or electric fields to create an excited state spin mixing as it is e.g. the case for the NV. The individual ZPL transitions have been observed up to temperatures of 77 K. This potentially allows the realization of QIP devices working at liquid nitrogen temperatures, greatly simplifying cryogenic setups. Moreover, in [258] a preferential alignment of the centres along a single (111) growth direction has been observed, resulting in ensembles displaying very good polarization properties as well as high optical densities, rendering the centre ideal for quantum memory applications. Note that the model presented here has been derived with the goal to reproduce the limited amount of spectroscopic data available for  $\text{NiV}^{2+}$  ensembles. In future work, the model needs to be complimented by density functional theoretical simulations and compared to high-resolution spectra of single centres to obtain a faithful picture of the  $\text{NiV}^{2+}$  centre's electronic structure.

## 6.2 Summary

During the course of this work we, for the first time, successfully investigated the coherence properties of single  $\text{SiV}^-$  centres as well as dense ensembles of these and we developed a number of all-optical techniques to coherently control their quantum state. To conclude this thesis, we will now summarize the main results:

### 6.2.1 Single $\text{SiV}^-$ centres

**Coherent population trapping** To measure the spin coherence time of single  $\text{SiV}^-$  centres we performed CPT measurements at 4.2 K in magnetic fields of up to 7 T. Using a four-level optical Bloch equation model ( $\Lambda$ -system with additional auxiliary state) including power broadening and limited laser coherences we analyzed the width of the dark-state resonance at 0.7 T and determined a ground state spin coherence time of  $T_2^* = 45(3)$  ns. Using additional CPT measurements at various magnetic field strengths we investigated the contribution of direct relaxations between the two ground state magnetic sublevels forming the dark state. These experiments reveal a significantly increased decoherence rate close to the level anti-crossing caused by spin orbit interactions as spin mixing within the ground state manifold increases. Moreover, these measurements suggest that decoherence in the low and the high field limit (away from the avoided crossings) is dominated by other

processes such as phonon-mediated thermalization between the different orbital branches of the ground state, such as magnetic field noise caused by an impurity spin bath.

**Millikelvin experiments** To further investigate the mechanisms causing the surprisingly fast decoherence of the ground state spin we, for the first time, designed, built and successfully operated a confocal microscope in a  $^3\text{He}/^4\text{He}$  dilution refrigerator enabling us to perform single-emitter investigations at temperatures down to 12 mK and in small magnetic fields of about 0.2 T. During cool-down, the spin relaxation time  $T_1^{\text{spin}}$  increases significantly from 303 ns at 3.7 K to 108  $\mu\text{s}$  at 12 mK. The long spin relaxation time also facilitates a high spin initialization fidelity of at least 99.93% at 12 mK. A phonon-assisted direct spin flip process has been identified as the limiting process at temperatures below  $\approx 500$  mK whereas a multi-phonon process plays an increasing role at temperatures between 500 mK and 2.3 K. To investigate the exact nature of this second process additional measurements at temperatures between 1.5 K and 4.2 K will be necessary. This temperature region will become accessible in the near future due to the installation of a new 1.5 K cryostat. At even higher temperatures a single-phonon process including thermalization to the upper orbital ground state level then determines the spin relaxation.

While the spin relaxation time in the millikelvin regime improves drastically, the enhancement of the total coherence time has been found to be much more moderate. Using further CPT measurements we determined a change of spin coherence time from  $T_2^*=19(3)$  ns at 3.7 K to  $T_2^*=32(5)$  ns at 12 mK. It is interesting to note that, despite the fact that the emitter investigated in these experiments is significantly less strained than the one used for the initial CPT measurements (and hence the phonon density of states should be lower), its spin coherence at 3.7 K is about a factor of two lower. This already indicates that phonon-mediated processes are not the only source of decoherence. Using all-optical Raman-based spin echo measurements we identified two decoherence processes limiting spin coherence while simultaneously demonstrating optical coherent control: First, a temperature- and magnetic field-dependent flip-flop process of the bath spins causing magnetic field noise. Secondly, a temperature- and field-independent resonant coupling of the  $\text{SiV}^-$  to the P1 bath (substitutional nitrogen defects  $[\text{N}_s^0]$ ). Especially this last process is detrimental to the  $\text{SiV}^-$  spin coherence as it can neither be suppressed by changing the temperature or magnetic field nor by applying dynamic decoupling sequences. From the temperature-dependent echo measurements we determined a spin bath concentration of about 3.8 ppm. This is about one to two orders of magnitude higher than the impurity concentrations usually found in type IIa HPHT diamonds. However we tentatively attribute this to unintentionally pre-selecting emitters in sample regions with locally increased impurity concentrations since we restrict ourselves to bright  $\text{SiV}^-$  centres. These bright emitters however, as discussed earlier in this thesis, seem to appear more frequently in nitrogen-rich diamond environments, most likely due to a stabilization of the negative charge state of the  $\text{SiV}^-$ . The limitation of spin coherence by resonant coupling to a spin bath in combination with the need of electron donors to create bright  $\text{SiV}^-$  centres highlights the importance of a thorough sample fabrication study to fabricate  $\text{SiV}^-$  samples with optimized optical as well as spin coherence properties.

**Ultrafast all-optical Coherent control** To overcome the limit of short coherence times for QIP applications of the  $\text{SiV}^-$  we then demonstrated for the first time coherent control of the orbital degree of freedom of a single  $\text{SiV}^-$  solely relying on ultrafast optical fields and remedying the need for magnetic fields. As a first experiment we realized full resonant control over a qubit consisting of a ground and an excited state level of the  $\text{SiV}^-$  by driving Rabi oscillations and Ramsey interference on one of the four ZPL transitions using 12 ps laser pulses. From these Rabi curves we also determined a transition dipole moment of  $\mu_C=14.3\text{D}$  and a quantum efficiency of  $\Phi=29.6\%$  for the strongest ZPL transition between the lowest ground and excited state. To utilize the full ground state coherence time of the  $\text{SiV}^-$ , we then also demonstrated full sub-cycle control of a qubit based solely on  $\text{SiV}^-$  ground state levels using a single 1 ps off-resonant Raman control pulse driving two-photon Rabi oscillations as well as Raman-based Ramsey interference. These techniques enable the use of the  $\text{SiV}^-$  for local QIP applications despite its short coherence time and in principle allow for the realization of thousands of qubit gate operations within one coherence period.

### 6.2.2 $\text{SiV}^-$ ensembles

Since the inversion symmetry of the  $\text{SiV}^-$  enables the fabrication of dense ensemble samples featuring homogeneities which are outstanding for solid state systems, we also extended the coherent manipulation techniques developed for single  $\text{SiV}^-$  centres to ensembles with the long-term goal of developing a Raman quantum memory. We theoretically estimated the storage efficiency and storage time of such a memory relying on the currently available and fully unoptimized ensemble samples. By calculating the Raman coupling we estimated a read-in efficiency of slightly less than 50% for the Sternschulte ensemble consisting of an only about 300 nm thick homoepitaxially grown diamond layer with an estimated  $\text{SiV}^-$  density of  $10^{13}\text{SiV}^-/\text{cm}^3$ . This already underlines the great potential of  $\text{SiV}^-$  ensembles for high-efficiency memory applications. Moreover, we estimated a storage time by relating the distribution of optical transition frequencies caused by static crystal strain to the distribution of two-photon transitions between the two orbital  $\text{SiV}^-$  ground states. The calculation indicates that with the currently available samples storage times on the order of 100 ps are feasible, limited by dephasing caused by the inhomogeneous broadening of about  $\delta\nu=10\text{GHz}$ . Our theory outlines that this improves quadratically for narrower broadenings. As a first proof-of-principle experiment using pulsed fields to coherently manipulate an  $\text{SiV}^-$  ensemble we performed a resonant Ramsey interference experiment. We used this to determine whether the available optical power suffices to manipulate the ensemble and to validate our optical Bloch equation model for ensembles. From these simulations we extract an excited state coherence time of about  $T_2^*=65(8)\text{ps}$ , again limited by the inhomogeneous broadening. Next, we performed resonant Hahn-echo experiments with the intend to counteract the dephasing induced by the inhomogeneous broadening. Already a simple three-pulse echo sequence lead to an improvement of the coherence time by a factor of three with  $T_2=187(31)\text{ps}$ . Similar sequences acting on the two-photon transitions can be included in future memory protocols to further prolong storage times. To explore the Raman-based manipulation of the orbital ground states of the ensemble we performed STIRAP measurements using strong control as well as signal fields with about 12 ps duration. Transfer efficiencies of 57% from the lower into

the upper ground state have been achieved, limited by the initialization fidelity and the available energy of the Raman pulses as indicated by our theoretical model. Finally, as another step towards the realization of a quantum memory, we decreased the power in one of the Raman beams of the STIRAP experiment to the nW level and measured the absorption of the beam transmitted through the ensemble in the presence of a strong control pulse. This corresponds to the memory read-in process and absorptions of over 90% have been reached. In addition to the absorption we also found a process causing signal gain depending on the relative phase of both Raman fields. This is most likely caused by either a four-wave-mixing process or a stimulated Raman scattering pumped by the strong control field. We tentatively attribute the phase dependence as a result of a closed interaction contour in the  $\Lambda$ -scheme (making it a  $\Delta$ -scheme) due to phonon-assisted transitions between the ground state levels. Based on these experiments also a retrieval of the stored signal photon by a second control pulse appears feasible in future experiments. There ensemble samples with decreased inhomogeneous broadenings should be used to further extent the storage times and to enable faithful separation of the read-out and read-in pulses.

To conclude, the experimental and theoretical investigations presented throughout this thesis provide a detailed picture of the coherence properties of  $\text{SiV}^-$  centres in diamond and lay out a variety of experimental techniques to coherently control their quantum state on ultrafast timescales. Utilizing these, the limiting fast decoherence of the  $\text{SiV}^-$  can be overcome, enabling future experiments towards QIP applications. Perhaps even more importantly, the insights gathered in here help shaping a deeper understanding of the fundamental physics of colour centres in diamond and might enable a targeted search for yet unexplored centres featuring optimal properties for QIP applications.



# Appendices



# Appendix A

## MATLAB scripts & functions

The theoretical models discussed in Chap. 2 and used to analyse the data in Chap. 4 and Chap. 5 have been implemented using MATLAB R2014b (Mathworks Inc.). In the first section of this chapter the functions used to simulate the coherent population trapping and millikelvin experiments while the second section contains code used to simulate the ultrafast coherent control experiments with single SiV<sup>-</sup> centres as well as the experiments involving SiV<sup>-</sup> ensembles. For the sake of brevity all data import, plotting and output parts have been removed and comments have been added for better readability.

### A.1 Simulations of coherent population trapping

#### define optical Bloch equations

```
1 function dy = OBE(t,y,p)
2
3 %initialise output matrix
4 dy=zeros(16,1);
5
6 %*****%
7 %probe detuning for specific time step
8 p.d31= (-p.rng+2*p.rng*t/p.tscan);
9
10 %*****%
11 %density matrix
12 rho = transpose(reshape(y,4,4));
13
14 %*****%
15 %Hamiltonian
16 H = [0, 0, p.r31/2, 0;...
17      0, p.d31-p.d32, p.r32/2, 0;...
18      p.r31/2, p.r32/2, p.d31, 0;...
19      0, 0, 0, 0];
20
21 %*****%
22 %Lindblad operators
23
24 C31=sqrt(p.Gamma31)*[1;0;0;0]*[0,0,1,0];
25 L31=-0.5*(C31'*(C31*rho)+rho*(C31'*C31))+C31*(rho*C31');
26
27 C32=sqrt(p.Gamma32)*[0;1;0;0]*[0,0,1,0];
28 L32=-0.5*(C32'*(C32*rho)+rho*(C32'*C32))+C32*(rho*C32');
```

```

29
30 C34=sqrt(p.Gamma34)*[0;0;0;1]*[0,0,1,0];
31 L34=-0.5*(C34'*(C34*rho)+rho*(C34'*C34))+C34*(rho*C34');
32
33 C43=sqrt(p.Gamma43)*[0;0;1;0]*[0,0,0,1];
34 L43=-0.5*(C43'*(C43*rho)+rho*(C43'*C43))+C43*(rho*C43');
35
36 C41=sqrt(p.Gamma41)*[1;0;0;0]*[0,0,0,1];
37 L41=-0.5*(C41'*(C41*rho)+rho*(C41'*C41))+C41*(rho*C41');
38
39 C42=sqrt(p.Gamma41)*[0;1;0;0]*[0,0,0,1];
40 L42=-0.5*(C42'*(C42*rho)+rho*(C42'*C42))+C42*(rho*C42');
41
42 L=L31+L32+L34+L43+L41+L42;
43
44 %*****
45 %dephasing matrix
46
47 D = -1.*[0,p.gamma21,p.gamma31, 0;...
48 p.gamma21, 0, p.gamma32, 0;...
49 p.gamma31, p.gamma32, 0, 0;...
50 0, 0, 0, 0;];
51
52 D = D.*rho;
53
54 %*****
55 %laser linewidths
56
57 Laser = -1.*[0,p.lrel,p.l31, 0;...
58 p.lrel, 0, p.l32, 0;...
59 p.l31, p.l32, 0, 0;...
60 0, 0, 0, 0;];
61
62 Laser = Laser.*rho;
63
64 %*****
65 %Master equation
66
67 rho_dot = 1i*(rho*H-H*rho) + L + D + Laser;
68
69 %return OBEs to main script
70 for a=1:4
71     for b=1:4
72         dy((4*a-4)+b) = rho_dot(a,b);
73     end
74 end

```

## solve optical Bloch equations

```

1 %calculate energies of states and intensities from group theoretical model
2 %input parameters for group theoretical model
3 B=0.73;
4 temp=12;
5 G1=310;
6 G2=210;
7 tg=0.15*pi;
8 pg=0.5*pi;
9 te=0.05*pi;
10 pe=0.0*pi;
11 tB=109;
12 f=0.1;
13 delta=0;
14 eta=200*0.7*(-(0.8 - 0.5)+(0.7 - 0.5)*1i);

```

```

15
16 %call group theoretical model
17 e = sivmodel(B,temp,G1,G2,tg,pg,te,pe,tB,f,delta,eta);
18
19 %%energy splittings between:
20 %D and C,B,A to approximate rates between |aux> and |3>
21 deltae43=(abs(e.ee(1,1)-e.ee(3,1))+abs(e.ee(1,1)-e.ee(2,1))...
22 +abs(e.ee(1,1)-e.ee(4,1)))/3;
23 %|1> and |2>
24 deltae21=abs(e.eg(4,1)-e.eg(3,1));
25
26 %normalize to transition D1
27 e.int=e.int./e.int(4,1);
28
29 %%relative transition dipole moments from group theory
30 mu31 = e.int(8,1);
31 mu32 = e.int(4,1);
32 %sum over all transitions except D1 and D2
33 mu34 = sum(e.int(:,1))-e.int(4,1)-e.int(8,1);
34 %sum over transitions A1,B1,C1
35 mu41 = e.int(1,1)+e.int(2,1)+e.int(3,1);
36 %sum over transitions A2,B2,C2
37 mu42 = e.int(5,1)+e.int(6,1)+e.int(7,1);
38
39 %*****
40 %%laser parameters
41 psat31 = 0.72; %probe transition saturation power (muW) (D2)
42 psat32 = 0.33; %pump transition saturation power (muW) (D1)
43 p31 = 0.33; %probe power (muW) (D2)
44 p32 = 0.33; %pump power (muW) (D1)
45 p.r31 = 2*pi*64; %probe Rabi frequency (MHz)
46 p.r32 = p.r31*(p32/p31)*(psat31/psat32); %pump Rabi frequency (MHz)
47 p.d32 = -11.5; %pump detuning (MHz)
48 p.l31 = 2*pi*0.1; %probe laser linewidth (MHz)
49 p.l32 = 2*pi*0.1; %pump laser linewidth (MHz)
50 p.lrel = 2*pi*5; %measured relative laser coherence (MHz)
51
52 %*****
53 %spontaneous decay rates
54 tauex = 1.66e-9; %excited state lifetime (s)
55 Gamma = ((1/tauex)*1e-6)/sum(e.int(:,1)); %common scaling rate
56 %rates
57 p.Gamma31=mu31*Gamma;
58 p.Gamma32=mu32*Gamma;
59 p.Gamma34=mu34*Gamma;
60 p.Gamma43=p.Gamma34*exp(-((deltae43)/(20.83*temp)));
61 p.Gamma41=mu41*Gamma;
62 p.Gamma42=mu42*Gamma;
63 p.Gamma21=0;
64 p.Gamma12=p.Gamma21*exp(-((deltae21)/(20.83*temp)));
65
66 %*****
67 %dephasing rates
68 p.gamma21=2*pi*3.5;
69 p.gamma31=2*pi*3250;
70 p.gamma32=2*pi*3250;
71
72 %*****
73 %scan parameters
74 inttime = 500; %integration time per point (mus)
75 numpoints = 5*300; %number of points in the experiment
76 p.rng = 5*350; %scan range (MHz)
77 p.tscan = inttime*numpoints; %scan duration

```

```

78 tint=0:(inttime):p.tscan;          %time trace vector for OBE solver
79
80 %*****
81 %solve Optical Bloch Equations
82 atol=1e-6*ones(1,16);
83 options = odeset('RelTol',1e-6,'AbsTol',atol);
84 init=zeros(1,16);init(1)=1;
85
86 tic
87 [T,Y] = ode23s(@(t,y) openlambda(t,y,p), tint,init,options);
88 toc
89
90 %*****
91 %prepare frequency x-axis
92 freq = -(p.rng/2)+T./T(end)*p.rng; %convert time trace to frequencies
93
94 %*****
95 %extract populations from OBE solutions
96
97 s1=real(Y(:,1));
98 s2=real(Y(:,6));
99 s3=real(Y(:,11));
100 s4=real(Y(:,16));

```

## A.2 Coherent control and ensemble simulations

### define optical Bloch equations

```

1 function dy = OBE(t,y,p)
2
3 dy=zeros(16,1);
4
5 omega=200;
6
7 p.r31 = 2*pi*0;
8 p.r32 = 2*pi*0;
9 p.r41 = 2*pi*0;
10 p.r42 = 2*pi*0;
11
12 w=0.015;
13
14 p.r311=p.amp*(w^2/(w^2+(2*t-2*p.t01)^2));
15 p.r312=p.amp2*(w^2/(w^2+(2*t-2*p.t02)^2));
16 p.r313=p.amp*(w^2/(w^2+(2*t-2*p.t03)^2));
17 p.r31=p.r311+p.r312+p.r313;
18
19 %Density matrix
20 rho = transpose(reshape(y,4,4));
21
22 %Hamiltonian
23 H = [0, 0, p.r31*exp(1i*omega*t), p.r41*exp(1i*omega*t);...
24 0, p.d31-p.d32, p.r32*exp(1i*omega*t), p.r42*exp(1i*omega*t);...
25 p.r31*exp(-1i*omega*t), p.r32*exp(-1i*omega*t), p.d31, 0;...
26 p.r41*exp(-1i*omega*t), p.r42*exp(-1i*omega*t), 0, p.d31+p.d32];
27
28 %Decoherence matrix
29
30 C31=sqrt(p.Gamma31)*[1;0;0;0]*[0,0,1,0];
31 L31=-0.5*(C31'*(C31*rho)+rho*(C31'*C31))+C31*(rho*C31');
32
33 C32=sqrt(p.Gamma32)*[0;1;0;0]*[0,0,1,0];
34 L32=-0.5*(C32'*(C32*rho)+rho*(C32'*C32))+C32*(rho*C32');

```

```

35
36 C34=sqrt(p.Gamma34)*[0;0;0;1]*[0,0,1,0];
37 L34=-0.5*(C34'*(C34*rho)+rho*(C34'*C34))+C34*(rho*C34');
38
39 C43=sqrt(p.Gamma43)*[0;0;1;0]*[0,0,0,1];
40 L43=-0.5*(C43'*(C43*rho)+rho*(C43'*C43))+C43*(rho*C43');
41
42 C41=sqrt(p.Gamma41)*[1;0;0;0]*[0,0,0,1];
43 L41=-0.5*(C41'*(C41*rho)+rho*(C41'*C41))+C41*(rho*C41');
44
45 C42=sqrt(p.Gamma41)*[0;1;0;0]*[0,0,0,1];
46 L42=-0.5*(C42'*(C42*rho)+rho*(C42'*C42))+C42*(rho*C42');
47
48 C21=sqrt(p.Gamma21)*[1;0;0;0]*[0,1,0,0];
49 L21=-0.5*(C21'*(C21*rho)+rho*(C21'*C21))+C21*(rho*C21');
50
51 C12=sqrt(p.Gamma12)*[0;1;0;0]*[1,0,0,0];
52 L12=-0.5*(C12'*(C12*rho)+rho*(C12'*C12))+C12*(rho*C12');
53
54 L=L31+L32+L34+L43+L41+L42+L21+L12;
55
56 D = -1.*[0,p.gamma21,p.gamma31, 0;...
57 p.gamma21, 0, p.gamma32, 0;...
58 p.gamma31, p.gamma32, 0, p.gamma43;...
59 0, 0, p.gamma43, 0;];
60
61 D = D.*rho;
62
63 Laser = -1.*[0,p.lrel,p.l31, 0;...
64 p.lrel, 0, p.l32, 0;...
65 p.l31, p.l32, 0, 0;...
66 0, 0, 0, 0;];
67
68 Laser = Laser.*rho;
69
70 %Liouville equation
71 rho_dot = 1i*(rho*H-H*rho) + L + D + Laser;
72
73 %return OBEs to main script
74 for a=1:4
75 for b=1:4
76 dy((4*a-4)+b) = rho_dot(a,b);
77 end
78 end

```

## solve optical Bloch equations

```

1 | %calculate energies of states and intensities from group theoretical model
2 | %input parameters for group theoretical model
3 | B=0; temp=5 ;G1=308;G2=206;tg=0.15*pi;pg=0*pi;te=0.05*pi;pe=0.0*pi;tB=109;f
   | =0.1;delta=0;eta=0;
4 | %call group theoretical model
5 | e = sivmodel(B,temp,G1,G2,tg,pg,te,pe,tB,f,delta,eta);
6 |
7 | %splittings
8 | deltae43=2*pi*259;
9 | deltae21=2*pi*48;
10 |
11 | p.r31 = 2*pi*0;
12 | p.r32 = 2*pi*0;
13 | p.r41 = 2*pi*0;
14 | p.r42 = 2*pi*0;
15 |

```

```

16 p.d31 = 0;
17 p.d32 = 0;
18 p.dex = deltae21;
19
20 p.l31 = 2*pi*4e-3;
21 p.l32 = 2*pi*4e-3;
22 p.lrel = 2*pi*1e-3;
23
24 %spontaneous decay rates
25 Gamma = ((1/1.85));
26 p.Gamma31=0.459*Gamma;
27 p.Gamma32=0.303*Gamma;
28 p.Gamma43=1/0.24;
29 p.Gamma34=p.Gamma43*exp(-((deltae43)/(20.83*temp)));
30 p.Gamma41=0.09*Gamma;
31 p.Gamma42=0.15*Gamma;
32 p.Gamma21=2*pi*3.5*1e-3;
33 p.Gamma12=p.Gamma21*exp(-(48/(20.83*temp)));
34
35 %dephasing rates
36 p.gamma21=2*pi*0.0035;
37 p.gamma31=2*pi*1.2;
38 p.gamma32=2*pi*0.0;
39 p.gamma43=2*pi*0;
40
41 tint=0:0.001:5;
42 detu=10;
43 stepsize=1;
44 fwhm=2.2;
45
46 q=1;
47 for n=-1*detu:stepsize:detu
48     p.d31 = 2*pi*n;
49
50     k=1;
51     for j=0.03:0.001:0.2
52
53         p.t01=0.05;
54         p.t02=p.t01+j;
55         p.t03=p.t01+2*j;
56
57         p.amp=38.5;
58         p.amp2=2*38.5;
59
60         atol=1e-5*ones(1,16);
61         options = odeset('RelTol',1e-5,'AbsTol',atol);
62         init=zeros(1,16);init(1)=1;
63
64         [T,Y] = ode45(@(t,y) OBE(t,y,p), tint,init,options);
65
66         %extract populations from OBE solutions
67
68         s1=real(Y(:,1));
69         s2=real(Y(:,6));
70         s3=real(Y(:,11));
71         s4=real(Y(:,16));
72         outx(k,q)=2*j;
73         outy(k,q)=(sum(s3)+sum(s4));
74
75     k=k+1;
76     end
77     q=q+1;
78 end

```

```
79 outges=zeros(length(outy),1);
80
81 j=1;
82 for w=-1*detu:stepsize:detu
83     norm(j,1)=(fwhm^2/(fwhm^2+(2*w)^2));
84     j=j+1;
85 end
86 norm=norm/sum(norm);
87
88 for z=1:(q-1)
89     outges=outges+norm(z,1)*outy(:,z);
90 end
91
92 outges=outges./z;
93 outges=outges./max(outges);
```



## Appendix B

# Transmission & reflection curves

### B.1 Fabry-Pérot etalon properties

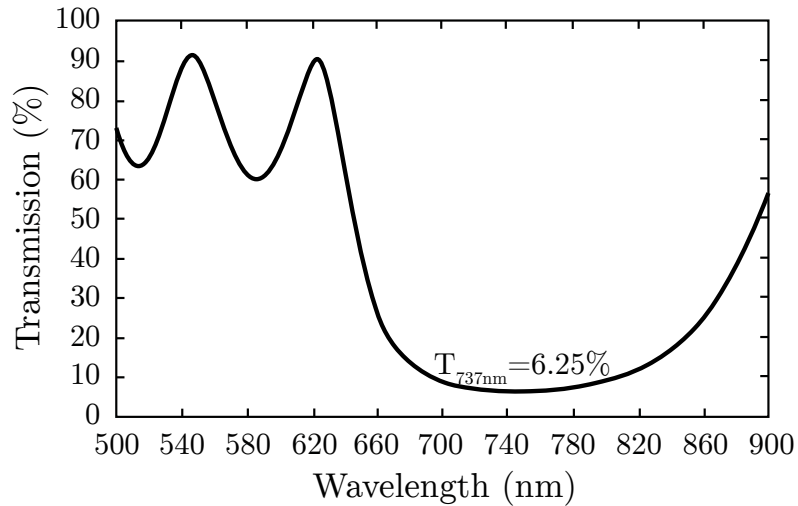


**Figure B.1:** Transmission curve of the Fabry Pérot etalon mirror coatings. At 737 nm a residual transmission of about 6.25% has been measured.

With the transmission curve shown below we obtain a finesse of

$$F = \frac{\pi\sqrt{R}}{1-R} = \frac{\pi\sqrt{0.9375}}{1-0.9375} = 48.67 \quad (\text{B.1})$$

with the specified reflectivity  $R$  at 737 nm. This coating has been applied to planar quartz substrates ( $n=1.455$ ) with thicknesses  $L$  of 50 $\mu\text{m}$ , 100 $\mu\text{m}$ , 300 $\mu\text{m}$  and 500 $\mu\text{m}$ . The resulting

free spectral ranges (FSR) of the etalons are then given by

$$FSR_{50\mu m} = \frac{c}{2nL} = 2060 \text{ GHz} \quad (\text{B.2})$$

$$FSR_{100\mu m} = 1030 \text{ GHz} \quad (\text{B.3})$$

$$FSR_{300\mu m} = 343.4 \text{ GHz} \quad (\text{B.4})$$

$$FSR_{500\mu m} = 206.6 \text{ GHz} \quad (\text{B.5})$$

$$(\text{B.6})$$

and the widths of the etalon modes by

$$\delta\nu_{50\mu m} = \frac{FSR}{F} = 42.33 \text{ GHz} \quad (\text{B.7})$$

$$\delta\nu_{100\mu m} = 21.16 \text{ GHz} \quad (\text{B.8})$$

$$\delta\nu_{300\mu m} = 7.06 \text{ GHz} \quad (\text{B.9})$$

$$\delta\nu_{500\mu m} = 4.25 \text{ GHz} \quad (\text{B.10})$$

$$(\text{B.11})$$

## B.2 Dilution refrigerator windows

The transmission curve shown below displays the properties of the custom-made optical windows used in the dilution refrigerator. Four identical windows have been used in the different layers of radiation shielding and with the reflectivity  $R=0.39\%$  at  $737 \text{ nm}$  we thus estimate a total transmission of  $T=1 - (1 - 0.0039)^4=98.4\%$ .

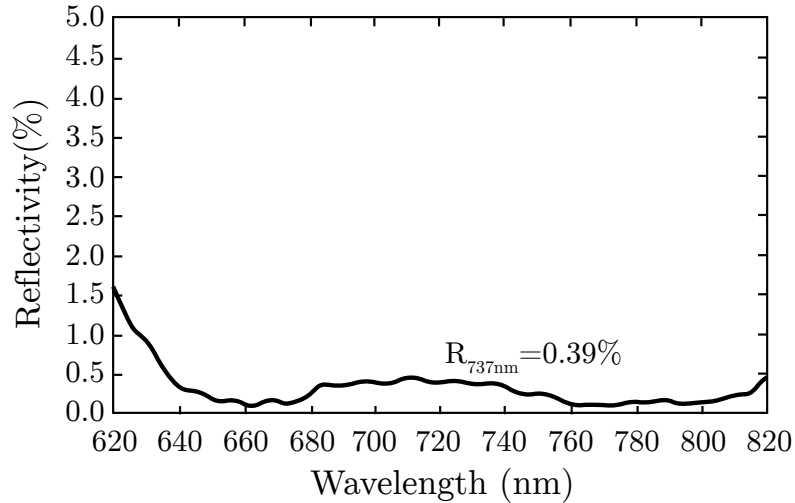


**Figure B.2:** Measured reflectivity of the custom-made windows (EKSMA Optics) used in the dilution refrigerator. At  $737 \text{ nm}$  a residual reflectivity of  $R=0.39\%$  has been measured. Four of these windows have been used in the different layers of heat shielding of the cryostat causing a total transmission of  $T=1 - (1 - 0.0039)^4=98.4\%$ .

# Bibliography

- [1] G. Boole. *The Mathematical Analysis of Logic: Being an Essay Towards a Calculus of Deductive Reasoning*. Cambridge Library Collection (1847).
- [2] C. A. Harper. *Electronic Assembly Fabrication*. McGraw-Hill Professional Engineering (2002).
- [3] G. E. Moore. Cramming more components on to integrated circuits. *Electronics Journal* **38**(8), 114 (1965).
- [4] D. Harel. *Computers LTD: What They Really Can't Do*. Oxford University Press (2003).
- [5] R. Crandall and C. Pomerance. *Prime Numbers*. Springer (2005).
- [6] J. Hromkovic. *Algorithmics for Hard Problems: Introduction to Combinatorial Optimization, Randomization, Approximation, and Heuristics*. Springer (2004).
- [7] R. P. Feynman. Simulating physics with computers. *International Journal of Theoretical Physics* **21**(6), 467 (1982).
- [8] M. M. Waldrop. The chips are down for Moore's law. *Nature* **530**, 144 (2016).
- [9] R. P. Feynman. *Feynman Lectures On Computation*. Westview Press (2000).
- [10] M. Fox. *Quantum Optics*. Oxford University Press (2006).
- [11] B. Schumacher. Quantum coding. *Phys. Rev. A* **51**, 2738 (1995).
- [12] D. Deutsch. Quantum Theory, the Church-Turing Principle and the Universal Quantum Computer. *Proceedings of the Royal Society of London A: Mathematical, Physical and Engineering Sciences* **400**(1818), 97 (1985).
- [13] P. W. Shor. Polynomial-Time Algorithms for Prime Factorization and Discrete Logarithms on a Quantum Computer. *SIAM J. Comput.* **26**(5), 1484 (1997).
- [14] L. K. Grover. A Fast Quantum Mechanical Algorithm for Database Search. *Proceedings of the Twenty-eighth Annual ACM Symposium on Theory of Computing* 212–219 (1996).

- [15] C. H. Bennett and G. Brassard. Quantum cryptography: Public key distribution and coin tossing. *Theoretical Computer Science* **560**, 7 (2014).
- [16] C. L. Degen, F. Reinhard, and P. Cappellaro. Quantum sensing (2016).
- [17] D. P. DiVincenzo. The Physical Implementation of Quantum Computation. *Fortschritte der Physik* **48**(9-11), 771 (2000).
- [18] A. M. Steane. Error Correcting Codes in Quantum Theory. *Phys. Rev. Lett.* **77**, 793 (1996).
- [19] C. Monroe, D. M. Meekhof, B. E. King, W. M. Itano, and D. J. Wineland. Demonstration of a Fundamental Quantum Logic Gate. *Phys. Rev. Lett.* **75**, 4714 (1995).
- [20] I. Buluta, S. Ashhab, and F. Nori. Natural and artificial atoms for quantum computation. *Reports on Progress in Physics* **74**(10), 104401 (2011).
- [21] D. L. Moehring, P. Maunz, S. Olmschenk, K. C. Younge, D. N. Matsukevich, L. M. Duan, and C. Monroe. Entanglement of single-atom quantum bits at a distance. *Nature* **449**(7158), 68 (2007).
- [22] R. Blatt and D. Wineland. Entangled states of trapped atomic ions. *Nature* **453**(7198), 1008 (2008).
- [23] J. V. Porto, S. Rolston, B. Laburthe Tolra, C. J. Williams, and W. D. Phillips. Quantum information with neutral atoms as qubits. *Philosophical Transactions of the Royal Society of London A: Mathematical, Physical and Engineering Sciences* **361**(1808), 1417 (2003).
- [24] M. Atatüre, J. Dreiser, A. Badolato, A. Högele, K. Karrai, and A. Imamoglu. Quantum-dot spin-state preparation with near-unity fidelity. *Science* **312**(5773), 551 (2006).
- [25] D. Press, T. D. Ladd, B. Zhang, and Y. Yamamoto. Complete quantum control of a single quantum dot spin using ultrafast optical pulses. *Nature* **456**(7219), 218 (2008).
- [26] P. Neumann, N. Mizuochi, F. Rempp, P. Hemmer, H. Watanabe, S. Yamasaki, V. Jacques, T. Gaebel, F. Jelezko, and J. Wrachtrup. Multipartite Entanglement Among Single Spins in Diamond. *Science* **320**(5881), 1326 (2008).
- [27] P. Neumann, R. Kolesov, B. Naydenov, J. Beck, F. Rempp, M. Steiner, V. Jacques, G. Balasubramanian, M. L. Markham, D. J. Twitchen, S. Pezzagna, J. Meijer, J. Twamley, F. Jelezko, and J. Wrachtrup. Quantum register based on coupled electron spins in a room-temperature solid. *Nat Phys* **6**(4), 249 (2010).
- [28] M. V. G. Dutt, L. Childress, L. Jiang, E. Togan, J. Maze, F. Jelezko, A. S. Zibrov, P. R. Hemmer, and M. D. Lukin. Quantum Register Based on Individual Electronic and Nuclear Spin Qubits in Diamond. *Science* **316**(5829), 1312 (2007).

- [29] C. Negrevergne, T. S. Mahesh, C. A. Ryan, M. Ditty, F. Cyr-Racine, W. Power, N. Boulant, T. Havel, D. G. Cory, and R. Laflamme. Benchmarking Quantum Control Methods on a 12-Qubit System. *Phys. Rev. Lett.* **96**, 170501 (2006).
- [30] L. M. K. Vandersypen, M. Steffen, G. Breyta, C. S. Yannoni, M. H. Sherwood, and I. L. Chuang. Experimental realization of Shor's quantum factoring algorithm using nuclear magnetic resonance. *Nature* **414**(6866), 883 (2001).
- [31] M. Ansmann, H. Wang, R. C. Bialczak, M. Hofheinz, E. Lucero, M. Neeley, A. D. O'Connell, D. Sank, M. Weides, J. Wenner, A. N. Cleland, and J. M. Martinis. Violation of Bell's inequality in Josephson phase qubits. *Nature* **461**(7263), 504 (2009).
- [32] L. DiCarlo, J. M. Chow, J. M. Gambetta, L. S. Bishop, B. R. Johnson, D. I. Schuster, J. Majer, A. Blais, L. Frunzio, S. M. Girvin, and R. J. Schoelkopf. Demonstration of two-qubit algorithms with a superconducting quantum processor. *Nature* **460**(7252), 240 (2009).
- [33] T. D. Ladd, F. Jelezko, R. Laflamme, Y. Nakamura, C. Monroe, and J. L. O'Brien. Quantum computers. *Nature* **464**(7285), 45 (2010).
- [34] R. Blatt and C. F. Roos. Quantum simulations with trapped ions. *Nat Phys* **8**(4), 277 (2012).
- [35] C. Wang, C. Kurtsiefer, H. Weinfurter, and B. Burchard. Single photon emission from SiV centres in diamond produced by ion implantation. *Journal of Physics B: Atomic, Molecular and Optical Physics* **39**(1), 37 (2006).
- [36] A. M. Zaitsev. *Optical Properties of Diamond: A Data Handbook*. Springer (2001).
- [37] R. C. Burns, A. I. Chumakov, S. H. Connell, D. Dube, H. P. Godfried, J. O. Hansen, J. Härtwig, J. Hoszowska, F. Masiello, L. Mkhonza, M. Rebak, A. Rommevaux, R. Setshedi, and P. Van Vaerenbergh. HPHT growth and x-ray characterization of high-quality type IIa diamond. *Journal of Physics: Condensed Matter* **21**(36), 364224 (2009).
- [38] J. J. Gracio, Q. H. Fan, and J. C. Madaleno. Diamond growth by chemical vapour deposition. *Journal of Physics D: Applied Physics* **43**(37), 374017 (2010).
- [39] K. Nakamura, S. Yamashita, T. Tojo, M. Mitsuishi, K. Kataoka, and M. Yoshimoto. Single-crystal synthesis of highly thermal conductive  $^{12}\text{C}$ -enriched diamond from pyrolytic carbon powder by the high-pressure, high-temperature method. *Diamond and Related Materials* **16**(9), 1765 (2007).
- [40] G. Balasubramanian, P. Neumann, D. J. Twitchen, M. Markham, R. Kolesov, N. Mizuochi, J. Isoya, J. Achard, J. Beck, J. Tessler, V. Jacques, P. R. Hemmer, F. Jelezko, and J. Wrachtrup. Ultralong spin coherence time in isotopically engineered diamond. *Nat Mater* **8**(5), 383 (2009).

- [41] J. Riedrich-Moller, L. Kipfstuhl, C. Hepp, E. Neu, C. Pauly, F. Mücklich, A. Baur, M. Wandt, S. Wolff, M. Fischer, S. Gsell, M. Schreck, and C. Becher. One- and two-dimensional photonic crystal microcavities in single crystal diamond. *Nat Nano* **7**(1), 69 (2012).
- [42] A. Sipahigil, R. E. Evans, D. D. Sukachev, M. J. Burek, J. Borregaard, M. K. Bhaskar, C. T. Nguyen, J. L. Pacheco, H. A. Atikian, C. Meuwly, R. M. Camacho, F. Jelezko, E. Bielejec, H. Park, M. Lončar, and M. D. Lukin. An integrated diamond nanophotonics platform for quantum-optical networks. *Science* **354**(6314), 847 (2016).
- [43] T. Schröder, S. L. Mouradian, J. Zheng, M. E. Trusheim, M. Walsh, E. H. Chen, L. Li, I. Bayn, and D. Englund. Quantum nanophotonics in diamond. *J. Opt. Soc. Am. B* **33**(4), B65 (2016).
- [44] C. D. Clark and C. A. Norris. Photoluminescence associated with the 1.673, 1.944 and 2.498 eV centres in diamond. *Journal of Physics C: Solid State Physics* **4**(14), 2223 (1971).
- [45] J. R. Maze, A. Gali, E. Togan, Y. Chu, T. A., E. Kaxiras, and M. D. Lukin. Properties of nitrogen-vacancy centers in diamond: the group theoretic approach. *New Journal of Physics* **13**(2), 025025 (2011).
- [46] M. W. Doherty, N. B. Manson, P. Delaney, and L. C. L. Hollenberg. The negatively charged nitrogen-vacancy centre in diamond: the electronic solution. *New Journal of Physics* **13**(2), 025019 (2011).
- [47] A. Dréau, M. Lesik, L. Rondin, P. Spinicelli, O. Arcizet, J.-F. Roch, and V. Jacques. Avoiding power broadening in optically detected magnetic resonance of single NV defects for enhanced dc magnetic field sensitivity. *Phys. Rev. B* **84**, 195204 (2011).
- [48] T. Wolf, P. Neumann, K. Nakamura, H. Sumiya, T. Ohshima, J. Isoya, and J. Wrachtrup. Subpicotesla Diamond Magnetometry. *Phys. Rev. X* **5**, 041001 (2015).
- [49] D. Drung, C. Abmann, J. Beyer, A. Kirste, M. Peters, F. Ruede, and T. Schurig. Highly Sensitive and Easy-to-Use SQUID Sensors. *IEEE Transactions on Applied Superconductivity* **17**(2), 699 (2007).
- [50] P. Neumann, J. Beck, M. Steiner, F. Rempp, H. Fedder, P. R. Hemmer, J. Wrachtrup, and F. Jelezko. Single-Shot Readout of a Single Nuclear Spin. *Science* **329**(5991), 542 (2010).
- [51] V. M. Huxter, T. A. A. Oliver, D. Budker, and G. R. Fleming. Vibrational and electronic dynamics of nitrogen-vacancy centres in diamond revealed by two-dimensional ultrafast spectroscopy. *Nat Phys* **9**(11), 744 (2013).
- [52] H. Bernien, L. Childress, L. Robledo, M. Markham, D. Twitchen, and R. Hanson. Two-Photon Quantum Interference from Separate Nitrogen Vacancy Centers in Diamond. *Phys. Rev. Lett.* **108**, 043604 (2012).

- [53] B. Hensen, H. Bernien, A. E. Dreau, A. Reiserer, N. Kalb, M. S. Blok, J. Ruitenbergh, R. F. L. Vermeulen, R. N. Schouten, C. Abellan, W. Amaya, V. Pruneri, M. W. Mitchell, M. Markham, D. J. Twitchen, D. Elkouss, S. Wehner, T. H. Taminiau, and R. Hanson. Loophole-free Bell inequality violation using electron spins separated by 1.3 kilometres. *Nature* **526**(7575), 682 (2015).
- [54] R. Albrecht, A. Bommer, C. Deutsch, J. Reichel, and C. Becher. Coupling of a Single Nitrogen-Vacancy Center in Diamond to a Fiber-Based Microcavity. *Phys. Rev. Lett.* **110**, 243602 (2013).
- [55] E. Neu, D. Steinmetz, J. Riedrich-Möller, S. Gsell, M. Fischer, M. Schreck, and C. Becher. Single photon emission from silicon-vacancy colour centres in chemical vapour deposition nano-diamonds on iridium. *New Journal of Physics* **13**(2), 025012 (2011).
- [56] E. Neu, M. Fischer, S. Gsell, M. Schreck, and C. Becher. Fluorescence and polarization spectroscopy of single silicon vacancy centers in heteroepitaxial nanodiamonds on iridium. *Phys. Rev. B* **84**, 205211 (2011).
- [57] C. Hepp, T. Müller, V. Waselowski, J. N. Becker, B. Pingault, H. Sternschulte, D. Steinmüller-Nethl, A. Gali, J. R. Maze, M. Atatüre, and C. Becher. Electronic Structure of the Silicon Vacancy Color Center in Diamond. *Phys. Rev. Lett.* **112**, 036405 (2014).
- [58] C. Hepp. *Electronic Structure of the Silicon Vacancy Color Center in Diamond*. Ph.D. thesis, Universität des Saarlandes (2014).
- [59] A. Sipahigil, K. D. Jahnke, L. J. Rogers, T. Teraji, J. Isoya, A. S. Zibrov, F. Jelezko, and M. D. Lukin. Indistinguishable Photons from Separated Silicon-Vacancy Centers in Diamond. *Phys. Rev. Lett.* **113**, 113602 (2014).
- [60] L. C. Bassett, F. J. Heremans, D. J. Christle, C. G. Yale, G. Burkard, B. B. Buckley, and D. D. Awschalom. Ultrafast optical control of orbital and spin dynamics in a solid-state defect. *Science* (2014).
- [61] G. D. Fuchs, V. V. Dobrovitski, D. M. Toyli, F. J. Heremans, and D. D. Awschalom. Gigahertz Dynamics of a Strongly Driven Single Quantum Spin. *Science* **326**(5959), 1520 (2009).
- [62] H. Sternschulte, K. Thonke, J. Gerster, W. Limmer, R. Sauer, J. Spitzer, and P. J. Münzinger. Uniaxial stress and Zeeman splitting of the 1.681 eV optical center in a homoepitaxial CVD diamond film. *Diamond and Related Materials* **4**(10), 1189 (1995).
- [63] W. K. Wootters and W. H. Zurek. A single quantum cannot be cloned. *Nature* **299**(5886), 802 (1982).
- [64] K.-J. Boller, I. A., and S. E. Harris. Observation of electromagnetically induced transparency. *Phys. Rev. Lett.* **66**, 2593 (1991).

- [65] M. Nilsson and S. Kröll. Solid state quantum memory using complete absorption and re-emission of photons by tailored and externally controlled inhomogeneous absorption profiles. *Optics Communications* **247**(4-6), 393 (2005).
- [66] M. Afzelius, C. Simon, H. de Riedmatten, and N. Gisin. Multimode quantum memory based on atomic frequency combs. *Phys. Rev. A* **79**, 052329 (2009).
- [67] A. E. Kozhekin, K. Mølmer, and E. Polzik. Quantum memory for light. *Phys. Rev. A* **62**, 033809 (2000).
- [68] R. W. G. Wyckoff. *Crystal Structures*. Interscience Publishers (1963).
- [69] W. Saslow, T. K. Bergstresser, and M. L. Cohen. Band Structure and Optical Properties of Diamond. *Phys. Rev. Lett.* **16**, 354 (1966).
- [70] G. Peckham. The phonon dispersion relation for diamond. *Solid State Communications* **5**(4), 311 (1967).
- [71] L. S. Pan and D. R. Kania. *Diamond: Electronic Properties and Applications*. Springer (1995).
- [72] H. Clevenston, M. E. Trusheim, C. Teale, T. Schröder, D. Braje, and D. Englund. Broadband magnetometry and temperature sensing with a light-trapping diamond waveguide. *Nat Phys* **11**(5), 393 (2015).
- [73] T. M. Babinec, H. B. J. M., M. Khan, Y. Zhang, J. R. Maze, P. R. Hemmer, and M. Loncar. A diamond nanowire single-photon source. *Nat Nano* **5**(3), 195 (2010).
- [74] S. Praver and I. Aharonovich. *Quantum Information Processing with Diamond*. Woodhead Publishing (2014).
- [75] R. Gross and A. Marx. *Festkörperphysik*. Oldenburg Verlag (2012).
- [76] M. Lax. *Symmetry principles in solid state and molecular physics*. Wiley-Interscience (1974).
- [77] G. Davies. The Jahn-Teller effect and vibronic coupling at deep levels in diamond. *Reports on Progress in Physics* **44**(7), 787 (1981).
- [78] E. Ehrlich and W. Dan Hausel. *Diamond Deposits: Origin, Exploration, and History of Discovery*. Society for Mining, Metallurgy, and Exploration (2002).
- [79] F. P. Bundy. The P, T phase and reaction diagram for elemental carbon, 1979. *Journal of Geophysical Research: Solid Earth* **85**(B12), 6930 (1980).
- [80] G. E. Harlow. *The Nature of Diamonds*. Cambridge University Press (1998).
- [81] I. I. Vlasov, A. A. Shiryayev, T. Rendler, S. Steinert, S.-Y. Lee, D. Antonov, M. Voros, F. Jelezko, A. V. Fisenko, L. F. Semjonova, J. Biskupek, U. Kaiser, O. I. Lebedev, I. Sildos, P. R. Hemmer, V. I. Konov, A. Gali, and J. Wrachtrup. Molecular-sized fluorescent nanodiamonds. *Nat Nano* **9**(1), 54 (2014).

- [82] D. W. Olson. *2011 Minerals Yearbook*. U.S. Geological Survey (2011).
- [83] R. Robertson, J. J. Fox, and A. E. Martin. Two Types of Diamond. *Philosophical Transactions of the Royal Society of London A: Mathematical, Physical and Engineering Sciences* **232**(707-720), 463 (1934).
- [84] J. Walker. Optical absorption and luminescence in diamond. *Reports on Progress in Physics* **42**(10), 1605 (1979).
- [85] H. P. Bovenkerk, F. P. Bundy, H. T. Hall, H. M. Strong, and R. H. Wentorf. Preparation of Diamond. *Nature* **184**(4693), 1094 (1959).
- [86] H. Sumiya and S. Satoh. High-pressure synthesis of high-purity diamond crystal. *Diamond and Related Materials* **5**(11), 1359 (1996).
- [87] R. S. Balmer, J. R. Brandon, S. L. Clewes, H. K. Dhillon, J. M. Dodson, I. Friel, P. N. Inglis, T. D. Madgwick, M. L. Markham, T. P. Mollart, N. Perkins, G. A. Scarsbrook, D. J. Twitchen, A. J. Whitehead, J. J. Wilman, and S. M. Woollard. Chemical vapour deposition synthetic diamond: materials, technology and applications. *Journal of Physics: Condensed Matter* **21**(36), 364221 (2009).
- [88] T. Teraji. Chemical vapor deposition of homoepitaxial diamond films. *physica status solidi (a)* **203**(13), 3324 (2006).
- [89] S. Gsell, T. Bauer, J. Goldfuß, M. Schreck, and B. Stritzker. A route to diamond wafers by epitaxial deposition on silicon via iridium/yttria-stabilized zirconia buffer layers. *Applied Physics Letters* **84**(22), 4541 (2004).
- [90] C. D. Clark, H. Kanda, I. Kiflawi, and G. Sittas. Silicon defects in diamond. *Phys. Rev. B* **51**, 16681 (1995).
- [91] J. P. Goss, R. Jones, S. J. Breuer, P. R. Briddon, and S. Öberg. The Twelve-Line 1.682 eV Luminescence Center in Diamond and the Vacancy-Silicon Complex. *Phys. Rev. Lett.* **77**, 3041 (1996).
- [92] U. F. S. D'Haenens-Johansson, A. M. Edmonds, B. L. Green, M. E. Newton, G. Davies, P. M. Martineau, R. U. A. Khan, and D. J. Twitchen. Optical properties of the neutral silicon split-vacancy center in diamond. *Phys. Rev. B* **84**, 245208 (2011).
- [93] S. S. Moliver. Electronic structure of neutral silicon-vacancy complex in diamond. *Technical Physics* **48**(11), 1449 (2003).
- [94] K. Iakoubovskii, G. J. Adriaenssens, M. Nesládek, and L. M. Stals. Photoluminescence excitation and quenching spectra in CVD diamond films. *Diamond and Related Materials* **8**(2), 717 (1999).
- [95] B. C. Rose, D. Huang, Z.-H. Zhang, A. M. Tyryshkin, S. Sangtawesin, S. Srinivasan, L. Loudin, M. L. Markham, A. M. Edmonds, D. J. Twitchen, A. S. Lyon, and N. P.

- de Leon. Observation of an environmentally insensitive solid state spin defect in diamond. *arXiv* 1706.01555 (2017).
- [96] V. Vavilov, A. Gippius, A. Zaitsev, B. S. B. Deryagin, and A. Aleksenko. Investigation of the cathodoluminescence of epitaxial diamond films. *Sov. Phys. Semicond.* **14**, 1078 (1980).
- [97] A. M. Zaitsev, V. S. Vavilov, and A. A. Gippius. Cathodoluminescence of diamond associated with silicon impurity. *Sov. Phys. Leb. Inst. Rep* **10**, 15 (1981).
- [98] A. T. Collins, M. Kamo, and Y. Sato. A spectroscopic study of optical centers in diamond grown by microwave-assisted chemical vapor deposition. *Journal of Materials Research* **5**(11), 2507 (1990).
- [99] J. Ruan, W. J. Choyke, and W. D. Partlow. Si impurity in chemical vapor deposited diamond films. *Applied Physics Letters* **58**(3), 295 (1991).
- [100] A. M. Edmonds, M. E. Newton, P. M. Martineau, D. J. Twitchen, and S. D. Williams. Electron paramagnetic resonance studies of silicon-related defects in diamond. *Phys. Rev. B* **77**, 245205 (2008).
- [101] C. Clark and C. Dickerson. The 1.681 eV centre in polycrystalline diamond. *Surface and Coatings Technology* **47**(1), 336 (1991).
- [102] J. Franck and E. G. Dymond. Elementary processes of photochemical reactions. *Trans. Faraday Soc.* **21**, 536 (1926).
- [103] E. Condon. A Theory of Intensity Distribution in Band Systems. *Phys. Rev.* **28**, 1182 (1926).
- [104] V. Hizhnyakov. Zero-phonon line: Effect of quadratic electron-phonon coupling. *Chemical Physics Letters* **493**(1), 191 (2010).
- [105] E. Togan, Y. Chu, A. S. Trifonov, L. Jiang, J. Maze, L. Childress, M. V. G. Dutt, A. S. Sorensen, P. R. Hemmer, A. S. Zibrov, and M. D. Lukin. Quantum entanglement between an optical photon and a solid-state spin qubit. *Nature* **466**(7307), 730 (2010).
- [106] H. Bernien, B. Hensen, W. Pfaff, G. Koolstra, M. S. Blok, L. Robledo, T. H. Taminiau, M. Markham, D. J. Twitchen, L. Childress, and R. Hanson. Heralded entanglement between solid-state qubits separated by three metres. *Nature* **497**(7447), 86 (2013).
- [107] K. Iakoubovskii and G. J. Adriaenssens. Optical detection of defect centers in cvd diamond. *Diamond and Related Materials* **9**(7), 1349 (2000).
- [108] K. Iakoubovskii, G. J. Adriaenssens, and M. Nesladek. Photochromism of vacancy-related centres in diamond. *Journal of Physics: Condensed Matter* **12**(2), 189 (2000).

- [109] L. J. Rogers, K. D. Jahnke, M. W. Doherty, A. Dietrich, L. P. McGuinness, C. Müller, T. Teraji, H. Sumiya, J. Isoya, N. B. Manson, and F. Jelezko. Electronic structure of the negatively charged silicon-vacancy center in diamond. *Phys. Rev. B* **89**, 235101 (2014).
- [110] A. Gali and J. R. Maze. An Ab initio study on split silicon-vacancy defect in diamond: electronic structure and related properties. *Phys. Rev. B* **88**, 235205 (2013).
- [111] S. Häußler, G. Thiering, A. Dietrich, N. Waasem, T. Teraji, J. Isoya, T. Iwasaki, M. Hatano, F. Jelezko, A. Gali, and A. Kubanek. Photoluminescence excitation spectroscopy of  $\text{SiV}^-$  and  $\text{GeV}^-$  color center in diamond. *arXiv* 1705.10486 (2017).
- [112] J. N. Becker. *Spectroscopic investigation and theoretical modeling of the electronic structure of the silicon vacancy colour centre in diamond*. Master's thesis, Universität des Saarlandes (2013).
- [113] S. W. Brown and S. C. Rand. Site symmetry analysis of the 738 nm defect in diamond. *Journal of Applied Physics* **78**(6), 4069 (1995).
- [114] H. Sternschulte, K. Thonke, R. Sauer, P. C. Münzinger, and P. Michler. 1.681eV luminescence center in chemical-vapor-deposited homoepitaxial diamond films. *Phys. Rev. B* **50**, 14554 (1994).
- [115] A. Dietrich, K. D. Jahnke, J. M. Binder, T. Teraji, J. Isoya, L. J. Rogers, and F. Jelezko. Isotopically varying spectral features of silicon-vacancy in diamond. *New Journal of Physics* **16**(11), 113019 (2014).
- [116] A. A. Gorokhovskiy, A. V. Turukhin, R. R. Alfano, and W. Phillips. Photoluminescence vibrational structure of Si center in chemical-vapor deposited diamond. *Applied Physics Letters* **66**(1), 43 (1995).
- [117] A. T. Collins, L. Allers, C. J. H. Wort, and G. A. Scarsbrook. The annealing of radiation damage in De Beers colourless CVD diamond. *Diamond and Related Materials* **3**(4), 932 (1994).
- [118] T. Feng and B. D. Schwartz. Characteristics and origin of the 1.681 eV luminescence center in chemical- vapor-deposition diamond films. *Journal of Applied Physics* **73**(3), 1415 (1993).
- [119] E. Neu. *Silicon vacancy color centers in chemical vapor deposition diamond: New insights into promising solid state single photon sources*. Ph.D. thesis, Universität des Saarlandes (2012).
- [120] E. Neu, C. Hepp, M. Hauschild, S. Gsell, M. Fischer, H. Sternschulte, D. Steinmüller-Nethl, M. Schreck, and C. Becher. Low-temperature investigations of single silicon vacancy colour centres in diamond. *New Journal of Physics* **15**(4), 043005 (2013).
- [121] K. D. Jahnke, S. A., J. M. Binder, M. W. Doherty, M. M., L. J. Rogers, N. B. Manson, M. D. Lukin, and F. Jelezko. Electron-phonon processes of the silicon-vacancy centre in diamond. *New Journal of Physics* **17**(4), 043011 (2015).

- [122] K. D. Jahnke. *Low temperature spectroscopy of single colour centres in diamond*. Ph.D. thesis, Universität Ulm (2015).
- [123] H. A. Jahn and E. Teller. Stability of polyatomic molecules in degenerate electronic states. i. orbital degeneracy. *Proceedings of the Royal Society of London. Series A, Mathematical and Physical Sciences* **161**(905), 220 (1937).
- [124] M. Tinkham. *Group theory and quantum mechanics*. Dover Publications (1964).
- [125] T. Müller, C. Hepp, B. Pingault, E. Neu, S. Gsell, M. Schreck, H. Sternschulte, D. Steinmüller-Nethl, C. Becher, and M. Atatüre. Optical signatures of silicon-vacancy spins in diamond. *Nat. Commun.* **5**, 3328 (2014).
- [126] E. Neu, M. Agio, and C. Becher. Photophysics of single silicon vacancy centers in diamond: implications for single photon emission. *Opt. Express* **20**(18), 19956 (2012).
- [127] E. Neu, R. Albrecht, M. Fischer, S. Gsell, M. Schreck, and C. Becher. Electronic transitions of single silicon vacancy centers in the near-infrared spectral region. *Phys. Rev. B* **85**, 245207 (2012).
- [128] M. A. Nielsen and I. L. Chuang. *Quantum Computation and Quantum Information*. Cambridge University Press (2011).
- [129] R. Loudon. *The Quantum theory of Light*. Oxford Science Publications (2001).
- [130] B. W. Shore. *Manipulating Quantum Structures Using Laser Pulses*. Cambridge University Press (2011).
- [131] P. Meystre and M. Sargent. *Elements of Quantum Optics*. Springer (1998).
- [132] I. I. Rabi. Space Quantization in a Gyration Magnetic Field. *Phys. Rev.* **51**, 652 (1937).
- [133] L. F. Shampine and M. W. Reichelt. The MATLAB ODE Suite. *SIAM Journal on Scientific Computing* **18**, 1 (1997).
- [134] R. P. Mildren and J. R. Rabeau. *Optical Engineering of Diamond*. Wiley-VCH (2013).
- [135] N. F. Ramsey. A Molecular Beam Resonance Method with Separated Oscillating Fields. *Phys. Rev.* **78**, 695 (1950).
- [136] E. L. Hahn. Spin Echoes. *Phys. Rev.* **80**, 580 (1950).
- [137] S. M. Clark, K.-M. C. Fu, Q. Zhang, T. D. Ladd, C. Stanley, and Y. Yamamoto. Ultrafast Optical Spin Echo for Electron Spins in Semiconductors. *Phys. Rev. Lett.* **102**, 247601 (2009).
- [138] D. Suter and G. A. Álvarez. Colloquium: Protecting quantum information against environmental noise. *Rev. Mod. Phys.* **88**, 041001 (2016).

- [139] H. Y. Carr and E. M. Purcell. Effects of Diffusion on Free Precession in Nuclear Magnetic Resonance Experiments. *Phys. Rev.* **94**, 630 (1954).
- [140] S. Meiboom and D. Gill. Modified Spin-Echo Method for Measuring Nuclear Relaxation Times. *Review of Scientific Instruments* **29**(8), 688 (1958).
- [141] A. M. Souza, G. A. Alvarez, and D. Suter. Robust dynamical decoupling. *Philosophical Transactions of the Royal Society of London A: Mathematical, Physical and Engineering Sciences* **370**(1976), 4748 (2012).
- [142] M. Fleischhauer, A. Imamoglu, and J. P. Marangos. Electromagnetically induced transparency: Optics in coherent media. *Rev. Mod. Phys.* **77**, 633 (2005).
- [143] S. Barnett and P. Radmore. *Methods in Theoretical Quantum Optics*. Oxford Science Publications (2002).
- [144] S. H. Autler and C. H. Townes. Stark Effect in Rapidly Varying Fields. *Phys. Rev.* **100**, 703 (1955).
- [145] G. Alzetta, A. Gozzini, L. Moi, and G. Orriols. An experimental method for the observation of r.f. transitions and laser beat resonances in oriented Na vapour. *Il Nuovo Cimento B* **36**(1), 5 (1976).
- [146] S. Khan, M. P. Kumar, V. Bharti, and V. Natarajan. Coherent population trapping (CPT) versus electromagnetically induced transparency (EIT). *The European Physical Journal D* **71**(2), 38 (2017).
- [147] A. Lazoudis, T. Kirova, E. H. Ahmed, L. Li, J. Qi, and A. M. Lyyra. Electromagnetically induced transparency in an open  $\Lambda$ -type molecular lithium system. *Phys. Rev. A* **82**, 023812 (2010).
- [148] K. Bergmann, N. V. Vitanov, and B. W. Shore. Perspective: Stimulated Raman adiabatic passage: The status after 25 years. *The Journal of Chemical Physics* **142**(17), 170901 (2015).
- [149] B. W. Shore. *The Theory of Coherent Atomic Excitation*. Wiley-VCH (1990).
- [150] J. H. Eberly, L. Mandel, and E. Wolf. *Coherence and Quantum Optics VII: Proceedings of the Seventh Rochester Conference on Coherence and Quantum Optics*. Springer (1995).
- [151] E. Brion, L. H. Pedersen, and K. Mølmer. Adiabatic elimination in a lambda system. *Journal of Physics A: Mathematical and Theoretical* **40**(5), 1033 (2007).
- [152] D. V. Kosachiov, B. G. Matisov, and Y. V. Rozhdestvensky. Coherent phenomena in multilevel systems with closed interaction contour. *Journal of Physics B: Atomic, Molecular and Optical Physics* **25**(11), 2473 (1992).
- [153] J. W. Dally and W. F. Riley. *Experimental Stress Analysis*. McGraw-Hill Inc. (1991).

- [154] A. R. Lang. Causes of Birefringence in Diamond. *Nature* **213**(5073), 248 (1967).
- [155] I. Vlasov, V. Ralchenko, D. Zakharov, and N. Zakharov. Intrinsic Stress Origin in High Quality CVD Diamond Films. *physica status solidi (a)* **174**(1), 11 (1999).
- [156] C. Santori, P. E. Barclay, K.-M. C. Fu, R. G. Beausoleil, S. Spillane, and M. Fisch. Nanophotonics for quantum optics using nitrogen-vacancy centers in diamond. *Nanotechnology* **21**(27), 274008 (2010).
- [157] J. F. Ziegler, M. Ziegler, and J. Biersack. SRIM, The stopping and range of ions in matter (2010). *Nuclear Instruments and Methods in Physics Research Section B: Beam Interactions with Materials and Atoms* **268**(11–12), 1818 (2010). 19th International Conference on Ion Beam Analysis.
- [158] M. T. Robinson. The binary collision approximation: Background and introduction. *Radiation Effects and Defects in Solids* **0**(1), 3 (1994).
- [159] J. Koike, D. M. Parkin, and T. E. Mitchell. Displacement threshold energy for type IIa diamond. *Applied Physics Letters* **60**(12), 1450 (1992).
- [160] J. Riedrich-Möller, S. Pezzagna, J. Meijer, C. Pauly, F. Mücklich, M. Markham, A. M. Edmonds, and C. Becher. Nanoimplantation and Purcell enhancement of single nitrogen-vacancy centers in photonic crystal cavities in diamond. *Applied Physics Letters* **106**(22), 221103 (2015).
- [161] O. Lehtinen, B. Naydenov, P. Börner, K. Melentjevic, C. Müller, L. P. McGuinness, S. Pezzagna, J. Meijer, U. Kaiser, and F. Jelezko. Molecular dynamics simulations of shallow nitrogen and silicon implantation into diamond. *Phys. Rev. B* **93**, 035202 (2016).
- [162] P. R. Hanley, M. R. Cleland, C. F. Mason, K. H. Morganstern, and C. C. Thompson. The Tandem Dynamitron. *IEEE Transactions on Nuclear Science* **16**(3), 90 (1969).
- [163] G. D. Alton. High-intensity, heavy negative ion sources based on the sputter principle. *Review of Scientific Instruments* **65**(4), 1141 (1994).
- [164] C. Uzan-Saguy, C. Cytermann, R. Brener, V. Richter, M. Shaanan, and R. Kalish. Damage threshold for ion-beam induced graphitization of diamond. *Applied Physics Letters* **67**(9), 1194 (1995).
- [165] S. Osswald, G. Yushin, V. Mochalin, S. O. Kucheyev, and Y. Gogotsi. Control of sp<sup>2</sup>/sp<sup>3</sup> Carbon Ratio and Surface Chemistry of Nanodiamond Powders by Selective Oxidation in Air. *Journal of the American Chemical Society* **128**(35), 11635 (2006).
- [166] E. Neu and C. Becher. Diamond-based single-photon sources and their application in quantum key distribution. In S. Praver and A. I., editors, *Quantum Information Processing with Diamond*, chapter 6, 127–159. Woodhead Publishing (2014).
- [167] P. Fuchs. *Theoretische und praktische Implementierung nanophotonischer Strukturen in Diamant*. Master’s thesis, Universität des Saarlandes (2015).

- [168] W. L. Barnes, G. Björk, J. M. Gérard, P. Jonsson, J. A. Wasey, P. T. Worthing, and V. Zwiller. Solid-state single photon sources: light collection strategies. *Eur. Phys. J. D* **18**(2), 197 (2002).
- [169] J. P. Hadden, J. P. Harrison, A. C. Stanley-Clarke, L. Marseglia, Y.-L. D. Ho, B. R. Patton, J. L. O'Brien, and J. G. Rarity. Strongly enhanced photon collection from diamond defect centers under microfabricated integrated solid immersion lenses. *Applied Physics Letters* **97**(24), 241901 (2010).
- [170] P. Siyushev, F. Kaiser, V. Jacques, I. Gerhardt, S. Bischof, H. Fedder, J. Dodson, M. Markham, D. Twitchen, F. Jelezko, and J. Wrachtrup. Monolithic diamond optics for single photon detection. *Applied Physics Letters* **97**(24), 241902 (2010).
- [171] L. Marseglia, J. P. Hadden, A. C. Stanley-Clarke, J. P. Harrison, B. Patton, Y.-L. D. Ho, B. Naydenov, F. Jelezko, J. Meijer, P. R. Dolan, J. M. Smith, J. G. Rarity, and J. L. O'Brien. Nanofabricated solid immersion lenses registered to single emitters in diamond. *Applied Physics Letters* **98**(13), 133107 (2011).
- [172] I. Friel, S. Clewes, H. Dhillon, N. Perkins, D. Twitchen, and G. Scarsbrook. Control of surface and bulk crystalline quality in single crystal diamond grown by chemical vapour deposition. *Diamond and Related Materials* **18**(5–8), 808 (2009).
- [173] S. Koizumi, C. Nebel, and M. Nesladek. *Physics and Applications of CVD Diamond*. Wiley-VCH Verlag GmbH (2008).
- [174] H. Okushi. High quality homoepitaxial CVD diamond for electronic devices. *Diamond and Related Materials* **10**(3–7), 281 (2001).
- [175] V. S. Sedov, I. I. Vlasov, V. G. Ralchenko, A. A. Khomich, V. I. Konov, A. G. Fabbri, and G. Conte. Gas-phase growth of silicon-doped luminescent diamond films and isolated nanocrystals. *Bulletin of the Lebedev Physics Institute* **38**(10), 291 (2011).
- [176] A. Bolshakov, V. Ralchenko, V. Sedov, A. Khomich, I. Vlasov, A. Khomich, N. Trofimov, V. Krivobok, S. Nikolaev, R. Khmel'nitskii, and V. Saraykin. Photoluminescence of SiV centers in single crystal CVD diamond in situ doped with Si from silane. *physica status solidi (a)* **212**(11), 2525 (2015).
- [177] S. Praver and R. J. Nemanich. Raman spectroscopy of diamond and doped diamond. *Philosophical Transactions of the Royal Society of London A: Mathematical, Physical and Engineering Sciences* **362**(1824), 2537 (2004).
- [178] D. Kirillov and G. J. Reynolds. Linewidths of phonon lines of natural and synthetic diamonds. *Applied Physics Letters* **65**(13), 1641 (1994).
- [179] R. H. Webb. Confocal optical microscopy. *Reports on Progress in Physics* **59**(3), 427 (1996).
- [180] L. Novotny and B. Hecht. *Principles of Nano-Optics*. Cambridge University Press (2012).

- [181] S. Wilhelm, G. B., M. Gluch, and H. Heinz. *Die konfokale Laser Scanning Mikroskopie*. Carl Zeiss Mikroskopsysteme, Jena (2003).
- [182] R. W. P. Drever, J. L. Hall, F. V. Kowalski, J. Hough, G. M. Ford, A. J. Munley, and H. Ward. Laser phase and frequency stabilization using an optical resonator. *Applied Physics B* **31**(2), 97 (1983).
- [183] P. McMillan, B. Piriou, and R. Couty. A Raman study of pressure-densified vitreous silica. *The Journal of Chemical Physics* **81**(10), 4234 (1984).
- [184] R. Hanbury Brown and R. Q. Twiss. A Test of a New Type of Stellar Interferometer on Sirius. *Nature* **178**(4541), 1046 (1956).
- [185] D. W. Pohl. Dynamic piezoelectric translation devices. *Rev. Sci. Instrum.* **58**, 54 (1987).
- [186] E. L. Wooten, K. M. Kissa, A. Yi-Yan, E. J. Murphy, D. A. Lafaw, P. F. Hallemeier, D. Maack, D. V. Attanasio, D. J. Fritz, G. J. McBrien, and D. E. Bossi. A review of lithium niobate modulators for fiber-optic communications systems. *IEEE Journal of Selected Topics in Quantum Electronics* **6**(1), 69 (2000).
- [187] G. Batey and G. Teleberg. *Principles of dilution refrigeration: A brief technology guide*. Oxford Instruments NanoScience (2015).
- [188] F. Pobell. *Matter and Methods at Low Temperatures*. Springer Verlag (2007).
- [189] R. N. Richardson and E. B. E. A review of pulse tube refrigeration. *International Journal of Refrigeration* **20**(5), 367 (1997).
- [190] H. London, G. R. Clarke, and E. Mendoza. Osmotic Pressure of  $^3\text{He}$  in Liquid  $^4\text{He}$ , with Proposals for a Refrigerator to work below 1K. *Phys. Rev.* **128**, 1992 (1962).
- [191] G. L. Pollack. Kapitza Resistance. *Rev. Mod. Phys.* **41**, 48 (1969).
- [192] L. M. García, J. Chaboy, F. Bartolomé, and J. B. Goedkoop. Orbital Magnetic Moment Instability at the Spin Reorientation Transition of  $\text{Nd}_2\text{Fe}_{14}\text{B}$ . *Phys. Rev. Lett.* **85**, 429 (2000).
- [193] S. R. Trout. *Technical Note: Using Permanent Magnets at Low Temperatures*. Arnold (2003).
- [194] C. Bödefeld and S. Falk. *Technical Note (TN04): Number of Wires for Different Positioner Combinations*. attocube systems AG (2015).
- [195] C. Bödefeld. *Technical Note (TN03): Wiring of an attocube Piezo Positioner and Effects of Resistive Wiring*. attocube systems AG (2015).
- [196] G. R. Huggett. Mode-locking of cw lasers by regenerative RF feedback. *Applied Physics Letters* **13**(5), 186 (1968).

- [197] B. Golubovic, R. R. Austin, M. K. Steiner-Shepard, M. K. Reed, S. A. Diddams, D. J. Jones, and A. G. Van Engen. Double Gires–Tournois interferometer negative-dispersion mirrors for use in tunable mode-locked lasers. *Opt. Lett.* **25**(4), 275 (2000).
- [198] J. Görlitz. *Experimentelle Untersuchung der Eignung von SiV-Zentren in Diamant als Quantenspeicher*. Master’s thesis, Universität des Saarlandes (2016).
- [199] B. Pingault, J. N. Becker, C. H. H. Schulte, C. Arend, C. Hepp, T. Godde, A. I. Tartakovskii, M. Markham, C. Becher, and M. Atatüre. All-Optical Formation of Coherent Dark States of Silicon-Vacancy Spins in Diamond. *Phys. Rev. Lett.* **113**, 263601 (2014).
- [200] J. N. Becker, J. Görlitz, C. Arend, M. Markham, and C. Becher. Ultrafast all-optical coherent control of single silicon vacancy colour centres in diamond. *Nature Communications* **7**, 13512 (2016).
- [201] C. Wang. *A Solid-State Single Photon Source Based on Color Centers in Diamond*. Ph.D. thesis, Universität des Saarlandes (2007).
- [202] S. Singh and S. A. Catledge. Silicon vacancy color center photoluminescence enhancement in nanodiamond particles by isolated substitutional nitrogen on (111) surfaces. *Journal of Applied Physics* **113**(4), 044701 (2013).
- [203] R. E. Evans, A. Sipahigil, D. D. Sukachev, A. S. Zibrov, and M. D. Lukin. Narrow-Linewidth Homogeneous Optical Emitters in Diamond Nanostructures via Silicon Ion Implantation. *Phys. Rev. Applied* **5**, 044010 (2016).
- [204] S. Tamura, G. Koike, A. Komatsubara, T. Teraji, S. Onoda, L. P. McGuinness, L. Rogers, B. Naydenov, E. Wu, L. Yan, F. Jelezko, T. Ohshima, J. Isoya, T. Shinada, and T. Tanii. Array of bright silicon-vacancy centers in diamond fabricated by low-energy focused ion beam implantation. *Applied Physics Express* **7**(11), 115201 (2014).
- [205] U. Jantzen, A. B. Kurz, D. S. Rudnicki, C. Schäfermeier, K. D. Jahnke, U. L. Andersen, V. A. Davydov, V. N. Agafonov, A. Kubanek, L. J. Rogers, and F. Jelezko. Nanodiamonds carrying silicon-vacancy quantum emitters with almost lifetime-limited linewidths. *New Journal of Physics* **18**(7), 073036 (2016).
- [206] L. J. Rogers, K. D. Jahnke, M. H. Metsch, A. Sipahigil, J. M. Binder, T. Teraji, H. Sumiya, J. Isoya, M. D. Lukin, P. Hemmer, and F. Jelezko. All-Optical Initialization, Readout, and Coherent Preparation of Single Silicon-Vacancy Spins in Diamond. *Phys. Rev. Lett.* **113**, 263602 (2014).
- [207] S. Zaske, A. Lenhard, C. A. Kefler, J. Kettler, C. Hepp, C. Arend, R. Albrecht, W.-M. Schulz, M. Jetter, P. Michler, and C. Becher. Visible-to-Telecom Quantum Frequency Conversion of Light from a Single Quantum Emitter. *Phys. Rev. Lett.* **109**, 147404 (2012).

- [208] B. Pingault, D.-D. Jarausch, C. Hepp, L. Klintberg, J. N. Becker, M. Markham, C. Becher, and M. Atatüre. Coherent control of the silicon-vacancy spin in diamond. *Nature Communications* **8**, 15579 (2017).
- [209] A. Albrecht, A. Retzker, F. Jelezko, and M. B. Plenio. Coupling of nitrogen vacancy centres in nanodiamonds by means of phonons. *New Journal of Physics* **15**(8), 083014 (2013).
- [210] L. Kipfstuhl, F. Guldner, J. Riedrich-Möller, and C. Becher. Modeling of optomechanical coupling in a phoxonic crystal cavity in diamond. *Opt. Express* **22**(10), 12410 (2014).
- [211] C. Arend, J. N. Becker, H. Sternschulte, D. Steinmüller-Nethl, and C. Becher. Photoluminescence excitation and spectral hole burning spectroscopy of silicon vacancy centers in diamond. *Phys. Rev. B* **94**, 045203 (2016).
- [212] Y.-I. Sohn, S. Meesala, B. Pingault, H. A. Atikian, J. Holzgrafe, M. Gundogan, C. Stavrakas, M. J. Stanley, A. Sipahigil, J. Choi, M. Zhang, J. L. Pacheco, J. Abraham, E. Bielejec, M. D. Lukin, M. Atatüre, and M. Loncar. Engineering a diamond spin-qubit with a nano-electro-mechanical system (2017).
- [213] J.-M. Cai, B. Naydenov, R. Pfeiffer, L. P. McGuinness, K. D. Jahnke, F. Jelezko, M. B. Plenio, and A. Retzker. Robust dynamical decoupling with concatenated continuous driving. *New Journal of Physics* **14**(11), 113023 (2012).
- [214] N. D. Bhaskar, J. Camparo, W. Happer, and A. Sharma. Light narrowing of magnetic resonance lines in dense, optically pumped alkali-metal vapor. *Phys. Rev. A* **23**, 3048 (1981).
- [215] S. Appelt, A. Ben-Amar Baranga, A. R. Young, and W. Happer. Light narrowing of rubidium magnetic-resonance lines in high-pressure optical-pumping cells. *Phys. Rev. A* **59**, 2078 (1999).
- [216] K. Jensen, V. M. Acosta, A. Jarmola, and D. Budker. Light narrowing of magnetic resonances in ensembles of nitrogen-vacancy centers in diamond. *Phys. Rev. B* **87**, 014115 (2013).
- [217] K. N. Shrivastava. Theory of Spin-Lattice Relaxation. *physica status solidi (b)* **117**(2), 437 (1983).
- [218] A. Abragam and B. Bleaney. *Electron Paramagnetic Resonance of Transition Ions*. Oxford University Press (2012).
- [219] L. Bogani and W. Wernsdorfer. Molecular spintronics using single-molecule magnets. *Nat Mater* **7**(3), 179 (2008).
- [220] C. Kutter, H. P. Moll, J. van Tol, H. Zuckermann, J. C. Maan, and P. Wyder. Electron-Spin Echoes at 604 GHz Using Far Infrared Lasers. *Phys. Rev. Lett.* **74**, 2925 (1995).

- [221] S. Takahashi, R. Hanson, J. van Tol, M. S. Sherwin, and D. D. Awschalom. Quenching Spin Decoherence in Diamond through Spin Bath Polarization. *Phys. Rev. Lett.* **101**, 047601 (2008).
- [222] R. Hanson, O. Gywat, and D. D. Awschalom. Room-temperature manipulation and decoherence of a single spin in diamond. *Phys. Rev. B* **74**, 161203 (2006).
- [223] P. Hu and S. R. Hartmann. Theory of spectral diffusion decay using an uncorrelated-sudden-jump model. *Phys. Rev. B* **9**, 1 (1974).
- [224] Y. V. Babich and B. N. Feigelson. Distribution of nitrogen-related defects in diamond single crystals grown under nonisothermal conditions. *Inorganic Materials* **42**(9), 971 (2006).
- [225] T. Schröder, M. E. Trusheim, M. Walsh, L. Li, J. Zheng, M. Schukraft, A. Sipahigil, R. E. Evans, D. D. Sukachev, C. T. Nguyen, J. L. Pacheco, R. M. Camacho, E. S. Bielejec, M. D. Lukin, and D. Englund. Scalable focused ion beam creation of nearly lifetime-limited single quantum emitters in diamond nanostructures. *Nature Communications* **8**, 15376 (2017).
- [226] K. M. Etmimi, P. R. Briddon, A. M. Abutruma, A. Sghayer, and F. S. S. Density functional theory study of substitutional oxygen in diamond. *Cond. Mat. Phys.* **19**, 33301 (2016).
- [227] S. D., J. Adler, and R. Kalish. Sulfur: A potential donor in diamond. *Applied Physics Letters* **77**(6), 878 (2000).
- [228] W. Nagourney, J. Sandberg, and H. Dehmelt. Shelved optical electron amplifier: Observation of quantum jumps. *Phys. Rev. Lett.* **56**, 2797 (1986).
- [229] C. Wolpert. *Ultrafast spectroscopy of a single quantum dot*. Ph.D. thesis, Universität Stuttgart (2012).
- [230] M. J. Booth and T. Wilson. Refractive-index-mismatch induced aberrations in single-photon and two-photon microscopy and the use of aberration correction. *Journal of Biomedical Optics* **6**(3), 266 (2001).
- [231] R. C. Hilborn. Einstein coefficients, cross sections, f values, dipole moments, and all that. *American Journal of Physics* **50**(11), 982 (1982).
- [232] J. Riedrich-Möller. *Deterministic coupling of single color centers to monolithic photonic crystal cavities in single crystal diamond*. Ph.D. thesis, Universität des Saarlandes (2014).
- [233] Y. Wu. Effective Raman theory for a three-level atom in the  $\Lambda$  configuration. *Phys. Rev. A* **54**, 1586 (1996).
- [234] K.-M. C. Fu, S. M. Clark, C. Santori, C. R. Stanley, M. C. Holland, and Y. Yamamoto. Ultrafast control of donor-bound electron spins with single detuned optical pulses. *Nat Phys* **4**(10), 780 (2008).

- [235] S. E. Harris and Y. Yamamoto. Photon Switching by Quantum Interference. *Phys. Rev. Lett.* **81**, 3611 (1998).
- [236] K. Heshami, D. G. England, P. C. Humphreys, P. J. Bustard, V. M. Acosta, J. Nunn, and B. J. Sussman. Quantum memories: emerging applications and recent advances. *Journal of Modern Optics* **63**(20), 2005 (2016).
- [237] V. M. Akulin. *Coherent Dynamics of Complex Quantum Systems*. Springer (2006).
- [238] J. Nunn, I. A. Walmsley, M. G. Raymer, K. Surmacz, F. C. Waldermann, Z. Wang, and D. Jaksch. Mapping broadband single-photon wave packets into an atomic memory. *Phys. Rev. A* **75**, 011401 (2007).
- [239] K. F. Reim, J. Nunn, V. O. Lorenz, B. J. Sussman, K. C. Lee, N. K. Langford, D. Jaksch, and I. A. Walmsley. Towards high-speed optical quantum memories. *Nat Photon* **4**(4), 218 (2010).
- [240] K. C. Lee. *Generation of room-temperature entanglement in diamond with broadband pulses*. Ph.D. thesis, University of Oxford (2012).
- [241] E. Poem, C. Weinzetl, J. Klatzow, K. T. Kaczmarek, J. H. D. Munns, T. F. M. Champion, D. J. Saunders, J. Nunn, and I. A. Walmsley. Broadband noise-free optical quantum memory with neutral nitrogen-vacancy centers in diamond. *Phys. Rev. B* **91**, 205108 (2015).
- [242] K. Heshami, C. Santori, B. Khanaliloo, C. Healey, V. M. Acosta, P. E. Barclay, and C. Simon. Raman quantum memory based on an ensemble of nitrogen-vacancy centers coupled to a microcavity. *Phys. Rev. A* **89**, 040301 (2014).
- [243] J. Nunn. *Quantum Memory in Atomic Ensembles*. Ph.D. thesis, University of Oxford (2008).
- [244] J. Klein, F. Beil, and T. Halfmann. Robust Population Transfer by Stimulated Raman Adiabatic Passage in a  $\text{Pr}^{3+}:\text{Y}_2\text{SiO}_5$  Crystal. *Phys. Rev. Lett.* **99**, 113003 (2007).
- [245] P. S. Michelberger, T. F. M. Champion, M. R. Sprague, K. T. Kaczmarek, M. Barbieri, X. M. Jin, D. G. England, W. S. Kolthammer, D. J. Saunders, J. Nunn, and I. A. Walmsley. Interfacing GHz-bandwidth heralded single photons with a warm vapour Raman memory. *New Journal of Physics* **17**(4), 043006 (2015).
- [246] D. G. England, K. A. G. Fisher, J.-P. W. MacLean, P. J. Bustard, R. Lausten, K. J. Resch, and B. J. Sussman. Storage and Retrieval of THz-Bandwidth Single Photons Using a Room-Temperature Diamond Quantum Memory. *Phys. Rev. Lett.* **114**, 053602 (2015).
- [247] C. W. Freudiger, W. Min, B. G. Saar, S. Lu, G. R. Holtom, C. He, J. C. Tsai, J. X. Kang, and X. S. Xie. Label-Free Biomedical Imaging with High Sensitivity by Stimulated Raman Scattering Microscopy. *Science* **322**(5909), 1857 (2008).

- [248] R. W. Boyd. *Nonlinear Optics*. Elsevier (2008).
- [249] P. S. Michelberger. Room temperature caesium quantum memory for quantum information applications. *arXiv* 1706.01104 (2017).
- [250] J. D. Franson. Bell inequality for position and time. *Phys. Rev. Lett.* **62**, 2205 (1989).
- [251] J. Brendel, N. Gisin, W. Tittel, and H. Zbinden. Pulsed Energy-Time Entangled Twin-Photon Source for Quantum Communication. *Phys. Rev. Lett.* **82**, 2594 (1999).
- [252] M. A. M. Versteegh, M. E. Reimer, A. A. van den Berg, G. Juska, V. Dimastrodonato, A. Gocalinska, E. Pelucchi, and V. Zwiller. Single pairs of time-bin-entangled photons. *Phys. Rev. A* **92**, 033802 (2015).
- [253] S. Ritter, C. Nolleke, C. Hahn, A. Reiserer, A. Neuzner, M. Uphoff, M. Mücke, E. Figueroa, J. Bochmann, and G. Rempe. An elementary quantum network of single atoms in optical cavities. *Nature* **484**(7393), 195 (2012).
- [254] T. Iwasaki, F. Ishibashi, Y. Miyamoto, Y. Doi, S. Kobayashi, T. Miyazaki, K. Tahara, K. D. Jahnke, L. J. Rogers, B. Naydenov, F. Jelezko, S. Yamasaki, S. Nagamachi, T. Inubushi, N. Mizuochi, and M. Hatano. Germanium-Vacancy Single Color Centers in Diamond. *Scientific Reports* **5**, 12882 (2015).
- [255] M. K. Bhaskar, D. D. Sukachev, A. Sipahigil, R. E. Evans, M. J. Burek, C. T. Nguyen, L. J. Rogers, P. Siyushev, M. H. Metsch, H. Park, F. Jelezko, M. Lončar, and M. D. Lukin. Quantum Nonlinear Optics with a Germanium-Vacancy Color Center in a Nanoscale Diamond Waveguide. *Phys. Rev. Lett.* **118**, 223603 (2017).
- [256] J. E. Lowther. Nickel defect centers in diamond. *Phys. Rev. B* **51**, 91 (1995).
- [257] E. Gheeraert, A. Kumar, E. Bustarret, L. Ranno, L. Magaud, Y. Joly, S. Pascarelli, M. Ruffoni, D. K. Avasthi, and H. Kanda. Investigation of nickel lattice sites in diamond: Density functional theory and x-ray absorption near-edge structure experiments. *Phys. Rev. B* **86**, 054116 (2012).
- [258] K. Iakoubovskii. Ni-vacancy defect in diamond detected by electron spin resonance. *Phys. Rev. B* **70**, 205211 (2004).
- [259] R. Larico, J. F. Justo, W. V. M. Machado, and L. V. C. Assali. Electronic properties and hyperfine fields of nickel-related complexes in diamond. *Phys. Rev. B* **79**, 115202 (2009).
- [260] S. C. Lawson, H. Kanda, and M. Sekita. New nickel-related optical absorption in high-pressure synthetic diamond. *Philosophical Magazine Part B* **68**(1), 39 (1993).



# Publications

## peer-reviewed journal publications

- B. Pingault, D.-D. Jarausch, C. Hepp, L. Klintberg, J. N. Becker, M. Markham, C. Becher, and M. Atatüre, *Coherent control of the silicon-vacancy spin in diamond*, Nature Commun. **8**, 15579 (2017).
- J. N. Becker, J. Görlitz, C. Arend, M. Markham, and C. Becher, *Ultrafast all-optical coherent control of single silicon vacancy colour centres in diamond*, Nature Commun. **7**, 13512 (2016).
- B. Kambs, J. Kettler, M. Bock, J. N. Becker, C. Arend, A. Lenhard, S. L. Portalupi, M. Jetter, P. Michler, and C. Becher, *Low-noise quantum frequency down-conversion of indistinguishable photons*, Opt. Express **24**, 22250 (2016).
- C. Arend, J. N. Becker, H. Sternschulte, D. Steinmüller-Nethl, and C. Becher, *Photoluminescence excitation and spectral hole burning spectroscopy of silicon vacancy centers in diamond*, Phys. Rev. B **94**, 045203 (2016).
- C. Arend, P. Appel, J. N. Becker, M. Schmidt, M. Fischer, S. Gsell, M. Schreck, C. Becher, P. Maletinsky, and E. Neu, *Site selective growth of heteroepitaxial diamond nanoislands containing single SiV centers*, Appl. Phys. Lett. **108**, 063111 (2016).  
*Selected as APL Editor's pick (week of February 21, 2016).*
- B. Pingault\*, J. N. Becker\*, C. H. H. Schulte, C. Arend, C. Hepp, T. Godde, A.I. Tartakovskii, M. Markham, C. Becher, and M. Atatüre, *All-optical formation of coherent dark states of silicon-vacancy spins in diamond*, Phys. Rev. Lett. **113**, 263601 (2014).  
\* equally contributing  
*Editor's suggestion, highlighted as Viewpoint in Physics 7, 131 (2014), selected as one of the Highlights of the Year 2014 in Physics 7, 132 (2014).*
- C. Hepp, T. Müller, V. Waselowski, J. N. Becker, B. Pingault, H. Sternschulte, D. Steinmüller-Nethl, A. Gali, J. R. Maze, M. Atatüre, and C. Becher, *Electronic structure of the silicon vacancy color center in diamond*, Phys. Rev. Lett. **112**, 036405 (2014).

## Review articles

- J. N. Becker and C. Becher, *Ein Netzwerk aus Diamanten*, Physik Journal **16**(2), 18 (2017).

## Invited conference presentations

- J. N. Becker, J. Görlitz, P. Fuchs, T. Jung, E. Neu, C. Arend, and C. Becher, *Coherent Control and Photonic Interfacing of Color Centers in Diamond*, Conference on Lasers and Electro-Optics (CLEO) 2017, San Jose, USA, May 14-19, 2017.
- J. N. Becker, J. Görlitz, C. Arend, M. Markham, and C. Becher, *Coherent control of silicon-vacancy centers in diamond*, Hasselt Diamond Workshop 2017 - SBDD XXII, Hasselt, Belgium, March 8-10, 2017.
- T. Jung, P. Fuchs, L. Kreiner, J. N. Becker, J. Görlitz, and C. Becher, *Photonic structures for interfacing color centers in diamond*, Photonic and Phononic Properties of Engineered Nanostructures VII, (Conference 10112), SPIE Photonics West 2017, San Francisco, CA, USA, January 30-February 02, 2017.
- J. N. Becker, C. Arend, S. Lindner, A. Bommer, T. Jung, and C. Becher, *Spectroscopy and optical interfacing of single color centers in bulk- and nano-diamond*, 2015 MRS Fall Meeting, Symposium DD (Diamond Electronics, Sensors & Biotechnology - Fundamentals to Applications), Boston, MA, USA, November 29-December 04, 2015.
- J. N. Becker, B. Pingault, C. Arend, C. Hepp, J. Riedrich-Möller, M. Atatüre, and C. Becher, *Spin properties and optical interfacing of silicon vacancy color centers in diamond*, Advances in Photonics of Quantum Computing, Memory, and Communication VIII, (Conference 9377), SPIE Photonics West 2015, San Francisco, CA, USA, February 9-12, 2015.
- C. Hepp, T. Müller, V. Waselowski, J. N. Becker, B. Pingault, H. Sternschulte, A. Gali, J. R. Maze, M. Atatüre, and C. Becher, *Electronic structure of the silicon vacancy color center in diamond*, Workshop on Quantum Optics and Spin Dynamics in Few Fermion Systems, University of Konstanz, Germany, February 17-18, 2014.

## Invited seminars

- J. N. Becker, *The silicon vacancy colour centre: A promising system for diamond-based quantum information processing*, Clarendon Laboratory, University of Oxford, Oxford, United Kingdom March 23, 2016.

## Contributed conference talks/proceedings

- J. N. Becker, C. Weinzetl, J. Görlitz, E. Poem, J. Nunn, I. A. Walmsley, and C. Becher, *A silicon vacancy-based broadband optical quantum memory in diamond*, The

- 68<sup>th</sup> Diamond Conference, University of Warwick, UK, July 10-13, 2017.
- J. N. Becker, J. Görliz, C. Arend, C. Weinzetl, E. Poem, J. Nunn, I. A. Walmsley, and C. Becher, *Ultrafast all-optical coherent control of silicon vacancy colour centres in diamond*, CLEO/Europe-EQEC 2017, Munich, Germany, June 25-29, 2017.
  - J. N. Becker, J. Görliz, C. Arend, M. Markham, and C. Becher, *Coherent control of silicon vacancy colour centres in diamond*, Quantum 2017, Torino, Italy, May 07-13, 2017.
  - J. N. Becker, C. Weinzetl, J. Görlitz, E. Poem, J. Nunn, I. A. Walmsley, and C. Becher, *Optical quantum memories with colour centre ensembles in diamond*, DPG Spring Meeting (SAMOP), Johannes Gutenberg-University, Mainz, Germany, March 06-10, 2017.
  - J. N. Becker, J. Görlitz, C. Arend, M. Markham, and C. Becher, *All-optical ultrafast coherent control of single silicon vacancy color centers in diamond*, 2016 MRS Fall Meeting, Symposium EM.12 (Diamond Electronics, Sensors and Biotechnology - Fundamentals to Applications), Boston, MA, USA, November 27-December 02, 2016.
  - J. N. Becker, J. Görlitz, C. Arend, M. Markham, and C. Becher, *All-optical ultrafast coherent control of single silicon vacancy color centers in diamond*, International Conference on Coherent and Nonlinear Optics (ICONO 2016), Minsk, Belarus, September 26-30, 2016.
  - J. N. Becker, J. Görlitz, C. Arend, M. Markham, and C. Becher, *Ultrafast all-optical coherent control of silicon vacancy colour centres in diamond*, Topical Meeting on Single Photons Single Spins (SPSS), Oxford, UK, September 12-13, 2016.
  - J. N. Becker, J. Görlitz, C. Arend, M. Markham, and C. Becher, *All-optical coherent control of single silicon vacancy colour centres in diamond using picosecond laser pulses*, The 67<sup>th</sup> Diamond Conference, University of Warwick, UK, July 11-14, 2016.
  - J. N. Becker, C. Arend, B. Pingault, M. Atatüre, and C. Becher, *Coherent manipulation of silicon vacancy color centers in diamond using picosecond laser pulses*, Hasselt Diamond Workshop 2016, SBDD XXI, Hasselt, Belgium, March 9-11, 2016.
  - J. N. Becker, C. Arend, B. Pingault, C. Hepp, M. Atatüre, and C. Becher, *All-optical coherent control of silicon vacancy color centers in diamond using picosecond laser pulses*, DPG Spring Meeting (SAMOP), Leibnitz University, Hannover, Germany, February 29-March 04, 2016.
  - J. N. Becker, B. Pingault, C. Hepp, C. H. H. Schulte, C. Arend, M. Markham, M. Atatüre, and C. Becher, *Spin coherence properties of silicon-vacancy colour centres containing <sup>28</sup>Si and <sup>29</sup>Si*, The 66<sup>th</sup> Diamond Conference, University of Warwick, UK, July 6-9, 2015.
  - J. N. Becker, B. Pingault, C. Hepp, C. Schulte, C. Arend, M. Markham, M. Atatüre, and C. Becher, *All-Optical Formation of Coherent Dark States in Single Silicon*

*Vacancy Color Centers in Diamond*, CLEO/Europe-EQEC 2015, Munich, Germany, June 21-25, 2015;  
(received an EPS-QEOD Travel Grant Student Award).

- J. N. Becker, B. Pingault, C. Hepp, C. Arend, V. Waselowski, J. Maze, M. Atatüre, and C. Becher, *Spin properties of the silicon-vacancy color center in diamond*, DPG Spring Meeting (SAMOP), Ruprecht-Karls University, Heidelberg, Germany, March 23-27, 2015.
- J. N. Becker, B. Pingault, C. Hepp, C. Arend, V. Waselowski, M. Markham, J. R. Maze, M. Atatüre, and C. Becher, *Electronic properties and spin coherence of silicon-vacancy color centers in diamond containing  $^{28}\text{Si}$  and  $^{29}\text{Si}$* , Hasselt Diamond Workshop 2015, SBDD XX, Hasselt, Belgium, February 25-27, 2015.
- B. Pingault, J. N. Becker, C. Schulte, C. Arend, C. Hepp, T. Godde, A. Tartakovskii, M. Markham, C. Becher, and M. Atatüre, *All-optical formation of coherent dark states of silicon-vacancy spins in diamond*, DPG Spring Meeting (SAMOP), Ruprecht-Karls University, Heidelberg, Germany, March 23-27, 2015.
- E. Neu, P. Appel, M. Schmidt, J. N. Becker, C. Arend, M. Fischer, S. Gsell, M. Schreck, C. Becher, and P. Maletinsky, *Site selective growth of heteroepitaxial diamond nanoislands for single photon emission from SiV centers*, Hasselt Diamond Workshop 2015, SBDD XX, Hasselt, Belgium, February 25-27, 2015.
- C. Hepp, T. Müller, V. Waselowski, B. Pingault, J. N. Becker, A. Gali, J. R. Maze, M. Atatüre, and C. Becher, *Spin in silicon vacancy color centers in diamond*, Condensed Matter in Paris 2014, CMD25-JMC14, Paris, France, August 24-29, 2014.
- J. N. Becker, C. Hepp, T. Müller, V. Waselowski, B. Pingault, A. Gali, J. R. Maze, M. Atatüre, and C. Becher, *The electronic structure of the silicon vacancy color center in diamond*, The 65<sup>th</sup> Diamond Conference, University of Warwick, UK, July 7-10, 2014;  
(received best oral presentation award).
- J. N. Becker, C. Hepp, T. Müller, V. Waselowski, B. Pingault, H. Sternschulte, A. Gali, J. Maze, M. Atatüre, and C. Becher, *Electronic structure of the silicon vacancy color center in diamond*, DPG Spring Meeting (SAMOP), Humboldt University, Berlin, Germany, March 17-21, 2014.
- C. Arend, C. Hepp, J. Becker, and C. Becher, *Photoluminescence excitation and spectral hole burning spectroscopy of silicon vacancy centers in diamond*, DPG Spring Meeting (SAMOP), Humboldt University, Berlin, Germany, March 17-21, 2014.
- C. Hepp, T. Müller, V. Waselowski, J. N. Becker, B. Pingault, A. Gali, J. R. Maze, M. Atatüre, and C. Becher, *The electronic structure of the silicon vacancy color center*, Hasselt Diamond Workshop 2014, SBDD XIX, Hasselt, Belgium, February 19-21, 2014.

## Contributed conference posters

- C. Weinzetl, J. N. Becker, J. Görlitz, E. Poem, J. Klatzow, P. Ledingham, D. J. Saunders, I. A. Walmsley, C. Becher, and J. Nunn, *Localized Orbital Electronic States of Colour Centres in Diamond for Strong and Fast Light-Matter Interactions*, CLEO/Europe-EQEC 2017, Munich, Germany, June 25-29, 2017.
- D. Groß, J. N. Becker, C. Arend, P. Bushev, and C. Becher, *Towards quantum optical experiments with silicon vacancy color centers in diamond at millikelvin temperatures*, DPG Spring Meeting (SAMOP), Johannes Gutenberg-University, Mainz, Germany, March 06-10, 2017.
- C. Stavrakas, B. Pingault, C. Hepp, T. Müller, M. Gündogan, J. N. Becker, C. Schulte, C. Arend, T. Godde, A. Tartakovskii, M. Markham, C. Becher, E. Neu, S. Gsell, M. Schreck, H. Sternschulte, D. Steinmüller-Nethl, M. Atatüre, *Silicon-vacancy: a colourful defect of diamond as solid-state single-spin for quantum information*, International Conference on Quantum Communication, Measurement and Computing (QCMC 2016), National University of Singapore, Singapore, July 4-8, 2016.
- J. Görlitz, J. N. Becker, E. Poem, J. Nunn, I. A. Walmsley, and C. Becher, *A silicon vacancy-based quantum memory in diamond*, DPG Spring Meeting (SAMOP), Leibnitz University, Hannover, Germany, February 29-March 04, 2016.
- B. Pingault, J. N. Becker, C. H. H. Schulte, C. Arend, C. Hepp, T. Godde, A. I. Tartakovskii, M. Markham, C. Becher and M. Atatüre, *All-optical formation of coherent dark states of silicon-vacancy spins in diamond*, Hasselt Diamond Workshop 2015, SBDD XX, Hasselt, Belgium, February 25-27, 2015.
- C. Hepp, T. Müller, V. Waselowski, J. N. Becker, B. Pingault, A. Gali, J. R. Maze, M. Atatüre, and C. Becher, *Electronic Structure of the Silicon Vacancy Color Center in Diamond*, Spin-based quantum information processing, Konstanz, Germany, August 18-21, 2014.
- C. Arend, J. N. Becker, C. Hepp, and C. Becher, Coherent population trapping, photoluminescence excitation and spectral hole burning spectroscopy of silicon vacancy centers in diamond, The 65<sup>th</sup> Diamond Conference, University of Warwick, UK, July 7-10, 2014;  
(received best poster award).



# Cheers!

Zum Abschluss dieser Arbeit möchte ich die Gelegenheit nutzen, um einigen Menschen zu danken, die entscheidend zum Gelingen dieses Unterfangens beigetragen haben: Allen voran möchte ich mich bei Professor Christoph Becher dafür bedanken, dass er mir, einem Exil-Chemiker, die Möglichkeit gegeben hat, diese Arbeit unter seiner Betreuung in der Physik anzufertigen. Er war stets zu lehrreichen physikalischen Diskussionen bereit und hat es immer geschafft mich dazu zu motivieren auch das nächste, scheinbar wahnwitzige, Experiment anzugehen.

Professor Gregor Jung möchte ich an dieser Stelle für seine Bereitschaft danken diese Arbeit zu begutachten.

Bei meinen aktuellen und ehemaligen Kollegen aus der Arbeitsgruppe möchte ich mich für die schöne Zeit mit vielen lehrreichen und teils absurden Diskussionen, unterhaltsamen Konferenzaufenthalten und Ausflügen sowie für die Unterstützung bei unzähligen Messungen bedanken.

During my PhD studies I had the pleasure to spend several weeks at the Universities of Oxford and Cambridge. I would like to take this opportunity to thank Professor Mete Atatüre (University of Cambridge) and his team for their hospitality. In particular, I would like to thank Benjamin Pingault with whom I endured countless nights and weekends in the lab during the coherent population trapping experiments and who introduced me to working with liquid helium refrigerators and high-field magnets.

I would also like to thank Professor Ian Walmsley and his group (University of Oxford), in particular Dr. Joshua Nunn, Dr. Eilon Poem and Christian Weinzetl for making my visit a very pleasant and educating experience and I would like to thank them for a very productive collaboration in pioneering colour centre-based quantum memories. I am looking forward joining you in Oxford for the next couple of years and many more exciting experiments!

I'd also like to acknowledge financial support by the European COST network for funding a "Short Term Scientific Mission" and by that enabling my research visit to Oxford.

Die in dieser Arbeit präsentierten Ergebnisse wären ohne die Präparation einer neuen SiV-Probe nicht möglich gewesen. Ich möchte mich daher bei Detlef Rogalla bedanken, der mir bei der Implantation der Probe am RUBION der Universität Bochum geholfen hat und sich viel Zeit nahm, mir einen tiefen Einblick in die Funktionsweise und Bedienung des Teilchenbeschleunigers zu geben. Auch möchte ich mich bei Christoph Pauly (Lehrstuhl F. Mücklich, Universität des Saarlandes) für die Bedienung des FIB bedanken, welches zur Fabrikation der Festkörper-Immersionlinsen genutzt wurde.

Die meisten der in dieser Arbeit gezeigten Experimente wären nicht ohne eine Vielzahl von

Sonderanfertigungen aus der Metallwerkstatt möglich gewesen. Ich danke daher Michael Schmitt und seinem Team für die schnelle und passgenaue Anfertigung unzähliger und teils seltsam anmutender Bauteile und eine stets kompetente technische Beratung bei der Konstruktion dieser.

Zum Abschluss möchte ich meinen Eltern und meiner besseren Hälfte Jessica meinen herzlichsten Dank aussprechen. Ohne eure kontinuierliche Unterstützung während meines Studiums und meiner Promotion wäre all dies niemals möglich gewesen. Ihr habt mir viele Lasten von den Schultern genommen, damit ich mich voll auf die Physik konzentrieren kann, mir zahlreiche launische Phasen stets verziehen und mich bei der Vorbereitung und Durchführung meiner unzähligen und teils zeitlich eng getakteten dienstlichen Reisen immer voll unterstützt. Danke!